

Heat-affected zone in welded cold-formed rectangular hollow section joints

Yan, R.

DOI

[10.4233/uuid:49d4dd26-d228-4362-ba2b-ad9c70fa29fe](https://doi.org/10.4233/uuid:49d4dd26-d228-4362-ba2b-ad9c70fa29fe)

Publication date

2023

Document Version

Final published version

Citation (APA)

Yan, R. (2023). *Heat-affected zone in welded cold-formed rectangular hollow section joints*. [Dissertation (TU Delft), Delft University of Technology]. <https://doi.org/10.4233/uuid:49d4dd26-d228-4362-ba2b-ad9c70fa29fe>

Important note

To cite this publication, please use the final published version (if applicable). Please check the document version above.

Copyright

Other than for strictly personal use, it is not permitted to download, forward or distribute the text or part of it, without the consent of the author(s) and/or copyright holder(s), unless the work is under an open content license such as Creative Commons.

Takedown policy

Please contact us and provide details if you believe this document breaches copyrights. We will remove access to the work immediately and investigate your claim.

**HEAT-AFFECTED ZONE IN WELDED COLD-
FORMED RECTANGULAR HOLLOW SECTION
JOINTS**

HEAT-AFFECTED ZONE IN WELDED COLD-FORMED RECTANGULAR HOLLOW SECTION JOINTS

Dissertation

for the purpose of obtaining the degree of doctor
at Delft University of Technology
by the authority of the Rector Magnificus Prof.dr.ir. T.H.J.J. van der Hagen,
chair of the Board for Doctorates
to be defended publicly on
Friday 3rd February 2023 at 10:00 am

by

YAN Rui 延睿

Master of Engineering in Architectural and Civil Engineering
Harbin Institute of Technology, China
born in Xianyang, China

This dissertation has been approved by the promotor.

Composition of the doctoral committee:

Rector Magnificus	Chairperson
Prof. dr. M. Veljkovic	Delft University of Technology, promotor
Prof. dr. ir. M.A.N. Hendriks	Delft University of Technology, promotor Norwegian University of science and technology

Independent members:

Prof. dr. ir. L.J. Sluijs	Delft University of Technology
Prof. dr. -ing. M. Feldmann	RWTH Aachen University
Prof. dr. -ing. R. Stroetmann	Technische Universität Dresden
Prof. dr. X. Zhao	The Hong Kong Polytechnic University
Dr. C.L. Walters	Delft University of Technology
Prof.dr.ir. J.G. Rots	Delft University of Technology, reserve member

Keywords: Heat-affected zone, Welded connection, High-strength steel, Digital image correlation, Transverse constraint, Constitutive model, Gurson-Tvergaard-Needleman damage model, Two-scale homogenisation, Stress triaxiality, Welded hollow section joints, X-joint

Cover: Designed by Rui Yan and Yuxuan Feng

Copyright © 2022 by Rui Yan. All rights reserved.

ISBN: 978-94-6366-651-0

An electronic copy of this dissertation is available at <http://repository.tudelft.nl/>

To my beloved family

谨以此书献给我的家人们

Contents

Contents	vii
Summary	xi
Samenvatting.....	xiii
1. Introduction.....	1
1.1. Background.....	2
1.1. Objectives	2
1.2. Research questions	3
1.3. Outline of the thesis.....	4
Reference	5
2. Experimental investigation of the heat-affected zone in butt-welded cold-formed square hollow sections	7
2.1. Introduction	8
2.2. Experiments.....	10
2.2.1. Test specimens	10
2.2.2. Metallurgical investigation.....	14
2.2.3. Tensile coupon tests	15
2.2.4. DIC setup	16
2.3. Results and discussions	17
2.3.1. Metallurgical investigations	17
2.3.2. Results of standard coupon specimens	27
2.3.3. Results of welded coupon specimens.....	30
2.3.4. Discussion on the coupon test results.....	36
2.4. Conclusions	38
Reference	39
3. A method for identifying boundaries of the heat-affected zone in welded coupon specimens using digital image correlation	43
3.1. Introduction	44
3.2. Method.....	45
3.2.1. Principal strain analysis.....	45
3.2.2. Finite element analysis	46
3.2.3. Transverse constraint at the boundary of zones	48
3.3. Results and discussions	49
3.3.1. HV 0.5 hardness and microstructure results.....	49
3.3.2. Tensile test results	50
3.3.3. Comparison of the hardness and the strain ratio results	52
3.4. Conclusions	54
Reference	56
4. The constitutive model of the heat-affected zone	59

4.1.	Introduction	60
4.2.	Method.....	62
4.2.1.	Uniaxial stress-strain relationship	62
4.2.2.	A linear stress modification factor	63
4.2.3.	Finite element analysis.....	65
4.3.	Results and discussions	67
4.3.1.	Calibration of the modification factor	67
4.3.2.	Calibration results	69
4.3.3.	Effect of transverse constraint on the HAZ resistance	79
4.4.	A semi-empirical constitutive model for HAZ.....	81
4.4.1.	The theoretical model.....	81
4.4.2.	Determination of the parameters	82
4.4.3.	Results of the semi-empirical constitutive model.....	85
4.5.	Conclusions	86
	Reference	88
5.	Calibration of Gurson-Tvergaard-Needleman (GTN) damage model for the heat-affected zone and the base material.....	89
5.1.	Introduction	90
5.2.	Theoretical background	92
5.2.1.	GTN model	92
5.2.2.	Periodic boundary condition	93
5.2.3.	Undamaged uniaxial stress-strain relationship.....	94
5.3.	Calibration method	95
5.3.1.	Representative volume element models	95
5.3.2.	Correlation between the void volume fraction and initial hardening strains 96	
5.3.3.	Coupon specimen models.....	98
5.4.	Results	99
5.4.1.	Identification of parameters q_1 and q_2	99
5.4.2.	Calibration of the parameters f_c and f_f	102
5.4.3.	Validation against notched coupon specimens.....	103
5.5.	Conclusions	113
	Reference	114
	Appendix.....	117
6.	Experimental investigation on the tensile behaviour of welded rectangular hollow section X-joints	119
6.1.	Introduction	120
6.2.	Experiments.....	125
6.2.1.	X-joint tensile tests.....	125
6.2.2.	Tensile coupon tests	128
6.3.	Results and discussions	130
6.3.1.	Coupon test results	130
6.3.2.	X-joint test results	130
6.3.3.	Characterization of the joint yield resistance	134

6.3.4.	Comparison of experimental and semi-analytical results	135
6.3.5.	Comparison of specific failure modes	139
6.4.	Conclusions	143
	Reference	145
	Appendix	148
7.	Fracture simulation of welded rectangular hollow section X-joints using Gurson-Tvergaard-Needleman (GTN) damage model	155
7.1.	Introduction	156
7.2.	Finite element analysis	157
7.2.1.	X-joint models	157
7.2.2.	Calibrated material damage model	159
7.2.3.	A semi-empirical material damage model	160
7.3.	Results and discussions	162
7.3.1.	Using the calibrated material model	162
7.3.2.	Without considering HAZ	166
7.3.3.	Using the semi-empirical material model	169
7.4.	Conclusions	173
	Reference	175
	Appendix	177
8.	Conclusions and future work	179
8.1.	Conclusions	180
8.2.	Future work	182
	Acknowledgement	185
	Curriculum vitae	189
	List of publications	191

Summary

High-strength steel (HSS) has higher strength but lower ductility than mild steel. The cross-section of the structural members may be reduced using HSS instead of mild steel, provided the buckling of elements does not govern the failure. The reduced member size benefits the environment and economy by means of less energy consumption, less carbon dioxide emission, and less labour work during the fabrication and structure construction stages.

The current design rules in prEN 1993-1-8 for welded hollow section joints are developed based on extensive experimental and numerical studies on joints made of mild steel (S235 and S355). A material factor C_f is stipulated to reduce the design resistance of the joint given the lower ductility of HSS than mild steel. In addition, the design yield strength of the material should be lower than 0.8 times the ultimate strength (f_u) to calculate the resistance of punching shear failure and tension brace failure. However, these two strength restrictions are proposed based on limited experimental and numerical investigations on welded HSS tubular joints. The mechanical background behind the two restrictions is vague. Applying both C_f and the $0.8f_u$ restriction would eliminate the benefits of using HSS, reducing the competitiveness in the market. Besides, the heat-affected zone (HAZ) often has the lowest strength in a weld region. The strength difference between HAZ and the base material (BM) is more significant for HSS than mild steel, indicating that HAZ plays a more critical role in welded HSS joints. Hence, the HAZ constitutive model should be considered in the numerical study of welded HSS joints in order to predict the load-deformation relationship and failure mode correctly.

This dissertation proposes a systematic approach to include HAZ in the finite element (FE) analysis of welded joints considering ductile failure mode. First, the mechanical and geometrical properties of HAZ were obtained from tensile tests on the milled welded coupon specimen, the low-force Vickers hardness test, and the microstructure observation. The full-field deformation of the milled welded coupon specimen was measured using the digital image correlation (DIC) technique. Using the DIC result, a method is proposed to identify the boundaries of different regions in the milled welded coupon specimen. The identified boundary matches the hardness result well. Based on the identified boundaries, the width of HAZ and the weld metal (WM) are determined, which provides geometric information for the measuring range of the virtual extensometer in DIC and for creating the FE model with different partitions (HAZ, BM, and WM). Due to the transverse constraint imposed by BM and WM, HAZ was under a biaxial or triaxial stress state during the tensile coupon test. The measured stress of HAZ is higher than that under the uniaxial stress state at a given strain. Hence, a method is proposed to correct the measured stress-strain relationship of HAZ. The modified stress-

strain relationship is successfully validated against the tensile coupon test regarding the load-deformation relationship and the strain distribution on the specimen surface.

In order to accurately predict the load-deformation relationship and failure mode of welded joints, the Gurson-Tvergaard-Needleman (GTN) damage model is employed to simulate the failure of HAZ and BM. A computational homogenization analysis using representative volume element models was carried out to calibrate the yield-surface-related parameters (q_1 , q_2 , and q_3). The effect of the hydrostatic pressure, the accumulated initial hardening strain, and the void volume fraction (VVF) on the yield surface were evaluated. An equation is proposed to describe the relationship between VVF and q_1 value with a constant q_2 . The fracture-related parameters (f_c and f_f) were calibrated against the tensile coupon test. In addition, as the procedures for modifying the constitutive model and calibrating the damage model are rather complicated, a semi-empirical material damage model for HAZ correlating to the mechanical properties of BM is proposed to facilitate the FE analysis of welded joints.

Monotonic tensile tests were conducted on 18 welded cold-formed rectangular hollow section (RHS) X-joints made of S355, S500, and S700 to investigate the validity of C_f and the $0.8f_u$ restriction. The test result shows that a conservative resistance is predicted using the current design rules without applying C_f and the $0.8f_u$ restriction. The calibrated GTN damage model for HAZ and BM was implemented in the fracture simulation of welded X-joints. The FE results agree well with the experimental results concerning the load-deformation relationship and the failure mode. Based on the validated X-joint FE model, the importance of including HAZ in the FE model was revealed by the FE analysis without the HAZ constitutive model. Finally, the semi-empirical material damage model for HAZ was employed to predict the tensile behaviour of all 18 welded X-joints.

Samenvatting

Hoge-sterktestaal (HSS) heeft een hogere sterkte maar een lagere ductiliteit dan conventioneel staal. De doorsnede van de constructiedelen kan worden gereduceerd door gebruik te maken van HSS ten opzichte van conventioneel staal, op voorwaarde dat knik niet de maatgevende bezwijkvorm wordt. Een kleinere doorsnede heeft gunstige gevolgen voor het milieu en de economie omdat er minder energie wordt verbruikt, minder kooldioxide wordt uitgestoten en er minder arbeidsuren nodig zijn tijdens de productie en de bouw van de constructie.

De huidige ontwerpvoorschriften in prEN 1993-1-8 voor gelaste buisverbindingen zijn gebaseerd op uitgebreide experimentele en numerieke studies naar verbindingen gemaakt van conventioneel staal (S235 en S355). Een materiaalfactor C_f is voorgeschreven om de rekenwaarde van de weerstand van de verbinding te reduceren gezien de lage ductiliteit van HSS. Bovendien moet de vloeigrens (f_y) van het materiaal lager zijn dan 0.8 maal de treksterkte (f_u) voor de berekening van de rekenwaarde van weerstand tegen bezwijken van de wandstaaf en bezwijken door ponsen. Deze twee sterktebeperkingen worden echter voorgesteld op grond van beperkt experimenteel en numeriek onderzoek naar gelaste HSS-buisverbindingen. De technische achtergrond van de twee beperkingen is onduidelijk. De toepassing van zowel C_f als de $0.8f_u$ beperking elimineert de voordelen van de toepassing van HSS, waardoor het concurrentievermogen op de markt afneemt. Verder heeft de warmte-beïnvloede zone (WBZ) vaak de laagste sterkte in een laszone. Het sterkteverschil tussen WBZ en het moedermateriaal (BM) is groter voor HSS dan voor conventioneel staal, wat erop wijst dat WBZ een kritischere rol speelt in gelaste HSS-verbindingen. Vandaar dat in de numerieke studie naar gelaste HSS-verbindingen het WBZ-constitutieve model in aanmerking moet worden genomen om de kracht-vervormingsrelatie en de bezwijkvorm op een correcte manier te voorspellen.

Dit proefschrift beoogt een systematische benadering voor te stellen om WBZ met een ductiele bezwijkvorm op te nemen in de eindige elementen (EE) analyse van lasverbindingen. Eerst zijn de mechanische en geometrische eigenschappen van de WBZ bepaald door het uitvoeren van trekproeven op gefreesde proefstukken, Vickers-hardheidsproef met lage kracht en de analyse van de microstructuur. De volledige veldvervorming van het gefreesde gelaste proefstuk werd gemeten met behulp van de digitale beeld correlatie (DIC) techniek. Met behulp van het DIC-resultaat wordt een methode voorgesteld om de grenzen van de verschillende zones in het gefreesde gelaste proefstuk vast te stellen. De geïdentificeerde grenzen komen goed overeen met het hardheidsresultaat. Op basis van de geïdentificeerde grenzen wordt de breedte van de WBZ en het lasmetaal (LM) bepaald, die geometrische informatie oplevert voor het meetbereik van de virtuele extensometer in DIC en voor het maken van het EE-model

met verschillende delen (WBZ, BM en LM). Als gevolg van de dwarse oplegging van BM en LM stond WBZ tijdens de trekproef onder een biaxiale of triaxiale spanning. De gemeten spanning van WBZ is hoger dan de spanning onder uniaxiale toestand bij een gegeven rek. Daarom wordt een methode voorgesteld om de gemeten spanning-rek relatie van WBZ te corrigeren. De aangepaste spanning-rek relatie is met succes gevalideerd ten opzichte van de trekproef waarbij de relatie tussen kracht en vervorming en de rekverdeling over het proefstukoppervlak is vastgesteld.

Om de kracht-vervormingsrelatie en de bezwijkvorm van gelaste verbindingen nauwkeurig te voorspellen, wordt het Gurson-Tvergaard-Needleman (GTN) schade model gebruikt om de bezwijkvormen in WBZ en BM te simuleren. Een numerieke analyse met behulp van representatieve volume-elementmodellen werd uitgevoerd om de parameters van het vloeigedeelte (q_1 , q_2 en q_3) te kalibreren. Het effect van de hydrostatische druk, de geaccumuleerde initiële verhardingsspanning en de poriën volumefractie (VVF) op het vloeigedeelte werden geëvalueerd. Er wordt een vergelijking voorgesteld om de relatie tussen VVF en q_1 waarde te beschrijven met een constante q_2 . De breuk-gerelateerde parameters (f_c en f_t) werden gekalibreerd aan de hand van de trekproef. Aangezien de procedures voor het wijzigen van het constitutieve model en het kalibreren van het schademodel nogal ingewikkeld zijn, wordt daarnaast een semi-empirisch materiaalschademodel voor WBZ voorgesteld dat gecorreleerd is met de mechanische eigenschappen van BM om de EE-analyse van lasverbindingen te vergemakkelijken.

Trekproeven zijn uitgevoerd op 18 gelaste koudgevormde kokervormige X-verbindingen gemaakt van S355, S500 en S700 om de geldigheid van C_f en de $0.8f_u$ -beperking te onderzoeken. De test resultaten tonen aan dat de huidige ontwerpvoorschriften een conservatieve weerstand voorspellen wanneer de C_f en de $0.8f_u$ -restrictie niet worden toegepast. Het gekalibreerde GTN-schademodel voor WBZ en BM werd toegepast in de breuksimulatie van de gelaste X-verbindingen. De EE-resultaten komen goed overeen met de experimentele resultaten met betrekking tot de kracht-vervormingsrelatie en de bezwijkvorm. Op basis van het gevalideerde EE-model voor de X-verbindingen werd het belang van het opnemen van WBZ in het EE-model aangetoond door deze te vergelijken met de resultaten van de EE-analyse zonder het WBZ-constitutieve model. Tenslotte werd het semi-empirische materiaalschademodel voor WBZ gebruikt om het trekgedrag van alle 18 gelaste X-verbindingen te voorspellen.

1.

Introduction

1.1. Background

Global warming threatens people's lives in many aspects, such as extreme weather and the water shortage. The rising temperature is mainly due to the excessive emissions of carbon dioxide (CO₂) and other air pollutants. In 2020, the construction sector accounted for 36% of global final energy consumption and 37% of energy-related CO₂ emissions, compared to other end-use industries [1]. In order to reduce the environmental impact of the construction sector, pioneers have put great effort into applying high performance materials in structures, such as high-strength steel (HSS). Compared to mild steel ($f_y \leq 460$ MPa), HSS has a higher yield strength ($460 \text{ MPa} < f_y \leq 700$ MPa). The size of structural members can be effectively reduced using HSS, resulting in a lower self-weight, less welding for thinner profiles, and, consequently, substantial economic and environmental benefits.

Due to the advanced material manufacturing techniques, such as the Thermo-mechanical control process (TMCP) and Quenching & Tempering (QT), HSS hollow sections have become more readily available in recent years. To design welded hollow section joints, the standard EN 1993-1-8 [2] presents a series of design rules developed based on extensive experimental and numerical investigations on joints made of mild steel (S235 and S355). A material factor (C_f) of 0.9 for reducing the design resistance has been stipulated for joints using materials higher than S355 and up to S460. C_f is extended for steel grade up to S700 in EN 1993-1-12 [3] and the newest vision of prEN1993-1-8 [4]. In addition, a yield strength restriction is imposed for punching shear failure (PSF) and tension brace failure (BF), stating that in design, the value of the yield strength should be limited to 0.8 times the ultimate strength (f_u). However, applying both C_f and the $0.8f_u$ restriction partially eliminates the benefits of using HSS, limiting its competitiveness. Given the limited experimental and numerical studies on welded HSS hollow section joints, rather conservative C_f and the $0.8f_u$ restriction are proposed. Hence, the validity of C_f and the $0.8f_u$ restriction should be investigated.

On the other hand, the heat-affected zone (HAZ) often has a lower strength compared to the base material (BM) and the weld metal (WM). The HAZ strength degradation is more significant for HSS than mild steel, which is not considered in the current design rules [2–4]. Hence, an effective method to obtain HAZ stress-strain relationship should be developed for the advanced finite element (FE) analysis considering HAZ.

1.1. Objectives

The validity of C_f and the $0.8f_u$ restriction for welded HSS cold-formed rectangular hollow section (RHS) X-joints in tension can be evaluated through experimental and numerical studies. As the joints often fail in HAZ, a validated damage model for HAZ is essential for the FE analysis of welded joints. The final goal of this dissertation is to provide a systematic approach to include HAZ in the FE model of welded joints, which could be further used in numerical studies to evaluate the necessity of C_f and the $0.8f_u$ restriction. In order to achieve this goal, five objectives are planned as follows:

The first objective is to obtain the stress-strain relationship of HAZ through the tensile test on the milled welded coupon specimen. The engineering stress-strain relationship is measured from the digital image correlation (DIC) result. The measured constitutive model is then corrected and validated based on the FE analysis and the DIC result.

The second objective is to calibrate the Gurson-Tvergaard-Needleman (GTN) damage model for HAZ and BM. The calibrated damage model could be used in the fracture simulation of the welded cold-formed RHS X-joint to predict the ultimate resistance and failure mode.

The third objective is to propose a generic semi-empirical material damage model for HAZ, based on the mechanical properties of BM, to simplify the procedures of including HAZ in the FE analysis of welded hollow section joints.

The fourth objective is to investigate the HAZ width for different profile thicknesses and material steel grades. A generic HAZ width is needed for creating HAZ in X-joint FE models.

The fifth objective is to conduct monotonic tensile tests on welded cold-formed RHS X-joints to evaluate the necessity of C_f and the $0.8f_u$ restriction experimentally.

The sixth objective is to validate the X-joint FE model against the experiment using the calibrated GTN damage model. The necessity of including HAZ in the FE model and the validity of the semi-empirical model for HAZ should be evaluated.

1.2. Research questions

The research questions corresponding to each objective are presented below:

- How to determine the measuring range of HAZ in the milled welded coupon specimen using the DIC result? What HAZ and WM width should be used in generating the FE model? How to correct the overestimated stress in the measured stress-strain relationship of HAZ due to the transverse constraint?
- How to calibrate the GTN damage model, considering the different combinations of the accumulated initial hardening strain and the void volume fraction (VVF) due to a varying stress triaxiality?
- How to establish a semi-empirical material damage model for HAZ based on the mechanical properties of BM?
- What is the varying range of the HAZ width in profiles with different steel grades and thicknesses? Could a generic HAZ width be determined for the X-joint model?
- Could the current design rule predict a safe resistance for the tested X-joints without applying C_f and the $0.8f_u$ restriction?
- Could the X-joint FE model, using the generic HAZ width and the calibrated GTN model for HAZ and BM, correctly predict the load-deformation

relationship and failure mode? What if the HAZ is not included in the FE model?
What if the semi-empirical damage model for HAZ is used?

1.3. Outline of the thesis

The thesis contains eight chapters. The outline of each chapter is as follows:

Chapter 1 introduces the research background, objectives, and research questions of the thesis.

Chapter 2 presents the conducted experiments on the butt-welded cold-formed RHS connection. The geometric and mechanical properties of HAZ are investigated based on the low-force Vickers hardness tests, the microstructure observation, and the tensile coupon test. The width of HAZ and the engineering stress-strain relationship of HAZ and WM are obtained from experiments.

Chapter 3 develops a method to identify the boundary of different zones in DIC results. Consequently, the width of HAZ and WM is determined. The identified HAZ and WM regions are verified against hardness results.

Chapter 4 proposes a method to determine the true stress-strain relationship of HAZ. The effect of the transverse constraint, imposed by BM and/or WM, on the measured stress of HAZ is eliminated by a linear modification factor correlating to the true strain. The modification factor is calibrated through a trial-and-error process based on the FE analysis. In addition, a semi-empirical constitutive model is proposed for HAZ based on the mechanical properties of BM.

Chapter 5 focuses on the calibration of the GTN damage model for HAZ and BM. The yield-surface-related parameters (q_1 , q_2 , and q_3) are calibrated through a computational homogenization analysis using representative volume element models. The effect of hydrostatic pressure, the accumulated initial hardening strain, and the void volume fraction (VVF) on the yield surface are evaluated. An equation is proposed to describe the relationship between VVF and q_1 value. The parameters f_c and f_t are calibrated against tensile coupon tests, including standard coupon specimens for BM and milled welded coupon specimens for HAZ.

Chapter 6 evaluates the validity of C_f and the $0.8f_u$ restriction experimentally based on 18 monotonic tensile tests on welded cold-formed RHS X-joints. Besides, a bi-linear model, which is suitable for an elasto-plastic global analysis considering the post-yielding stiffness, is proposed to characterize the non-linear behaviour of the joint.

Chapter 7 implements the calibrated GTN model in the fracture simulation of welded X-joints. The X-joint FE model is validated against the experiment. The necessity of including HAZ in the FE model is discussed by conducting an FE analysis without considering the HAZ constitutive model. Besides, the semi-empirical HAZ constitutive model is extended to a semi-empirical material damage model, which is further used in the X-joint simulation of all 18 tested joints.

Chapter 8 summarises the key conclusions of the thesis and provides recommendations for future study.

Reference

- [1] I. Hamilton, O. Rapf, D.J. Kockat, D.S. Zuhaib, 2021 global status report for buildings and construction, United Nations Environmental Programme. (2020).
- [2] EN 1993-1-8:2005 - Design of steel structures - Part 1-8: Design of joints, (2005).
- [3] EN 1993-1-12:2007 - design of steel structures - part 1–12: additional rules for the extension of EN 1993 up to steel grades S700, (2007).
- [4] prEN 1993-1-8:2021 - Design of steel structures - Part 1-8: Design of joints, (2022).

2.

Experimental investigation of the heat-affected zone in butt-welded cold-formed square hollow sections

In this chapter, the material properties of the heat-affected zone (HAZ) in butt-welded hollow section connections are investigated experimentally. Vickers hardness and microstructure investigations are reported for determining the HAZ hardness variations and the width of HAZ. The stress-strain relationships of HAZ, the weld metal (WM), and the base material (BM) are measured from tensile coupon tests.

This chapter is organised as follows. Section 2.1 introduces four major approaches for obtaining HAZ stress-strain relationship. The design of the experiment, including the specimens and the setup, is presented in Section 2.2. The test results are shown and discussed in Section 2.3. Finally, the conclusions are drawn in Section 2.4.

Parts of this chapter appear in the journal article: ‘Rui Yan et al., Equivalent material properties of the heat-affected zone in welded cold-formed rectangular hollow section connections, Thin-walled structures, 2022’. Minor modifications have been made to suit the thesis.

2.1. Introduction

In steel construction, welding is one of the most essential methods of joining steel parts. A welded connection comprises three main zones, namely the base material (BM), the heat-affected zone (HAZ), and the weld metal (WM). The mechanical properties of HAZ depend on several parameters, such as the steel manufacturing process, the cooling time from 800°C to 500°C ($t_{8/5}$) during welding, and the heat input [1,2]. HAZ may have comparable strength to BM for Quenching and Tempering (QT) steels with a low heat input [1,3–5]. Otherwise, a significant strength degradation in HAZ may be observed for QT and Thermo-Mechanically Controlled Process (TMCP) steels [1,6], especially for high-strength steels (HSS). The difference in the strength degradation in HAZ could also be observed from the hardness test results, as the hardness reflects the material strength. The test results available in literature, which have similar steel grades to the material investigated in this study, are presented in Table 2.1. A limited strength degradation in HAZ was observed from S420 and S500 materials with low heat input, while the strength degradation in S700 may reach up to 23%, as found in [7].

Table 2.1 Comparison of HAZ hardness reduction.

References	Steel grade	Yield strength [MPa]	Processing method	Heat input [kJ/mm]	Hardness reduction in HAZ [%]
Pisarski and Dolby, 2003 [8]	RQT 501	550	QT	2.40	16-24
Hochhauser et al., 2012 [9]	S700	700	TMCP	0.42-0.76	12-16
Khurshid et al., 2015 [10]	S700	700	TMCP	0.41	16
	S420	420		0.48-1.48	0.3-7.5
Nguyen, 2018, [7]	S500	500	TMCP	0.48-1.47	1.7-12
	S700	700		0.61-1.37	19-23
	Q550	550	QT	1-1.9	9-15
	Q550	550	TMCP	1-1.9	11-17
Cai et al., 2022, [6]	Q690	690	QT	1-1.9	9-20
	Q690	690	TMCP	1-1.9	15-21

Three approaches have been proposed in the literature to directly obtain the HAZ stress-strain relationship from the tensile coupon tests. In the first approach (micro specimen approach), a micro tensile coupon specimen fabricated from a single material zone, such as HAZ, can be used to establish the stress-strain constitutive model [11–14]. The advantage of this method is that the stress and strain of a single zone could be directly measured from the experiment, provided that the testing material in one specimen is homogeneous. However, the microstructure of HAZ varies in directions perpendicular to the welding seam direction, resulting in an irregular width of HAZ. It is rather difficult to ensure the homogeneity of the material in the micro-specimen. In addition, the fabrication and testing procedures are time-consuming and costly compared to the standard coupon tests. Alternatively, a thermal simulation machine can be employed to reproduce the temperature-time history in different HAZ sub-zones of a welded connection [1,4,15]. In this approach (thermal simulation approach), the thermal cycles are applied on steel plates to make the microstructure identical to the corresponding HAZ sub-zone. Note that obtaining a homogenous HAZ microstructure is essential for this method in order to correctly calibrate the material model for each zone. Finally, the constitutive models of each HAZ sub-zones are obtained using the coupon specimens fabricated from the thermal-treated plates.

In another (semi-)direct approach (equivalent material approach), a coupon specimen with a butt weld in the middle transverse to the loading direction is tested in tension to establish the stress-strain relationship of HAZ and WM, using the digital image correlation (DIC) measuring technique [16–25]. The specimen is often milled to a thin layer before testing to obtain a constant width of HAZ through the thickness. Note that the measured stress-strain relationship of WM is extended using a theoretical model to complete the relationship when the weld failure doesn't occur. This approach is often accompanied by an inverse method to calibrate the material constitutive model of HAZ with the aid of finite element (FE) analysis. In the inverse method, the constitutive model is calibrated by fitting the FE results to the experimental results. The key parameters are adjusted based on the difference between FE and experimental results. The stress is obtained based on the uniform stress assumption [16], which is the total load divided by the cross-sectional area. The strain is derived using the measured local deformation of each zone. Note that the initial gauge length for measuring the local deformation may vary in different zones.

In addition to the three direct approaches, attempts have been made to generate the HAZ constitutive model through two indirect experimental approaches. Firstly, the Vickers hardness test [6,14,26,27] can be used to predict the material yield and ultimate strength according to the empirical correlation between the material hardness and strength. The constitutive model parameters are determined based on the material strength derived from the material hardness. Another indirect approach evaluates the material constitutive model by the highest temperature measured during the welding process [28,29]. First, a thermal FEA is conducted to obtain the highest temperature of each element in a welded connection. Then, every element in the mechanical FEA is assigned a modified stress-strain relationship depending on the highest temperature. Finally, the material model is

validated by comparing the load-deformation relationships obtained from the experiment and FEA.

In this chapter, nine butt-welded cold-formed rectangular hollow section connections, encompassing three steel grades and three thicknesses, were used to investigate the geometric and mechanical properties of HAZ. The low-force Vickers hardness tests and microstructure observation were conducted to determine the width of HAZ and investigate the hardness deterioration in HAZ. The stress-strain relationship of HAZ and WM was obtained from the tensile coupon tests.

2.2. Experiments

2.2.1. Test specimens

The stress-strain constitutive model of HAZ is investigated using nine profiles in three steel grades (S355J2H, S500MH, and S700MLH) and three thicknesses for each steel grade (4 or 5 mm, 8 mm, and 10 mm). Note that the S355 material has double steel grades S355J2H/S420MH. Five nominally identical tubular specimens for each profile were fabricated by welding two tube pieces together, as shown in Fig. 2.1. The profiles were square hollow sections (SHS) except for one rectangular hollow section (RHS) with a 5 mm thickness made of S355. The profile nominal dimensions, the thickness (t), and the outer corner radius (r) of the hollow sections are presented in Table 2.2. The material name of each profile consists of the steel grade and the nominal thickness. For example, S355t8 stands for the profile with S355 material and 8 mm nominal thickness. All tubes were manufactured by cold-forming thermo-mechanically rolled steel strips.



a) S355t5.



b) S355t8.



c) S355t10.



d) S500t4.



e) S500t8.



f) S500t10.



g) S700t5.



h) S700t8.



i) S700t10.

Fig. 2.1 Welded tubes.

Table 2.2 Nominal dimensions of hollow sections and the position of coupon specimens.

Material	Steel grade	Profile	t [mm]	r [mm]	d [mm]
S355t5		100×50×5	5	9	20
S355t8	S355	140×140×8	8	20	25
S355t10		160×160×10	10	25	35
S500t4		140×140×4	4	8.5	25
S500t8	S500	140×140×8	8	20	25
S500t10		160×160×10	10	25	35
S700t5		120×120×5	5	9	25
S700t8	S700	120×120×8	8	20	26
S700t10		120×120×10	10	25	17

A single-bevel V groove was prepared for both tubes in a connection before welding, as shown in Fig. 2.2. Two beveled tubes were manually welded by a full-penetration butt weld at a Dutch fabricator experienced in welding high-strength steels. The metal active gas (MAG) welding process was used according to the standard EN ISO 3834-2:2005 [30]. The minimum preheat temperature and the maximum interpass temperature were 20 °C and 200 °C, respectively. The heat input ranged between 1 kJ/mm and 1.4 kJ/mm. The shield gas contained 60% Ar, 30% He, and 10% CO₂. The filler metal Carbofil 1 was used for S355 tubes, whereas S500 and S700 tubes were welded by Union NiMoCr. The mechanical properties of filler metals provided by the fabricator are presented in Table 2.3. The chemical compositions of the base material and the filler metal given in the product certificate in weight percentage are shown in Table 2.4.

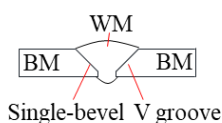


Fig. 2.2 The cross section of the weld zone.

Table 2.3 Mechanical properties of filler metals.

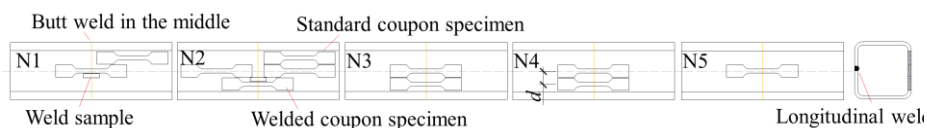
Material	Yield strength [MPa]	Tensile strength [MPa]	A [%]
Carbofil 1	502	574	28
Union NiMoCr	720	780	17

where A is the percentage elongation after the fracture based on the 5.65 coefficient of proportionality, according to [31].

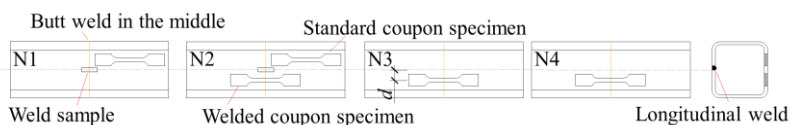
Table 2.4 Nominal chemical composition of the base material and the filler metal [wt%].

Material	C	Si	Mn	P	S	Cr	Ni	Cu	Mo	Ti	Al
S355t5	0.07	0.19	1.43	0.013	0.010	0.047	0.044	0.019	0.010	0.014	0.026
S355t8	0.07	0.19	1.42	0.012	0.006	0.051	0.037	0.015	0.008	0.015	0.037
S355t10	0.08	0.19	1.43	0.012	0.004	0.040	0.036	0.013	0.002	0.018	0.037
S500t4	0.06	0.19	1.20	0.011	0.004	0.047	0.036	0.015	0.003	0.002	0.036
S500t8	0.06	0.17	1.21	0.010	0.004	0.044	0.037	0.012	0.003	0.002	0.031
S500t10	0.05	0.17	1.19	0.009	0.003	0.037	0.035	0.012	0.005	0.002	0.030
S700t5	0.06	0.21	1.72	0.012	0.001	0.055	0.043	0.209	0.011	0.100	0.032
S700t8	0.05	0.19	1.81	0.011	0.002	0.041	0.037	0.014	0.005	0.110	0.036
S700t10	0.06	0.18	1.81	0.011	0.003	0.045	0.034	0.012	0.005	0.113	0.041
Carbofil 1	0.078	0.85	1.45	0.008	0.004	0.03	0.01	0.01	0.01	0.02	<0.01
Union Nimocr	0.09	0.61	1.71	0.005	0.01	0.19	1.47	0.03	0.51	0.06	<0.01

Three types of specimens were fabricated by water-jet cutting from the flat part of the wall opposite the side with the longitudinal weld, as depicted in Fig. 2.3. Conventional coupon specimens were extracted to obtain the BM stress-strain relationship. Two weld samples, cut from welded tubes (N1 and N2), were used to conduct the low-force Vickers hardness test (HV 0.5) and the microstructure observation. Welded coupon specimens with a butt weld in the middle were taken from the fabricated tube. Due to the weld reinforcement, the uniform stress assumption is not valid for HAZ, and the deformation of a distinct material zone (HAZ or WM) is not measurable using DIC. Hence, the welded coupon specimen was milled to a central thickness zone of 3 mm to have as "parallel" as possible boundaries of HAZ and "perpendicular" to the applied load. In addition, since the S355t10, S500t10, and S700t8 tubes were sufficiently wide, one additional row of coupon specimens was cut from the centre of the tube. Two extra welded specimens were not milled (weld reinforcement remained) to investigate the tensile behaviour of the complete weld zone. The two cutting schemes for the wide and narrow tubes are presented in Fig. 2.3. Note that the specimens, except for the central specimens, were symmetrically positioned around the central axis of the tube with a distance (d), as shown in Table 2.2.



a) For wide profiles (S355t10, S500t10, S700t8).



b) For narrow profiles (S355t5, S355t8, S500t4, S500t8, S700t5, S700t10).

Fig. 2.3 Specimen cutting scheme.

The coupon specimen was designed with a 5.65 proportional coefficient following EN ISO 6892-1 [31]. The basic dimensions of the coupon specimen are presented in Fig. 2.4. The measured width (b_0) and thickness (t_0) before tests are summarized in Table 2.5, where the abbreviation 'No.' indicates the tube number. 'W' and 'UMW' stand for the milled and unmilled welded coupon specimens, respectively. The last letter, 'M', indicates the specimen was taken from the centre row of the tube. Note there is no defined thickness for the unmilled welded coupon since the weld reinforcement results in a varying thickness. Besides, specimen S700t5WN2 is not available.

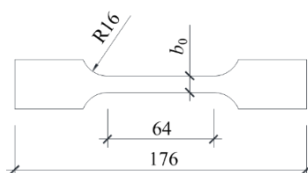


Fig. 2.4 Basic dimensions of coupon specimen.

Table 2.5 Measured dimensions and annotation of coupon specimens.

Material	No.	Standard [mm]		No.	Milled welded [mm]		No.	Unmilled welded [mm]	
		t_0	b_0		t_0	b_0		t_0	b_0
S355t5	N1	4.9	16.0	WN2	3.0	16.0	-	-	-
	N2	4.9	16.0	WN3	3.0	15.6	-	-	-
	-	-	-	WN4	3.0	16.0	-	-	-
S355t8	N1	8.1	10.0	WN2	3.0	10.1	-	-	-
	N2	8.1	10.0	WN3	3.0	9.9	-	-	-

	-	-	-	WN4	3.0	10.0	-	-	-
S355t10	N1	10.0	8.2	WN2	3.0	8.0	UMWN1M	-	7.9
	N2	9.9	8.0	WN3	3.0	8.1	UMWN5M	-	8.1
	N2M1	9.8	7.9	WN3M	3.0	8.0	-	-	-
	N2M2	9.8	8.0	WN4	3.0	8.0	-	-	-
	-	-	-	WN4M	3.0	8.0	-	-	-
S500t4	N1	4.0	20.2	WN2	3.0	19.8	-	-	-
	N2	4.0	20.2	WN3	3.0	9.9	-	-	-
	-	-	-	WN4	3.0	9.9	-	-	-
S500t8	N1	7.9	10.1	WN2	3.0	10.0	-	-	-
	N2	7.9	10.0	WN3	3.0	9.9	-	-	-
	-	-	-	WN4	3.0	9.9	-	-	-
S500t10	N1	9.8	7.9	WN2	3.0	7.9	UMWN1M	-	7.8
	N2	9.9	8.0	WN3	3.0	8.0	UMWN5M	-	8.0
	N2M1	9.8	8.0	WN3M	3.0	8.0	-	-	-
	N2M2	10.0	8.0	WN4	3.0	8.1	-	-	-
	-	-	-	WN4M	3.0	8.0	-	-	-
S700t5	N1	5.0	16.1	WN2	-	-	-	-	-
	N2	5.1	16.2	WN3	2.9	19.9	-	-	-
	-	-	-	WN4	3.0	19.9	-	-	-
S700t8	N1	7.9	10.1	WN2	3.0	10.0	UMWN1M	-	9.9
	N2	7.9	10.1	WN3	3.0	10.0	UMWN5M	-	10.1
	N2M1	7.7	10.9	WN3M	3.0	10.1	-	-	-
	N2M2	7.8	10.4	WN4	2.9	9.9	-	-	-
	-	-	-	WN4M	3.0	10.0	-	-	-
S700t10	N1	10.0	8.1	WN2	3.0	7.9	-	-	-
	N2	10.0	8.0	WN3	3.0	8.0	-	-	-
	-	-	-	WN4	2.9	7.6	-	-	-

2.2.2. Metallurgical investigation

The weld sample of 40 mm, including an entire weld zone composed of BM, HAZ, and WM, was prepared for the metallurgical investigation and low-force Vickers hardness measurement. First, the sample was mounted in resin, allowing for convenient handling for subsequent operations. The sample was then sanded using SiC abrasive papers with 196 μm , 75 μm , 46 μm , 21.8 μm , 15.2 μm , and 10 μm grit. Next, the sample was polished using MD/DP-Nap (1 μm cloth) to achieve a perfect mirror-like surface. Then, the 2% Nital solution was used to etch the prepared surface until the reflective surface became gloomy. The etching time was approximately 25 s. Finally, a Keyence VHX-7000 digital microscope was employed to observe the microstructure of the etched surface.

Since a mirror-like surface is preferred for the HV 0.5 hardness test, the polishing procedure was repeated after the microstructure observation. The standard HV 0.5 test [32,33] was conducted by an EMCO DuraScan 70 G5 automatic hardness tester. Fig. 2.5 shows the four indentation lines (in blue) for 8 mm and 10 mm thick samples, while three

indentation lines were made on 4 mm and 5 mm thick samples. The parameter y_i describes the distance from the top edge of the surface to each indentation line. An overview of the used y_i is shown in Table 2.6. The orange lines in Fig. 2.5 indicate the HAZ boundary preliminarily identified by the observed microstructure. A 0.25 mm interval of indentation was used in regions including and close to HAZ, while a 1 mm interval was applied for the other regions. Note that the boundary identified by the microstructure is only used to determine approximate boundaries for the dense (0.25 mm interval) hardness test. Fig. 2.6 presents the employed samples for metallurgical investigation.

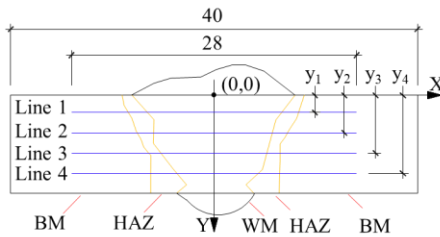


Fig. 2.5 Hardness testing scheme [mm].

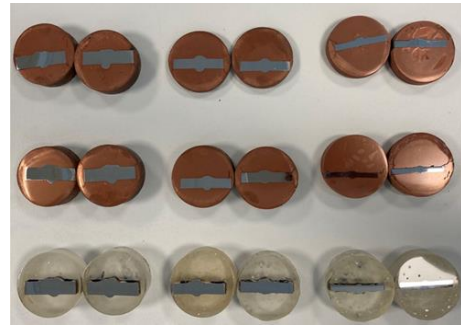


Fig. 2.6 Samples for the metallurgical investigation.

Table 2.6 The distance of the indentation line from the top edge [mm].

Material	y_1	y_2	y_3	y_4
S355t5, S500t4, S700t5	0.5	2.0	3.5	-
S355t8, S500t8, S700t8	1.5	3.0	5.0	6.5
S355t10, S500t10, S700t10	2.0	4.0	6.0	8.0

2.2.3. Tensile coupon tests

An Instron testing machine with 200 kN capacity was used to conduct the tensile coupon tests. Displacement-controlled loading with the rate of 0.01 mm/s was employed, according to the requirements in [31]. Since the proportional coefficient of the coupon specimen was 5.65, the initial gauge length for all coupon specimens was 50 mm. The coupon specimens for BM have an initial bow due to residual stresses generated in the tube during the cold-forming process. An extensometer was installed on the concave side of the specimen. In addition to the extensometer, a 3D DIC (ARAMIS) was employed to measure the deformation on the convex side, as shown in Fig. 2.7. The load-deformation relationships measured from the two devices were averaged to eliminate the effect of the initial bow [34]. The same measuring scheme applies to the milled welded coupon specimen. The DIC and the extensometer results were identical, as the milled coupon specimens were not curved. Hence, the testing results only from 3D DIC were used. For

the unmilled coupon specimens, 3D DIC measured the deformation on the side with the complete weld zone, as shown in Fig. 2.8.

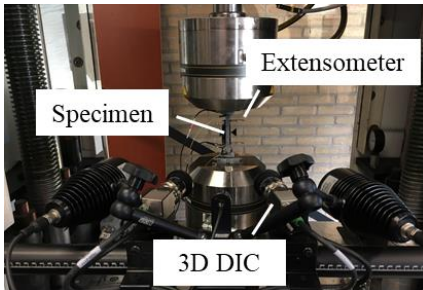


Fig. 2.7 Arrangement of measurements in the tensile test.



Fig. 2.8 Measured surface of the unmilled welded coupon specimen.

2.2.4. DIC setup

The specimen's surface, facing the DIC camera, was prepared with a speckle pattern. The quality of the speckle has a significant influence on the accuracy of the results. Reu [35,36] suggests that the speckle size should be between 3-by-3 and 7-by-7 pixels. The imaging resolution is 67 microns/pixel (150 pixels for 10 mm) in the current research. Therefore, the ideal range of the speckle size yields between 0.2 mm to 0.6 mm. The size of the majority of sprayed speckles was between 0.2 mm and 0.3 mm in the tested specimens.

The DIC system was calibrated using the calibration panel "CP40/MV320". During the calibration, the panel was moved and rotated following the instructions from the software "GOM ARAMIS professional". The calibration was accomplished with 0.063 pixels deviation, which satisfies the required limit deviation value of 0.1 pixels. In addition, comparing the engineering strain measured by the extensometer and DIC, the maximum deviation at the fracture point is less than 0.6%. This leads to the conclusion that the DIC system is properly validated.

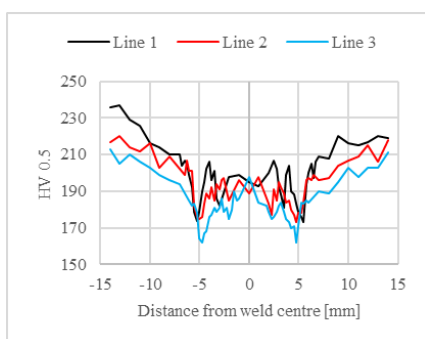
In the data processing, the deformation of the specimen is calculated based on the motion of the subset (facet), which is a set of pixels in a square region. The number of involved pixels on one side of the square region is the subset size. Sutton [37] recommends that at least three speckles should be included in one subset in order to keep the uniqueness of each subset. Hence, a three-time speckle size (9 pixels) is employed as the subset size. Another critical dimension is the step size which is the distance between two adjacent subset centres. A 5-pixels step size is adapted, resulting in 0.34 mm of the physical

dimension. The step size is smaller than the minimum interval of the strain-ratio data point (0.5 mm as illustrated in Section 3.3), indicating that the step size could satisfy the accuracy requirement of the strain ratio analysis.

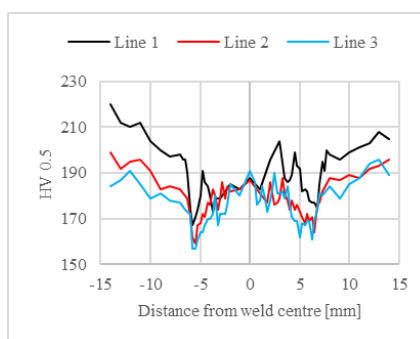
2.3. Results and discussions

2.3.1. Metallurgical investigations

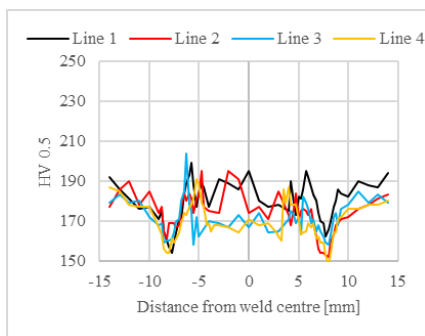
The hardness results are plotted against the indentation position corresponding to the centre of the weld in Fig. 2.9. In general, HAZ has the lowest hardness, indicating that HAZ is the weakest region in the welded connection. The WM hardness is roughly equal, higher, and lower than BM for S355, S500, and S700, respectively, indicating a matching, overmatching, and undermatching filler metal was used correspondingly.



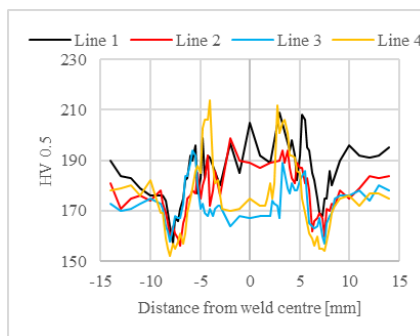
a) S355t5N1.



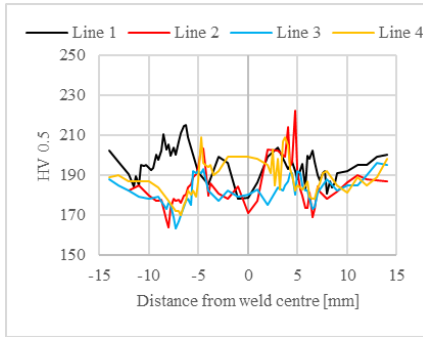
b) S355t5N2.



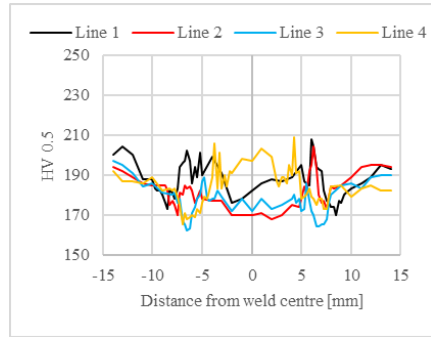
c) S355t8N1.



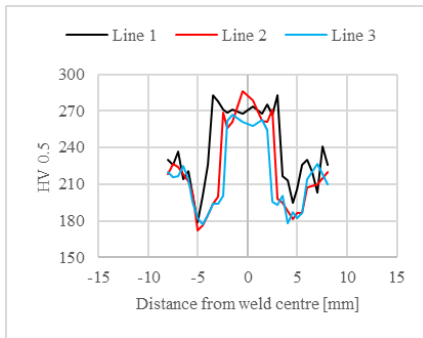
d) S355t8N2.



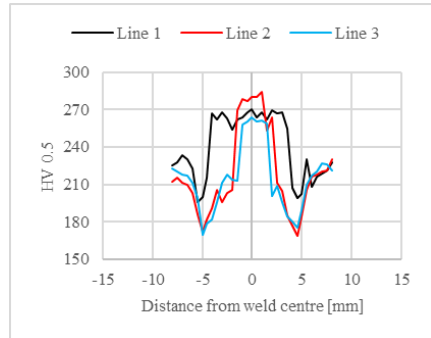
e) S355t10N1.



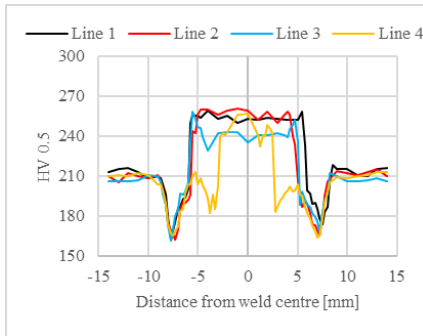
f) S355t10N2.



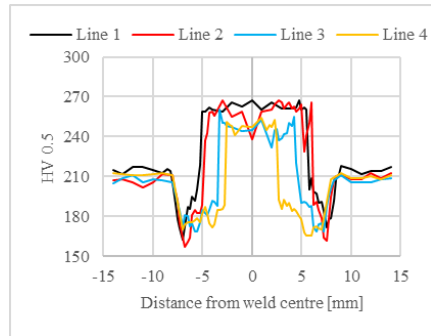
g) S500t4N1.



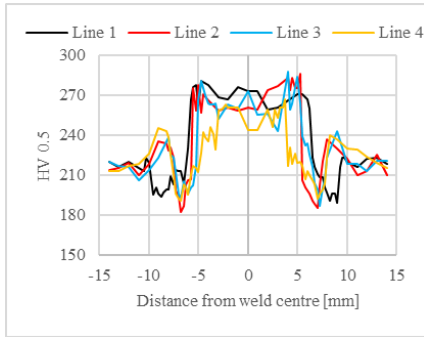
h) S500t4N2.



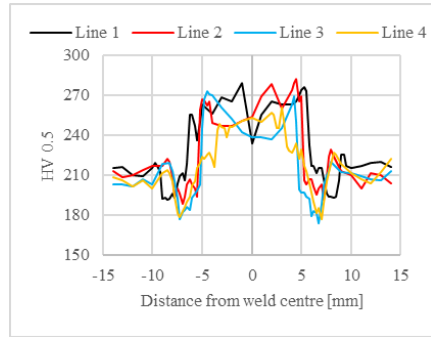
i) S500t8N1.



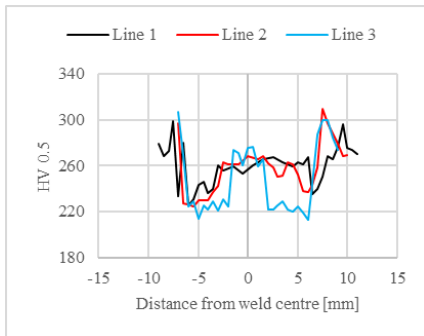
j) S500t8N2.



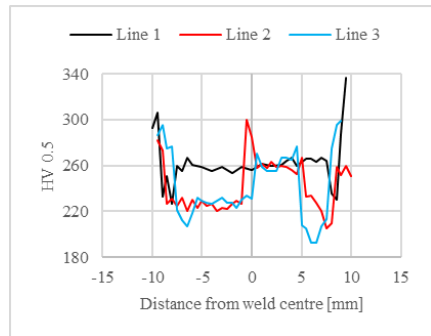
k) S500t10N1.



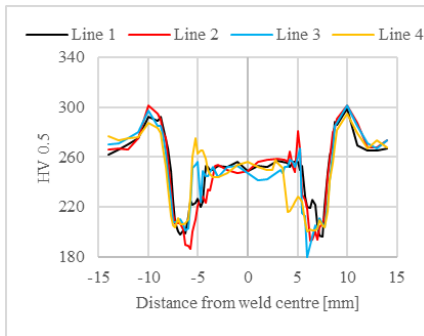
l) S500t10N2.



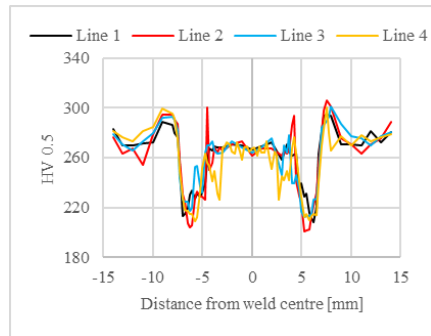
m) S700t5N1.



n) S700t5N2.



o) S700t8N1.



p) S700t8N2.

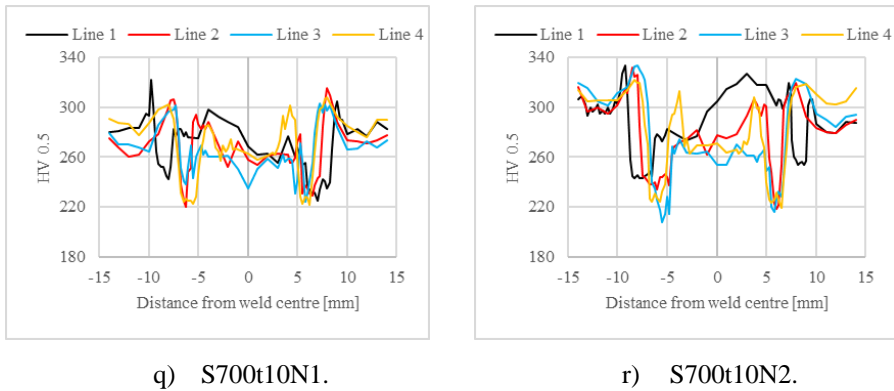


Fig. 2.9 HV 0.5 hardness results.

Table 2.7 presents the HV 0.5 hardness results of all weld samples. An example of the hardness characteristics is illustrated in Fig. 2.10. The measuring point with hardness below the average BM/WM hardness is considered to be the boundary between HAZ and BM/WM. The width of the HAZ is determined using these points, as shown in Fig. 2.10. The maximum, minimum, and average HAZ widths of 6 or 8 measurements (2×3 or 4 indentation lines) in each sample are presented in Table 2.7. The difference between the maximum and minimum HAZ width is not larger than 1 mm for half of the samples and not larger than 2 mm for 13 out of 18 samples. Considering all indentation lines, the majority (92%) of HAZ width varies between 2 mm and 4 mm. Since the HAZ width does not show a clear correlation to the BM thickness and the steel grade, an average 3.2 mm HAZ width is obtained including all HAZ but not the significantly large HAZ in S700t5N2 where an irregular shape of the weld was produced, as shown in Fig. 2.11. The result excluding the extreme wide HAZ is presented in the parentheses in Table 2.7.

Table 2.7 HV 0.5 Hardness test results.

Material	N1						N2					
	Hardness			HAZ Width [mm]			Hardness			HAZ Width [mm]		
	BM _{ave}	HAZ _{min}	R	Max	Min	Ave	BM _{ave}	HAZ _{min}	R	Max	Min	Ave
S355t5	208	169	0.19	3.0	2.5	2.8	193	161	0.17	3.5	2.8	3.1
S355t8	180	153	0.15	4.0	2.3	3.0	179	156	0.13	3.5	2.5	2.9
S355t10	188	169	0.10	4.0	3.0	3.3	189	166	0.12	3.8	2.8	3.3
S500t4	221	176	0.20	4.3	2.3	3.4	220	178	0.19	4.5	2.0	3.6
S500t8	210	162	0.23	3.3	2.5	3.0	211	164	0.22	5.5	3.0	4.1
S500t10	222	187	0.16	4.5	2.0	3.2	213	183	0.14	3.5	2.5	3.2
S700t5	285	221	0.22	5.5	3.0	4.2	287	208	0.27	8.5(3.5)	2.0	4.7(3.0)
S700t8	277	191	0.31	5.0	2.8	3.5	281	208	0.26	3.3	2.5	2.8
S700t10	287	223	0.22	3.5	2.0	2.5	306	222	0.27	3.5	1.5	2.6

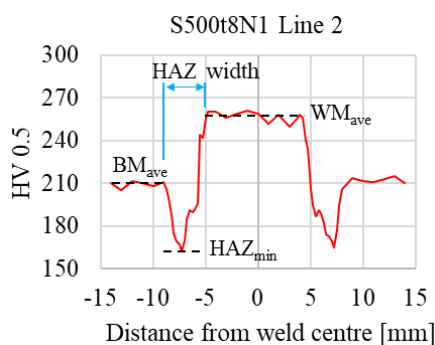


Fig. 2.10 An example of the hardness test result.

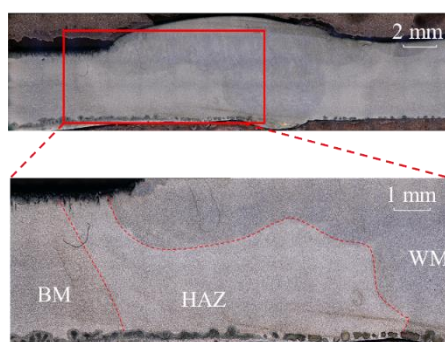


Fig. 2.11 Irregular weld (S700t5N2).

The minimum HAZ hardness is compared to the average BM hardness by the ratio $R = 1 - \text{HAZ}_{\min}/\text{BM}_{\text{ave}}$, which reflects the strength reduction in HAZ. The results from two samples for each profile show good agreement. The hardness difference increases as the steel grade increases. For S355 weld samples, the hardness of HAZ is 10% to 19% lower than BM. The varying range increases to 14% – 23% for S500 weld samples and 22% – 31% for S700. The hardness difference indicates that the strength reduction in HAZ is clearly greater in S700 than in S500 and S355. Note that no correlation is observed between the HAZ hardness reduction and the plate thickness. The hardness difference of the material investigated in this study is shown in Table 2.8, while the hardness difference of material found in the literature is presented in Table 2.1.

Table 2.8 Hardness reduction in HAZ.

Steel grade	Yield strength [MPa]	Processing method	Heat input [kJ/mm]	Hardness reduction in HAZ [%]
S355	355	TMCP	1-1.4	10-19
S500	500		1-1.4	14-23
S700	700		1-1.4	22-31

The hardness reduction in HAZ is plotted against the BM nominal yield strength in Fig. 2.12. The reference number is given for each result. The result of the current study is represented by [*]. It is worth mentioning again that the S355 material used in this study has double steel grades S355J2H/S420MH. The hardness reduction in HAZ is more significant in the present study than in previous studies. One of the reasons is that the minimum HAZ hardness is compared to the average hardness of BM, while the average HAZ hardness is used in the literature. In addition, Pisarski and Dolby [8] found that the hardness degradation in HAZ is greater with an undermatching weld than with an overmatching weld, which might also explain the large hardness reduction of S700 HAZ (undermatching) in the present study.

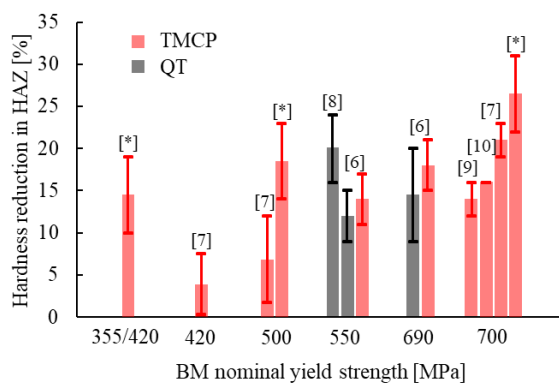
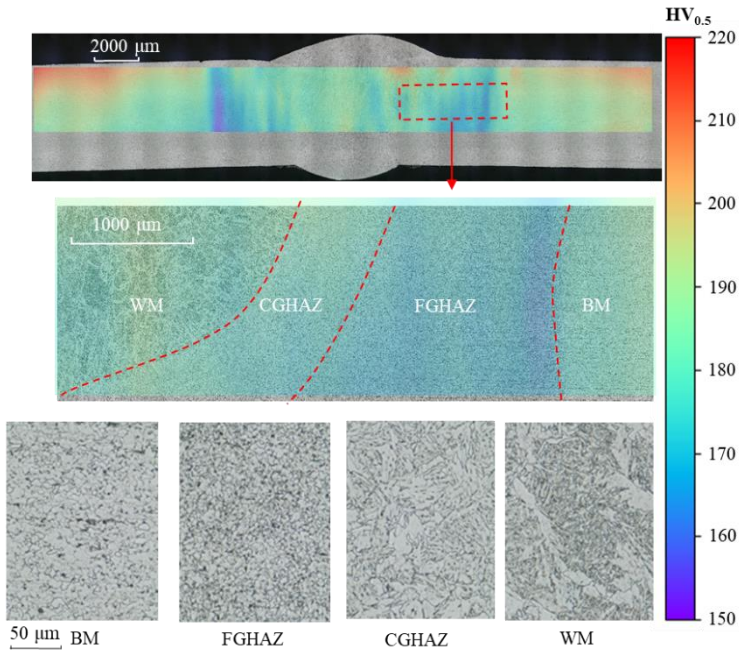
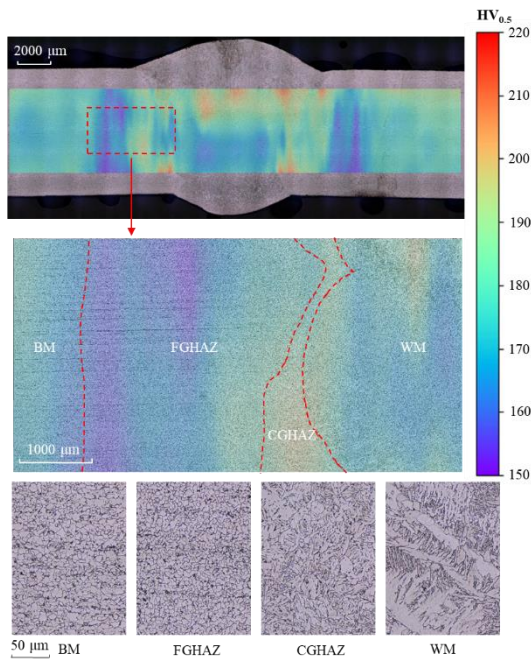


Fig. 2.12 Hardness reduction in HAZ vs BM nominal yield strength.

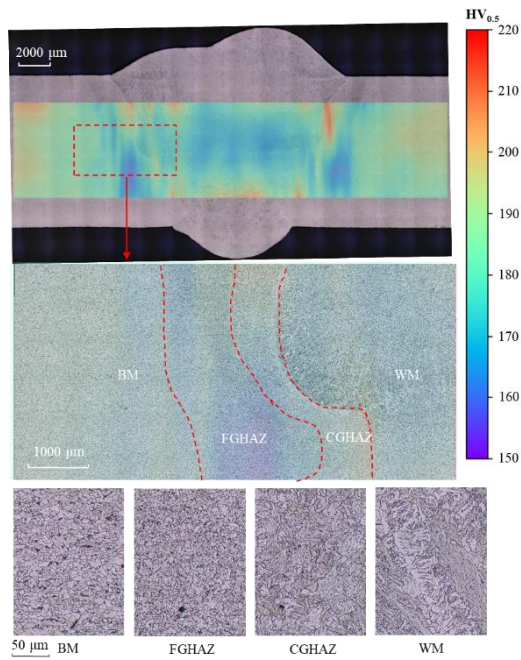
Fig. 2.13 shows the microstructure of the N2 sample for each profile. The microstructure of the material in the red dashed box is divided into four categories: i) BM, ii) the fine-grain heat-affected zone (FGHAZ), iii) the coarse-grain heat-affected zone (CGHAZ), and iv) WM. Typical microstructures of four regions are also presented. The boundary of these regions, represented by the red dashed line, is identified based on the distinct difference in the microstructure, which is also used to determine the regions with different intervals in the hardness test. It can be seen that the identified microstructure boundaries are in good agreement with the hardness results. The lowest hardness appears in FGHAZ. The lowest hardness appears in FGHAZ, which is aligned with the results in [15,28,38].



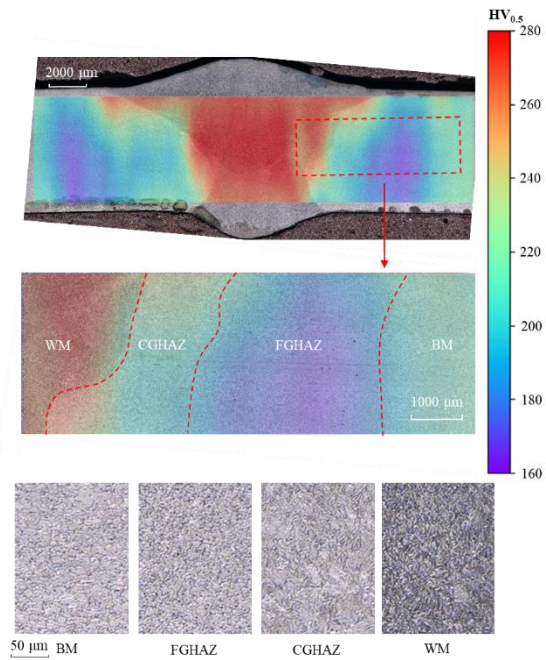
a) S355t5N2.



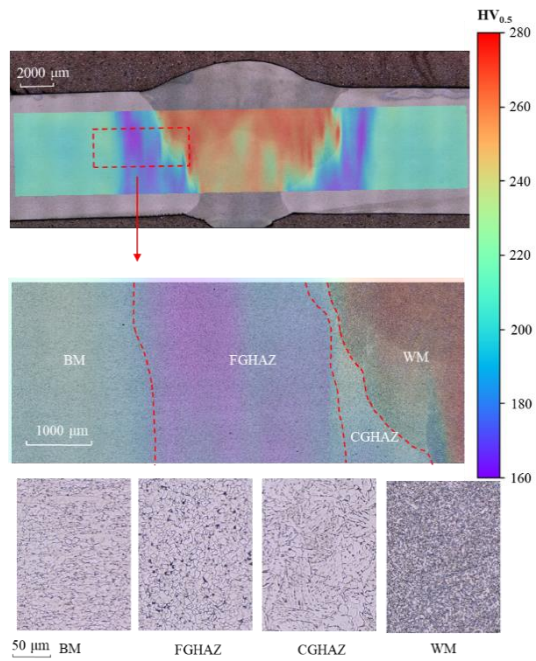
b) S355t8N2.



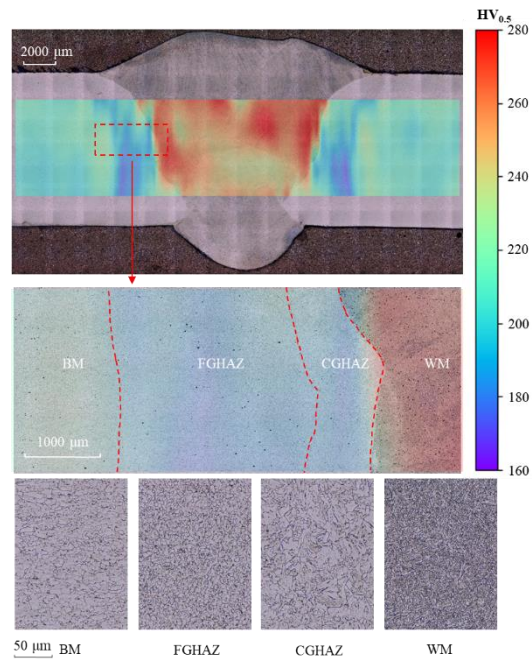
c) S355t10N2.



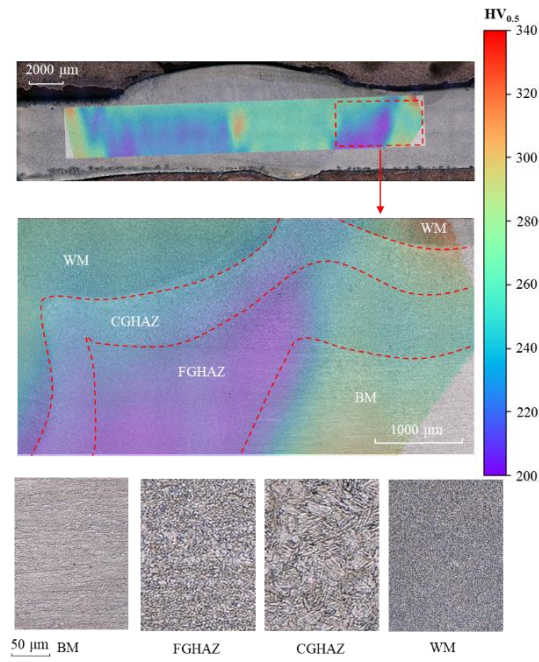
d) S500t4N2.



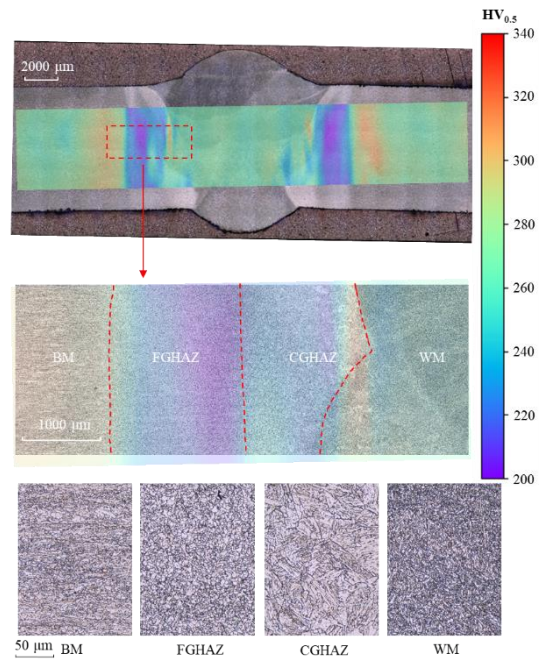
e) S500t8N2.



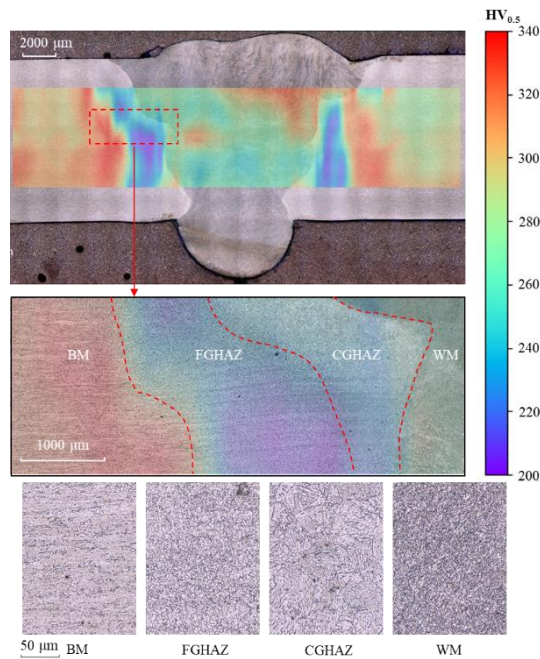
f) S500t10N2.



g) S700t5N2.



h) S700t8N2.

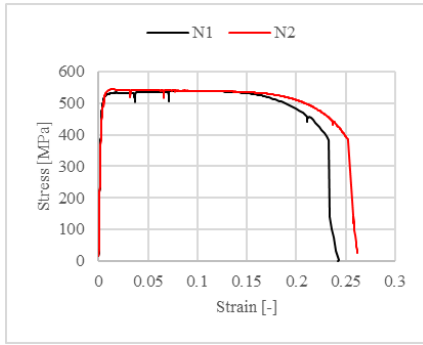


i) S700t10N2.

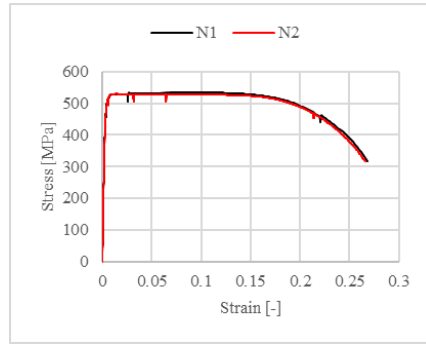
Fig. 2.13 Microstructure observation and hardness contour plot. (FGHAZ: fine-grain heat-affected zone; CGHAZ: Coarse-grain heat-affected zone)

2.3.2. Results of standard coupon specimens

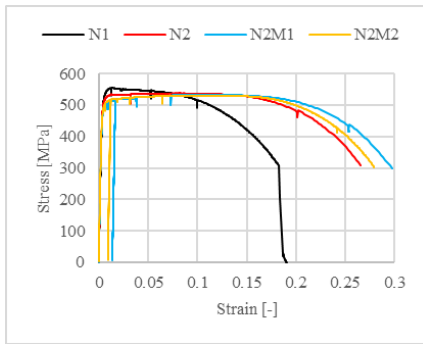
The BM engineering stress-strain relationship based on a 50 mm initial gauge length is shown in Fig. 2.14. The yield strength f_y (0.2% proof stress), the ultimate strength f_u , Young's modulus E , the ultimate strain ϵ_u , and the elongation at failure ϵ_f are presented in Table 2.9 for each specimen. The stress-strain relationships obtained from different specimens show very close results. However, it is very interesting to recognise that the results of S355t10N1 and S500t10N2 show a rather low fracture strain, and the fracture zone is very close to the position where the extensometer clip is attached, see Fig. 2.15. The measured f_u/f_y ratio is relatively low, and the measured yield strength is much higher than the nominal yield strength.



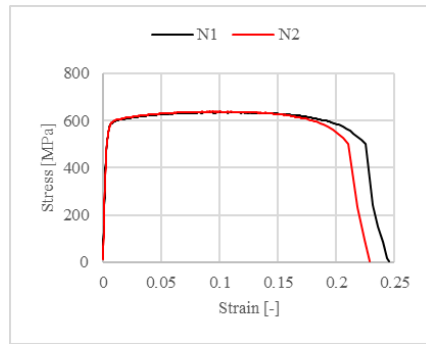
a) S355t5.



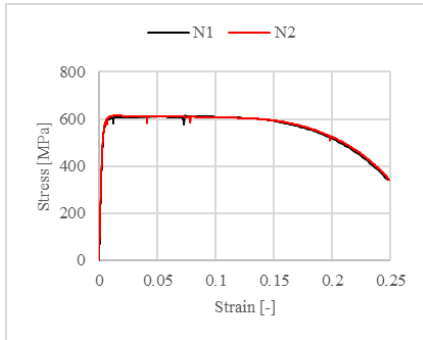
b) S355t8.



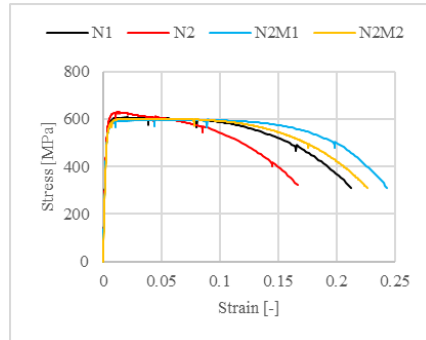
c) S355t10.



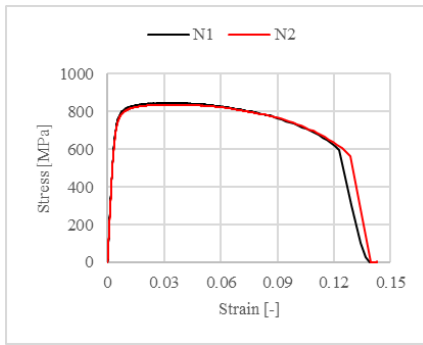
d) S500t4.



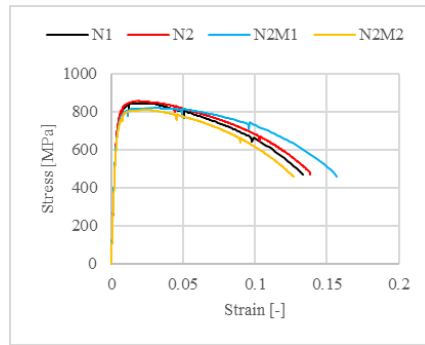
e) S500t8.



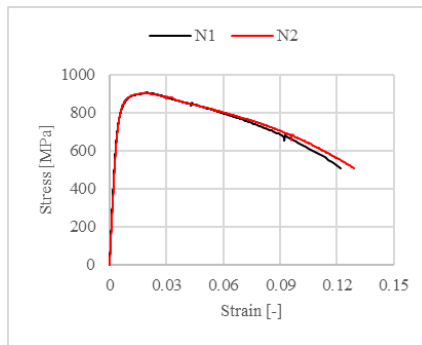
f) S500t10.



g) S700t5.

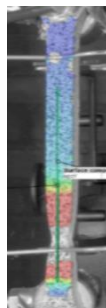


h) S700t8.

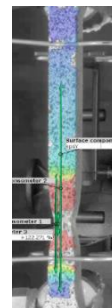


i) S700t10.

Fig. 2.14 Engineering stress-strain relationship of BM.



a) S355t10N1.



b) S500t10N2.

Fig. 2.15 Fracture position.

Table 2.9 Material properties of BM.

Material	Specimen	E [MPa]	f_y [MPa]	f_u [MPa]	ϵ_u [%]	ϵ_f [%]
S355t5	N1	186833	510	539	8.8	23.3
	N2	183609	499	546	5.0	25.3
S355t8	N1	185500	504	535	1.5	26.9
	N2	186406	508	528	8.1	26.6
S355t10	N1	183087	524	555	1.3	18.2
	N2	182329	507	537	8.4	26.6
	N2M1	180145	491	534	10.2	29.7
	N2M2	181409	514	531	11.1	27.9
S500t4	N1	189596	565	635	9.9	22.5
	N2	191203	566	638	10.1	21.0
S500t8	N1	188965	575	609	5.2	24.8
	N2	188252	585	614	1.9	24.9
S500t10	N1	190383	568	607	2.1	21.2
	N2	192398	597	630	1.2	16.7
	N2M1	185432	560	595	2.7	24.3
	N2M2	184956	564	602	4.5	22.6
S700t5	N1	204981	767	846	3.7	12.3
	N2	201576	756	837	3.5	12.9
S700t8	N1	195246	772	845	2.1	13.4
	N2	197939	784	857	2.0	13.8
	N2M1	201090	742	820	3.0	15.7
	N2M2	191178	737	811	2.2	12.7
S700t10	N1	201792	812	907	2.0	12.2
	N2	195227	819	902	1.9	12.9

2.3.3. Results of welded coupon specimens

Virtual extensometers are created to measure HAZ and WM deformation in the DIC result of milled welded coupon specimens. The metallurgical investigation shows that the HAZ width is around 3 mm, and the WM width is usually larger than 7 mm. The fracture in HAZ aligns with the centre of the 3 mm extensometer, which measures the HAZ deformation. In the only two cases where the fracture does not appear in HAZ (S355t5WN3 and S500t10WN4 failed in BM), a 3 mm region with the highest strain at the beginning of the plastic stage is measured. The WM deformation is measured from the centre 5 mm of WM, smaller than the complete WM width (generally at least 7 mm) to avoid possible transverse constraints from HAZ. An example that illustrates the measuring range of virtual extensometers (range of red arrow lines) is shown in Fig. 2.16.

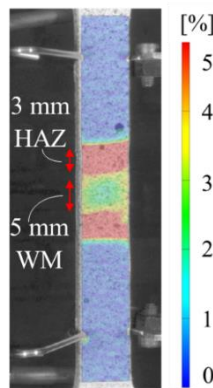
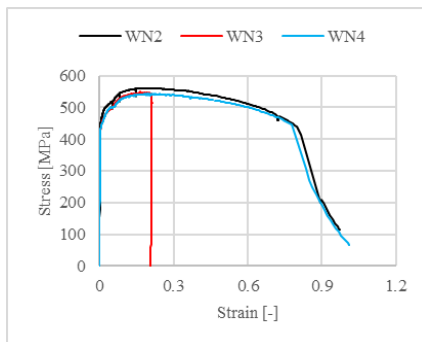
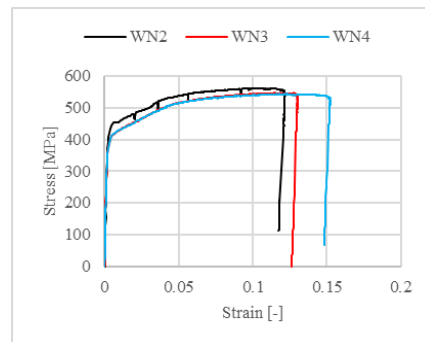


Fig. 2.16 Measuring range of virtual extensometers in DIC.

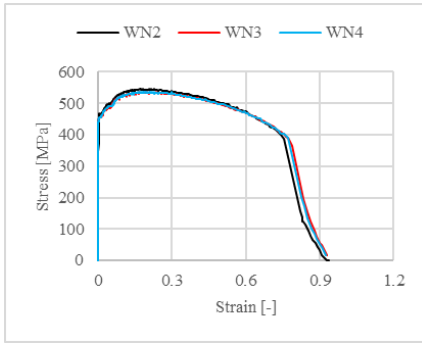
The engineering stress-strain relationship of HAZ and WM is presented in Fig. 2.17. The characterized mechanical properties are summarized in Table 2.10. In general, the stress-strain relationships obtained from different specimens show a good agreement. The final fracture appeared in HAZ for most specimens, except for S355t5WN3 and S500t10WN4, where the specimen failed in BM. For S500 welded joint, since the filler metal is much stronger than the base material, a limited deformation could be observed in WM. The 0.2% proof stress is not reached in specimens S500t10WN3 and S500t10WN4. Besides, the data of specimen S700t5WN2 is not available.



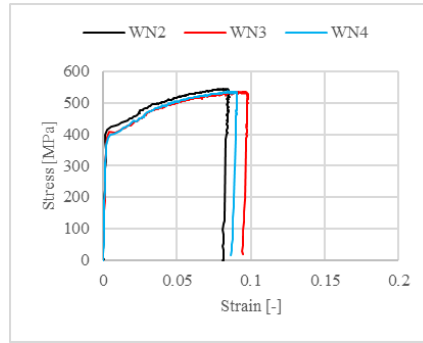
a) S355t5 HAZ.



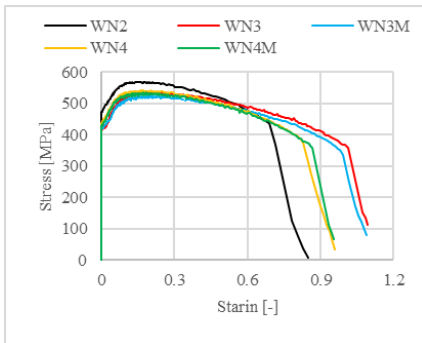
b) S355t5 WM.



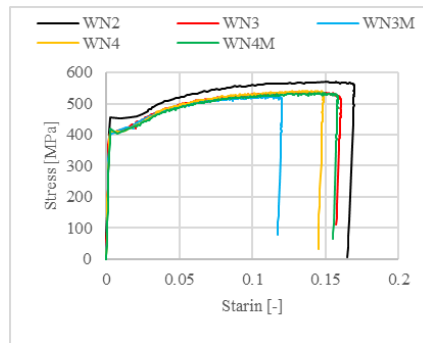
c) S355t8 HAZ.



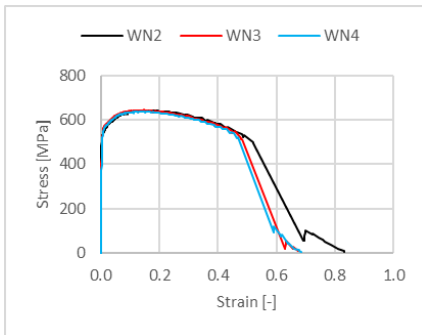
d) S355t8 WM.



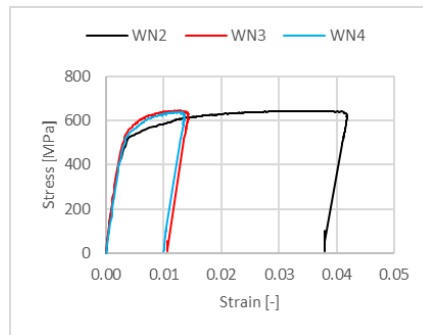
e) S355t10 HAZ.



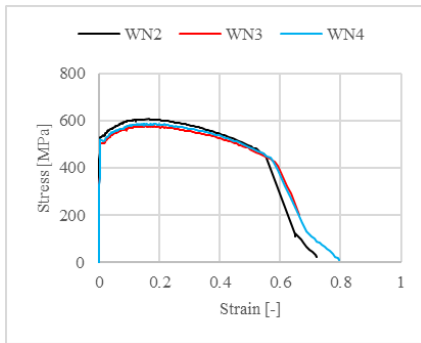
f) S355t10 WM.



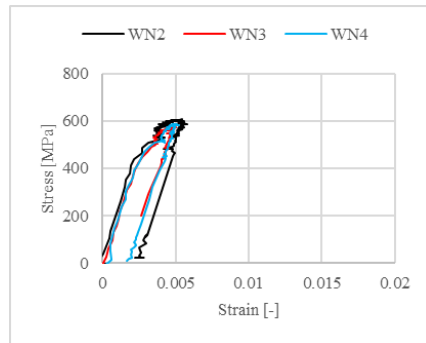
g) S500t4 HAZ.



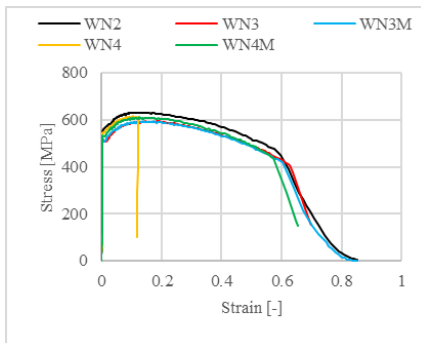
h) S500t4 WM.



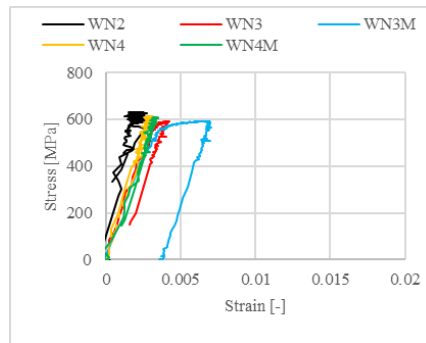
i) S500t8 HAZ.



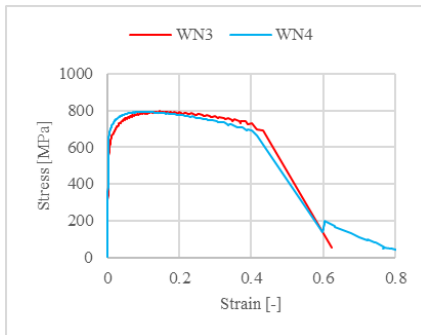
j) S500t8 WM.



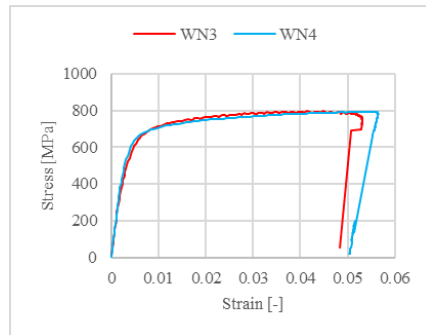
k) S500t10 HAZ.



l) S500t10 WM.



m) S700t5 HAZ.



n) S700t5 WM.

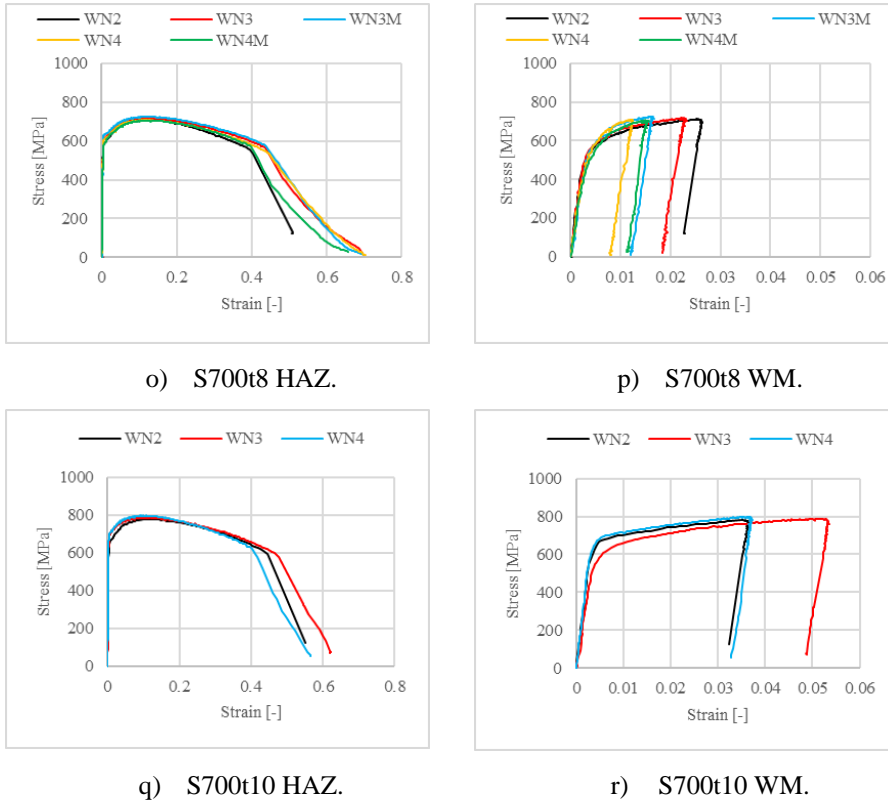


Fig. 2.17 Engineering stress-strain relationship of HAZ and WM.

Table 2.10 Material properties of HAZ and WM.

Material	Specimen	HAZ				WM	
		E [MPa]	f_y [MPa]	f_u [MPa]	ϵ_u [%]	E [MPa]	f_y [MPa]
S355t5	WN2	201667	453	561	18.5	198757	451
	WN3	195676	430	549	16.6	213088	398
	WN4	199704	431	545	20.0	205705	403
S355t8	WN2	197465	465	545	23.0	198876	421
	WN3	199105	451	535	16.8	199841	405
	WN4	199688	454	538	16.7	198364	393
S355t10	WN2	192433	474	569	16.2	202069	454
	WN3	195970	419	537	18.8	197755	408
	WN3M	191727	426	524	20.6	201232	402
	WN4	194436	441	541	17.1	207247	409
	WN4M	197363	430	535	18.6	201829	417
S500t4	WN2	224179	522	643	15.5	191840	536
	WN3	190073	518	645	14.9	197261	588

	WN4	193515	522	638	16.2	189468	567
S500t8	WN2	198800	531	606	17.0	196376	605
	WN3	191158	504	577	16.0	197312	577
	WN4	193780	520	586	13.2	194907	586
S500t10	WN2	195981	564	632	13.3	204595	606
	WN3	193549	513	593	19.2	200354	593
	WN3M	190341	515	593	13.9	187204	585
	WN4	193011	545	615	10.4	188181	-
	WN4M	186305	532	610	12.7	199790	-
S700t5	WN2	-	-	-	-	-	-
	WN3	195360	585	795	14.7	197070	666
	WN4	204304	673	793	10.1	207061	658
S700t8	WN2	193877	589	712	11.7	197179	577
	WN3	190010	608	717	12.3	201486	584
	WN3M	183993	632	726	11.3	187414	601
	WN4	189003	606	709	12.7	184650	623
	WN4M	186777	574	707	10.9	190230	581
S700t10	WN2	188766	656	780	11.5	198675	672
	WN3	191829	696	789	13.9	203587	592
	WN4	200371	701	798	9.2	210142	684

Fig. 2.18 presents the load-deformation relationship of the unmilled welded coupon tests. The results of the two specimens for each profile are in good agreement. The fracture of S355t10 and S500t10 specimens shifts from HAZ in the milled welded coupon specimen to BM in the unmilled welded coupon specimen, while the S700t8 specimen failed in HAZ in both the milled and unmilled specimens. Hence, the deformation capacity of S355t10 and S500t10 specimens are significantly higher than S700t8 specimens. The shift fracture position implies that the transverse constraint in the thickness direction, especially resulting from the reinforcement of WM, may also contribute to the HAZ resistance, which is also indicated by S700t8 unmilled specimens (S700t8UMWN1M and S700t8UMWN5M). The equivalent ultimate strength (the total load divided by the cross-sectional area of the parallel part) of the S700t8 unmilled specimens is around 769 MPa which is 8% higher than the average ultimate strength of S700t8 milled specimens.

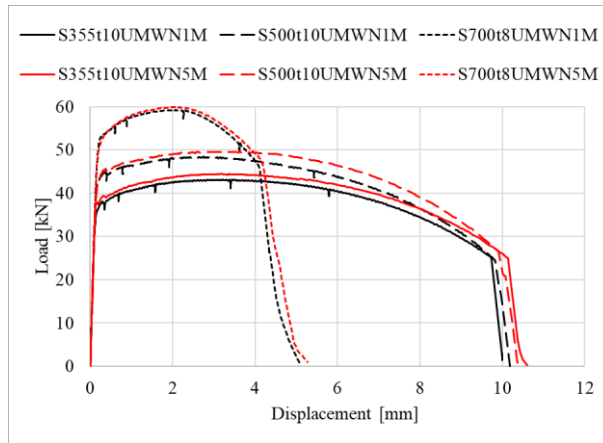


Fig. 2.18 Load-displacement relationship of unmilled welded coupon specimens.

2.3.4. Discussion on the coupon test results

The mechanical properties of BM are summarized in Table 2.9. Since the testing results of each profile have a limited deviation, the yield strength f_y , the ultimate strength f_u , and the elongation at fracture ε_f are averaged and compared to the measured mechanical properties of HAZ in Table 2.11. Fig. 2.19 presents the engineering stress-strain relationship of the S355t8 profile. It can be seen that the ultimate strain (corresponding to the ultimate stress) of the two specimens may differ significantly (0.015 for S355t8N1 and 0.081 for S355t8N2), although the two curves are almost identical from a global perspective. Hence, the BM elongation at failure ε_f , which can also reflect the ductility of the material, is used to compare with the ultimate strain of HAZ.

Table 2.11 Comparison of HAZ and BM mechanical properties.

Material	Specimen	$f_{y,BM}$ [MPa]	$f_{y,HAZ}$ [MPa]	$\frac{f_{y,HAZ}}{f_{y,BM}}$	$f_{u,BM}$ [MPa]	$f_{u,HAZ}$ [MPa]	$\frac{f_{u,HAZ}}{f_{u,BM}}$	$\varepsilon_{f,BM}$ [%]	$\varepsilon_{u,HAZ}$ [%]	$\frac{\varepsilon_{u,HAZ}}{\varepsilon_{f,BM}}$
S355t5	WN2		453	0.90		561	1.03		18.5	0.76
	WN3	505	430	0.85	543	549	1.01	24.3	16.6	0.68
	WN4		431	0.85		545	1.00		20.0	0.82
S355t8	WN2		465	0.92		545	1.03		23.0	0.86
	WN3	506	451	0.89	531	535	1.01	26.8	16.8	0.63
	WN4		454	0.90		538	1.01		16.7	0.62
S355t10	WN2		474	0.92		569	1.04		16.2	0.63
	WN3		419	0.81		537	0.98		18.8	0.73
	WN3M	516	426	0.83	546	524	0.96	25.6	20.6	0.80
	WN4		441	0.85		541	0.99		17.1	0.67
	WN4M		430	0.83		535	0.98		18.6	0.73
S500t4	WN2		522	0.92		643	1.01		15.5	0.71
	WN3	566	518	0.92	637	645	1.01	21.8	14.9	0.69
	WN4		522	0.92		638	1.00		16.2	0.74

S500t8	WN2		531	0.92		606	0.99	17.0	0.68	
	WN3	580	504	0.87	612	577	0.94	24.9	16.0	0.64
	WN4		520	0.90		586	0.96	13.2	0.53	
S500t10	WN2		564	0.97		632	1.02	13.3	0.63	
	WN3		513	0.88		593	0.96	19.2	0.91	
	WN3M	582	515	0.88	618	593	0.96	21.2	13.9	0.66
	WN4		545	0.94		615	1.00	10.4	0.49	
	WN4M		532	0.91		610	0.99	12.7	0.60	
S700t5	WN2		-	-		-	-	-	-	
	WN3	762	585	0.77	841	795	0.95	12.6	14.7	1.17
	WN4		673	0.88		793	0.94	10.1	0.80	
S700t8	WN2		589	0.76		712	0.84	11.7	0.84	
	WN3		608	0.78		717	0.84	12.3	0.88	
	WN3M	778	632	0.81	851	726	0.85	13.9	11.3	0.81
	WN4		606	0.78		709	0.83	12.7	0.91	
	WN4M		574	0.74		707	0.83	11.1	0.80	
S700t10	WN2		656	0.80		780	0.86	11.5	0.92	
	WN3	816	696	0.85	904	789	0.87	12.6	13.9	1.11
	WN4		701	0.86		798	0.88	9.2	0.73	

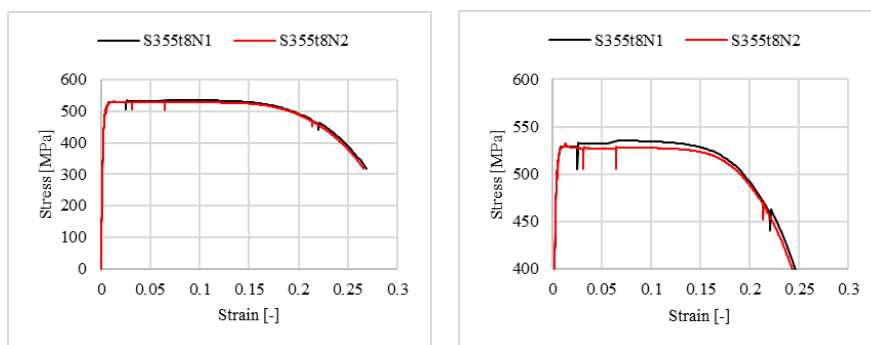
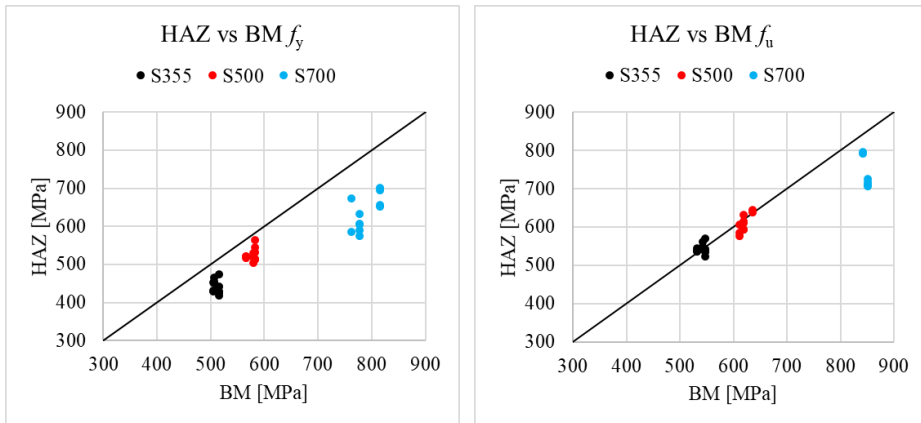


Fig. 2.19 Example of different ultimate strains.

According to the data presented in Table 2.11, the measured material strength of HAZ is plotted against the BM in Fig. 2.20. Fig. 2.20 a) demonstrates that the yield strength of HAZ is lower than that of BM in all cases. The yield strength ratio shows that HAZ of S355 and S500 material has a similar level of degradation, 0.87 and 0.91 on average, respectively. However, the ultimate strength of HAZ does not show any degradation compared to BM, where a matching or overmatching weld is used, as shown in Fig. 2.20 b). A significant strength reduction in HAZ could be observed in S700 welded coupon specimens with an undermatching weld. The average yield strength ratio and the ultimate strength ratio are 0.81 and 0.88, respectively. The average strain ratio of S355, S500, and S700 are 0.72, 0.66 and 0.84, respectively. The strain ratio of the majority of specimens (at least 9 out of 11 or 10) is not smaller than 0.6, 0.6, and 0.8 for S355, S500, and S700, respectively, which is further used in Section 4.4. In addition, there is no clear relationship between the ratios and the thickness of the original profile for all materials.



a) Yield strength comparison.

b) Ultimate strength comparison.

Fig. 2.20 HAZ and BM material strength comparison.

2.4. Conclusions

The mechanical and geometric properties of the heat-affected zone (HAZ) are investigated experimentally in this chapter. Based on the presented results, the following conclusions are drawn:

- 1) The measured yield strength of S355 (with a matching weld) and S500 (with an overmatching weld) HAZ are averagely 13% and 9% lower than the base material (BM). However, the ultimate strength of HAZ does not show any degradation compared to BM. A significant strength reduction is observed in S700 HAZ, where an undermatching weld is applied. The average measured yield strength ratio and the ultimate strength ratio are 0.81 and 0.88, respectively.
- 2) The ultimate strain of S355, S500, and S700 HAZ are 0.72, 0.66 and 0.84 times of the BM elongation at fracture, respectively. The strain ratio of the majority of specimens (at least 9 out of 11 or 10) is not smaller than 0.6, 0.6, and 0.8 for S355, S500, and S700, respectively. Note that the weld matching type might influence the ratios presented above.
- 3) The low-force Vickers hardness test results show that the majority (92%) of HAZ has a width ranging from 2 mm to 4 mm. The HAZ width does not show any correlation to the steel grade and plate thickness. The mean value of HAZ width is 3.2 mm.

Reference

- [1] R. Stroetmann, T. Kästner, A. Hälsig, P. Mayr, Influence of the cooling time on the mechanical properties of welded HSS-joints, *Steel Construction*. 11 (2018) 264–271. <https://doi.org/10.1002/stco.201800019>.
- [2] R. Stroetmann, T. Kästner, Numerical analyses on welded joints at high-strength steels, *Ce/Papers*. 3 (2019) 725–730. <https://doi.org/10.1002/cepa.1165>.
- [3] M. Amraei, A. Ahola, S. Afkhami, T. Björk, A. Heidarpour, X.L. Zhao, Effects of heat input on the mechanical properties of butt-welded high and ultra-high strength steels, *Engineering Structures*. 198 (2019). <https://doi.org/10.1016/j.engstruct.2019.109460>.
- [4] H.C. Ho, K.F. Chung, M.X. Huang, D.A. Nethercot, X. Liu, H. Jin, G.D. Wang, Z.H. Tian, Mechanical properties of high strength S690 steel welded sections through tensile tests on heat-treated coupons, *Journal of Constructional Steel Research*. 166 (2020) 105922. <https://doi.org/10.1016/j.jcsr.2019.105922>.
- [5] X. Liu, K.F. Chung, H.C. Ho, M. Xiao, Z.X. Hou, D.A. Nethercot, Mechanical behavior of high strength S690-QT steel welded sections with various heat input energy, *Engineering Structures*. 175 (2018) 245–256. <https://doi.org/10.1016/j.engstruct.2018.08.026>.
- [6] W. Cai, Y. Wang, G. Li, R. Stroetmann, Comparative study on strength of TMCP and QT high-strength steel butt-welded joints, *Journal of Constructional Steel Research*. 197 (2022) 107447. <https://doi.org/10.1016/j.jcsr.2022.107447>.
- [7] V.P. Nguyen, Effect of heat input on the mechanical properties of welded joints, 2018. <https://doi.org/https://urn.fi/URN:NBN:fi:amk-2018091915234>.
- [8] H.G. Pisarski, R.E. Dolby, The significance of softened HAZs in high strength structural steels, *Welding Research Abroad*. 50 (2003) 22–30.
- [9] F. Hochhauser, W. Ernst, R. Rauch, R. Vallant, Influence of the soft zone on the strength of welded modern HSLA steels, *Welding in the World*. 56 (2012). <https://doi.org/DOI:10.1007/BF03321352>.
- [10] M. Khurshid, Z. Barsoum, I. Barsoum, Load carrying capacities of butt welded joints in high strength steels, *Journal of Engineering Materials and Technology, Transactions of the ASME*. 137 (2015) 1–9. <https://doi.org/10.1115/1.4030687>.
- [11] R.M. Molak, K. Paradowski, T. Brynk, L. Ciupinski, Z. Pakiela, K.J. Kurzydowski, Measurement of mechanical properties in a 316L stainless steel welded joint, *International Journal of Pressure Vessels and Piping*. 86 (2009) 43–47. <https://doi.org/10.1016/j.ijpvp.2008.11.002>.
- [12] J. Kim, Y.-W. Kim, B.-S. Kang, S.-M. Hwang, Finite element analysis for bursting failure prediction in bulge forming of a seamed tube, *Finite Elements in Analysis and Design*. 40 (2004) 953–966. <https://doi.org/10.1016/j>.
- [13] M. Flansbjer, T. Sjögren, Using digital image correlation techniques and finite element models for strain-field analysis of a welded aluminium structure, *Applied Mechanics and Materials*. 70 (2011) 123–128.

- <https://doi.org/10.4028/www.scientific.net/AMM.70.123>.
- [14] Y. Peng, C. Wu, J. Gan, J. Dong, Characterization of heterogeneous constitutive relationship of the welded joint based on the stress-hardness relationship using micro-hardness tests, *Construction and Building Materials*. 202 (2019) 37–45. <https://doi.org/10.1016/j.conbuildmat.2018.12.218>.
- [15] M. Amraei, S. Afkhami, V. Javaheri, J. Larkiola, T. Skriko, T. Björk, X.L. Zhao, Mechanical properties and microstructural evaluation of the heat-affected zone in ultra-high strength steels, *Thin-Walled Structures*. 157 (2020). <https://doi.org/10.1016/j.tws.2020.107072>.
- [16] A.P. Reynolds, F. Duvall, Digital image correlation for determination of weld and base metal constitutive behavior, *Welding Journal (Miami, Fla)*. 78 (1999) 355-s.
- [17] W.D. Lockwood, B. Tomaz, A.P. Reynolds, Mechanical response of friction stir welded AA2024: Experiment and modeling, *Materials Science and Engineering A*. 323 (2002) 348–353. [https://doi.org/10.1016/S0921-5093\(01\)01385-5](https://doi.org/10.1016/S0921-5093(01)01385-5).
- [18] W.D. Lockwood, A.P. Reynolds, Simulation of the global response of a friction stir weld using local constitutive behavior, *Materials Science and Engineering A*. 339 (2003) 35–42. [https://doi.org/10.1016/S0921-5093\(02\)00116-8](https://doi.org/10.1016/S0921-5093(02)00116-8).
- [19] M.A. Sutton, J.H. Yan, S. Avril, F. Pierron, S.M. Adeb, Identification of heterogeneous constitutive parameters in a welded specimen: Uniform stress and virtual fields methods for material property estimation, *Experimental Mechanics*. 48 (2008) 451–464. <https://doi.org/10.1007/s11340-008-9132-6>.
- [20] R. Bai, Y. Wei, Z. Lei, H. Jiang, W. Tao, C. Yan, X. Li, Local zone-wise elastic-plastic constitutive parameters of Laser-welded aluminium alloy 6061 using digital image correlation, *Optics and Lasers in Engineering*. 101 (2018) 28–34. <https://doi.org/10.1016/j.optlaseng.2017.09.023>.
- [21] X. Wu, J. Shuai, K. Xu, Z. Lv, Local Constitutive Behavior of Undermatched Welded Joints in Pipeline Steel Using Digital Image Correlation Technology, *Journal of Pressure Vessel Technology, Transactions of the ASME*. 142 (2020) 1–6. <https://doi.org/10.1115/1.4047271>.
- [22] Y. Peng, C. Wu, J. Gan, J. Dong, Determination of the local constitutive properties of the welded steel joints using digital image correlation method, *Construction and Building Materials*. 171 (2018) 485–492. <https://doi.org/10.1016/j.conbuildmat.2018.03.182>.
- [23] G. Li, F. Xu, G. Sun, Q. Li, Identification of mechanical properties of the weld line by combining 3D digital image correlation with inverse modeling procedure, *International Journal of Advanced Manufacturing Technology*. 74 (2014) 893–905. <https://doi.org/10.1007/s00170-014-6034-x>.
- [24] M.I. Costa, D.M. Rodrigues, C. Leitão, Analysis of AA 6082-T6 welds strength mismatch: stress versus hardness relationships, *International Journal of Advanced Manufacturing Technology*. 79 (2015) 719–727. <https://doi.org/10.1007/s00170-015-6866-z>.

- [25] C. Leitão, I. Galvão, R.M. Leal, D.M. Rodrigues, Determination of local constitutive properties of aluminium friction stir welds using digital image correlation, *Materials and Design*. 33 (2012) 69–74. <https://doi.org/10.1016/j.matdes.2011.07.009>.
- [26] A. Khalfallah, Experimental and numerical assessment of mechanical properties of welded tubes for hydroforming, *Materials and Design*. 56 (2014) 782–790. <https://doi.org/10.1016/j.matdes.2013.11.051>.
- [27] M.L. Zhu, F.Z. Xuan, Correlation between microstructure, hardness and strength in HAZ of dissimilar welds of rotor steels, *Materials Science and Engineering A*. 527 (2010) 4035–4042. <https://doi.org/10.1016/j.msea.2010.03.066>.
- [28] C. Chen, S.P. Chiew, M.S. Zhao, C.K. Lee, T.C. Fung, Welding effect on tensile strength of grade S690Q steel butt joint, *Journal of Constructional Steel Research*. 153 (2019) 153–168. <https://doi.org/10.1016/j.jcsr.2018.10.009>.
- [29] C. Chen, S.P. Chiew, M.S. Zhao, C.K. Lee, T.C. Fung, Influence of cooling rate on tensile behaviour of S690Q high strength steel butt joint, *Journal of Constructional Steel Research*. 173 (2020) 106258. <https://doi.org/10.1016/j.jcsr.2020.106258>.
- [30] EN ISO 3834-2:2006 Quality requirements for fusion welding of metallic materials - Part 2: Comprehensive quality requirements, (2006).
- [31] Metallic materials - Tensile testing - Part 1: Method of test at room temperature (ISO 6892-1:2019), 1 (2019).
- [32] NEN-EN-ISO 6507-1 Metallic materials - Vickers hardness test - Part 1: Test method, 1 (2018).
- [33] NEN-EN-ISO 6507-4 Metallic materials - Vickers hardness test - Part 4: Tables of hardness values, 4 (2018).
- [34] B. Adegeest, Material Factors for High Strength Rectangular Hollow Section X Joints, (2020).
- [35] P. Reu, All about speckles: Speckle size measurement, *Experimental Techniques*. 39 (2014) 1–2. <https://doi.org/10.1111/ext.12161>.
- [36] P. Reu, All about speckles: Aliasing, *Experimental Techniques*. 38 (2014) 1–3. <https://doi.org/10.1111/ext.12111>.
- [37] M.A. Sutton, J.-J. Orteu, H.W. Schreier, Image correlation for shape, motion and deformation measurements, 2009.
- [38] D. Wojnowski, Y.K. Oh, J.E. Indacochea, Metallurgical assessment of the softened HAZ region during multipass welding, *Journal of Manufacturing Science and Engineering, Transactions of the ASME*. 122 (2000) 310–315. <https://doi.org/10.1115/1.538920>.

3.

A method for identifying boundaries of the heat-affected zone in welded coupon specimens using digital image correlation

The coupon specimen with a transverse butt weld in the middle could be used for determining local constitutive properties of the heat-affected zone (HAZ) and the weld metal (WM) based on the digital image correlation (DIC). However, limited research is reported to demonstrate how to identify the boundary of each region in DIC results. Accordingly, it is difficult to determine the width of HAZ and WM which should be considered when creating virtual extensometers in DIC to measure the strain of each zone and when generating the finite element (FE) model for the milled welded coupon specimen to validate the stress-strain relationship of HAZ.

In this chapter, a method for identifying boundaries of different zones in DIC results is proposed. First, the boundaries are determined based on the results of the Vickers hardness test and the microstructure observation. Then, the boundary is identified in the DIC results using the proposed method. Finally, the identified HAZ regions were verified against hardness results.

Parts of this chapter appear in the journal article: ‘Rui Yan et al., A method for identifying the boundary of regions in welded coupon specimens using digital image correlation. *Materials & Design*, 2021’. Minor modifications have been made to suit the thesis.

3.1. Introduction

Although many researches have been carried out on the material property investigation using the milled welded coupon specimens [1–10], paper demonstrating how to obtain the deformation from each zone is rare. It is indeed possible to extract strain from a single facet point. However, a single point cannot represent the material of the whole HAZ, considering the heterogeneity of HAZ. And the strain from a single facet point may contain some noise which has a significant influence at the elastic stage and the onset of yielding. Therefore, it is necessary to obtain the strain of each zone based on a virtual extensometer with a certain gauge length in DIC. Moreover, the determined width of HAZ and WM is needed for creating the finite element (FE) model to validate the measured stress-strain relationship of each zone. A question arises on how to determine the gauge length for each zone.

Fig. 3.1 presents an example of the major strain contour plot of an S700 welded coupon tested in this study. The figures are generated based on 3D DIC results at the ultimate load. The only difference among these figures is the maximum strain value used in the legend, e.g. the refinement level of the contour plots. Two high strain stripes corresponding to two HAZs exist in each figure. The width of the red colour stripe decreases with the increase of the maximum strain in the legend. Therefore, the HAZ boundary cannot be determined by the colour (width of the maximum strain strip) and consequently by the magnitude of the strain used for the contour plot. Additionally, Lockwood and Reynolds [4] conducted experiments on coupons with a transverse butt weld. It was found that negative stress perpendicular to the loading direction existed in zones (WM and BM) closing to HAZ boundaries during the experiments. The negative stress would lower the yield strength of the material, resulting in the mitigation of strain localisation. BM and WM adjacent to HAZ may have a larger strain than the material far from the boundary. Hence, it is difficult to distinguish the "over-deformed" BM and WM from HAZ, especially if the strength of BM, WM, and HAZ are very close. Therefore, it is essential to develop a method for identifying the zone's boundary so that the strain can be measured from the virtual extensometer within a single material zone using DIC.

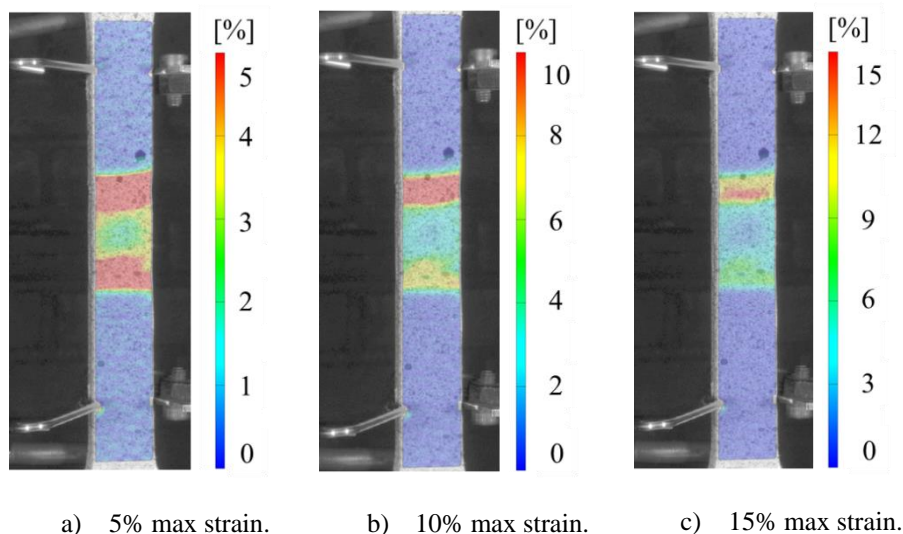


Fig. 3.1 Strain contour plot of an S700 welded coupon at the ultimate load with different strain legends.

In this chapter, the results of milled welded coupon tests, presented in Chapter 2, are analysed. First, the boundaries of different zones were determined using the low-force Vickers hardness test (HV 0.5) and the microstructure observation. Then, the slope of the minor strain-major strain relationship measured by 3D DIC is used to identify the boundary of HAZ. Finally, the identified boundary is verified against the hardness test results. The innovation of the proposed method is to directly identify the boundary of HAZ from a single welded coupon test using DIC without any additional metallurgical investigation. The identified width of HAZ and WM should be considered in generating FE models to validate the measured stress-strain relationship. Since the proposed method is independent of the material category, it might be used not only for steel but also for aluminium, for example, in the case of the friction stir welded aluminium coupon.

3.2. Method

3.2.1. Principal strain analysis

Leitao et al. [1] verified a linear strain path (whereby the slope of the $\varepsilon_{tr,x}-\varepsilon_{tr,y}$ relationship is a constant in the stage beyond the yield strain, see Fig. 3.3) registered in the weld zone by analysing the major and minor true strains evolution. The slope of the minor true strain-major true strain relationship indicated the existence of constraints from the adjacent zones. Therefore, the principal strain analysis is conducted based on the true principal strains measured from single points in DIC. Fig. 3.2 shows the positions of the strain measurement points, the white squares, on specimen S700t10WN2. The measuring interval in HAZ is 0.5 mm, while the interval in the other zones is 1mm. The data

measured from Point 8 in HAZ is used as an example to demonstrate the analysis approach.

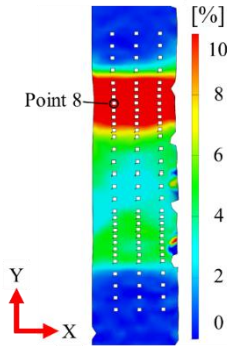


Fig. 3.2 Measuring points on specimen S700t10WN2 in DIC.

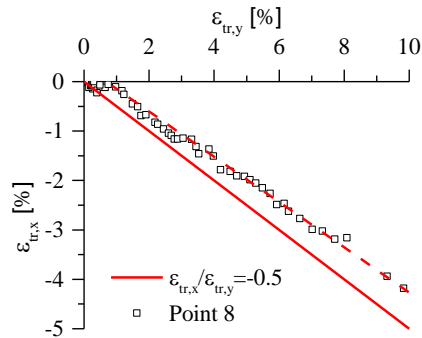


Fig. 3.3 $\varepsilon_{tr,x} - \varepsilon_{tr,y}$ relationship of Point 8 in HAZ during the loading.

Since the specimen is loaded in the Y direction, the major and minor true strains are $\varepsilon_{tr,y}$ and $\varepsilon_{tr,x}$, respectively. The minor true strain-major true strain ($\varepsilon_{tr,x}-\varepsilon_{tr,y}$) relationship is plotted until the maximum load in Fig. 3.3. Considering the volume preservation assumption at the plastic stage approximated by Eq. (3.1), the strain ratio $\varepsilon_{tr,x}/\varepsilon_{tr,y}$ becomes close to -0.5 in a uniaxial tensile loading condition, see the solid red line in Fig. 3.3. Therefore, the principal strain ratio, which is the slope of the $\varepsilon_{tr,x}-\varepsilon_{tr,y}$, is approximated by the red dash line at the plastic stage, see Fig. 3.3. For simplicity, the slope of the $\varepsilon_{tr,x}-\varepsilon_{tr,y}$ relationship is called the strain ratio hereafter. It is worth mentioning that the true plastic strain should be used in this analysis. However, because the specimen is under a bi-axial stress state and stress components are not predictable, the true plastic strain in X and Y directions cannot be calculated based on DIC results. Moreover, the elastic strain is much smaller than the plastic strain and has a small influence on the strain ratio. Therefore, the true strains are used instead of true plastic strains to calculate the strain ratio.

$$\varepsilon_{tr,x} + \varepsilon_{tr,y} + \varepsilon_{tr,z} = 0 \quad (3.1)$$

3.2.2. Finite element analysis

A FE analysis is conducted to verify the effect of the zones' boundary constraint on the strain ratio using the ABAQUS:2019 software package [11]. The following assumptions are used in the model: 1) a sufficient length of every zone is possible to distinguish; 2) the hardness difference between adjacent zones is clear; 3) plastic strains exist in every zone. This ideal situation is introduced to illustrate the interaction between adjacent zones. The model consists of two 100 mm zones, resulting in 200 mm in total. The width and the thickness are constant, 10 mm and 3 mm, respectively, which are identical to the milled dimensions of the tested specimen. A 0.5 mm fine mesh is used except for the

outer edges in the Y direction, "far" from the centre, where 2 mm coarse mesh is used, as shown in Fig. 3.4. Two material properties, namely the Strong and Weak material, are used in the model. The mechanical properties are presented in Table 3.1. The only difference between these two materials is that the Weak material has a 100 MPa lower ultimate true stress than the Strong material. The MPC beam constraint is applied to constrain the end surface to a reference point at its centre by all degrees of freedom. The load is applied by a 30 mm displacement at RP2 in the Y direction. The remaining displacement degree of freedom at RP1 and RP2 is fully constrained.

The strain ratio is calculated based on the average strain of elements in three rows for each cross section, shown as the solid red squares in Fig. 3.4. The strain ratio is plotted against the distance from the zones' boundary in the middle. It can be seen that the strain ratio smaller and larger than -0.5 exists in the vicinity of the Strong and Weak zones' boundary. With the cross-section away from the zones' boundary, the strain ratio gradually approaches -0.5, indicating that the constraint from the adjacent zone disappears at a certain distance from the boundary.

Table 3.1 Mechanical property of a Strong and Weak material.

Material	E [MPa]	f_y [MPa]	$\sigma_{t,u}$ [MPa]	$\varepsilon_{t,u}$ [%]
Strong	200000	500	1000	20
Weak	200000	500	900	20

where E is Young's modulus; f_y is the yield strength; $\sigma_{t,u}$ is the ultimate true strength; $\varepsilon_{t,u}$ is the ultimate true strain.

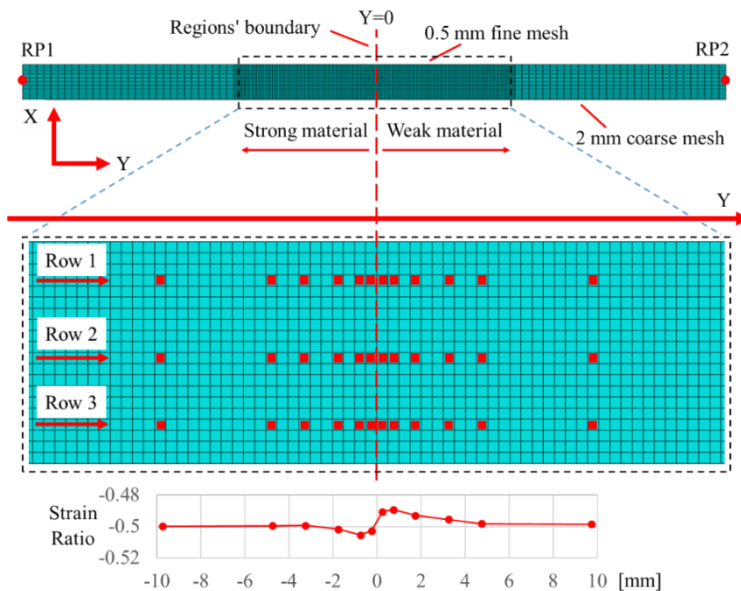


Fig. 3.4 Results of FEA using the Strong and Weak material connected in series.

3.2.3. Transverse constraint at the boundary of zones

The tested milled welded coupon specimen consists of five zones in series, resulting in four boundaries, as presented in Fig. 3.5. Due to the heterogeneity in the grain size of two adjacent zones, transverse constraints in X and Z directions exist at the boundary. Take the BM and HAZ boundary, for instance. BM is stronger than HAZ. Consequently, BM has a less transverse deformation than HAZ during the tensile test, indicating that BM tends to resist the transverse deformation of HAZ at the boundary due to the continuity of the material. Accordingly, the HAZ longitudinal deformation in the loading direction is reduced.

Since the thickness of the tested specimen is only 3 mm, a limited constraint is expected in the thickness direction [1,4]. Hence, the out-of-plane deformation ($\epsilon_{tr,z}$) is independent of the constraint at the boundary. Eq. (3.1) is rewritten as:

$$\frac{\epsilon_{tr,x}}{\epsilon_{tr,y}} = -1 - \frac{\epsilon_{tr,z}}{\epsilon_{tr,y}} \quad (3.2)$$

Eq. (3.2) shows that the strain ratio decreases with the increase of the major true strain $\epsilon_{tr,y}$, given the independent out-of-plane deformation. The HAZ major strain is smaller at the boundary than the middle of HAZ due to the transverse constraint of BM. Hence, a relatively larger strain ratio is expected in HAZ closing to the boundary than in the other zones. On the contrary, HAZ would increase the strain of BM at the boundary. Consequently, a relatively smaller strain ratio is expected in BM closing to the boundary than in the other zones. The more significant the hardness difference between BM and HAZ, the greater the strain ratio difference.

Based on FEA results in Section 3.2.2, a conceptual strain ratio plot for a simplified coupon satisfying the three assumptions mentioned above is presented in Fig. 3.5 a). However, the assumptions do not hold so distinctly in different zones of a real welded specimen. Therefore, Fig. 3.5 b) depicts the strain ratio distribution closer to the physical evidence.

In Fig. 3.5 b), the first two assumptions are modified to: 1) the length of HAZ is not sufficient to allow for the vanishment of the boundary constraint; 2) the significant hardness difference only exists between WM and HAZ, while the last assumption remains as in the simplified model. Because of limits in the length of HAZ, the strain ratio cannot decrease to -0.5 in the middle of HAZ. The hardness difference between HAZ and BM is relatively small. BM cannot impose a strong transverse constraint on HAZ. Hence, the strain ratio in HAZ is still large at the boundary of WM and HAZ but gradually decreases to -0.5 with a minor increase at the boundary of HAZ and BM. If the hardness transition from HAZ to BM is very smooth, the minor increase in the strain ratio may not exist. A close to "V" shape or a "Monotonic" shape of the strain ratio distribution could be observed in HAZ. These hypotheses are verified by experimental evidence, as shown in the following section.

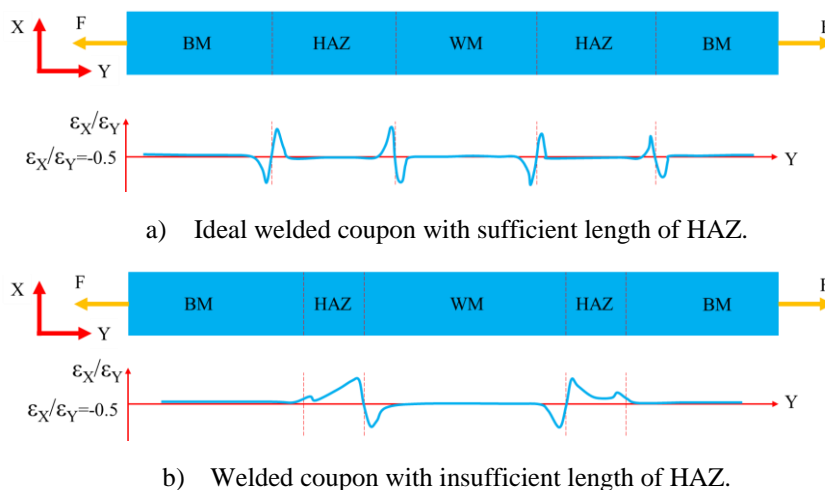


Fig. 3.5 Strain ratio distribution along with the welded coupon.

3.3. Results and discussions

3.3.1. HV 0.5 hardness and microstructure results

Table 3.2 presents the average hardness of the base material (labelled BM_{ave}), the average hardness of the weld metal (labelled WM_{ave}), and the minimum hardness of HAZ (labelled HAZ_{min}) from N2 weld samples of six profiles. The reason for using the minimum hardness of HAZ and the average hardness of BM and WM is that the weakest material layer in HAZ governs the strength of the coupon, while BM and WM are relative homogeneous materials (which do not govern the failure mode of the specimen). BM and WM are compared to HAZ concerning the hardness difference in columns BM-HAZ and WM-HAZ of Table 3.2, respectively. Three combinations of the material strength difference are identified in the specimens, assuming a constant link between the hardness and the material strength in different zones of the welded specimens. Both BM and WM are slightly stronger than HAZ in S355 coupons. For S500 coupons, BM is slightly stronger, while WM is much stronger than HAZ. S700 coupons have much stronger material in BM and WM. The larger the hardness difference, the stronger the transverse constraint at the boundary of two zones. Therefore, three constraint combinations for HAZ, which are the weak-weak, weak-strong, and strong-strong constraint, could be recognized in the corresponding six tensile tests.

Table 3.2 HV 0.5 hardness test results.

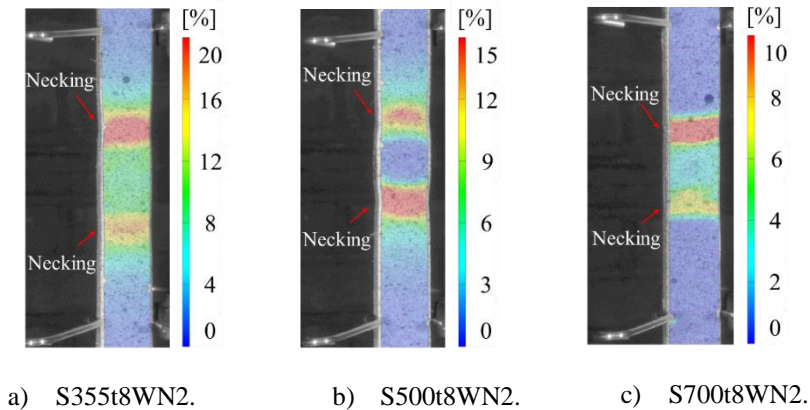
Specimen	BM_{ave}	HAZ_{min}	WM_{ave}	BM-HAZ	WM-HAZ	Constraint combination
S355t8N2	179	156	183	23	23	weak-weak
S355t10N2	189	166	185			

S500t8N2	211	164	253	39	82	weak-strong
S500t10N2	213	183	257			
S700t8N2	281	208	264	80	59	strong-strong
S700t10N2	306	219	282			

3.3.2. Tensile test results

Fig. 3.6 depicts the major (longitudinal) true strain distribution at the ultimate load of six milled welded coupon tests. Two zones showing high strain accompanying the necking phenomenon could be observed in all tests. It indicates that the deformation primarily concentrates on HAZ, which governs the failure.

The engineering stress-strain relationships of six tensile coupon tests are plotted in Fig. 3.7. The engineering strain is obtained from a 50mm extensometer covering BM, HAZ, and WM zones, indicating that a "constant" strain is assumed along the extensometer base length. The 0.2% proof yield stress and the tensile strength are compared to BM in Table 3.3. Significant yield and tensile strength reductions exist in S700 welded coupons, while S355 and S500 welded coupons show much smaller (if any) strength reductions. The reduction discrepancy could be explained by the hardness results shown in Table 3.2. The strength of the welded coupon is governed by HAZ, where the lowest hardness value is obtained compared to BM and WM. The minimum hardness of S700 HAZ has the most significant hardness reduction (80 on average), while S355 and S500 grade specimens show a reduction of 23 and 39 hardness on average compared to BM, respectively.



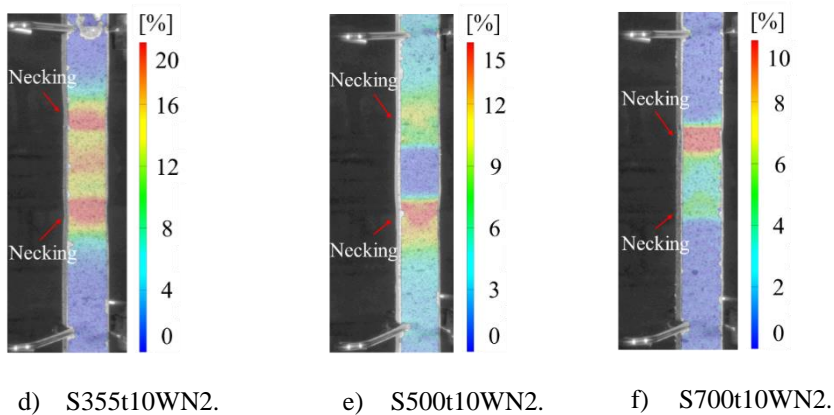


Fig. 3.6 Contour plots of the major strain at the ultimate load.

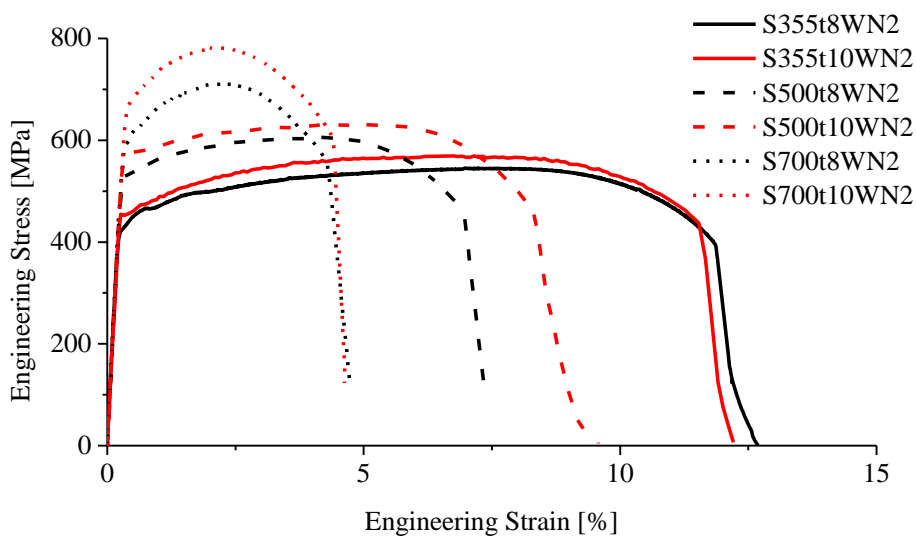


Fig. 3.7 Engineering stress-strain relationships of the milled welded coupons.

Table 3.3 Comparison of mechanical properties obtained from the base material and welded coupons.

Specimen	Base material coupon		Welded coupon	
	Yield strength [MPa]	Tensile strength [MPa]	Yield strength [MPa]	Tensile strength [MPa]
S355t8	506	536	442	545
S355t10	506	539	456	570
S500t8	580	617	534	607

S500t10	593	630	576	632
S700t8	789	861	615	711
S700t10	830	902	688	781

3.3.3. Comparison of the hardness and the strain ratio results

The strain ratio is examined for all the "white points" shown in Fig. 3.2. Three points are measured in each cross section. The average strain ratio of each cross section is compared to the hardness results in Fig. 3.8. Since the coupon specimens were milled to the centre zone of 3 mm thickness, the presented hardness results only include Line 2 and Line 3, as shown in Fig. 2.5. The HAZ regions determined by the strain ratio are shown as the grey stripes with a red dash box, see Fig. 3.8.

3.3.3.1. S355 coupons (matching weld)

HAZ in S355 coupons has the weak-weak boundary constraint, as demonstrated in Table 3.2. Fig. 3.8 a) and b) show that the variation of the strain ratio in the whole range is relatively small compared to S500 and S700. A typical strain ratio distribution in WM, referring to Fig. 3.5, is observed in the S355 coupons. The strain ratio is around -0.5 in the middle of WM and slightly decreased at the boundary. A high strain ratio exists in HAZ close to the WM boundary. Hence, the boundary of HAZ and WM is identified between the highest ratio point in HAZ and the lowest ratio point in WM. The point next to the highest ratio point is determined as the boundary. The boundary of HAZ and BM does not show a significant discrepancy in the strain ratio plot because the hardness transition is relatively smooth from HAZ to BM. Hence, the HAZ and BM boundary is identified by the point where the strain ratio is on the average level of BM. Therefore, two shapes of the strain ratio distribution for HAZ, which are the "Monotonic" shape in S355t8 and the "V" shape in S355t10, are characterised.

3.3.3.2. S500 coupons (overmatching weld)

Fig. 3.8 c) and d) demonstrate the results of S500 coupons. Since WM is much stronger than HAZ, a significant constraint effect is observed in HAZ close to WM. The boundary of HAZ and WM is identified accordingly. Similar to S355 coupons, the hardness of HAZ and BM are very close. The strain ratio does not show a distinct variation at the boundary. Therefore, it is identified by the point where the strain ratio is on the average level as BM.

Additionally, the strain ratio is missing (not reliable) in a part of WM. According to the hardness results in Table 3.2, WM is much stronger than HAZ, resulting in smaller major strain (around 0.3%) developing in WM at the ultimate load. The deformation is too small to generate a trend line similar to the one shown in Fig. 3.3, considering the actual accuracy of DIC. Hence, the strain ratio could not be calculated.

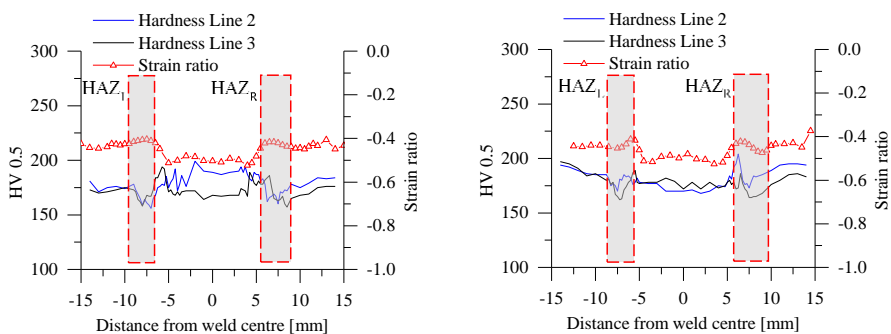
3.3.3.3. S700 coupons (undermatching weld)

BM and WM are much stronger than HAZ in S700 coupons. Due to the significant hardness difference, a pronounced boundary constraint effect is observed in the strain

ratio plot, and the boundary of HAZ is identified accordingly. A "V" shape strain ratio distribution is observed in both specimens. Besides, the strain ratio in BM cannot be processed for the same reason as WM in S500 coupons.

To summarise, from Fig. 3.8, it is clear that a good correlation exists between the strain ratio and the hardness results. The HAZ zone identified by the strain ratio matches the low hardness zone well. A "V" shape or a "Monotonic" shape of the strain ratio distribution exists in the determined HAZ region. The widths of left and right HAZ (HAZ_L and HAZ_R) determined by the hardness and the strain ratio are compared in Table 3.4. Note that the hardness result is the average of two widths determined by two indentation lines. An absolute value of the width difference is calculated for each HAZ. The maximum and average differences are 0.4 mm and 0.2 mm, respectively. Therefore, it is concluded that a satisfactory result is obtained using the strain ratio method, and the proposed method could identify the boundary of zones. Note that it is possible to improve the accuracy of the strain ratio results if a smaller interval (smaller than 0.5 mm) is adapted, as presented in Fig. 3.2. A smaller interval requires smaller facet and step sizes, consequently a higher imaging resolution and a finer speckle size.

The final issue regarding the repeatability of the experiment should be addressed since only one welded coupon was tested for each profile. Generally, HAZ may have a similar material scattering as the BM, making it necessary to test many specimens to determine the material property. Strictly interpreting experimental results, it is not sufficient to obtain the material property based on one test for each profile. However, the main purpose of this chapter is to propose a methodology for determining the zones' boundary in a coupon with the strong and weak materials connected in series rather than to investigate specific characteristics of the zones for various steel grades. Although HAZ material scatters, the specimens still follow that HAZ is weaker than the base material and the weld. Because the proposed method works for the situation where the strong and weak materials are connected in series regardless of the specific strength of HAZ, the HAZ material scattering does not influence the results. In addition, two specimens were tested for each steel grade/matching type. The experiments are repeated from the steel grade perspective, and the HAZ boundary could be identified in both specimens for each steel grade.



a) S355t8.

b) S355t10.

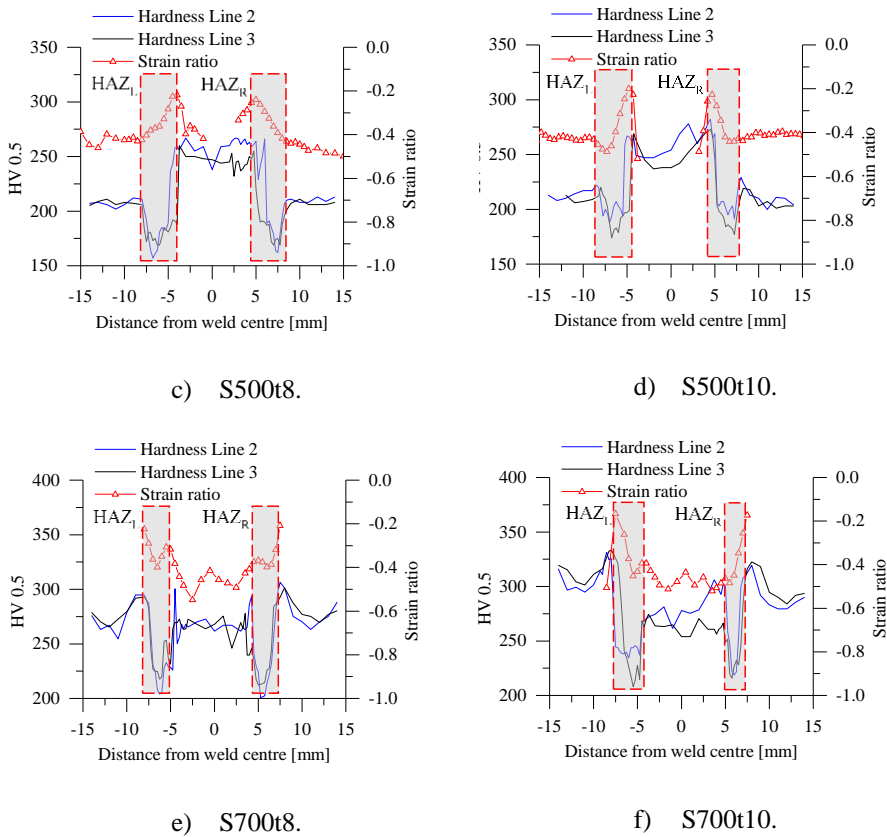


Fig. 3.8 Comparison of the hardness and the strain ratio results.

Table 3.4 Comparison of HAZ width determined by the hardness test and the strain ratio.

Specimen	HAZ _L [mm]			HAZ _R [mm]		
	Hardness	Strain ratio	difference	Hardness	Strain ratio	difference
S355t8	3.3	3.0	0.3	3.6	3.5	0.1
S355t10	3.3	3	0.3	3.6	4	0.4
S500t8	4.0	4.0	0.0	3.9	4.0	0.1
S500t10	3.6	4.0	0.4	3.6	3.5	0.1
S700t8	2.9	3.0	0.1	3.1	3.0	0.1
S700t10	3.5	3.5	0.0	2.4	2.5	0.1

3.4. Conclusions

The boundaries of the heat-affected zone (HAZ) are analysed through the metallurgical investigation and the tensile coupon test on the milled welded coupon specimen. A

method is proposed to identify the boundaries of HAZ in the digital image correlation (DIC) results. Based on the presented results, the following conclusions are drawn:

- 1) The transverse constraint at the boundary of two zones could be identified by comparing the slope of the minor true strain-major true strain relationship in the stage beyond the yield strain (also called the strain ratio for simplicity), considering a thin plate (3 mm) assuming almost no constraint in the thickness direction. The strain ratio on the strong side is smaller than that on the weak side. The strain ratio difference between the strong and weak sides is more significant with an increasing hardness difference. Among the tested specimens, the strain ratio difference is less distinct if the hardness difference between two zones is equal to or smaller than 37, indicating that the proposed method is more suitable for the welded high-strength steel where a severe strength reduction exists in HAZ.
- 2) The strain ratio in HAZ is close to the "V" shape or "Monotonic" shape distribution. The starting and the ending points correspond to the HAZ boundaries constrained the most by the weld metal (WM) and the base material (BM).
- 3) The HAZ zone determined by the strain ratio method shows a good agreement with the hardness results, accompanying 0.4 mm maximum and 0.2 mm average absolute deviation.

Reference

- [1] C. Leitão, I. Galvão, R.M. Leal, D.M. Rodrigues, Determination of local constitutive properties of aluminium friction stir welds using digital image correlation, *Materials and Design*. 33 (2012) 69–74. <https://doi.org/10.1016/j.matdes.2011.07.009>.
- [2] A.P. Reynolds, F. Duvall, Digital image correlation for determination of weld and base metal constitutive behavior, *Welding Journal (Miami, Fla)*. 78 (1999) 355-s.
- [3] W.D. Lockwood, B. Tomaz, A.P. Reynolds, Mechanical response of friction stir welded AA2024: Experiment and modeling, *Materials Science and Engineering A*. 323 (2002) 348–353. [https://doi.org/10.1016/S0921-5093\(01\)01385-5](https://doi.org/10.1016/S0921-5093(01)01385-5).
- [4] W.D. Lockwood, A.P. Reynolds, Simulation of the global response of a friction stir weld using local constitutive behavior, *Materials Science and Engineering A*. 339 (2003) 35–42. [https://doi.org/10.1016/S0921-5093\(02\)00116-8](https://doi.org/10.1016/S0921-5093(02)00116-8).
- [5] M.A. Sutton, J.H. Yan, S. Avril, F. Pierron, S.M. Adeb, Identification of heterogeneous constitutive parameters in a welded specimen: Uniform stress and virtual fields methods for material property estimation, *Experimental Mechanics*. 48 (2008) 451–464. <https://doi.org/10.1007/s11340-008-9132-6>.
- [6] R. Bai, Y. Wei, Z. Lei, H. Jiang, W. Tao, C. Yan, X. Li, Local zone-wise elastic-plastic constitutive parameters of Laser-welded aluminium alloy 6061 using digital image correlation, *Optics and Lasers in Engineering*. 101 (2018) 28–34. <https://doi.org/10.1016/j.optlaseng.2017.09.023>.
- [7] X. Wu, J. Shuai, K. Xu, Z. Lv, Local Constitutive Behavior of Undermatched Welded Joints in Pipeline Steel Using Digital Image Correlation Technology, *Journal of Pressure Vessel Technology, Transactions of the ASME*. 142 (2020) 1–6. <https://doi.org/10.1115/1.4047271>.
- [8] Y. Peng, C. Wu, J. Gan, J. Dong, Determination of the local constitutive properties of the welded steel joints using digital image correlation method, *Construction and Building Materials*. 171 (2018) 485–492. <https://doi.org/10.1016/j.conbuildmat.2018.03.182>.
- [9] G. Li, F. Xu, G. Sun, Q. Li, Identification of mechanical properties of the weld line by combining 3D digital image correlation with inverse modeling procedure, *International Journal of Advanced Manufacturing Technology*. 74 (2014) 893–905. <https://doi.org/10.1007/s00170-014-6034-x>.
- [10] M.I. Costa, D.M. Rodrigues, C. Leitão, Analysis of AA 6082-T6 welds strength mismatch: stress versus hardness relationships, *International Journal of Advanced Manufacturing Technology*. 79 (2015) 719–727. <https://doi.org/10.1007/s00170-015-6866-z>.
- [11] ABAQUS, *Abaqus Analysis User's Manual*, 2019 version, (2019).
- [12] M. Amraei, S. Afkhami, V. Javaheri, J. Larkiola, T. Skriko, T. Björk, X.L. Zhao, Mechanical properties and microstructural evaluation of the heat-affected zone in ultra-high strength steels, *Thin-Walled Structures*. 157 (2020).

<https://doi.org/10.1016/j.tws.2020.107072>.

- [13] C. Chen, S.P. Chiew, M.S. Zhao, C.K. Lee, T.C. Fung, Welding effect on tensile strength of grade S690Q steel butt joint, *Journal of Constructional Steel Research*. 153 (2019) 153–168. <https://doi.org/10.1016/j.jcsr.2018.10.009>.
- [14] D. Wojnowski, Y.K. Oh, J.E. Indacochea, Metallurgical assessment of the softened HAZ region during multipass welding, *Journal of Manufacturing Science and Engineering, Transactions of the ASME*. 122 (2000) 310–315. <https://doi.org/10.1115/1.538920>.

4.

The constitutive model of the heat-affected zone

The strength of HAZ depends on the BM grade and manufacturing process, electrode grade, and welding parameters. Under certain conditions, the heat-affected zone (HAZ) has a lower strength than the base material (BM) and the weld metal (WM), especially for high-strength steel. BM and WM impose a transverse constraint on HAZ during tensile loading due to their different mechanical properties. Therefore, it is essential to understand the strength reduction and the transverse constraint leading to strength increase in HAZ, to properly evaluate and predict the behaviour of the welded connections.

In this chapter, a semi-empirical methodology for determining the true stress-strain relationship of HAZ is proposed. This methodology is based on an engineering approach to consider HAZ as an isotropic and homogeneous material, with no consideration of different volumetric fractions of microstructures within a HAZ. The effect of the transverse constraint, imposed by BM and/or WM, on the measured stress of HAZ is eliminated by a linear modification factor correlating to the true strain. The modified constitutive model of HAZ is validated against the experimental results obtained by DIC. Finally, the new methodology of a semi-empirical constitutive model based on the Swift model was used to propose equivalent characteristics of HAZ as a function of the mechanical properties of BM for a specific welding procedure considered in this study.

Parts of this chapter appear in the journal article: ‘Rui Yan et al., A method for determining the constitutive model of the heat-affected zone using digital image correlation. Construction and Building Materials, 2022’ and ‘Rui Yan et al., Equivalent material properties of the heat-affected zone in welded cold-formed rectangular hollow section connections, Thin-Walled Structures, 2022’. Minor modifications have been made to suit the thesis.

4.1. Introduction

A welded joint consists of the following three major zones: the base material (BM), the heat-affected zone (HAZ), and the weld metal (WM). HAZ often has the lowest material strength among all three zones. Therefore, a proper constitutive model of HAZ is crucial for predicting the behaviour of welded joints.

From a structural engineering perspective, it is essential to establish a HAZ stress-strain relationship suitable for FEA of large-scale welded joints, such as welded hollow section joints. Further detailed zone partition, such as the fine-grain heat-affected zone (FGHAZ) and the coarse-grain heat-affected zone (CGHAZ), may not be practical in the large-scale joint analysis. Since HAZ comprises different types of grain, the measured stress-strain relationship before necking is not well fitted by the existing theoretical constitutive model. Hence, the measured stress-strain relationship is used as the basis for input in the analysis instead of a new theoretical constitutive model. The measured stress-strain relationship should be modified, as illustrated below, in an attempt to simplify the modelling of the HAZ effect. Given the scale of hollow section joints and the FEA result difference due to the minimum parameter increment, the trial-and-error process is used in the proposed simplified method.

Two issues should be addressed to obtain the correct stress-strain relationship of HAZ using the (semi-)direct approach (equivalent material approach) introduced in Chapter 2. The first issue is regarding the effect of the transverse constraint on HAZ. The welded coupon specimen has a "strong" (BM and WM) and a "weak" (HAZ) zone connected in series in the loading direction. The strong material would impose a transverse constraint on the weak material, resulting in a biaxial tensile stress state (for a thin specimen) or a triaxial tensile stress state (for a thick specimen) in the weak material. The von Mises stress, σ_M , written in terms of the general stresses is presented in Eq. (4.1).

$$\sigma_M = \sqrt{\frac{1}{2} \left[(\sigma_x - \sigma_y)^2 + (\sigma_y - \sigma_z)^2 + (\sigma_z - \sigma_x)^2 + 6(\tau_{xy}^2 + \tau_{yz}^2 + \tau_{zx}^2) \right]} \quad (4.1)$$

where σ_x , σ_y , and σ_z are normal stresses in three directions. Considering the HAZ elements close to the centre of the cross-section perpendicular to the loading direction (Y direction), the influence of shear stresses τ_{xy} , τ_{yz} and τ_{zx} are very limited and is neglected in the analysis below. For a given value of σ_M , σ_y is higher under the biaxial and triaxial stress states than under the uniaxial tensile stress state (without transverse constraint). Accordingly, the measured stress (σ_y) under biaxial and triaxial stress states is higher than the yield strength in the uniaxial stress state. For example, with $\sigma_M = 100$ MPa, $\sigma_y = 100$ MPa under the uniaxial stress state while $\sigma_y = 120$ MPa if σ_x and σ_z are 20 MPa under the triaxial tensile stress state. Lockwood et al. [1] compared the yield strength of different zones in a butt-welded thick (around 8 mm) specimen and a thin (2.5 mm, milled from the thick specimen) specimen. The thin specimen has a lower and higher yield strength in the weak (HAZ) and the strong (BM and WM) zone, respectively, compared to the thick specimen. It indicates that the transverse constraint exists in the

thickness direction of the thick specimen at the onset of yielding. Hochhauser et al. [2] found that the tensile strength of the thick specimen is higher than that of the thin specimen due to the transverse constraint in the thickness direction at the onset of necking. Hence, the transverse constraint in the thickness direction may exist during the entire loading process if HAZ has a lower yield and tensile strength than BM and WM. Similarly, the transverse constraint would also exist in the width direction of the milled thin specimen. Therefore, the stress-strain relationship of HAZ measured by DIC has a higher stress at the strain hardening stage than the real material property.

The second issue concerns the gauge length used for measuring the deformation of HAZ, as the boundary of HAZ is not visible on the specimen in DIC. A method to evaluate the transverse constraint at the boundary of two zones using DIC is proposed in Chapter 3. Milled coupon specimens (3 mm thickness) with a butt weld in the middle were tested in tension. The major (along the loading direction) and minor strain were extracted from the individual points along the loading direction. The slope of the minor-major strain relationship for each measuring point at the plastic stage is used to identify the boundary of HAZ. Consequently, the virtual extensometer, which measures the deformation between two points in DIC, is created within the identified boundaries for HAZ and WM.

The design rules for welded connections (up to S460) in EN 1993-1-8 [3] do not consider the strength reduction in HAZ and the strength enhancement due to the transverse constraint. Since the strength reduction in HAZ is rather limited for mild steels in practical applications, it is reasonable to design the connection without considering the effect of HAZ. The new version of prEN 1993-1-8 [4] stipulates that the strength of the filler metal should be included in design of a butt weld if BM is higher than S460 and different filler metal and BM are used. However, for HSS and ultra-high-strength steel (UHSS, steel grade higher than S700), the strength of HAZ may be significantly lower than BM and WM. Using only the strength of filler metal in the design may lead to an unsafe prediction of the connection resistance. On the other hand, the resistance of the HAZ could be significantly improved by the strong transverse constraint from BM and WM. Consequently, the effect of transverse constraints on both the strength degradation and the strength enhancement in HAZ should be considered to provide a safe and economical design recommendation for welded connections made of HSS and UHSS.

In this chapter, the constitutive model of HAZ is developed to account for the transverse constraint imposed by the material differences among the BM, WM, and HAZ. The aim is to provide an improved material model that can be used in the advanced simulation of welded hollow section joints involving high-strength steels. The engineering stress-strain relationships for HAZ and WM were obtained from milled welded coupon specimens based on the identified zones' boundaries. FEA was carried out to calibrate a linear modification factor for reducing the true stress of the measured HAZ constitutive model. The modified stress-strain relationship is validated against the experimental results measured by DIC. The novelty of the proposed method is in correcting the overestimated material strength by a linear modification factor. Using the modified HAZ material property, the effect of the transverse constraint on the HAZ constitutive model is eliminated. Numerical simulations demonstrate that, using the proposed method, the

tensile behaviour of the welded joint can be accurately predicted by the FE model, especially for the joint with a significant strength difference between HAZ and BM/WM, such as HSS undermatching welded joints. Besides, the linear modification factor brings light onto the effect of the transverse constraint on the welded joint behaviour, which could be further used in evaluating the resistance and deformation of the welded joint made of HSS and ultra-HSS. Finally, from a practical perspective, a semi-empirical stress-strain constitutive model following the Swift model [5] is proposed for HAZ, based on the mechanical properties of BM.

4.2. Method

4.2.1. Uniaxial stress-strain relationship

The six milled welded coupon specimens analysed in Chapter 3 are employed in this chapter. The determined widths of two HAZs, namely HAZ₁ and HAZ₂, are shown in Table 4.1. The HAZ deformation is measured from one of the HAZs, where the fracture appears. The gauge length is equal to the determined HAZ width. Since the HAZ boundaries are identified, the width of WM is determined accordingly, as presented in Table 4.1. WM has a relatively homogeneous material. It was reported that the yield strength of WM measured from the thick and thin specimen was very close [1], indicating that a limited transverse constraint exists in the middle of WM. Therefore, it is assumed that the effect of the transverse constraint on the longitudinal deformation does not exist at the centre 5 mm of WM. An extensometer covering the centre 5 mm of WM is used to measure the WM deformation. The load-deformation relationship of WM and HAZ is converted to an engineering stress-strain relationship based on the measured cross-section area and the gauge length. The engineering stress-strain relationship of BM is obtained from the tensile test of the standard coupon specimen (see Fig. 2.3) with a 50 mm gauge length.

Table 4.1 The determined width of HAZ and WM. [mm]

Specimen	S700t8 WN2	S700t10 WN2	S500t8 WN2	S500t10 WN2	S355t8 WN2	S355t10 WN2
HAZ ₁	3.0	3.5	4.0	4.0	3.0	3.0
HAZ ₂	3.0	2.5	4.0	3.5	3.5	4.0
WM	9.5	9.0	9.0	9.0	14.0	11.5

The purpose of this study is to propose a method to determine the true material property of HAZ (without the transverse constraint) for the FE analysis. Such a model is suitable for the range before necking. The calibrated material model is useful for establishing the post-necking stress-strain relationship by extrapolating the existing theoretical models. Therefore, the stress-strain relationship of HAZ, until the ultimate engineering stress, is used in FEA. A linear combination of the power law (the Swift model) [5] and the linear law [6] is used to generate the BM undamaged material model, which is validated against the standard coupon test following the procedures presented in Chapter 5. The equations

of the linear combination, the linear model, and the Swift model are given in Eq. (4.2), Eq. (4.3), and Eq. (4.4), respectively.

$$\sigma_t = W\sigma_{t,L} + (1-W)\sigma_{t,S} \quad (4.2)$$

$$\sigma_{t,L} = a + b\varepsilon_t \quad (4.3)$$

$$\sigma_{t,S} = k(\varepsilon_t + \varepsilon_0)^n \quad (4.4)$$

where W is the weighting factor; k , ε_0 , and n are the Swift parameters; $\sigma_{t,S}$ is the true stress predicted by the Swift model; a and b are the linear law parameters; $\sigma_{t,L}$ is the true stress predicted by the linear law; σ_t and ε_t are the true stress and the true strain, respectively. Since the failure does not appear in WM, the obtained true stress-true strain relationship of WM is extended by fitting the Swift model [5]. The calibrated parameters for each specimen are shown in Table 4.2. Note that the equations are valid for the plastic deformation stage.

Table 4.2 Parameters for material property extrapolation.

Specimen	BM						WM		
	W	k	n	ε_0	a	b	k	n	ε_0
S700t8	0	949	0.0191	-0.0075	1433	845	1075	0.1030	-0.0027
S700t10	0	1000	0.0185	-0.0081	1636	889	1299	0.1500	0.0111
S500t8	0.9	757	0.0626	0.0196	493	617	1075	0.1030	-0.0027
S500t10	0.8	851	0.0900	0.0235	554	649	940	0.0735	0.0000
S355t8	1.0	785	0.1400	0.0142	549	528	982	0.2120	0.0144
S355t10	0.8	575	0.0120	-0.0065	1181	526	894	0.1540	-0.0053

4.2.2. A linear stress modification factor

The welded coupon specimen consists of three materials. The "strong" (BM and WM) and "weak" (HAZ) materials connect in series along the loading direction. Since the strong material imposes a transverse constraint on the weak material during the tensile loading, the measured stress-strain relationship of the weak material cannot represent the constitutive model under the uniaxial stress state. According to the von Mises yield criterion, the transverse tensile stress (σ_x) would result in higher stress in the loading direction (σ_y) than that of the uniaxial tensile stress state at the plastic stage. Meanwhile, considering the volume preservation assumption at a plastic stage, the strain in the loading direction (ε_y) under the biaxial tensile stress state is smaller than that would be in the uniaxial stress state. Thus, the measured stress and strain, using DIC, are larger and smaller than the stress and strain measured under the uniaxial stress state, respectively.

If the measured stress-strain relationship is directly used in FEA, the predicted resistance would be higher than the experiment due to the transverse constraint in the 3D FE model. The overestimated resistance results in a higher strain in BM and WM. Consequently, the total deformation of the welded connection predicted by FEA is more significant than that of the experiment. The overestimated deformation would be even larger if a longer gauge length is used.

The extent of the transverse constraint depends on the difference in the hardening level between the strong and weak materials. With a strong BM and WM, the transverse constraint may increase with the plasticity in HAZ, such as S700 and S355 welded connections in this study. With a less strong BM and WM, the transverse constraint may vanish at the HAZ onset of necking, such as S500 welded connections in this study. Therefore, a linear modification factor is proposed to consider different combinations of the materials.

Young's modulus of HAZ, BM, and WM at the elastic stage has a limited variation, resulting in a negligible transverse constraint at the zones' boundary. The transverse constraint appears, and the stress modification starts when HAZ yields. Two modification factors, MF_1 and MF_2 , which are calibrated based on FEA, are applied to the modification initiation point and the onset of necking, respectively, as shown in Fig. 4.1. The linear interpolation equation for the modification factor at the hardening stage is given in Eq. (4.5). The true stress could be modified following Eq. (4.6). It has to be emphasized that the constraint level is related to the relative hardening performance (the difference in the stress-strain stiffness) between HAZ and BM/WM. The constraint gradually increases after the proportional limit of HAZ, resulting in an increasing modification factor. The stiffness of the HAZ stress-strain relationship reduces to a relatively low and stable value at the 0.2% proof stress yield point. Therefore, as a practical approach, the yield point of HAZ is considered the modification initiation point. Besides, the ultimate strength point is taken as the onset of the necking point.

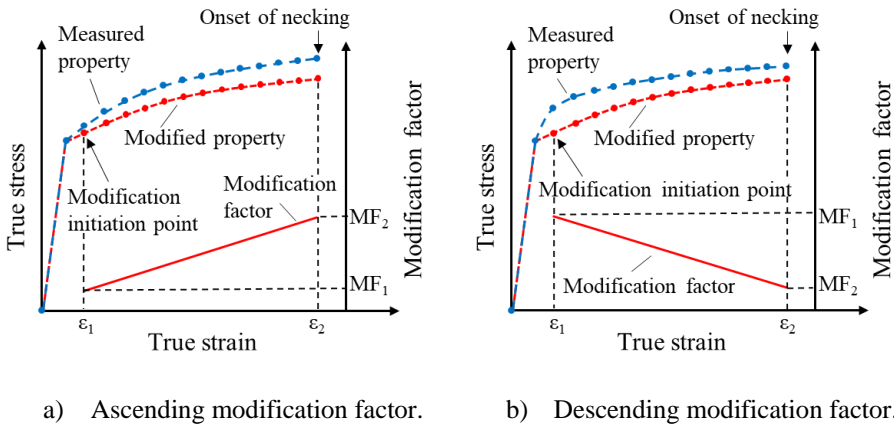


Fig. 4.1 Schematic diagram of the linear stress modification factor.

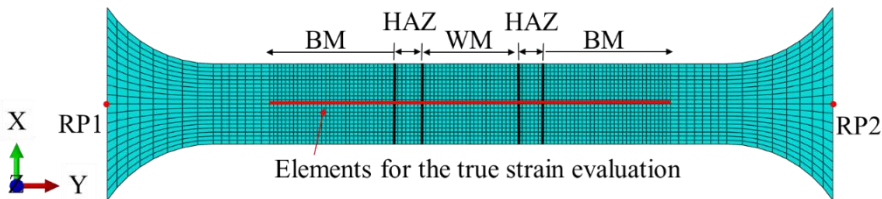
$$MF_{\varepsilon} = \frac{MF_2 - MF_1}{\varepsilon_2 - \varepsilon_1} (\varepsilon - \varepsilon_1) + MF_1 \quad (4.5)$$

$$\sigma_{\varepsilon, \text{modi}} = (1 - MF_{\varepsilon}) \sigma_{\varepsilon} \quad (4.6)$$

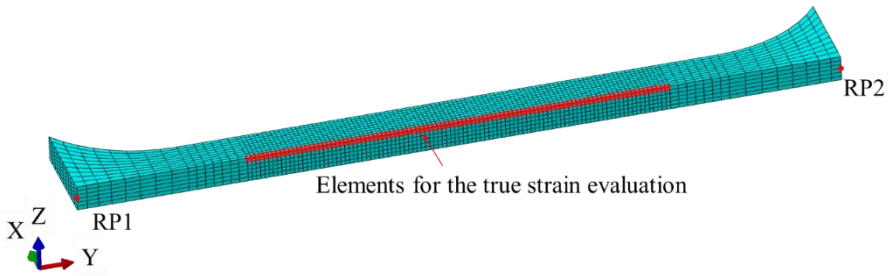
where ε_1 and ε_2 are the true strain corresponding to the modification initiation point and the onset of necking, respectively; $\sigma_{\varepsilon, \text{modi}}$ is the modified true stress. In the schematic diagram, the blue and red scatter lines represent the measured and modified true stress-strain relationship, respectively. Note that the linear modification factor could be ascending or descending depending on the material property difference between HAZ and adjacent materials (BM and WM).

4.2.3. Finite element analysis

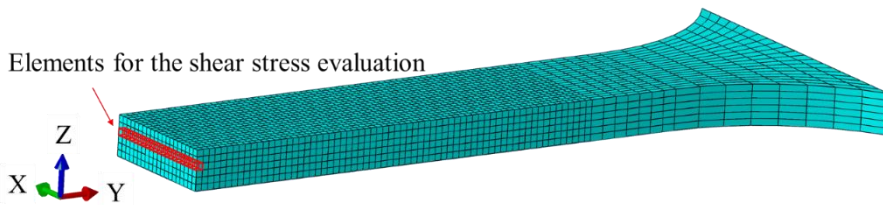
The ABAQUS:2019 software package [7] is used to conduct FEA. A 3D FE model is created for each milled welded coupon specimen based on the measured dimensions, as shown in Fig. 4.2. The model includes five parts separated by four boundaries (see black lines in Fig. 4.2 a)). The width of HAZ and WM is based on the experimentally determined width presented in Table 4.1. According to the hardness results from the central layer (referring to Line 2 and Line 3 in Fig. 2.5), a limited variation of the HAZ width through the thickness was found. Hence, a constant width for HAZ and WM is assumed in the FE model of the milled welded coupon specimen. Note that the width could be slightly adjusted considering the accuracy of DIC results compared to hardness results. In addition, a FE model containing the entire welded zone is created for S500 and S700 unmilled coupon specimens to verify the constitutive model of HAZ, as shown in Fig. 4.2 d). The widths of the welded zone components are in accordance with the metallurgical results of weld samples, as illustrated in Section 2.3.1. Furthermore, to evaluate the effect of the transverse constraint in the width direction (the X direction in Fig. 4.2 a) and d)) on the resistance of the welded connection, a quarter of welded SHS was created by extruding the weld cross-section of the S700 unmilled coupon specimen, as presented in Fig. 4.2 e). No experimental tests were conducted on a complete welded SHS cross-section.



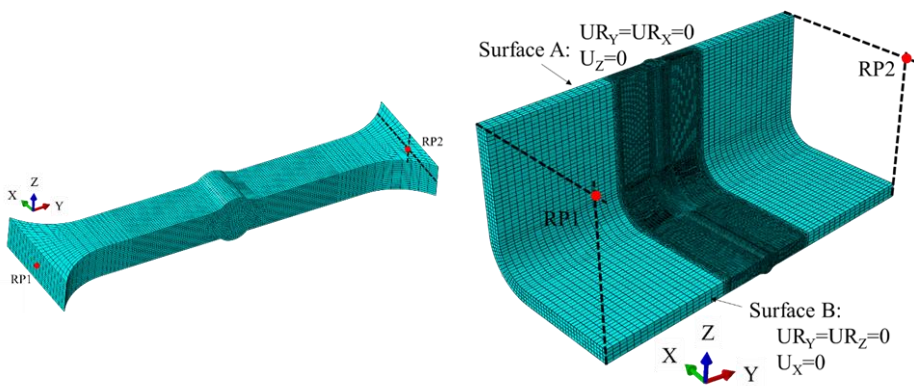
a) Plane view.



b) Elements for the true strain evaluation.



c) Elements for the shear stress evaluation.



d) Unmilled welded coupon specimen.

e) A quarter of welded SHS.

Fig. 4.2 FE model of the welded coupon specimen.

For the FE model of coupon specimens, the part within the 50 mm gauge length was meshed with 0.5 mm mesh size, while the remaining part uses a coarse mesh in the loading direction. The grip part of the specimen was not modelled to reduce the computational burden. For the FE model of the welded SHS, the 0.5 mm fine mesh was only used for HAZ, WM, and 5 mm BM region close to the HAZ boundary on both sides.

Two reference points (RP1 and RP2) were generated at the centre of two end surfaces or the centre of the entire SHS end surface. The end surface was controlled by the corresponding reference point in terms of all three translations and three rotations using the multi-point beam constraint (MPC beam). A positive displacement in the Y direction was applied at RP2 while the other degrees of freedom of the two reference points were fixed. Additionally, for the welded SHS, a symmetric boundary condition was applied on Surface A and B to model the entire SHS cross-section, as shown in Fig. 4.2 e). Quasi-static analysis was conducted using an explicit solver with a 100 s period and a 0.0001 s target time increment. Eight-node hexahedral solid elements with reduced integration (C3D8R) were used throughout the whole model except for a small transition zone (enlarging the element size in BM) where C3D10 is used.

4.3. Results and discussions

A parametric study is carried out based on the FE model introduced in Section 4.2. The load-deformation relationship (with 50 mm gauge length) and the true strain distribution (in elements in the middle of the surface marked with red colour in Fig. 4.2) are used to calibrate the modification factor MF_1 and MF_2 .

4.3.1. Calibration of the modification factor

The modification factor is calibrated by a trial-and-error process based on the load-deformation relationship and the strain distribution plot at two deformation levels. Fig. 4.3 presents three typical strain distribution plots during the calibration. The black solid line is the experimental result. The blue and the red dash line represents the FE result using the measured original HAZ material property and the modified material property, respectively.

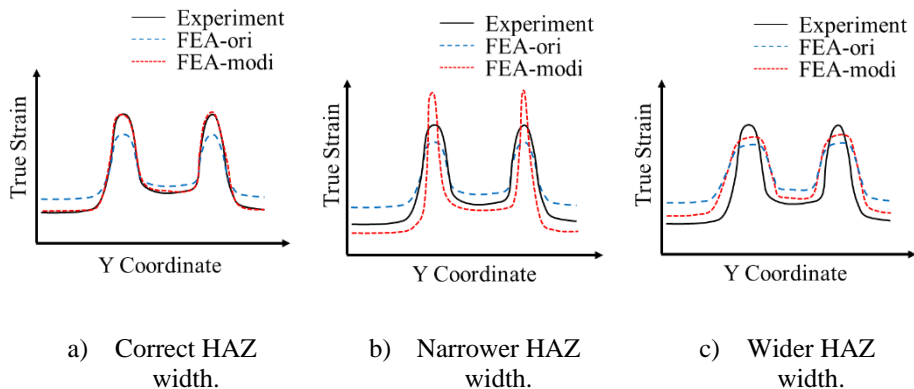


Fig. 4.3 Three typical longitudinal true strain distribution plots.

First, the FE model is created based on the measured and identified dimensions (HAZ and WM width), as illustrated in Section 4.2. The measured original HAZ stress-strain relationship is used in FEA for the first trial. If the predicted resistance is higher than the

experiment for a specific deformation level, a modification factor is needed, shown as Condition 3 in Fig. 4.4. Meanwhile, the predicted strain in HAZ is smaller while larger in BM and WM than the experiment shown as the blue dash line in Fig. 4.3. Therefore, in the second step, a modification factor should be applied to reduce the stress. Depending on the deviation level, the increment of the modification factor can be 3% in the beginning and gradually reduce to 1% in the subsequent iteration steps. The resistance and the strain distribution at the specific deformation level predicted by FEA should match the experimental results well if an appropriate modification factor is used. The strain distribution of FE results using the modified HAZ material property is presented by the red dash line in Fig. 4.3 a). The matching level is evaluated visually since the strain distribution shows an adequate difference with a 1% modification factor increment, which is the minimum increment used in this research. A cost function can be used to calibrate the modification factor with a finer increment. However, the current research object is to establish a HAZ stress-strain relationship suitable for the FEA of large-scale welded hollow section joints. The evaluation approach is sufficient considering the efficiency and the accuracy. If an excessive modification factor is applied, such as Condition 2 in Fig. 4.4, the predicted strain in HAZ and the predicted resistance would be greater and smaller, respectively, than the experiment. By repeating the second step, an appropriate modification factor could be calibrated. Note that if BM and WM impose a limited transverse constraint on HAZ, the modification factor may not be necessary. Consequently, the FE strain distribution may fit the experimental result well using the measured original HAZ stress-strain relationship.

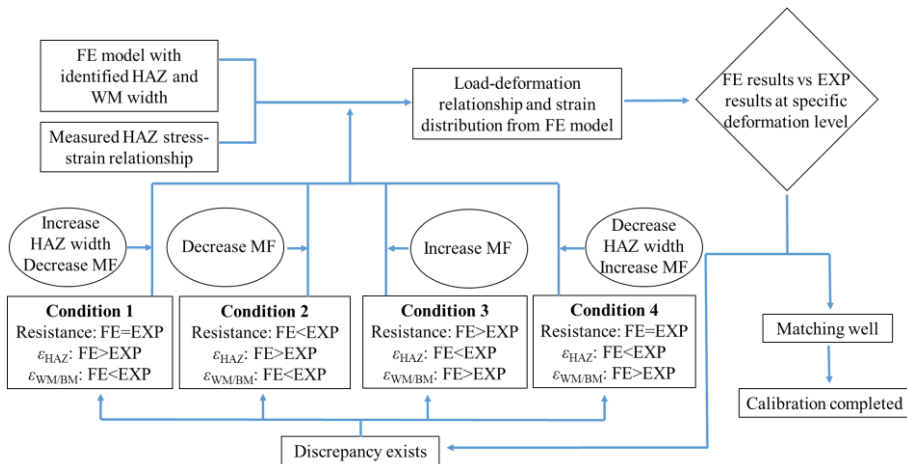


Fig. 4.4 The complete calibration procedures.

This calibration procedure should be done at least at the early hardening stage (0.5 mm deformation in this study) and the onset of the necking for calibrating the linear modification factor. More deformation levels should be involved in the calibration if a non-linear modification factor is required.

In addition, the identified HAZ width used in the FE model may slightly deviate from the experiment, given the accuracy of the DIC measurement. The width deviation could be eliminated in the calibration procedures. Fig. 4.3 b) and c) show the strain distribution in the FE model with a narrower and a wider HAZ, respectively. The red dash line represents the strain distribution of the FE model, where the modified stress-strain relationship is used, and the predicted resistance fits the experiment at a specific deformation level. Take the FE model with a narrower HAZ width, for example. The narrower HAZ width in the FE model results in a higher level of the transverse constraint from BM and WM. Hence, a more significant modification factor is required for accurately predicting the resistance, leading to the excessive strain localisation in HAZ, corresponding to Condition 1 in Fig. 4.4. By slightly increasing the HAZ width with a 0.5 mm increment, a smaller modification factor is required for fitting the resistance, and the problem of the excessive strain localisation in HAZ is solved. The adjusted width of HAZ and WM is summarised in Table 4.3. In the presented investigation, by 5 to 10 iterations, the HAZ constitutive model and width could be determined. A detailed flowchart illustrating the complete calibration procedures is shown in Fig. 4.4.

Table 4.3 The adjusted width of HAZ and WM. [mm]

Specimen	S700t8 WN2	S700t10 WN2	S500t8 WN2	S500t10 WN2	S355t8 WN2	S355t10 WN2
HAZ ₁	4	3.5	4	5	4	2.5
HAZ ₂	3	2.5	4.5	4	3.5	3
WM	9.5	10	8.5	9	14.5	12

4.3.2. Calibration results

The results of two FE analyses, FEA-ori and FEA-modi, are compared to the experimental results in Fig. 4.5-Fig. 4.7. FEA-ori uses the measured original HAZ material property without the modification factor, while FEA-modi uses the modified true stress-true strain relationship of HAZ with the calibrated modification factor.

The load-deformation curves obtained from the experiment and FEA are compared in Fig. 4.5-Fig. 4.7 b). A solid "Star" symbol is used to show the ultimate resistance point, at which HAZ reaches the necking strain, for each curve. After the "Star" symbol, the post-necking part of the FE result is shown in a grey colour. Note that further damage model analysis is required for fitting the post-necking part of the curve.

Two longitudinal true strain distribution diagrams at two levels of the longitudinal deformation, which are used for calibrating the modification factor, are presented in Fig. 4.5-Fig. 4.7 c) and g) for each specimen. The first deformation level is 0.5 mm and corresponds to the early hardening stage. The second deformation level corresponds to the ultimate resistance obtained in the experiment. The longitudinal strain distribution at the middle of the abovementioned two deformation levels is investigated for validation, as shown in Fig. 4.5-Fig. 4.7 e). Besides, the corresponding transverse true strain distributions at the three deformation levels are presented in Fig. 4.5-Fig. 4.7 d), f), and h), which are used to evaluate the validity of the Mises yield criterion considering the

material anisotropy in the weld region. The region of two HAZs is marked with a grey background in these true strain distribution plots. It has to be clarified that the same stress-strain relationship is used in two HAZs of each specimen (with the same modification factors). The difference in the maximum strain of two HAZs results from the different widths of two HAZs.

The coordinate system in the FE model is positioned such that the necking always appears in the left HAZ, referring to Fig. 4.2 a). Therefore, the shear stress (τ_{yx}) in the left HAZ at two boundary surfaces is investigated to illustrate the level of the transverse constraint based on FEA-modi. The shear stress distribution in HAZ boundary elements close to BM and WM is presented in Fig. 4.5-Fig. 4.7 i) and j), respectively. The elements are in the central layer of HAZ, as presented in Fig. 4.2 c). The shear stress is positive if it acts on a positive face in a positive direction or if it acts on a negative face in a negative direction. In addition to the two levels of the longitudinal deformation for obtaining the true strain distribution, two more levels at the elastic stage (0.1 mm) and the onset of the yielding (0.25 mm) is investigated.

The detailed result of the specimen with 8 mm original nominal thickness (before milling) for different steel grades is discussed below. The calibrated modification factor and the evaluation of the deviation between experiments and FEA predictions for all six specimens are presented in Table 4.7 at the end of this section.

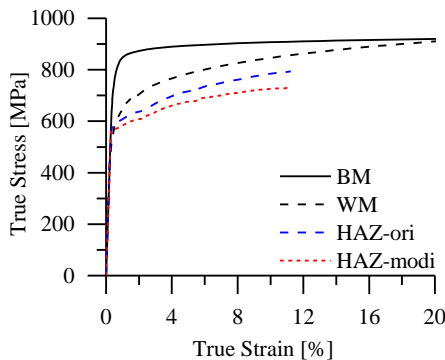
4.3.2.1. S700t8WN2 milled welded coupon specimen (undermatching weld)

Fig. 4.5 a) presents the true stress-true strain relationship of different zones used in the FE of the S700t8 welded coupon specimen. The black solid and dash lines represent BM and WM, respectively. The blue dash line, namely HAZ-ori, is the original relationship without the stress modification, while the red dash line is the modified relationship with the reduced true stress. The modification factors MF_1 and MF_2 are 4% and 8%, respectively. From Fig. 4.5 a), it is evident that BM and WM are stronger than HAZ. BM and WM would experience a limited plastic strain as HAZ reaches the necking point. The level of the transverse constraint increases during loading since the HAZ hardening performance (tangent of the true stress-true strain curve) reduces with the increase of the true strain. It can also be proved by Fig. 4.5 i) and j) where the shear stress imposed by BM and WM increases with the level of the deformation, indicating that the transverse constraint keeps increasing during loading. Consequently, the modification factor ascends with the increase of the true strain, conforming to the case in Fig. 4.1 a). It must be clarified that the transverse constraint does not exist at the elastic stage since the shear stress is nearly 0 MPa at 0.1 mm deformation. The non-existing transverse constraint at the elastic stage could also be observed in specimens S500t8 and S355t8.

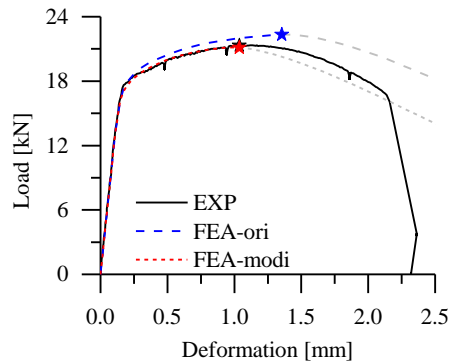
The load-deformation relationship obtained from the experiment and FE analysis based on 50 mm gauge length is compared in Fig. 4.5 b). The ultimate resistance and the corresponding deformation (peak deformation) are shown in Table 4.4. FEA-ori has a 5% higher resistance and 30% higher peak deformation compared to the experimental results.

Using the modified HAZ property, the ultimate resistance is 1% lower than the experimental results and the peak deformation is well predicted with 0% deviation.

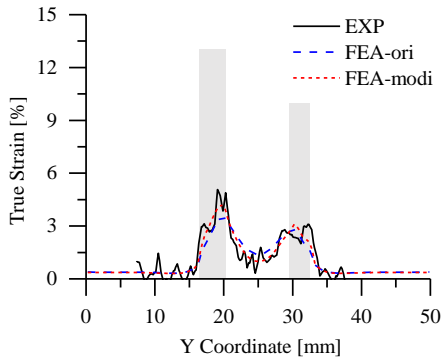
The true strain in the longitudinal direction (ε_y) and the transverse direction (ε_x) is extracted from elements (in DIC and the FE model) in the middle of the specimen surface, as shown in Fig. 4.2 b). The longitudinal true strain distribution at 0.5 mm, 0.75 mm, and 1.04 mm (corresponding to the ultimate resistance in the experiment) deformation is plotted against the elements' Y-coordinate in Fig. 4.5 c), e), and g), respectively. Compared to the experiments, results from FEA-ori have a smaller strain in HAZ while a larger strain in WM. It indicates that the HAZ strength is overestimated at all deformation stages, resulting in a higher resistance and, consequently, a higher strain level in WM and BM. With the same total deformation, the contribution from each zone to the total deformation is different between FEA-ori and the experiment. Using the modified material property, the true strain distribution of FEA-modi matches the experimental result much better. Besides, the transverse strain in experiments and FEA are compared in Fig. 4.5 d), f), and h). Good agreements are observed, demonstrating that HAZ and WM can be modelled as isotropic materials that follow the Mises yield criterion. Therefore, the modified HAZ stress-strain relationship is successfully calibrated until the onset of necking. In addition, considering all six true strain plots, it can be seen that the peak strain in HAZ does not appear in the middle of each HAZ but is slightly close to the side (BM or WM) with a weaker material which is WM in this case. This strain pattern also exists in S500 and S355 specimens.



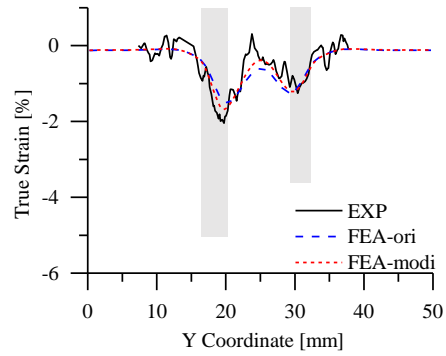
a) True stress-true strain relationship.



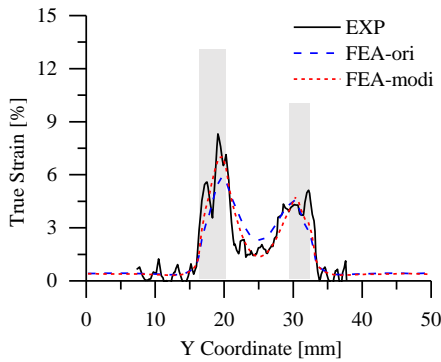
b) Load-deformation relationship.



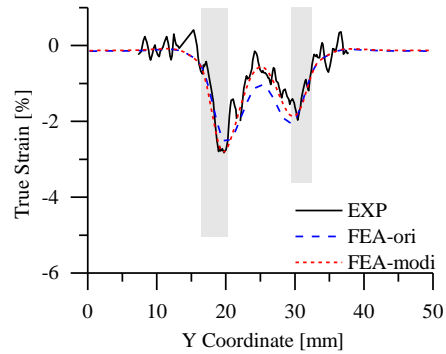
c) Longitudinal strain distribution at 0.5 mm deformation.



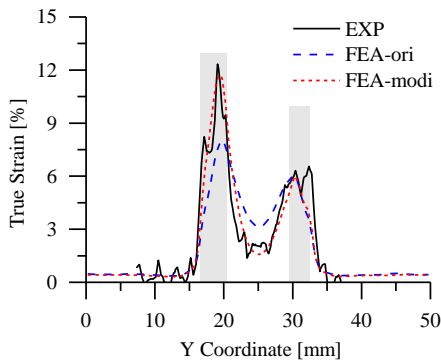
d) Transverse strain distribution at 0.5 mm deformation.



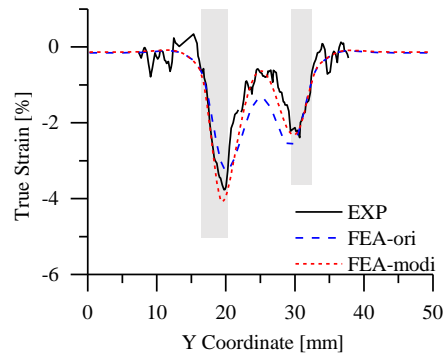
e) Longitudinal strain distribution at 0.75 mm deformation.



f) Transverse strain distribution at 0.75 mm deformation.



g) Longitudinal strain distribution at 1.04 mm deformation.



h) Transverse strain distribution at 1.04 mm deformation.

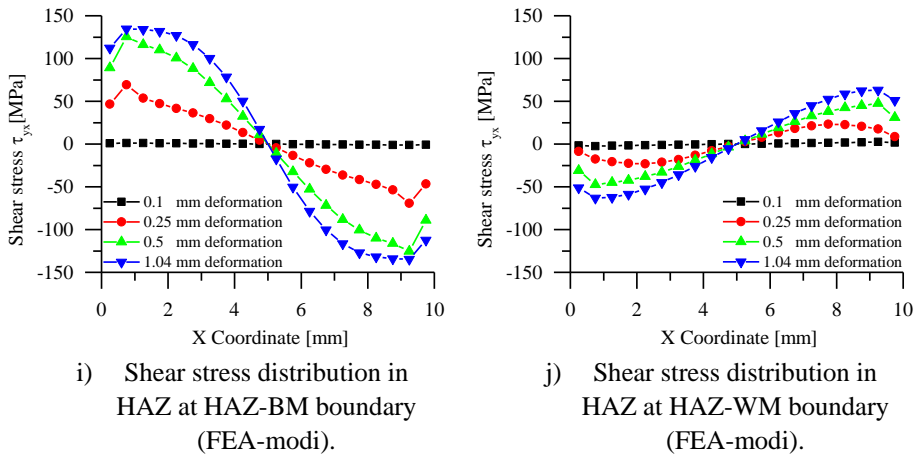


Fig. 4.5 Comparison of FE and DIC results (S700t8WN2).

Table 4.4 Comparison of the ultimate resistance and the peak deformation (S700t8WN2).

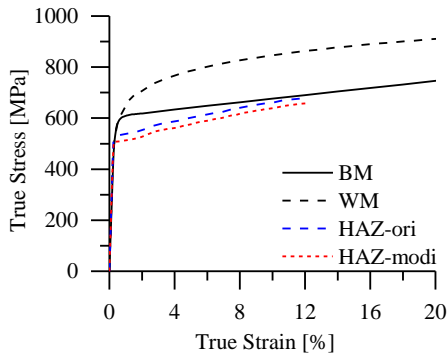
	EXP	FEA-ori	$\frac{\text{FEA-ori}}{\text{EXP}}$	FEA-modi	$\frac{\text{FEA-modi}}{\text{EXP}}$
Ultimate resistance	21.31 kN	22.33 kN	1.05	21.11 kN	0.99
Peak deformation	1.04 mm	1.35 mm	1.30	1.04 mm	1.00

4.3.2.2. S500t8WN2 milled welded coupon specimen (overmatching weld)

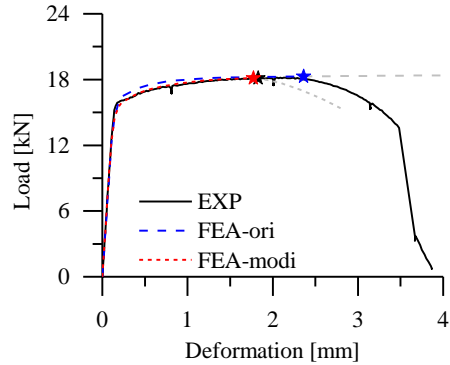
The true stress-strain relationship of different materials is shown in Fig. 4.6 a). MF_1 and MF_2 are 5% and 3%, respectively. Since the strain hardening of BM is relatively low, the true stress of BM and HAZ gets closer when the true strain approaches the HAZ necking strain, as shown in Fig. 4.6 a). In Fig. 4.6 i), the shear stress on the BM-HAZ side decreases as the deformation approaches the ultimate stage. Therefore, the level of the transverse constraint reduces, and the modification factor descends with the increase of the true strain, aligning with the case in Fig. 4.1 b). Besides, Fig. 4.6 i) and j) illustrate that the constraint level on the WM side is larger than the BM side, indicating that an overmatching weld was applied.

Fig. 4.6 b) presents the load-deformation relationship obtained from FEA and the experiment. The model (FEA-ori) with the original HAZ property has a higher resistance at the beginning of the plastic stage, while the ultimate resistance is very close to the experimental result (1% deviation). However, the peak deformation of FEA-ori is 28% larger than the experimental results, as shown in Table 4.5. In Fig. 4.6 g), the strain in BM of FEA-ori is much higher than that of the experiment, resulting in a hugely overestimated deformation in BM. Using the modified constitutive model, FEA-modi underestimates the peak deformation by 3%, while the ultimate resistance is well predicted with 0% deviation, as presented in Table 4.5. In addition, the overestimated resistance at the beginning of the plastic stage is corrected by using the modified constitutive model.

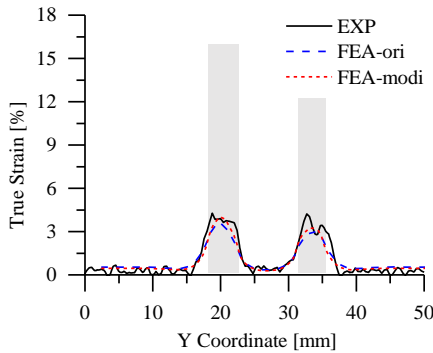
Similar to the S700t8 welded coupon specimen, the strain in HAZ predicted by FEA-ori is smaller than that of the experiment at three deformation stages (0.5 mm, 1 mm, and 1.7 mm), as shown in Fig. 4.6 c), e), and g). Using the modified material property, the strain distribution predicted by FEA-modi matches the experimental result well. Fig. 4.6 c), e), and g) also demonstrate that HAZ and WM are the isotropic material following the Mises yield criterion. Therefore, it can be concluded that the stress reduced property of HAZ is successfully calibrated until the onset of necking.



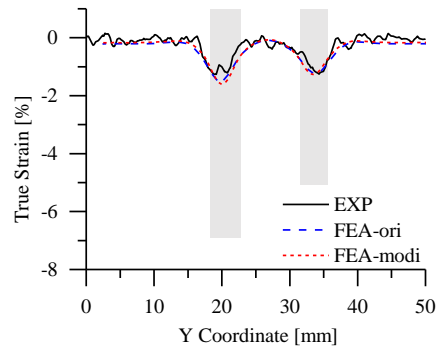
a) True stress-true strain relationship.



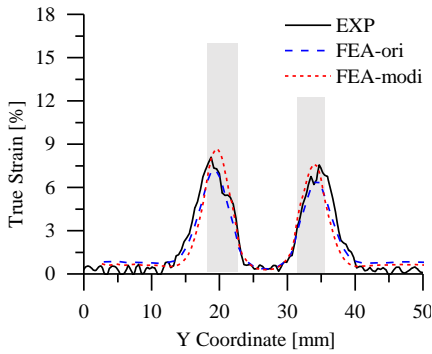
b) Load-deformation relationship.



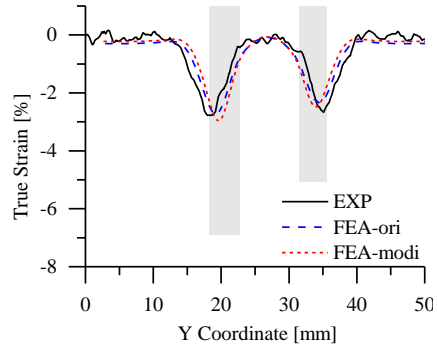
c) Longitudinal strain distribution at 0.5 mm deformation.



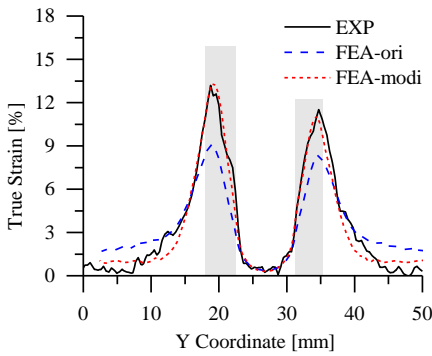
d) Transverse strain distribution at 0.5 mm deformation.



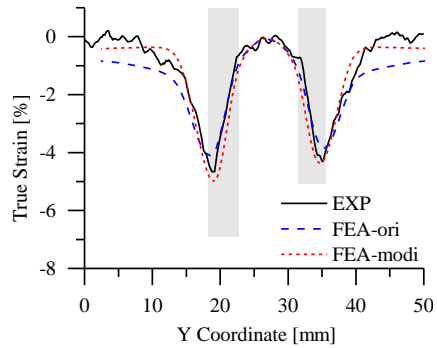
e) Longitudinal strain distribution at 1 mm deformation.



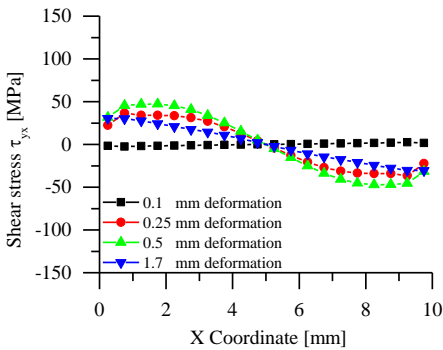
f) Transverse strain distribution at 1 mm deformation.



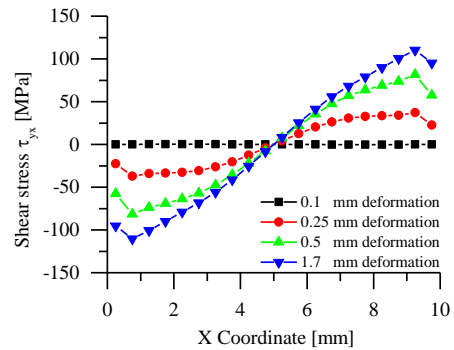
g) Longitudinal strain distribution at 1.7 mm deformation.



h) Transverse strain distribution at 1.7 mm deformation.



i) Shear stress distribution in HAZ at HAZ-BM boundary (FEA-modi).



j) Shear stress distribution in HAZ at HAZ-WM boundary (FEA-modi).

Fig. 4.6 Comparison of FE and DIC results (S500t8WN2).

Table 4.5 Comparison of the ultimate resistance and the peak deformation (S500t8WN2)

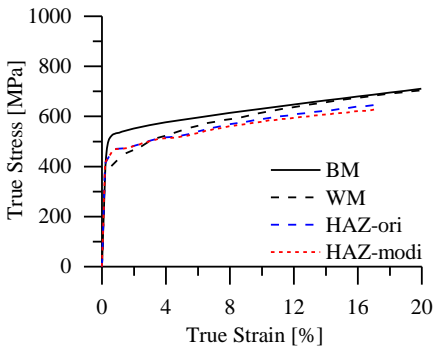
	EXP	FEA-ori	$\frac{\text{FEA-ori}}{\text{EXP}}$	FEA-modi	$\frac{\text{FEA-modi}}{\text{EXP}}$
Ultimate resistance	18.13 kN	18.28 kN	1.01	18.11 kN	1.00
Peak deformation	1.83 mm	2.35 mm	1.28	1.77 mm	0.97

4.3.2.3. S355t8WN2 milled welded coupon specimen (matching weld)

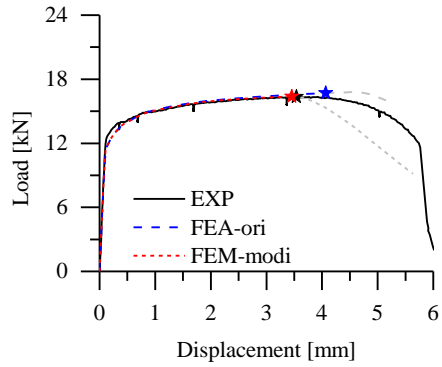
WM yields at a lower strength than HAZ, as shown in Fig. 4.7 a). Therefore, MF_1 is 0%. The 0% modification factor can also be justified by Fig. 4.7 c), where the strain distribution obtained from FEA-ori matches the experimental result well. Fig. 4.7 a) shows that WM has a stronger hardening performance than HAZ. Thus, the transverse constraint increases during the loading. At the onset of necking, the underestimated strain, consequently the overestimated stress, could be observed in Fig. 4.7 g) where the strain in FEA-ori HAZ is smaller than in the experiment. Based on the parametric study, a 4% reduction is calibrated for MF_2 . Fig. 4.7 i) and j) demonstrate that the shear stress is relatively low at the beginning of plastification, increasing to its maximum at the onset of the necking. A similar shear stress level is observed on BM and WM sides, indicating that the connection has a matching weld. Therefore, the modification factor is in an ascending trend matching the situation in Fig. 4.1 a). Besides, since WM has a lower yield strength than HAZ, HAZ imposes a transverse constraint on WM presented by curves with 0.25 mm and 0.5 mm deformation in Fig. 4.7 j).

The load-deformation relationships obtained from FEA and experiments are compared in Fig. 4.7 b). The ultimate resistance and the peak deformation are presented in Table 4.6. The ultimate resistance predicted by FEA-ori shows a good agreement with the experimental result within a 3% deviation. However, the peak deformation of FEA-ori is 14% larger than that of the experiment. With a modified material property, FEA-modi predicts the peak deformation to be 3% smaller than that of the experiment, while the ultimate resistance is predicted with a 0% deviation.

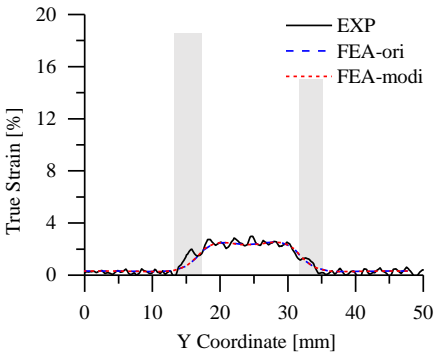
In Fig. 4.7 c), e), and g), the longitudinal strain distributions at three deformation stages (0.5 mm deformation at the beginning of the plastic stage, 1.5 mm at the middle of the hardening stage, and 3.5 mm at the ultimate load) predicted by FEA-modi with the stress reduced material property show good agreement with the experimental results. Besides, the HAZ and WM material isotropy are demonstrated in Fig. 4.7 d), f), and h). Therefore, it is concluded that the modified material property of HAZ is successfully calibrated until the onset of necking.



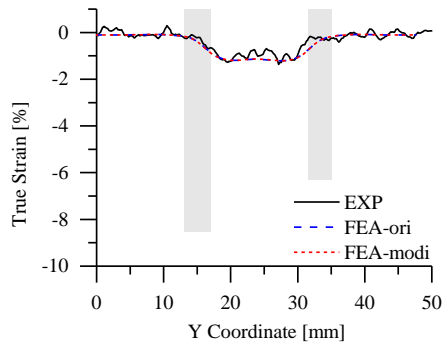
a) True stress-true strain relationship.



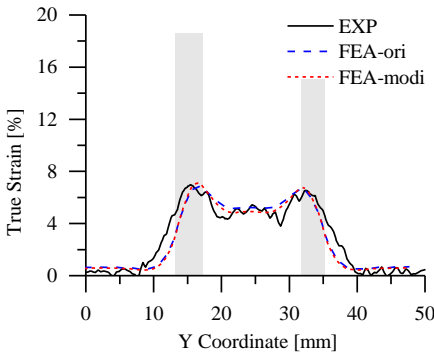
b) Load-deformation relationship.



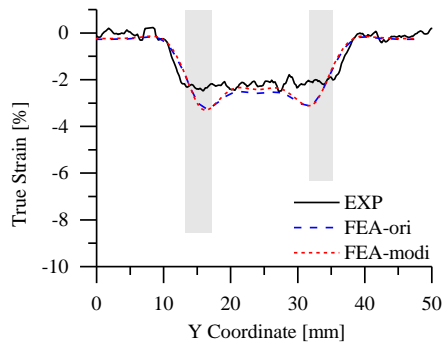
c) Longitudinal strain distribution at 0.5 mm deformation.



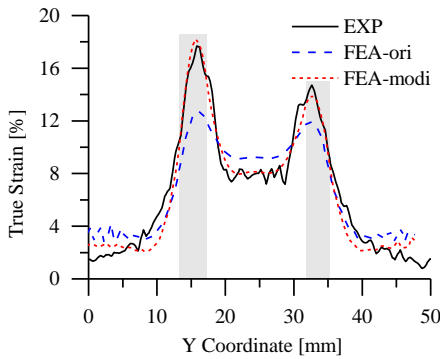
d) Transverse strain distribution at 0.5 mm deformation.



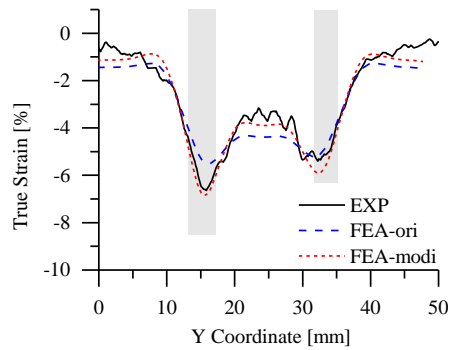
e) Longitudinal strain distribution at 1.5 mm deformation.



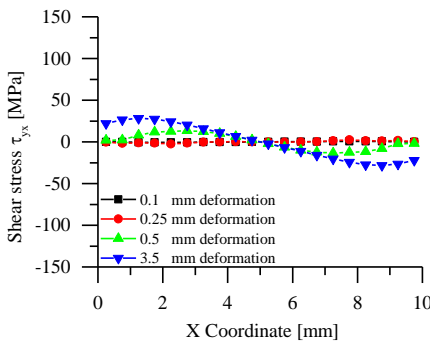
f) Transverse strain distribution at 1.5 mm deformation.



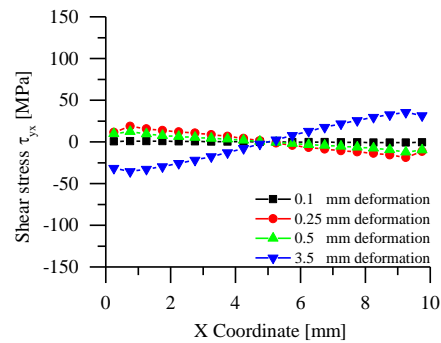
g) Longitudinal strain distribution at 3.5 mm deformation.



h) Transverse strain distribution at 3.5 mm deformation.



i) Shear stress distribution in HAZ at HAZ-BM boundary (FEA-modi).



j) Shear stress distribution in HAZ at HAZ-WM boundary (FEA-modi).

Fig. 4.7 Comparison of FE and DIC results (S355t8WN2).

Table 4.6 Comparison of the ultimate resistance and the peak deformation (S355t8WN2).

	EXP	FEA-ori	$\frac{\text{FEA-ori}}{\text{EXP}}$	FEA-modi	$\frac{\text{FEA-modi}}{\text{EXP}}$
Ultimate resistance	16.35 kN	16.83 kN	1.03	16.38 kN	1.00
Peak deformation	3.54 mm	4.05 mm	1.14	3.45 mm	0.97

The calibrated modification factor, the deformation ratio, and the resistance ratio are summarised in Table 4.7. The ultimate resistance predicted by FEA using the original HAZ material property is slightly higher than the experimental result within a maximum 5% deviation. However, the peak deformation is overestimated by at least 14% among all specimens, except for the specimen S500t10 where the BM material property is relatively soft resulting in a 0% MF₂.

Table 4.7 Summary of the calibrated parameters and the prediction results.

Specimen	$\frac{R_{ori}}{R_{EXP}}$	$\frac{D_{ori}}{D_{EXP}}$	$\frac{R_{modi}}{R_{EXP}}$	$\frac{D_{modi}}{D_{EXP}}$	MF ₁ [%]	MF ₂ [%]	ϵ_1 [%]	ϵ_2 [%]
S700t8	1.05	1.30	0.99	1.00	4	8	0.51	11.25
S700t10	1.04	1.29	0.99	1.00	4	6	0.52	9.16
S500t8	1.01	1.28	1.00	0.97	5	3	0.45	12.17
S500t10	1.00	1.03	1.00	0.98	5	0	0.49	10.04
S355t8	1.03	1.14	1.00	0.97	0	4	0.41	17.05
S355t10	1.02	1.19	1.00	0.97	0	5	0.44	14.97

where R_i/R_{EXP} and D_i/D_{EXP} ($i = ori$ or $modi$) are the resistance ratio and the deformation ratio, respectively.

In the scope of this experimental and numerical investigation, FEA-ori of the S700 specimen with an undermatching weld has the most significant overestimation (around 30%) on the peak deformation. Consequently, a large modification factor, with a combination of an average 4% MF₁ and 7% MF₂, is applied to the HAZ material property. For the S500 material with an overmatching weld, a descending linear modification factor with a 5% MF₁ and 2% MF₂ combination is obtained. For the S355 material with a matching weld, MF₁ is 0% since WM has a lower yield strength than HAZ. The modification factor increases to an average of 5% at the onset of necking. The deformation is overestimated at around 17% by FEA-ori.

Using the calibrated modification factor, the ultimate resistance and the peak deformation predicted by FEA-modi has a maximum 1 % and 3% deviation from the experiment, respectively.

4.3.3. Effect of transverse constraint on the HAZ resistance

The original and modified HAZ constitutive models are used to simulate the unmilled coupon specimen and the welded SHS connection. The load-deformation relationships are shown in Fig. 4.8. The full experimental curve is presented while the FE curves are plotted until the ultimate resistance. The ultimate resistance point is marked by a solid "star" with the same colour as the corresponding curve.

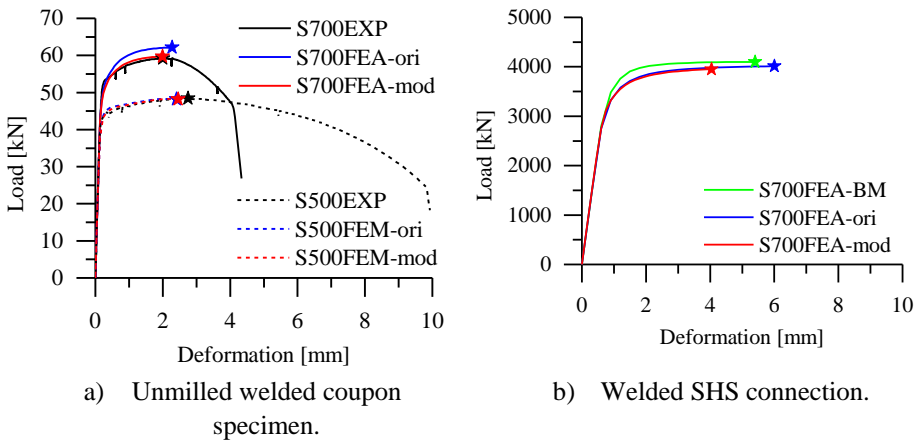


Fig. 4.8 Load-deformation relationships.

Fig. 4.8 a) shows the load-deformation relationship of the unmillied welded specimen. The FE model using the original and modified HAZ property does not show a significant difference in the predicted resistance and deformation at the ultimate stage for the S500 specimen. However, for the S700 specimen, the FE model overestimates the ultimate resistance and peak deformation by 5% and 14%, respectively, using the original HAZ property. The FE result deviates less than 1% from the experimental result using the modified HAZ property. The strain contour plot of the FE model using the modified HAZ property shows good agreement with the experiment, as shown in Fig. 4.9. The position of the high-strain region (in HAZ for the S700 specimen and BM for the S500 specimen) is well predicted.

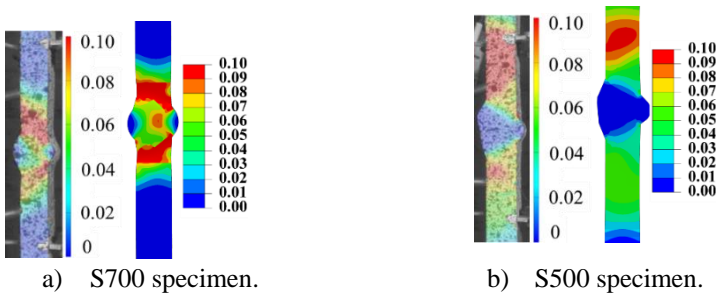


Fig. 4.9 True strain contour plot in the unmillied welded coupon specimen.

The effect of transverse constraint in the width direction on the resistance of the welded connection is evaluated based on the one-quarter welded SHS FE model (see Fig. 4.2 e)). Note that the width direction of the specimen refers to the X direction of the milled and unmillied specimen and the X/Z direction of the SHS model. S355 and S500 unmillied welded coupon specimens failed in BM, indicating the failure of SHS connections using S355 and S500 materials would be in BM as well. Therefore, the increasing effect of the transverse constraint in the width direction cannot be evaluated by testing S355 and S500 materials in the welded SHS connection. Hence, only the calibrated HAZ stress-strain relationship of S700t8 was used to further study the one-quarter welded SHS FE model.

In addition, a FE model using the BM property for all three regions (BM, HAZ, and WM), shown as FEA-BM, is made for comparison. Fig. 4.8 b) compares the load-deformation relationship obtained from FE models based on a 200 mm gauge length. Compared to the model using the modified HAZ property, the model using the original HAZ property and BM property have a 2% and 4% higher resistance, respectively, while a 49% and 34% higher peak deformation, respectively. On the other hand, although the model using the modified constitutive model still fails in HAZ, the HAZ equivalent ultimate strength (the total load divided by the SHS cross-section area) significantly increases to $f_{u,HAZ,SHS} = 848$ MPa, which is almost identical to the ultimate resistance (880MPa) of the model using the BM stress-strain relationship for all zones.

The verified MF_2 for S700t8 indicates that the transverse constraint in the width direction of the milled welded coupon specimen results in an 8% strength enhancement in HAZ at the ultimate state ($f_{u,HAZ}^* = 0.92 \times f_{u,HAZ,milled}$). Comparing the average ultimate strength (S700t8) of the unmilled welded coupon specimens to the milled welded coupon specimens, the ultimate strength increases by 8% due to the transverse constraint in the thickness direction ($f_{u,HAZ,unmilled} = 1.08 \times f_{u,HAZ,milled}$). Therefore, the BM and WM of a full-thickness weld connection may enhance the HAZ ultimate strength (without the transverse constraint) by 17% ($f_{u,HAZ,unmilled} = 1.08 / 0.92 \times f_{u,HAZ}^*$). Furthermore, the enhancement would be even higher if a wider specimen is considered, such as the welded SHS connection, where the HAZ ultimate strength is improved by 29% compared to the HAZ ultimate strength ($f_{u,HAZ,SHS} = 1.29 \times f_{u,HAZ}^*$).

Although the FE model with the calibrated modification factor is validated against the experiment, it is essential to calibrate the modification factor for other welded connections with different steel grades and filler metals to accurately predict the deformation in the weld zone, consequently the deformation capacity of the welded connection.

4.4. A semi-empirical constitutive model for HAZ

4.4.1. The theoretical model

All approaches introduced in Chapter 2 are rather complicated to implement in practice. A semi-empirical material model for HAZ based on the mechanical properties of BM would be ideal because it will significantly facilitate the advanced analysis of welded connections where HAZ is critical. Hence, a semi-empirical constitutive model for HAZ is proposed in this Section. The Swift model [5] (power law) is employed to generate the true stress-true strain relationship of HAZ. The expression of the original model is given in Eq. (4.4). Engineering stress σ_e and engineering strain ε_e can be converted to σ and ε for the constitutive model in the range before necking using Eq. (4.7). Hence, the $\sigma_e - \varepsilon_e$ relationship following the Swift model is obtained by substituting Eq. (4.7) into Eq. (4.4), as shown in Eq. (4.8).

$$\begin{aligned}\sigma_t &= \sigma_e (1 + \varepsilon_e) \\ \varepsilon_t &= \ln(1 + \varepsilon_e)\end{aligned}\quad (4.7)$$

$$\sigma_e = \frac{A [\ln(1 + \varepsilon_e) + \varepsilon_0]^n}{(1 + \varepsilon_e)} \quad (4.8)$$

The three Swift parameters can be determined by three equations, as presented in Eq. (4.9). The first two equations are established by substituting the stress and strain at the yield strength point and the ultimate strength point in Eq. (4.8). In addition, the derivative of σ_e with respect to ε_e equals 0 at the ultimate strength point, which is the third equation.

$$\begin{aligned}f_y &= \frac{A [\ln(1 + \varepsilon_y) + \varepsilon_0]^n}{(1 + \varepsilon_y)} \\ f_u &= \frac{A [\ln(1 + \varepsilon_u) + \varepsilon_0]^n}{(1 + \varepsilon_u)} \\ \left. \frac{d\sigma_e}{d\varepsilon_e} \right|_{\varepsilon_e = \varepsilon_u} &= - \frac{A [\ln(1 + \varepsilon_u) + \varepsilon_0]^{n-1} (\ln(1 + \varepsilon_u) + \varepsilon_0 - n)}{(1 + \varepsilon_u)^2} = 0\end{aligned}\quad (4.9)$$

where f_y and f_u are the yield and ultimate strength, respectively. In order to determine the Swift parameters for HAZ, engineering stress and engineering strain at the yield point and the ultimate point are required. Three reduction factors (RFs) are proposed to correlate the mechanical properties of BM and HAZ, as shown in Eq. (4.10). Note that the elongation at fracture ε_f of BM is correlated to the ultimate strain of HAZ. The reason is explained in Section 4.4.2.

$$\begin{aligned}f_{y,HAZ} &= RF_1 \times f_{y,BM} \\ f_{u,HAZ} &= RF_2 \times f_{u,BM} \\ \varepsilon_{u,HAZ} &= RF_3 \times \varepsilon_{f,BM}\end{aligned}\quad (4.10)$$

4.4.2. Determination of the parameters

The yield strength f_y (0.2% proof stress), the ultimate strength f_u , and the elongation at failure ε_f are determined for BM, as shown in Table 4.8.

Table 4.8 Mechanical properties of BM.

Material	No.	f_y [MPa]	f_u [MPa]	ε_f [%]	Material	No.	f_y [MPa]	f_u [MPa]	ε_f [%]
S355t5	N1	510	539	23.3	S355t10	N1	524	555	18.2

S355t8	N2	499	546	25.3		N2	507	537	26.6	
	N1	504	535	26.9		N2M1	491	534	29.7	
	N2	508	528	26.6		N2M2	514	531	27.9	
S500t5	N1	565	635	22.5	S500t10	N1	568	607	21.2	
	N2	566	638	21.0		N2	597	630	16.7	
S500t8	N1	575	609	24.8		N2M1	560	595	24.3	
	N2	585	614	24.9		N2M2	564	602	22.6	
S700t5	N1	767	846	12.3		S700t8	N1	772	845	13.4
	N2	756	837	12.9			N2	784	857	13.8
S700t10	N1	812	907	12.2	N2M1		742	820	15.7	
	N2	819	902	12.9	N2M2		737	811	12.7	

The modification factors MF_1 and MF_2 were calibrated for one specimen of each profile, as shown in Table 4.9. Compared to S355 and S500, S700 has higher MFs, which aligns with the hardness results. Besides, MFs of S700t5 are significantly higher than S700t8 and S700t10. The reason is that the width of S700t5 was 20 mm while the other two specimens are not wider than 10 mm, which also implies that the width of the specimen may affect the extent of the transverse constraint. The calibrated MFs were used to calculate the modified yield strength f_y^* and the modified ultimate strength f_u^* for the other specimens extracted from the same profile, see Eq.(4.6). The measured strength, the modified strength, and the ultimate strain ϵ_u of HAZ are presented in Table 4.10 for all welded coupon specimens. Since the yield and ultimate strength of BM for each profile show good consistency, the average mechanical properties of BM are compared to HAZ to reveal the correlation between HAZ and BM. Note that the ultimate strength of HAZ in specimens S500t10WN2 and S500t10WN4 is higher than BM, as the average ultimate strength is used for BM. The reason for using the elongation at fracture of BM is demonstrated in Section 2.3.4.

Table 4.9 The calibrated modification factors MF_1 and MF_2 [%].

MFs	S355t5	S355t8	S355t10	S500t4	S500t8	S500t10	S700t5	S700t8	S700t10
MF_1	0	0	0	5	5	5	14	4	4
MF_2	4.5	4	5	7.5	3	0	10	8	6

Table 4.10 Comparison of HAZ and BM.

Specimen	$f_{y,BM}$ [MPa]	$f_{y,HAZ}$ [MPa]	$f_{y,HAZ}^*$ [MPa]	$\frac{f_{y,HAZ}^*}{f_{y,BM}}$	$f_{u,BM}$ [MPa]	$f_{u,HAZ}$ [MPa]	$f_{u,HAZ}^*$ [MPa]	$\frac{f_{u,HAZ}^*}{f_{u,BM}}$	$\epsilon_{t,BM}$ [%]	$\epsilon_{u,HAZ}$ [%]	$\frac{\epsilon_{u,HAZ}}{\epsilon_{t,BM}}$
S355t5WN2	505	453	453	0.90	543	561	533	0.98	24.3	18.5	0.76
S355t5WN3		430	430	0.85		549	521	0.96		16.6	0.68
S355t5WN4		431	431	0.85		545	518	0.95		20.0	0.82
S355t8WN2	506	465	465	0.92	531	545	523	0.99	26.8	23.0	0.86
S355t8WN3		451	451	0.89		535	514	0.97		16.8	0.63
S355t8WN4		454	454	0.90		538	516	0.97		16.7	0.62

S355t10WN2		474	474	0.93		569	541	1.00		16.2	0.63
S355t10WN3		419	419	0.82		537	510	0.95		18.8	0.73
S355t10WN3M	509	426	426	0.84	539	524	498	0.92	25.6	20.6	0.80
S355t10WN4		441	441	0.87		541	514	0.95		17.1	0.67
S355t10WN4M		430	430	0.84		535	508	0.94		18.6	0.73
S500t4WN2		522	496	0.88		643	596	0.94		15.5	0.71
S500t4WN3	566	518	492	0.87	637	645	598	0.94	21.8	14.9	0.69
S500t4WN4		522	496	0.88		638	587	0.92		16.2	0.74
S500t8WN2		531	504	0.87		606	588	0.96		17.0	0.68
S500t8WN3	580	504	479	0.83	612	577	560	0.92	24.9	16.0	0.64
S500t8WN4		520	494	0.85		586	573	0.94		13.2	0.53
S500t10WN2		564	536	0.94		632	632	1.04		13.3	0.63
S500t10WN3		513	487	0.85		593	593	0.98		19.2	0.91
S500t10WN3M	572	515	489	0.85	609	593	593	0.97	21.2	13.9	0.66
S500t10WN4		545	518	0.91		615	615	1.01		10.4	0.49
S500t10WN4M		532	506	0.88		610	610	1.00		12.7	0.60
S700t5WN2		-	-	-		-	-	-		-	-
S700t5WN3	762	585	503	0.66	841	795	716	0.85	12.6	14.7	1.17
S700t5WN4		673	579	0.76		793	713	0.85		10.1	0.80
S700t8WN2		589	566	0.75		712	655	0.79		11.7	0.84
S700t8WN3		608	583	0.77		717	660	0.79		12.3	0.88
S700t8WN3M	759	632	607	0.80	833	726	668	0.80	13.9	11.3	0.81
S700t8WN4		606	581	0.77		709	654	0.79		12.7	0.91
S700t8WN4M		574	551	0.73		707	650	0.78		11.1	0.80
S700t10WN2		656	630	0.77		780	733	0.81		11.5	0.92
S700t10WN3	816	696	668	0.82	904	789	741	0.82	12.6	13.9	1.11
S700t10WN4		701	673	0.83		798	750	0.83		9.2	0.73

The yield strength ratio $f_{y,HAZ}^* / f_{y,BM}$, the ultimate strength ratio $f_{u,HAZ}^* / f_{u,BM}$, and the strain ratio $\varepsilon_{u,HAZ} / \varepsilon_{f,BM}$ of all tested welded coupon specimens are presented in Table 4.10. The ratios of S355 and S500 vary in a very similar range, where the yield strength and the ultimate strength of HAZ are on average 13% and 4% lower than BM, respectively. A significant strength reduction in HAZ is observed in the S700 material, as the average yield strength ratio and the ultimate strength ratio are 0.76 and 0.81, respectively. It is worth mentioning that the ultimate strength reduction in HAZ varies in a very similar range with a maximum 4% difference compared to another research [8], where the HAZ ultimate strength is predicted based on the hardness result. The average strain ratio of S355, S500, and S700 are 0.72, 0.66 and 0.84, respectively. Besides, there is no clear relationship between the ratios and the thickness of the original profile for all materials.

The yield strength ratio, the ultimate strength ratio, and the strain ratio of most specimens (at least 9 out of 11 or 10) are not smaller than 0.84, 0.94, and 0.6 for S355 and S500, and not smaller than 0.7, 0.79, and 0.8 for S700, respectively. Hence, a set of rather conservative reduction factors (RFs), introduced in Eq. (4.10), are determined for each steel grade, as presented in Table 4.11. Based on the BM average mechanical properties and the determined RFs, the three Swift parameters are derived for three profiles (S355t10, S500t10, S700t8); see Table 4.11. The derived constitutive model of HAZ is further validated by FEA of unmilled welded coupon tests. In addition, it has to be emphasised that the proposed RFs are only valid for the joints using the same BM and

welding parameters, as the mechanical properties of HAZ are very sensitive to the welding details [9–11].

Table 4.11 Determined constitutive parameters for HAZ.

Steel grade	RF ₁	RF ₂	RF ₃	Material	A	n	ε ₀
S355	0.85	0.95	0.6	S355t10	797	0.167	0.0236
S500	0.85	0.95	0.6	S500t10	851	0.132	0.0122
S700	0.7	0.8	0.8	S700t8	942	0.108	0.0024

4.4.3. Results of the semi-empirical constitutive model

Fig. 4.10 presents the load-deformation relationship of the unmilled welded coupon tests. The results of the two specimens for each profile are in good agreement. The fracture of S355t10 and S500t10 specimens shifts from HAZ in the milled welded coupon specimen to BM in the unmilled welded coupon specimen, while the S700t8 specimen failed in HAZ in both the milled and unmilled specimens, as shown in Fig. 4.11. Hence, the deformation capacity of S355t10 and S500t10 specimens are significantly higher than S700t8 specimens. Note that the low deformation capacity of S700t8 specimens is not attributed to the lower ductility of S700 BM compared to S355 BM and S500 BM, as a limited strain (around yielding) was observed in BM. The lower deformation capacity of S700t8 specimens is also demonstrated by the fact that the modified ultimate strength of HAZ is smaller than the yield strength of BM, implying that the HAZ fails before yielding in BM. Besides, with an increasing measuring length, the deformation capacity increase of S355 and S500 specimens would be even larger than S700 specimens since the S355 and S500 specimens have a significantly higher strain in BM than the S700 specimen.

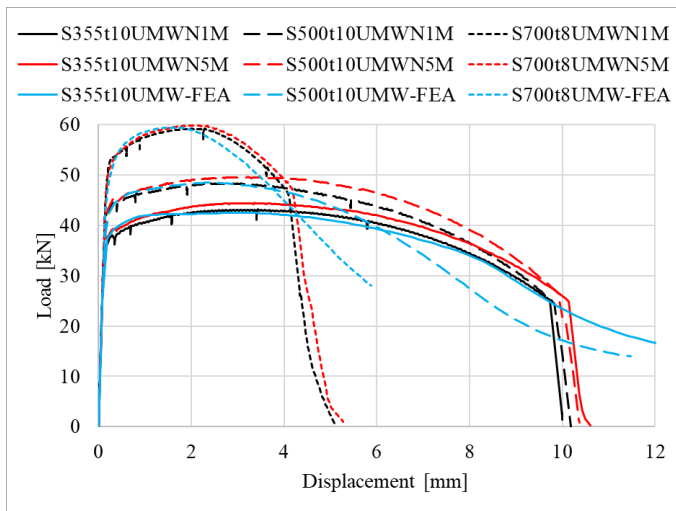


Fig. 4.10 Load-displacement relationship of unmilled welded coupon specimens.

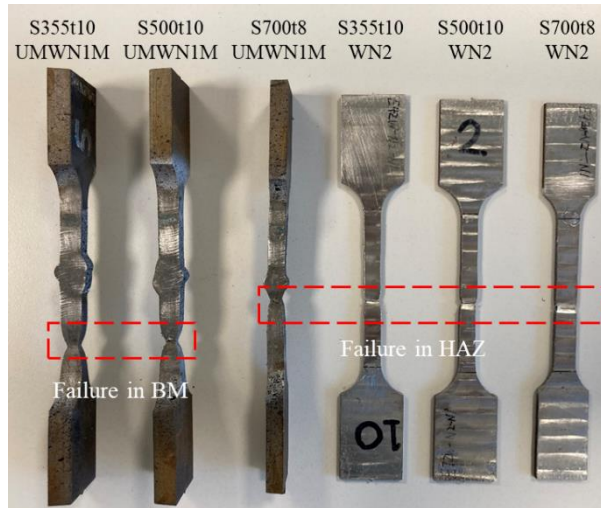


Fig. 4.11 Failure of milled and unmilled welded coupon specimens.

The FE models of the unmilled welded coupon specimen introduced in Section 4.2.3 are used for validating the semi-empirical constitutive model. The FE results are compared to the experiments in Fig. 4.10. It can be seen that the tensile behaviour of the unmilled coupon specimen is well predicted using the derived HAZ constitutive model based on the BM mechanical properties and corresponding RFs. Comparing the FE ultimate resistance to the experiment, the maximum deviation is less than 3%. In addition, the FE models successfully predicted the necking position in experiments (HAZ for S700 and BM for S355 and S500), which may reliably indicate the position of the final fracture if the damage model was applied. Hence, it is concluded that the derived HAZ equivalent constitutive model can effectively represent the HAZ mechanical properties.

4.5. Conclusions

The equivalent mechanical properties of the heat-affected zone (HAZ) are investigated using a semi-empirical methodology. HAZ is considered a homogeneous material, with no distinction of different volumetric fractions of microstructures. Based on the presented results, the following conclusions are drawn:

- 1) The weld metal (WM) and/or the base material (BM) impose a transverse constraint on HAZ regardless of the steel grade if HAZ is the weakest component of a welded connection. The larger difference in the material hardening behaviour between HAZ and WM and/or BM, the heavier the transverse constraint is. It leads to a higher overestimation of the HAZ material strength obtained from the digital image correlation (DIC) system.
- 2) A linear modification factor is proposed to modify (reduce) the true stress of the measured HAZ material property. A combination of an average 4% MF_1 (at yielding) and 7% MF_2 (at the onset of necking) modification factor is calibrated for S700 material. MF_1 and MF_2 are on average 5% and 2% for S500 material,

- respectively. For S355 material, the modification factors MF_1 and MF_2 are 0% and 5% on average, respectively. The modification factors account for the transverse constraint imposed by BM and WM on HAZ, as the transverse constraint increases the resistance of HAZ. In an S700t8 welded connection, the ultimate strength of HAZ in the unmilled welded coupon specimen is 17% higher than the modified ultimate strength of HAZ. The difference is increased to 29% due to the higher constraint in the case of the complete butt-welded SHS.
- 3) The finite element (FE) model using the original measured HAZ material property (FEA-ori) predicts a reasonably correct ultimate resistance within 5% overestimate, while the peak deformation, corresponding to the onset of HAZ necking, could be overestimated up to 30%. Regarding the butt welded S700 SHS joint, the predicted resistance using BM or original HAZ constitutive model for HAZ has a maximum 4% scattering in resistance, but a up to 49% overestimation on the ultimate deformation, compared to the model using the modified constitutive model.
 - 4) HAZ and WM are "sufficiently" the isotropic material, and therefore the Mises yield criterion is suitable.
 - 5) For S355 and S500, the modified yield strength and the modified ultimate strength of HAZ are on average 13% and 4% lower than the base material (BM). The S700 HAZ modified yield and ultimate strength degradation are 24% and 19% compared to BM, respectively.
 - 6) Three reduction factors (RFs) are proposed to correlate the mechanical properties of BM and HAZ. The proposed RFs for the yield strength, the ultimate strength, and the ultimate strain are 0.85, 0.95, 0.6 for S355 and S500, and 0.7, 0.8, 0.8 for S700, respectively. The derived HAZ mechanical properties are used to generate a semi-empirical stress-strain relationship before necking based on the Swift model. The derived HAZ constitutive model for each steel grade is successfully validated against the experiments.
 - 7) Although the modification factor is validated for three steel grades in this study, it is essential to calibrate the modification factor for other welded connections made of different steel grades, material processing methods, filler metals, and welding procedures. The true strain distribution along the loading direction and the load-deformation relationship obtained from DIC and FEA should be used to validate the material property before necking. Damage modelling is required to model the connection behaviour properly after necking.

Reference

- [1] W.D. Lockwood, A.P. Reynolds, Simulation of the global response of a friction stir weld using local constitutive behavior, *Materials Science and Engineering A*. 339 (2003) 35–42. [https://doi.org/10.1016/S0921-5093\(02\)00116-8](https://doi.org/10.1016/S0921-5093(02)00116-8).
- [2] F. Hochhauser, W. Ernst, R. Rauch, R. Vallant, Influence of the soft zone on the strength of welded modern HSLA steels, *Welding in the World*. 56 (2012). <https://doi.org/DOI:10.1007/BF03321352>.
- [3] EN 1993-1-8:2005 - Design of steel structures - Part 1-8: Design of joints, (2005).
- [4] prEN 1993-1-8:2021 - Design of steel structures - Part 1-8: Design of joints (draft of EN1993-1-8: 2021), (2022).
- [5] H.W. Swift, Plastic instability under plane stress, *Journal of the Mechanics and Physics of Solids*. 1 (1952) 1–18. [https://doi.org/10.1016/0022-5096\(52\)90002-1](https://doi.org/10.1016/0022-5096(52)90002-1).
- [6] Y. Ling, Uniaxial True Stress-Strain after Necking, *AMP Journal of Technology*. 5 (2004) 37–48.
- [7] ABAQUS, Abaqus Analysis User’s Manual, 2019 version, (2019).
- [8] W. Cai, Y. Wang, G. Li, R. Stroetmann, Comparative study on strength of TMCP and QT high-strength steel butt-welded joints, *Journal of Constructional Steel Research*. 197 (2022) 107447. <https://doi.org/10.1016/j.jcsr.2022.107447>.
- [9] R. Stroetmann, T. Kästner, A. Hälsig, P. Mayr, Influence of the cooling time on the mechanical properties of welded HSS-joints, *Steel Construction*. 11 (2018) 264–271. <https://doi.org/10.1002/stco.201800019>.
- [10] R. Stroetmann, T. Kästner, Numerical analyses on welded joints at high-strength steels, *Ce/Papers*. 3 (2019) 725–730. <https://doi.org/10.1002/cepa.1165>.
- [11] R. Stroetmann, T. Kastner, B. Rust, Welded connections of high-strength steels, in: *Current Perspectives and New Directions in Mechanics, Modelling and Design of Structural Systems*, 2022: pp. 1111–1116.

5.

Calibration of Gurson-Tvergaard-Needleman (GTN) damage model for the heat-affected zone and the base material

Prediction of fracture failure modes for welded joints by finite element simulations requires modelling of the material damage. An appropriate damage model effectively reveals the fracture zone of the joint.

In this chapter, the parameters of the Gurson-Tvergaard-Needleman (GTN) damage model are calibrated for the base material (BM) and the heat-affected zone (HAZ) of butt-welded cold-formed RHS connections. A computational homogenization analysis is carried out using representative volume element models to calibrate the pressure-dependent yield surface parameters of the GTN damage model, considering the different combinations of the accumulated initial hardening strain and the void volume fraction (VVF) due to a varying stress triaxiality. The critical and final VVFs are calibrated against tensile coupon tests.

Parts of this chapter appear in the journal article: ‘Rui Yan et al., Ductile fracture simulation of cold-formed high strength steel using GTN damage model. Journal of Constructional Steel Research, 2021’ and ‘Rui Yan et al., Fracture simulation of welded RHS X-joints using GTN damage model, Advances in Structural Engineering, 2022’. Minor modifications have been made to suit the thesis.

5.1. Introduction

The existing rules for steel structures according to the standard EN 1993-1-8 [1] are limited to the material behaviour of mild steels with the steel grade up to S460. Supplementary rules proposed in EN1993-1-12 [2] are used to design structures made of high-strength steel (HSS), which has higher strength but lower ductility compared to mild steel. It is an open question whether the research on HSS joints undertaken worldwide is sufficiently systematic and comprehensive to predict the ultimate state of HSS joints accurately. The precise prediction of fracture becomes very important in predicting the ultimate state and the post-ultimate load behaviour of HSS structural members and welded joints.

The traditional elastoplastic hardening model may overestimate the plasticity's localisation effect in the necking zone if the material damage is not considered [3,4]. Diverse damage theories combining elastoplastic constitutive models have been developed to simulate fracture initiation and propagation. Three main approaches classified from pioneering works are developed [5], namely the continuum damage model, the uncoupled damage model, and the micromechanics-based damage model, to simulate the fracture of the material. The uncoupled damage model generally uses the equivalent plastic strain as an external variable uncoupled from the yield surface to govern the failure criteria. The material is damaged when the external variable reaches a critical value, as shown by several proposed models [6,7]. However, the parameter calibration process is firmly based on reliable experimental data. The continuum damage mechanics approach considers damage by correlating the damage with an internal variable. Lemaitre [8] proposed a damage model under the thermodynamics framework by modifying the Cauchy stress tensor to an effective stress tensor with a damage factor. Effective stress is used in the constitutive equation, indicating that the damage is coupled with the yield surface. The last approach is the micromechanics-based damage model. Under the framework of micromechanics damage models, the ductile fracture process could be described as the nucleation, growth, and coalescence of the microvoids [9]. The process initiates when the microvoids nucleate at inclusions or second phase particles by particle-matrix interface de-cohesion or particle cracking. These voids grow and change the shape accompanying the plastic deformation of the matrix, and eventually, the microvoids coalesce resulting in the final failure of the material.

Several studies have shown that the Lode angle and the stress triaxiality are essential parameters for ductile fracture [7,10–14]. The growth and coalescence of microvoids could explain the stress triaxiality and Lode angle dependency phenomenon at the microscale. At a high-stress triaxiality level, the voids grow volumetrically, and the necking of inter-void ligaments results in the coalescence of the voids [13]. On the other hand, the voids may grow, but the shear localisation at the inter-void ligaments governs the fracture initiation under a low-stress triaxiality. It demonstrates that the final fracture also depends on the Lode parameter, which represents the shear state of the material [13,14]. Gurson-Tvergaard-Needleman (GTN) Damage Model, as one of the most popular micromechanics-based porous plasticity models, links the macroscopic damage

with the evolution of micro void volume fraction (VVF). It was initially proposed by Gurson [15], considering the growth of the voids only. Tvergaard [16,17] and Needleman and Tvergaard [18] improved the model by involving void nucleation and coalescence. Furthermore, researches [19–23] have been done to extend the application range of the GTN model to the low-stress triaxiality state.

Generally, the effects of the stress triaxiality and the Lode Angle on failure modes and fracture properties could be investigated experimentally and numerically. A large number of specimens are required to identify the parameters of the damage model for each test series. Different types of coupon specimens, such as smooth, notched bars, or compact tension specimens, can be used to determine the fracture process [7,10–13,21]. However, it is difficult to conduct all kinds of reliable experiments to generate different stress states through different initial specimen geometries or by applying different load combinations for specific parts in the civil engineering sector, such as welds, HAZ, bolts, headed studs and fillet corners of cold-formed tube. Hence, the micromechanical analysis could be used as a surrogate model to numerically calibrate the ductile fracture parameters. Fritzen et al. [24] investigated the pressure dependency of the deviatoric limit stress of three-dimensional microstructures. The stress triaxiality is varied by applying different load conditions in addition to the periodic boundary condition. The GTN parameters for elastoplastic porous metals are identified using three-dimensional representative volume elements (3D RVE). Xin et al. [25] calibrated the material parameters of the orthotropic GTN model inferred from microstructures generated from high-fidelity discrete element simulations. Xin et al. [26] calibrated the friction angle, the ratio of the yield stress in triaxial tension to the yield stress in triaxial compression, and the dilation angle of the linear Drucker-Prager plastic model based on the experimental result and the computational homogenisation.

In terms of the damage modelling of the cold-formed HSS, Pavlovic et al. [27] calibrated the damage model under the framework of the void growth model (VGM) for the HSS cold-formed material [28]. The FE prediction is generally agreed well with experimental observations, except that the resistance of FE results is larger than that of the test results at the descending stage, mainly because the fracture locus is not well considered at the lower stress triaxiality in the VGM model. Yan et al. [29] attempted to calibrate the GTN damage parameters for mild steel S355 based on the engineering stress-strain relationship. The 3D RVE is employed to determine the parameters q_1 , q_2 , and q_3 with constant values. A parametric study is carried out on the coupon simulation to calibrate VVF correlated parameters f_c and f_t .

In this chapter, the GTN damage model is calibrated for the base material and the heat-affected zone of welded cold-formed RHS connections. The computational homogenisation method is employed to investigate the pressure dependency of the deviatoric stress. Different load conditions corresponding to different stress triaxiality levels are applied to eighteen unit cells with random spherical pores. VVF of unit cells varies from 0.1% to 25%. The parameters q_1 and q_2 , which describe the yield surface of the material, are calibrated based on the inelastic deformation within the unit cell. An equation is proposed to describe the relationship between VVF and q_1 value. The

parameters f_c and f_f are calibrated against tensile coupon tests, including standard coupon specimens and milled welded coupon specimens. The calibrated GTN damage model is successfully validated under the stress triaxiality higher than 0.33 based on notched coupon tests for HSS.

5.2. Theoretical background

5.2.1. GTN model

The GTN model involves nine constitutive parameters. Three constitutive parameters q_1 , q_2 , and q_3 are used to describe the shape of the yield surface. The other six parameters are employed to define the evolution of VVF. The yield surface of the GTN model is presented in Eq. (5.1):

$$\phi = \left(\frac{\sigma_{\text{eq}}}{\sigma_t} \right)^2 + 2q_1 f^* \cosh \left(\frac{3q_2 \sigma_m}{2\sigma_y} \right) - 1 - q_3 f^{*2} = 0 \quad (5.1)$$

where: σ_{eq} , σ_m , and σ_t are the von Mises equivalent stress, the hydrostatic pressure, and the flow stress of the undamaged material matrix, respectively. The expressions for σ_{eq} and σ_m are given below:

$$\sigma_m = \frac{1}{3} \sigma_{ij} \delta_{ij} \quad (5.2)$$

$$\sigma_{\text{eq}} = \sqrt{\frac{3}{2} \left(\sigma_{ij} - \frac{1}{3} \sigma_{ij} \delta_{ij} \right) \left(\sigma_{ij} - \frac{1}{3} \sigma_{ij} \delta_{ij} \right)} \quad (5.3)$$

where σ_{ij} and δ_{ij} are the stress tensor and the Kronecker delta, respectively.

The evolution of VVF consists of the new void's nucleation and the growth of the existing void, see Eq. (5.4). The nucleation of the void may occur because of decohesion of the particle-matrix interface and microcracking. It follows a normal distribution regarding the equivalent plastic strain. Hence, the void nucleation rate involves three parameters: the total nucleated VVF f_n , the mean value of the normal distribution of the nucleation strain ε_n , and the standard deviation S_n . The expressions are given in Eq. (5.5) and Eq. (5.6). The growth of the existing void is based on the law of conservation of mass. The rate of the void growth is expressed in terms of the plastic hydrostatic strain rate, as shown in Eq. (5.7). f^* is the modified VVF, a function of the critical VVF f_c and final VVF f_f . The amplification of VVF starts and completes when f_c and f_f are reached, respectively. The expression is given in Eq. (5.8). When the damage variable VVF reaches f_f , the material fails. The parameters f_c and f_f describe the process of the void coalescence. f_c is VVF at the initiation of the void coalescence. f_f corresponds to the end

of the void coalescence but does not have a physical meaning, as f^* is modified to f_u^* , which is VVF at the onset of failure.

$$\dot{f} = \dot{f}_g + \dot{f}_n \quad (5.4)$$

$$\dot{f}_n = A \dot{\varepsilon}_{\text{eq}}^{\text{pl}} \quad (5.5)$$

$$A = \frac{f_n}{S_n \sqrt{2\pi}} e^{\left[\frac{1}{2} \left(\frac{\varepsilon_{\text{eq}}^{\text{pl}} - \varepsilon_n}{S_n} \right)^2 \right]} \quad (5.6)$$

$$\dot{f}_g = (1-f) \dot{\varepsilon}_{\text{kk}}^{\text{pl}} \quad (5.7)$$

$$f^* = \begin{cases} f & f < f_c \\ f_c + K(f - f_c) & f_c \leq f < f_f \\ f_u^* & f \geq f_f \end{cases} \quad K = \frac{f_u^* - f_c}{f_f - f_c} \quad (5.8)$$

5.2.2. Periodic boundary condition

The Hill-Mandel computational homogenisation method could establish the link between micro-scale and macro-scale behaviour. Under the micro-scale level, the Cauchy stress $\tilde{\sigma}_{ij}$ in the unit cell domain could be upscaled to the Cauchy stress σ_{ij} at the macro-scale level by the following form [30]:

$$\sigma_{ij} = \frac{1}{\Theta} \int_{\Theta} \tilde{\sigma}_{ij} d\Theta \quad (5.9)$$

where: $\tilde{\sigma}_{ij}$ is the micro-scale Cauchy stress, σ_{ij} is the macro-scale Cauchy stress, Θ is the domain of the unit cell. The micro-scale displacement $u_i^f(x, y)$ is expressed in Eq. (5.10) [30]. It can be given by the leading order translation-free micro-scale displacement.

$$u_i^f(x, y) = \varepsilon_{ij}^c y_j + u_i^{(1)}(x, y) \quad (5.10)$$

where: ε_{ij}^c is the strain tensor in the macro-scale domain, $u_i^{(1)}(x, y)$ is the perturbation displacement in the micro-scale, x is the macro-scale position vector in the macro-scale domain, and y is the micro-scale position vector in the unit cell domain.

The micro-scale displacement at a master node M and a slave node S, located on the opposite sides of the unit cell, is expressed as Eq. (5.11) and Eq. (5.12).

$$u_i^f(x, y^M) = \varepsilon_{ij}^c y_j^M + u_i^{(1)}(x, y_j^M) \quad (5.11)$$

$$u_i^f(x, y^S) = \varepsilon_{ij}^c y_j^S + u_i^{(1)}(x, y_j^S) \quad (5.12)$$

where: y^M and y^S are the micro-scale coordinates.

The periodic boundary condition on the unit cell requires the same perturbation displacement at M and S nodes. Hence, Eq. (5.11) and Eq. (5.12) yield a constraint equation between the master node and the slave node, as expressed in Eq. (5.13).

$$u_i^f(x, y_j^M) - u_i^f(x, y_j^S) = \varepsilon_{ij}^c (y_j^M - y_j^S) \quad (5.13)$$

5.2.3. Undamaged uniaxial stress-strain relationship

The undamaged true stress-true strain relationship consists of pre- and post-necking parts. The pre-necking part is obtained from the tensile coupon test by converting the engineering stress-strain relationship until the ultimate strength to the true stress-strain relationship following Eq. (5.14).

$$\begin{aligned} \sigma_t &= \sigma_e (1 + \varepsilon_e) \\ \varepsilon_t &= \ln(1 + \varepsilon_e) \end{aligned} \quad (5.14)$$

where subscripts 'e' and 't' denote 'engineering' and 'true', respectively. The post-necking part is generated based on the extrapolation of three theoretical models, which are the Voce model [31] (Eq. (5.15)), the Swift model [32] (Eq. (4.4)), and the linear model [4] (Eq. (4.3)). The parameters of the theoretical models are determined by fitting the pre-necking data using the least-squares method.

$$\sigma_{t,V} = k_0 + Q(1 - e^{-\beta_0 \varepsilon_t}) \quad (5.15)$$

where k_0 , Q , β_0 are the Voce parameters. A linear combination of the Swift model and the linear model using a weighting factor W is adopted to generate the undamaged true stress-true strain relationship of BM, as shown in Eq. (4.2). The Swift model and the Voce model are used for WM and HAZ, respectively. A detailed illustration for choosing the specific material model is presented in Section 5.4.2.

5.3. Calibration method

5.3.1. Representative volume element models

The steel material contains voids and steel matrix. It is impossible to create the voids in the coupon specimens or welded joints, as the extremely small voids result in problems with meshing and computation. Hence, the voids are created in a unit cell representing a homogenised material, as shown in Fig. 5.1. The mechanical response of the homogenised material is obtained by varying boundary conditions. Accordingly, some constitutive parameters, such as q_1 and q_2 in this study, could be determined based on the simulation results. This simulation procedure is called the computational homogenisation analysis.

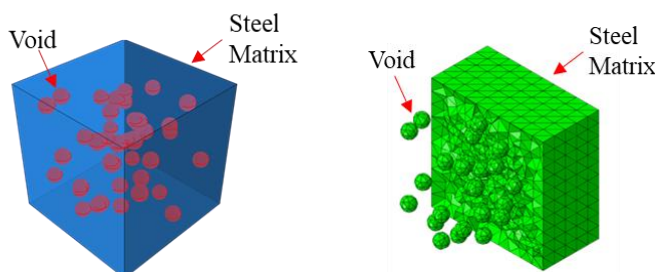


Fig. 5.1 An example of the representative volume element model.

The ABAQUS:2021 software package [33] is used to conduct the FE analysis. The computational homogenisation analysis is performed based on eighteen representative volume element (RVE) models with VVF varying from 0.1% to 25%. The side length of the cubic model is 1 mm. Non-overlapping voids with a constant radius R are randomly scattered in the unit cell, as presented in Fig. 5.1. All RVE models mesh with a 0.1 mm universal mesh, which is sufficient to avoid convergence problems, as illustrated in [24,29,34]. Table 5.1 presents detailed information about each RVE regarding VVF, the number of voids (N), and the radius of the void (R). The rationale for the selected VVF values is given in Section 5.3.2.

Table 5.1 Void details of RVEs.

f [%]	0.1	0.3	0.6	1.0	1.6	2.3	3.1	4.0	5.0
N	20	20	20	40	40	40	40	40	40
R [mm]	0.0229	0.0330	0.0415	0.0391	0.0457	0.0516	0.0570	0.0620	0.0668
f [%]	6.0	7.0	8.1	9.1	10.0	11.0	15.0	20.0	25.0
N	40	40	80	80	80	80	80	80	80
R [mm]	0.0710	0.0748	0.0623	0.0648	0.0668	0.0690	0.0765	0.0842	0.0907

A periodic boundary condition adopted by [24,29,34] is applied to the RVE model on three pairs of opposite surfaces. A uniform displacement along the normal of a surface

is applied on different surfaces of the RVE model to vary the stress triaxiality in the model. Fritzen et al. [24] proposed two parameters, α_1 and α_2 , to control the strain-driven load, as shown in Eq. (5.16). As the maximum stress triaxiality among all X-joint models is below 3, the relationship between the hydrostatic pressure dependency and the macroscopic yield surface is investigated by applying six loading conditions. The parameters for different loading conditions are presented in Table 5.2.

$$\left[\dot{\varepsilon} \right] = \alpha_1 \begin{pmatrix} 1 & 0 & 0 \\ 0 & -1 & 0 \\ 0 & 0 & 0 \end{pmatrix} + \alpha_2 \begin{pmatrix} 1 & 0 & 0 \\ 0 & 1 & 0 \\ 0 & 0 & 1 \end{pmatrix} \quad (5.16)$$

Table 5.2 Parameters for different loading conditions.

Loading conditions	1	2	3	4	5	6
α_1	1	1	1	1	1	1
α_2	0.1	0.3	0.5	0.7	0.9	1.2

5.3.2. Correlation between the void volume fraction and initial hardening strains

The input data (stress-strain relationship) in the RVE model is considered the constitutive model of the steel matrix, excluding the effect of the void on the stress-strain relationship of the material. The RVE model contains the steel matrix and the void, representing a material unit in the real specimen. It can be used to simulate the behaviour of the material unit under different loading conditions and various stages of damage. Hence, the mechanical response of the material unit under different stress states could be obtained from the RVE model. It is assumed that the volume of the steel matrix is unchangeable, indicating that the volume of the homogenised material may change during loading as the void volume changes. Hence, the plastic hydrostatic strain rate, see Eq. (5.7), is not zero.

With different stress triaxialities, the evolution of the plastic strain component is different. Take two sets of the plastic strain increment with the same plastic hydrostatic strain rate (0.003), for instance. The first set of the plastic strain rate is 0.011, 0.001, and -0.009 for ε_x , ε_y , and ε_z , respectively. The second set of the plastic strain rate is 0.012, 0.001, and -0.010 for ε_x , ε_y , and ε_z , respectively. The VVF increment of these two examples is identical since the plastic hydrostatic strain rate is the same. However, the equivalent plastic strain rate of the first and second sets is 0.012 and 0.013, respectively. It indicates that a given VVF corresponds to a range of equivalent plastic strain instead of a unique value, and vice versa. Hence, a modified stress-strain relationship should be used to analyse the RVE model with VVF larger than the initial VVF. The effect of the various combinations of initial hardening strains and VVFs on the material yield surface is evaluated. Fig. 5.2 depicts a schematic drawing of modifying the true stress-strain relationship based on different initial hardening strains. The black line represents the original true stress-strain relationship. The red, blue, and yellow lines are the modified relationships with an

ascending level of the initial hardening strain $\Delta\varepsilon_{t1}$, $\Delta\varepsilon_{t2}$, and $\Delta\varepsilon_{t3}$, respectively. The initial hardening strain of the modified relationship is set to zero (graphically offset the curves) to generate input data for the computational homogenization analysis.

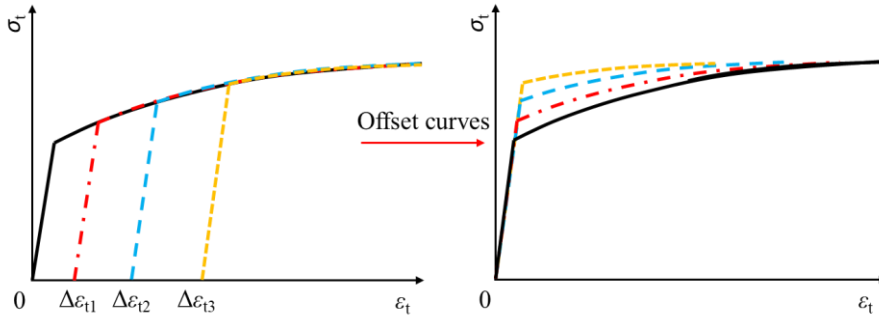


Fig. 5.2 True stress-strain relationship with different initial hardening strains.

A given VVF corresponds to a range of equivalent plastic strain instead of a unique value. An iteration analysis is conducted based on the RVE model to find the relationship between the range of the accumulated initial hardening strain and a specific VVF. The BM of the XS700A2 chord, denoted XS700A2B, is employed here for illustration. First, the original true stress-strain relationship is used in the RVE model with 0.1% VVF. For the model loaded with a minimum ($\alpha_2 = 0.1$) stress triaxiality, the equivalent plastic strain and VVF at the yield point are 0.062 and 0.258%, respectively. The model loaded with a maximum ($\alpha_2 = 1.2$) stress triaxiality has a 0.00382 equivalent strain and 0.343% VVF at the yield point. Comparing the results of the two models, VVF has a limited variation while the equivalent strain shows a significant difference. Hence, an RVE model with 0.3% VVF, which is approximately the average of two VVFs at the yield point (0.258% and 0.343%), is created for the second step analysis. As 0.062 and 0.00382 are the maximum and minimum equivalent plastic strains that may appear in the material with 0.3% VVF, the strains are used as the initial hardening strain (see Fig. 5.2) to modify the original true stress-strain relationship. Note that the maximum and minimum initial hardening strains are slightly adjusted within the varying range to have simple numbers. In addition, the average of the maximum and minimum initial hardening strain is used to generate a moderate constitutive model. The three modified stress-strain relationships are used in the second step analysis.

The model using the stress-strain relationship modified by the maximum initial hardening strain has the highest equivalent strain at the yield point under the $\alpha_2 = 0.1$ loading condition, while the model using the minimum-strain modified stress-strain relationship has the lowest equivalent yield strain under the $\alpha_2 = 1.2$ loading condition. VVF of these two models at the yield point shows a slight difference (0.554% and 0.663%). The average of two VVFs (approximately 0.6%) is used to create the RVE model for the third step. Similar to the first step, the original stress-strain relationship is modified using the accumulated initial hardening strain, which is the sum of maximum (or minimum) initial hardening strains. Again, a moderate modified constitutive model

is created using the average of the maximum and minimum accumulated initial hardening strains.

The iteration analysis is conducted up until models with an 11% VVF. In the last several steps (VVF from 7% to 11%), a minimum 0.01 and maximum 0.04 hardening strain increment is obtained for every 1% VVF increment. Hence, the modified stress-strain relationship is estimated for models with a 15%, 20%, and 25% VVF concerning the calculation efficiency. The used accumulated initial hardening strains ($\Delta\varepsilon_l$, $\Delta\varepsilon_m$, $\Delta\varepsilon_h$) for all RVE models are presented in Table 5.3. Note that the same combinations of VVF and the accumulated initial hardening strain are used for other materials, as a similar result is observed in XS355A3B and S700t10H (HAZ of S700t10).

Table 5.3 The accumulated initial hardening strains for different VVFs.

f [%]	0.1	0.3	0.6	1.0	1.6	2.3	3.1	4.0	5.0
$\Delta\varepsilon_l$	-	0.005	0.01	0.02	0.03	0.04	0.05	0.06	0.07
$\Delta\varepsilon_m$	0	0.03	0.05	0.08	0.1	0.16	0.19	0.22	0.25
$\Delta\varepsilon_h$	-	0.05	0.1	0.16	0.22	0.27	0.32	0.37	0.42
f [%]	6.0	7.0	8.1	9.1	10.0	11.0	15.0	20.0	25.0
$\Delta\varepsilon_l$	0.08	0.09	0.1	0.11	0.12	0.13	0.17	0.22	0.27
$\Delta\varepsilon_m$	0.27	0.3	0.32	0.36	0.38	0.4	0.51	0.63	0.76
$\Delta\varepsilon_h$	0.47	0.52	0.56	0.6	0.64	0.68	0.84	1.04	1.24

5.3.3. Coupon specimen models

FE models are created based on the measured dimensions for the standard coupon specimen and the milled welded coupon specimen to calibrate the GTN parameters for BM and HAZ, as shown in Fig. 5.3. The welded coupon specimen contains two HAZ zones and one WM zone. The FE models finely mesh with 0.5 mm element size in the central part 50 mm long, the base length where the extensometer was installed. The remaining part uses a coarse mesh in the loading direction. In order to reduce the computational burden, the grip part of the specimen is not created. Two reference points, RP1 and RP2, are employed to control all three translations and three rotations of the end surfaces using the multi-point beam constraint (MPC beam). A positive displacement in the Y direction is applied at RP2, while the other degrees of freedom of RP1 and RP2 are fixed. The explicit solver with a 100 s period and a 0.0001 s target time increment is used to perform the quasi-static analysis. Eight-node hexahedral solid elements with reduced integration (C3D8R) are employed in the model.

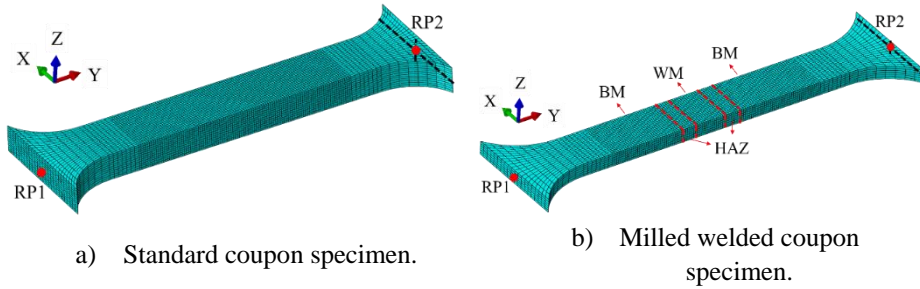


Fig. 5.3 Finite element model for coupon specimens.

The tensile behaviour of the coupon specimen could be well predicted up to the necking point. After the necking point, the critical cross-section starts to lose resistance due to the nucleation, growth, and coalescence of the void, although the true stress of the undamaged material might continuously increase. The calibration process is proceeded by comparing the FE and experimental engineering stress-strain relationship. The FE engineering stress-strain relationship is obtained by analysing the elongation of the gauge length and the reaction force at the reference point. The post-necking part of the experimental engineering stress-strain relationship is fitted by varying the weighting factor. Based on the determined weighting factor, the critical VVF f_c and final VVF f_f that govern the acceleration of VVF evolution are calibrated. Note that the nucleation of the void is not involved in the current research.

5.4. Results

5.4.1. Identification of parameters q_1 and q_2

An example of the RVE simulation result concerning a 5% VVF, a 0.07 accumulated initial hardening strain, and the Swift model extrapolation is presented in Fig. 5.4. The equivalent stress-strain relationship is used to characterise the yielding of the RVE model. When the slope of the curve decreases to 1% of the initial elastic stiffness, the point is considered the yield point. Fig. 5.4 b) illustrates the pressure dependence of the yield surface, where the von Mises yield stress decreases with the increase of the mean stress.

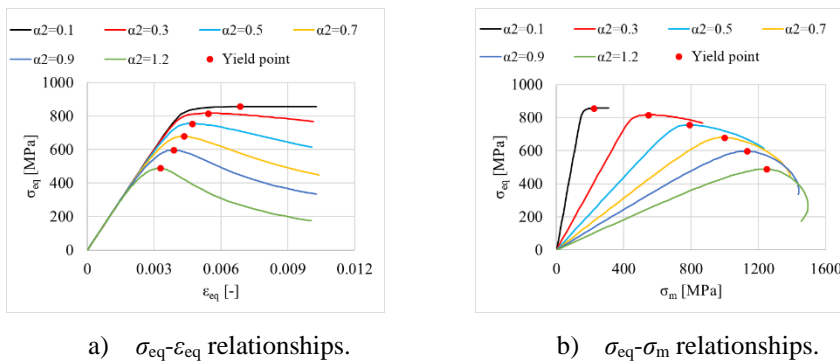


Fig. 5.4 Example of RVE results ($f=5\%$, 0.07 strain hardening, Swift model extrapolation).

The Mises stress, the mean stress, VVF, and the equivalent plastic strain at the yield point of all RVE models are used for determining the yield surface parameters q_1 and q_2 . According to the original GTN model, q_3 equals $q_1^2 \cdot f^*$ and σ_i in Eq. (5.1) are VVF of the RVE model and the flow stress corresponding to the equivalent plastic strain according to the input data of the true stress-true plastic strain relationship, respectively. Substituting the variable values obtained from one RVE model into Eq. (5.1), an error could be calculated using a specific combination of q_1 and q_2 . The errors from all RVE models, including different VVFs, accumulated initial hardening strains, and α_2 values, are used to calibrate a constant q_2 using the least-squares method. Based on the determined q_2 , the sum of errors from models with different α_2 values but the same VVF and accumulated initial hardening strain is used to identify q_1 , where a minimum sum of errors is obtained. The calibrated results for XS700A2B are presented in Table 5.4.

Table 5.4 Calibrated parameter q_1 .

f [%]	0.1	0.3	0.6	1.0	1.6	2.3	3.1	4.0	5.0
$q_{1,\Delta\epsilon l}$	-	2.20	2.38	2.22	2.30	2.12	2.08	2.04	1.99
$q_{1,\Delta\epsilon m}$	2.91	2.56	2.54	2.32	2.31	2.12	2.10	2.05	2.00
$q_{1,\Delta\epsilon h}$	-	2.61	2.57	2.32	2.32	2.12	2.10	2.06	2.00
f [%]	6.0	7.0	8.1	9.1	10.0	11.0	15.0	20.0	25.0
$q_{1,\Delta\epsilon l}$	1.85	1.99	1.76	1.79	1.77	1.66	1.62	1.57	1.51
$q_{1,\Delta\epsilon m}$	1.86	2.00	1.77	1.79	1.78	1.66	1.61	1.57	1.51
$q_{1,\Delta\epsilon h}$	1.86	2.00	1.77	1.79	1.78	1.67	1.59	1.57	1.51

Fritzen et al. [24] found that q_1 decreases with an increasing VVF and a constant q_2 . An expression correlating q_1 and VVF is proposed, as presented in Eq. (5.17).

$$q_1 = A \cdot f^B \quad (5.17)$$

where A and B are two constitutive parameters determined by fitting the data presented in Table 5.4. As the primary purpose of this study is to implement the GTN damage model on the fracture simulation of welded cold-formed rectangular hollow section X-joints, it will be very time-consuming to conduct the computational homogenization analysis for all materials involved in the X-joints, considering the number of RVE models. Hence, the materials with a similar strain hardening behaviour use the same A, B, and q_2 parameters. Fig. 5.5 presents two examples of materials with a similar strain hardening behaviour, a) for BM and b) for HAZ. The engineering stress is normalised by dividing the ultimate strength to compare the hardening behaviour of materials with different strengths. It can be seen that the curves in each diagram are almost identical until the ultimate strength point, where the extrapolation starts. Note the example of BM is from the chord of the A-series X-joint, which will be illustrated in detail in Chapter 6. X, S700, A1, and B in the name XS700A1B represent X-joint, S700 steel grade, first specimen in A series, and BM, respectively. S700t10H is HAZ of the S700t10 butt-welded RHS profile. BM and HAZ are sorted into four and two categories by visually

inspecting the curves' shape, respectively. The analysed material and the material with a similar hardening behaviour are presented in Table 5.5.

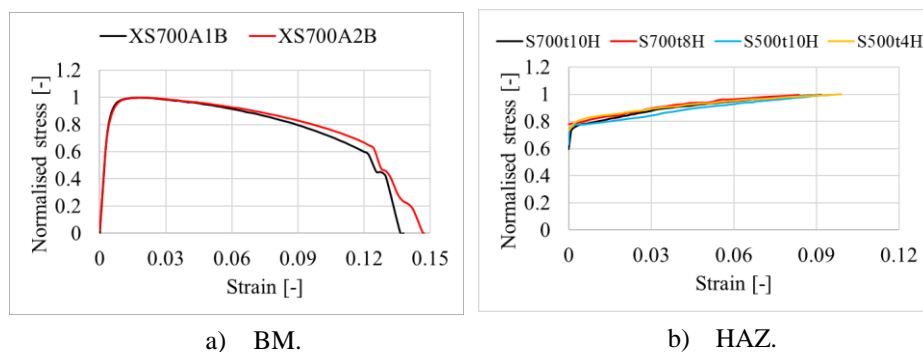


Fig. 5.5 Materials with a similar strain hardening behaviour.

Table 5.5 Material categories.

	Analysed material	Similar material
BM	XS700A3B	-
	XS700A2B	XS700A1B
	XS500A2B	XS500A1B, XS355A2B, XS355A1B, S355t5B, S355t8B, S500t8B
	XS355A3B	XS500A3B
HAZ	S700t10H	S500t4H, S500t10H, S700t8H
	S355t8H	S355t5H, S355t10H, S500t8H, S700t5H

The determined values of A , B , and q_2 are presented in Table 5.6. L , S , and V denote the linear, Swift, and Voce models, respectively. The undamaged true stress-strain relationship of BM can be generated using a weighting factor based on the Swift model and the linear model, as shown in Eq. (4.2). Accordingly, the constitutive parameters (A , B , and q_2) can also be determined using the same weighting factor, as reported in [34].

Table 5.6 Determined constitutive parameters.

Parameters	BM								HAZ	
	XS700A3B		XS700A2B		XS500A2B		XS355A3B		S700t10H	S355t8H
	L	S	L	S	L	S	L	S	V	V
A	1.263	1.338	1.294	1.351	1.288	1.334	1.363	1.383	1.417	1.443
B	-0.132	-0.106	-0.127	-0.116	-0.125	-0.107	-0.094	-0.085	-0.079	-0.068
q_2	0.968	1.016	0.961	1.006	0.982	1.014	1.010	1.019	1.015	1.015

5.4.2. Calibration of the parameters f_c and f_i

The undamaged true stress-strain relationship is used in the coupon specimen analysis. The pressure-dependent yield surface of the GTN model is realised by the porous metal plasticity in ABAQUS. A user subroutine VUSDFLD, as presented in Appendix 5.A, is used to consider the relationship between q_1 and VVF. The initial VVF f_0 is 0.001, resulting in a 0.999 relative density.

Fig. 5.6 a) presents the engineering stress-strain relationship of XS700A3B. The solid black line is the experimental result. The results of FE1, FE2, and FE3 are extracted from the FE model with a 0, 0.1, and 0.2 weighting factor referring to Eq. (4.2), respectively. The FE model with a 0.1 weighting factor fits the experimental result best. The VVF contour plot of the half FE model at the failure point, where the load decreases sharply, is presented in Fig. 5.6 b). It can be seen that the highest VVF appears at the centre of the cross-section, indicating the fracture initiates from the centre. The maximum VVF is taken as f_c . The value of f_i is determined based on a trial-and-error process by varying f_i . Fig. 5.6 c) compares the experimental and the FE results, where FE2-1, FE2-2, and FE2-3 use 0.05, 0.1 and 0.15 f_i , respectively. The model FE2-1 with a 0.05 f_i fits the experimental result best, although a minor difference could be observed among all three FE results. Note that the FE model with an f_i smaller than the proposed value would not notably influence the stress-strain relationship obtained from the FE result. Hence, an f_i which is maximally 0.05 larger than f_c is adopted in this study. The parameters calibrated for BM (referring to Eq. (4.2)-Eq. (4.4)) and HAZ (referring to Eq. (5.15)) are summarized in Table 5.7 and Table 5.8, respectively.

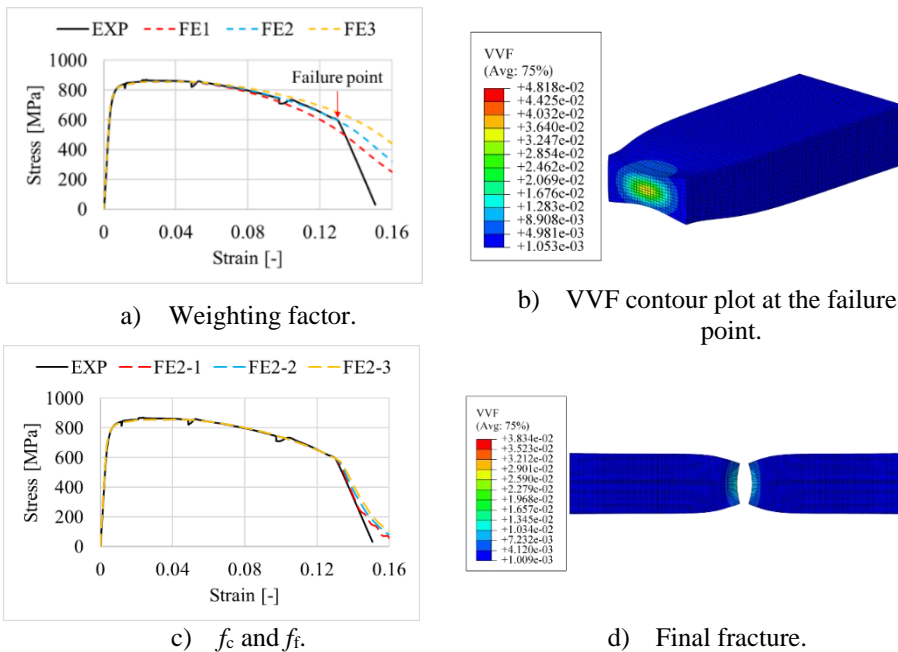


Fig. 5.6 Determination of constitutive parameters.

Table 5.7 Calibrated constitutive parameters for BM.

Material	W	k	n	ε_0	a	b	f_c	f_t
XS355A1B	0.9	836.2	0.1460	0.0095	598.2	549.9	0.0645	0.10
XS355A2B	0.9	772.7	0.1400	0.0068	563.3	511.8	0.0350	0.05
XS355A3B	1.0	750.0	0.1400	0.0336	473.3	520.7	0.0350	0.05
XS500A1B	0.8	738.1	0.0635	0.0150	508.1	595.8	0.1120	0.15
XS500A2B	0.6	696.0	0.0240	-0.0041	763.0	615.4	0.1290	0.15
XS500A3B	0.7	851.4	0.0631	-0.0022	739.0	667.0	0.0760	0.10
XS700A1B	0.1	942.9	0.0216	-0.0066	1237.4	834.6	0.0990	0.15
XS700A2B	0.1	919.0	0.0200	-0.0070	1293.2	816.7	0.0500	0.10
XS700A3B	0.1	997.2	0.0324	-0.0051	1052.0	853.4	0.0482	0.05
S355t5B	0.8	801.5	0.1400	0.0151	557.4	539.4	0.0267	0.05
S355t8B	1.0	785.4	0.1400	0.0142	549.0	527.6	0.110	0.15
S500t8B	0.9	757.1	0.0626	0.0196	493.2	616.6	0.123	0.15

Table 5.8 Calibrated constitutive parameters for HAZ.

Material	k_0	Q	β_0	f_c	f_t
S355t5H	480.7	274.7	4.26	0.0116	0.05
S355t8H	481.0	285.1	4.03	0.0329	0.05
S355t10H	459.5	191.6	13.89	0.0280	0.05
S500t4H	552.0	191.6	8.33	0.0094	0.05
S500t8H	363.3	336.7	17.25	0.0145	0.05
S500t10H	578.6	207.2	8.68	0.0226	0.05
S700t5H	627.7	355.7	5.28	0.0165	0.05
S700t8H	598.6	205.0	10.47	0.0337	0.05
S700t10H	661.0	179.4	13.59	0.0177	0.05

5.4.3. Validation against notched coupon specimens

The tensile test results of standard and notched coupon specimens (S700 steel grade) reported by Turan and Horvath [35] are employed to validate the GTN damage model under different stress triaxialities. The GTN model is calibrated following the general procedure in Section 5.3. The notched coupon specimen has a circular hole in the centre. The nominal diameter of the hole varies from 8 mm to 40 mm with an 8 mm interval. By varying the diameter of the hole in the specimen, the influence of the stress triaxiality, higher than 0.33, on the yield surface could be investigated experimentally. The measured dimension and the original name (in the literature) of the notched specimen are listed in Table 5.9, where b is the width of the parallel part, t is the thickness, d_0 is the diameter of the hole, e_1 and e_2 are the distance from the centre of the hole to the two edges of the specimen. FEMs are employed to simulate the tensile performance of the notched coupon specimen. The measured dimension is used in FEM. The same basic setting and parameter introduced for simulating standard coupon tests are used to

simulate the notched coupon tests. The meshed FE models are shown in Fig. 5.7. Comparing the FE result to the experimental result, the interaction of the hydrostatic stress and the Mises yield stress of the calibrated GTN model could be verified.

Table 5.9 Measured dimensions and maximum resistance of specimens.

Specimen name	b [mm]	t [mm]	d_0 [mm]	e_1 [mm]	e_2 [mm]	$F_{\max\text{-EXP}}$ [kN]	$F_{\max\text{-FE}}$ [kN]	Error [%]
S700/8 (B)	80.20	7.93	7.86	40.55	39.65	460.2	483.1	4.98
S700/16 (B)	80.11	7.91	15.85	40.36	39.75	405.5	427.9	5.52
S700/24 (B)	80.07	7.97	23.76	40.44	39.63	350.0	377.7	7.91
S700/32 (B)	80.11	7.86	31.87	40.39	39.72	302.0	319.4	5.76
S700/40 (B)	80.20	7.88	39.77	40.38	39.82	257.8	267.0	3.57

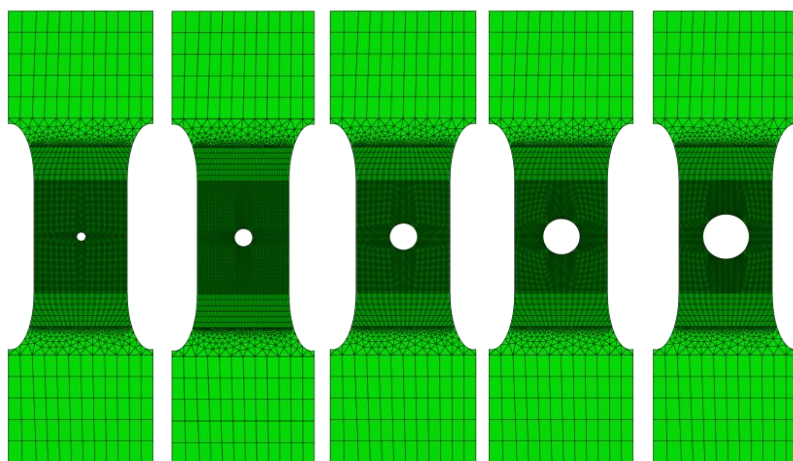


Fig. 5.7 Meshed model of notched coupon specimens. (8 mm to 40 mm hole from left to right)

The FE and experimental load-deformation relationships are compared in Fig. 5.8. The ultimate resistance of the FE result is approximately 5.7% higher than the experimental result, as indicated in Table 5.9. The discrepancy may result from two possible reasons, which are the effect of stress triaxiality and the effect of loading rate.

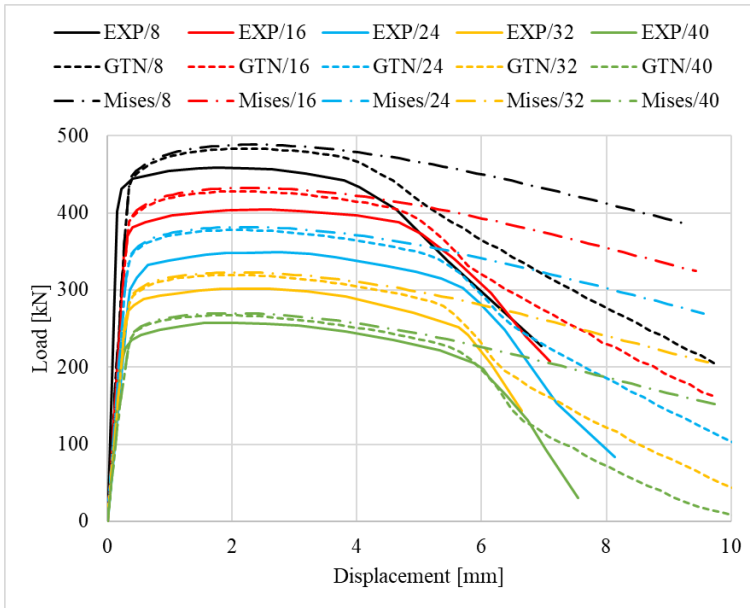


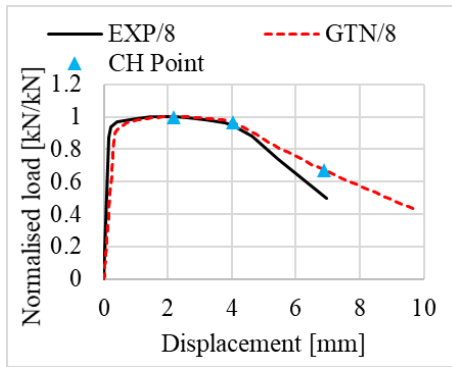
Fig. 5.8 Comparison of the load-deformation curves.

Yan-Bo Wang et al. [36] and Yuan-Zuo Wang et al. [37] conducted a comprehensive experimental and numerical investigation on the yield criterion and the damage model of HSS. It was found that the influence of high-stress triaxiality (greater than 0.33) on the Mises plasticity model of HSS is negligible, while the stress triaxiality plays a crucial role in the damage criterion. Hence, the Mises yield criterion is employed in the FEMs to verify the influence of stress triaxiality. The results are plotted in Fig. 5.8. It can be seen that the results using the Mises yield criterion fit the results using the GTN damage model well with 1% maximum resistance discrepancy, indicating that the higher resistance predicted by the FEM is not due to the effect of stress triaxiality.

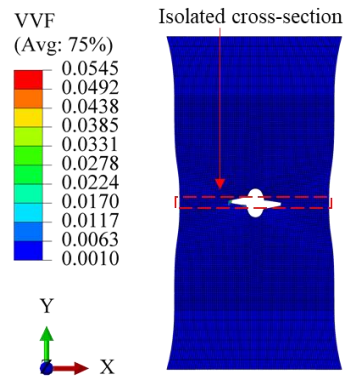
In the investigated testing series, the loading rate for the standard coupon specimen was higher than the notched coupon specimen, indicating that a higher material strength is obtained from the standard coupon test due to the strain rate effect. Therefore, it is reasonable to obtain a higher ultimate resistance in the FEM than in the experiment. In order to eliminate the strain rate effect, the displacement of the stroke should be held for at least 60 seconds during the coupon test [38]. Static stress is obtained from each loading suspension point. Then, the static stress-strain relationship from the standard coupon test and the static load-displacement relationship from the notched coupon test are obtained based on several static stress points. Finally, the static behaviour of the standard and the notched coupon tests are predicted using the static stress-strain relationship obtained from the standard coupon test. And the strength deviation in Fig. 5.8, due to the strain rate effect, could be eliminated. However, the standard coupon test and the notched coupon test were conducted without the loading suspension [35]. Consequently, it is not possible to eliminate the strain rate effect in the FE analysis. In order to compare the FE and the experimental results focusing on the post ultimate load behaviour, the load is

normalized by dividing the maximum load, respectively. Therefore, the maximum normalized load of each curve is 1. Note that the displacement is not normalized.

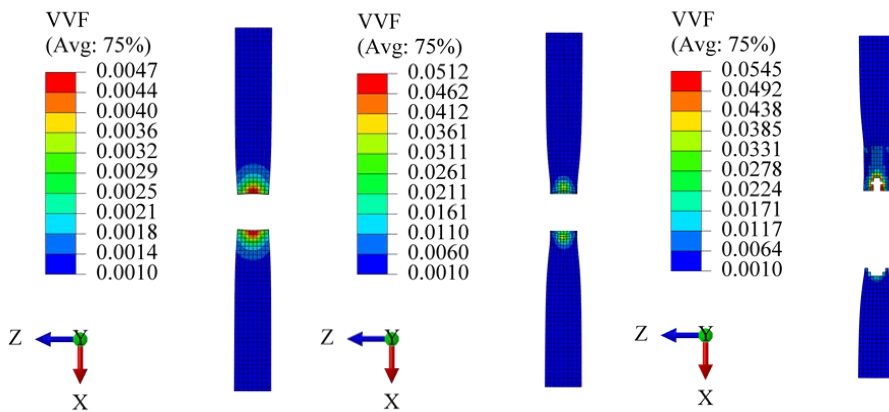
The normalised load-displacement relationships for each test are depicted in Fig. 5.9-Fig. 5.13. It can be seen that very good agreements exist between the FE and the experimental results. Three points are characterised in the FE result. The characterised (CH) points A, B, and C corresponds to the maximum load, the initiation of the fracture, and the largest deformation in the experiment, respectively. The fracture initiation happens when the first element deletion is observed in the critical net cross-section in FEM. VVF contour plot of the isolated net cross-section at each characterised point is shown in Fig. 5.9-Fig. 5.13. It can be seen that VVF at the centre of the cross-section develops faster than the edge. Consequently, the fracture initiates from the centre and grows to the edge. The maximum VVF in all figures is lower than the final VVF f_t , because the element is deleted from the model if f_t is reached. The displacement and the normalised load at fracture initiation point B are compared to the experimental result at the point when the load starts to drop significantly in Table 5.10. The average deviation of the displacement and the normalised load is -1.7% and 1.0%, respectively. It can be concluded that the calibrated GTN model could effectively predict the damage initiate point under different high-stress triaxialities. The validated up limit of the stress triaxiality is investigated based on the average stress triaxiality extracted from elements in the central two layers of the net cross section. The 1st, 5th, 10th, 15th, and 20th elements from the hole edge, as shown in Fig. 5.14, are employed to demonstrate the stress triaxiality level during the loading. The stress triaxiality is plotted against the loading step for each model in Fig. 5.15. The relationship is plotted up until the characterised fracture initiation point B. From Fig. 5.15, it can be concluded that the validated maximum stress triaxiality is around 1.6.



a) Normalised load-displacement relationships.

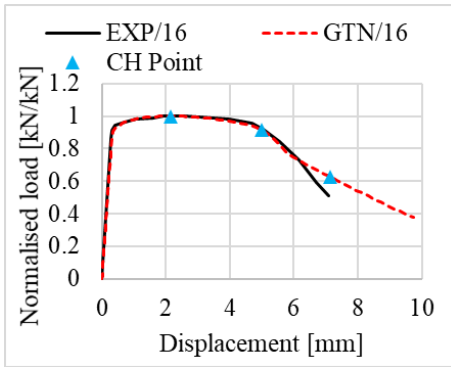


b) VVF distribution at point C.

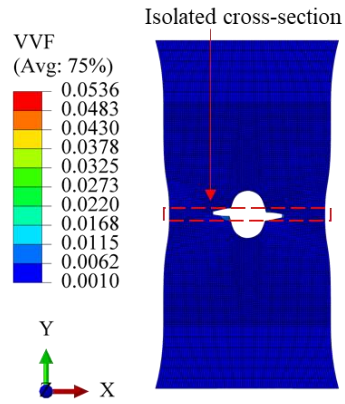


c) VVF distribution of isolated cross section at point A, B, C.

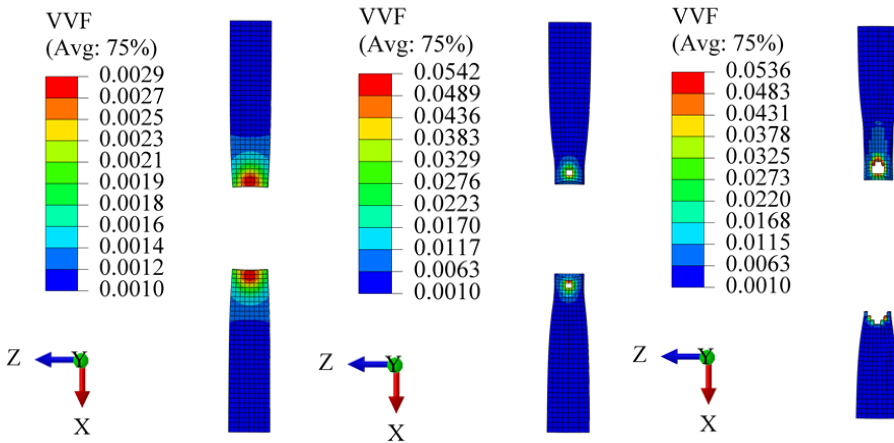
Fig. 5.9 8 mm notched coupon specimen.



a) Normalised load-displacement relationships.

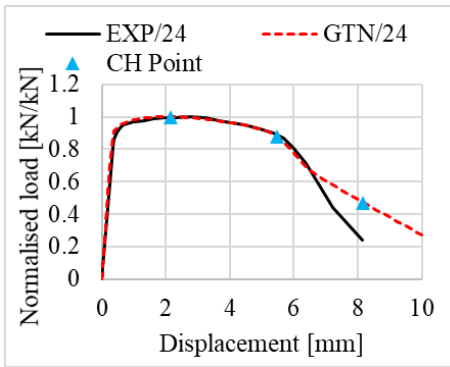


b) VVF distribution at point C.

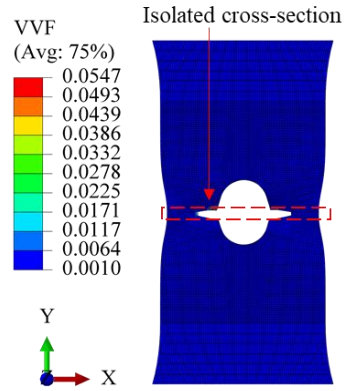


c) VVF distribution of isolated cross section at point A, B, C.

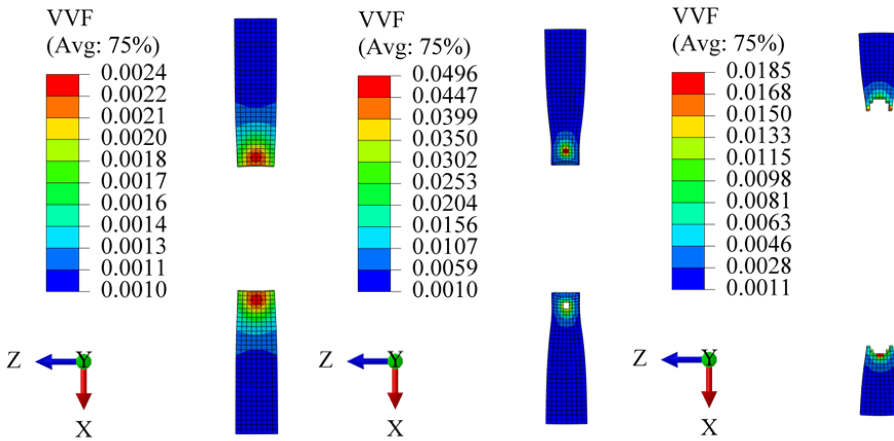
Fig. 5.10 16 mm notched coupon specimen.



a) Normalised load-displacement relationships.

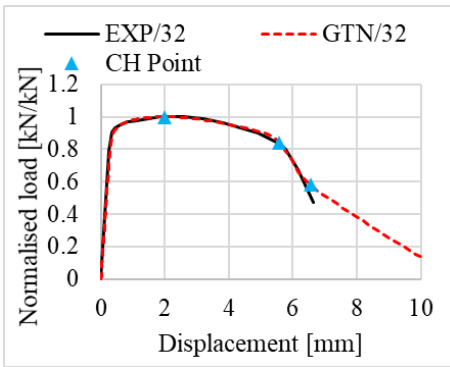


b) VVF distribution at point C.

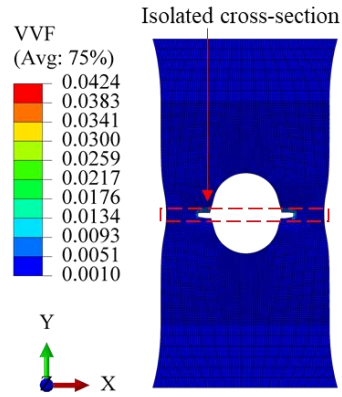


c) VVF distribution of isolated cross section at point A, B, C.

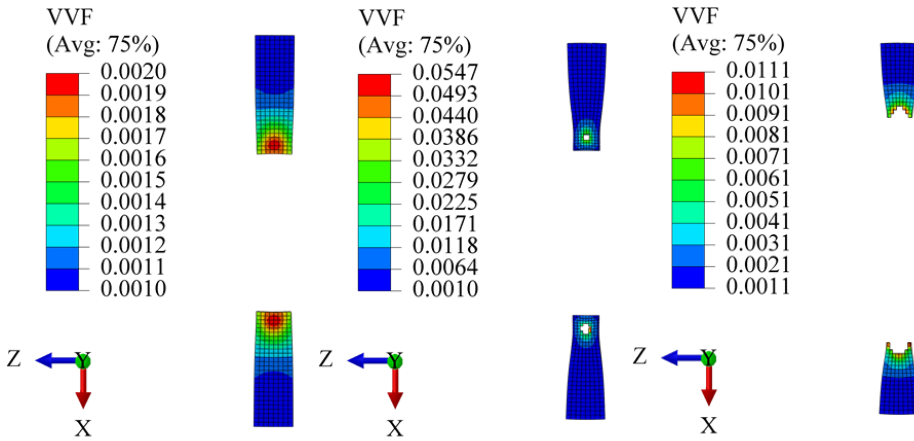
Fig. 5.11 24 mm notched coupon specimen.



a) Normalised load-displacement relationships.

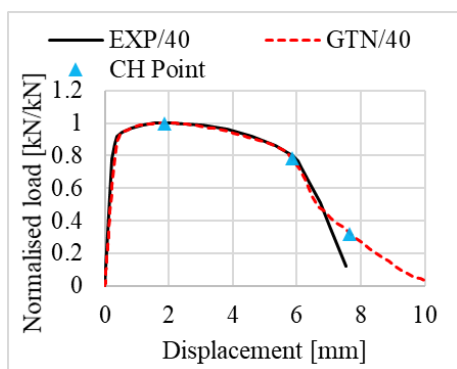


b) VVF distribution at point C.

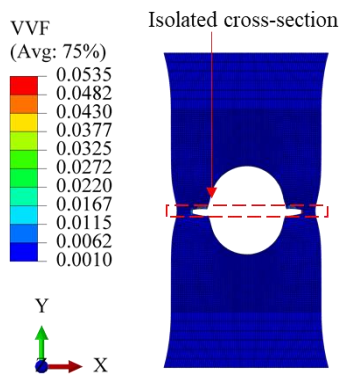


c) VVF distribution of isolated cross section at point A, B, C.

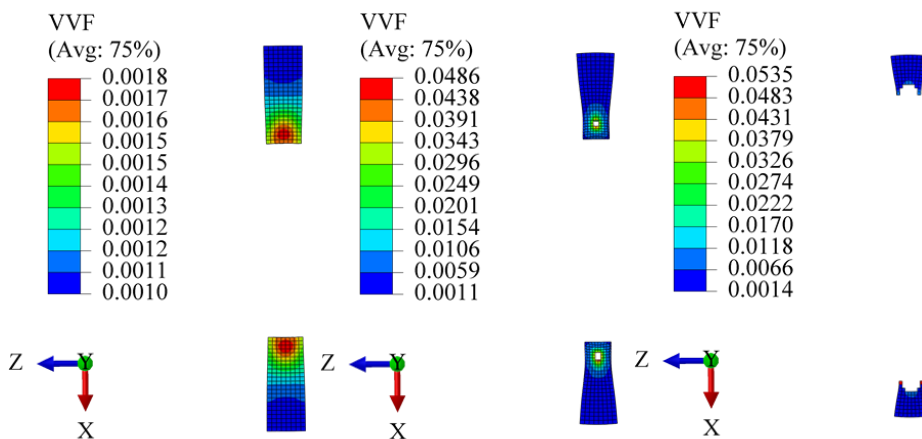
Fig. 5.12 32 mm notched coupon specimen.



a) Normalised load-displacement relationships.



b) VVF distribution at point C.



c) VVF distribution of isolated cross section at point A, B, C.

Fig. 5.13 40 mm notched coupon specimen.

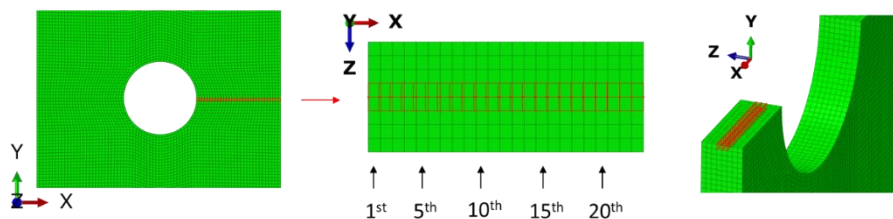


Fig. 5.14 Position of the investigated elements.

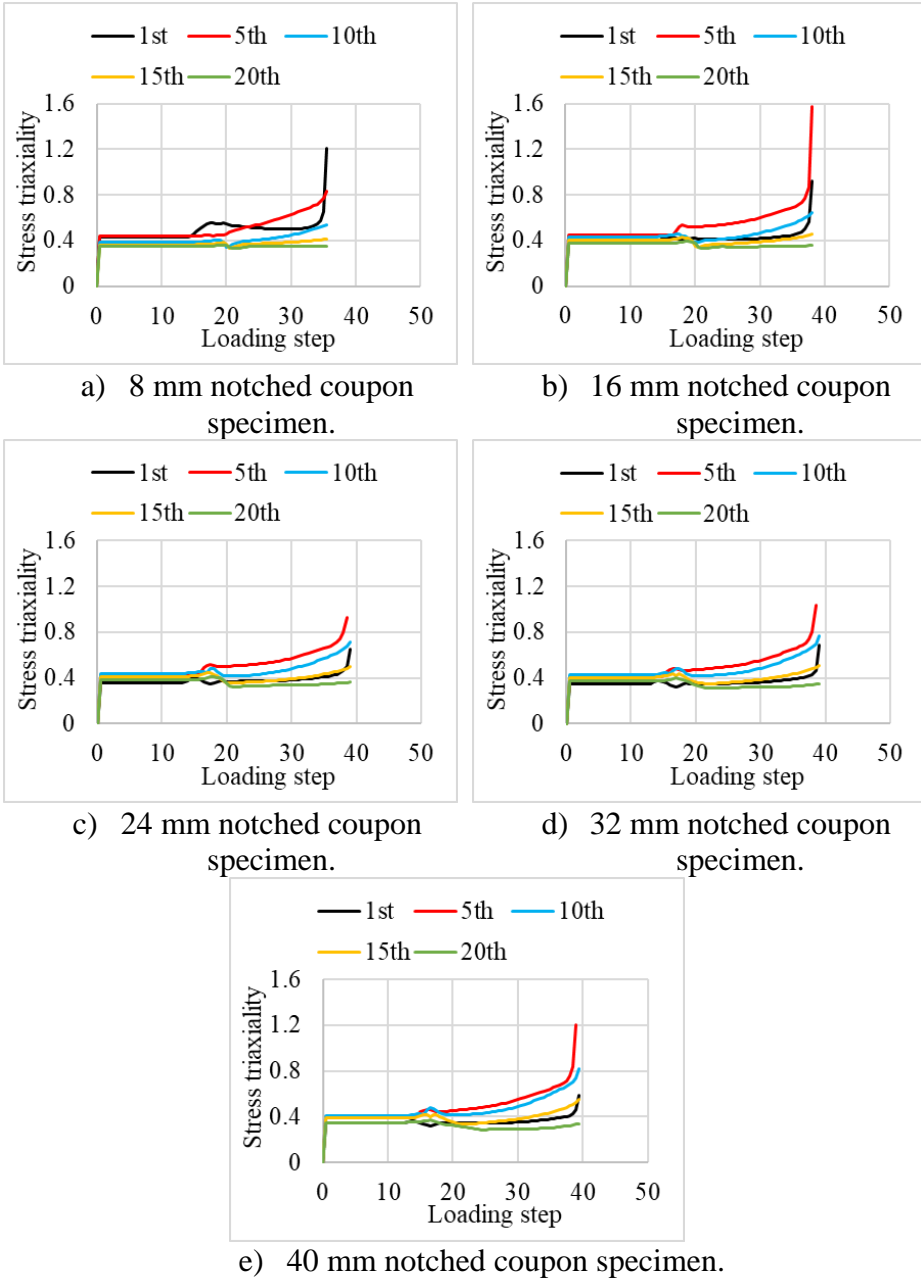


Fig. 5.15 Stress triaxiality versus loading step relationships.

Table 5.10 Comparison of the fracture initiation point.

Specimen name	Displacement			Normalised force		
	EXP [mm]	FE [mm]	Deviation [%]	EXP [kN/kN]	FE [kN/kN]	Deviation [%]
S700/8 (B)	4.05	4.04	-0.04	0.95	0.96	1.93
S700/16 (B)	5.04	5.00	-0.72	0.92	0.91	-0.81
S700/24 (B)	5.69	5.48	-3.82	0.87	0.88	1.46
S700/32 (B)	5.79	5.57	-3.72	0.80	0.84	4.90
S700/40 (B)	5.88	5.85	-0.37	0.80	0.78	-2.32

5.5. Conclusions

The GTN damage model is implemented into the fracture simulation of welded cold-formed rectangular hollow section (RHS) X-joints. Based on the presented results, the following conclusions are drawn:

- 1) The computational homogenisation is conducted to calibrate the GTN yield-surface parameters (q_1 and q_2), considering the different combinations of the accumulated initial hardening strain and the void volume fraction (f). Parameter q_1 is correlated to the void volume fraction f using the power law, $q_1 = Af^B$, for a constant q_2 calibrated for different models shown in Table 5.6. All values of q_2 for different materials considered are close to 1. Parameter q_1 gradually decreases from 3 to 1.5 with an increasing f .
- 2) The undamaged true stress-true strain relationship of the base material (BM) is generated using a weighting factor (W) based on the Swift model and the linear model. The weighting factor decreases with the increase of the steel grade, which is around 0.9, 0.7, and 0.1 for S355, S500, and S700 materials, respectively. It indicates that the BM undamaged constitutive model gradually transfers from the linear model to the Swift model concerning an ascending steel grade. The heat-affected zone (HAZ) material has a weaker post-necking strain hardening behaviour than BM. The Voce model is suitable for generating the undamaged constitutive model for all HAZ materials.
- 3) The damage of the element is sensitive to the value of the fracture parameter f_c . f_t has a minor influence on the failure process. The value of f_t , up to 5% larger than f_c , is validated in this study.
- 4) The calibrated GTN model could efficiently predict the behaviour of the notched coupon specimens. The average deviation of the displacement and the normalised load at the fracture initiation point is -1.7% and 1.0%, respectively. The validated range of stress triaxiality is up to 1.6.

Reference

- [1] EN 1993-1-8:2005 - Design of steel structures - Part 1-8: Design of joints, (2005).
- [2] EN 1993-1-12:2007 - design of steel structures - part 1–12: additional rules for the extension of EN 1993 up to steel grades S700, (2007).
- [3] K.S. Zhano, Z.H. Li, Numerical analysis of the stress-strain curve and fracture initiation for ductile material, *Engineering Fracture Mechanics*. 49 (1994) 235–241. [https://doi.org/10.1016/0013-7944\(94\)90006-X](https://doi.org/10.1016/0013-7944(94)90006-X).
- [4] Y. Ling, Uniaxial True Stress-Strain after Necking, *AMP Journal of Technology*. 5 (2004) 37–48.
- [5] T.S. Cao, Models for ductile damage and fracture prediction in cold bulk metal forming processes: a review, *International Journal of Material Forming*. 10 (2017) 139–171. <https://doi.org/10.1007/s12289-015-1262-7>.
- [6] J.R. Rice, D.M. Tracey, On the ductile enlargement of voids in triaxial stress fields*, *Journal of the Mechanics and Physics of Solids*. 17 (1969) 201–217. [https://doi.org/10.1016/0022-5096\(69\)90033-7](https://doi.org/10.1016/0022-5096(69)90033-7).
- [7] Y. Bai, T. Wierzbicki, A new model of metal plasticity and fracture with pressure and Lode dependence, *International Journal of Plasticity*. 24 (2008) 1071–1096. <https://doi.org/10.1016/j.ijplas.2007.09.004>.
- [8] J. Lemaitre, A continuum damage mechanics model for ductile fracture, *International Journal of Pressure Vessels and Piping*. 107 (1985) 335–344. [https://doi.org/10.1016/S0308-0161\(00\)00019-3](https://doi.org/10.1016/S0308-0161(00)00019-3).
- [9] A.A. Benzerga, J.B. Leblond, Ductile Fracture by Void Growth to Coalescence, Elsevier Inc., 2010. [https://doi.org/10.1016/S0065-2156\(10\)44003-X](https://doi.org/10.1016/S0065-2156(10)44003-X).
- [10] R. Kiran, K. Khandelwal, Experimental studies and models for ductile fracture in ASTM A992 steels at high triaxiality, *Journal of Structural Engineering*. 140 (2014).
- [11] G. Mirone, D. Corallo, A local viewpoint for evaluating the influence of stress triaxiality and Lode angle on ductile failure and hardening, *International Journal of Plasticity*. 26 (2010) 348–371. <https://doi.org/10.1016/j.ijplas.2009.07.006>.
- [12] X. Gao, T. Zhang, J. Zhou, S.M. Graham, M. Hayden, C. Roe, On stress-state dependent plasticity modeling: Significance of the hydrostatic stress, the third invariant of stress deviator and the non-associated flow rule, *International Journal of Plasticity*. 27 (2011) 217–231. <https://doi.org/10.1016/j.ijplas.2010.05.004>.
- [13] I. Barsoum, J. Faleskog, Rupture mechanisms in combined tension and shear-Experiments, *International Journal of Solids and Structures*. 44 (2007) 1768–1786. <https://doi.org/10.1016/j.ijsolstr.2006.09.031>.
- [14] K. Danas, P. Ponte Castañeda, Influence of the Lode parameter and the stress triaxiality on the failure of elasto-plastic porous materials, *International Journal*

- of Solids and Structures. 49 (2012) 1325–1342. <https://doi.org/10.1016/j.ijsolstr.2012.02.006>.
- [15] A.L. Gurson, Continuum Theory of Ductile Rupture by Void Nucleation and Growth: Part I—Yield Criteria and Flow Rules for Porous Ductile Media, *Journal of Engineering Materials and Technology*. 99 (1977) 2–15. <https://doi.org/10.1115/1.3443401>.
- [16] V. Tvergaard, Influence of void nucleation on ductile shear fracture at a free surface, *Journal of the Mechanics and Physics of Solids*. 30 (1982) 399–425. [https://doi.org/10.1016/0022-5096\(82\)90025-4](https://doi.org/10.1016/0022-5096(82)90025-4).
- [17] V. Tvergaard, Ductile fracture by cavity nucleation between larger voids, *Journal of the Mechanics and Physics of Solids*. 30 (1982) 265–286. [https://doi.org/10.1016/0022-5096\(82\)90033-3](https://doi.org/10.1016/0022-5096(82)90033-3).
- [18] V. Tvergaard, A. Needleman, Analysis of the cup-cone fracture in a round tensile bar, *Acta Metallurgica*. 32 (1984) 157–169. [https://doi.org/10.1016/0001-6160\(84\)90213-X](https://doi.org/10.1016/0001-6160(84)90213-X).
- [19] K. Nahshon, J.W. Hutchinson, Modification of the Gurson Model for shear failure, *European Journal of Mechanics, A/Solids*. 27 (2008) 1–17. <https://doi.org/10.1016/j.euromechsol.2007.08.002>.
- [20] K.L. Nielsen, V. Tvergaard, Ductile shear failure or plug failure of spot welds modelled by modified Gurson model, *Engineering Fracture Mechanics*. 77 (2010) 1031–1047. <https://doi.org/10.1016/j.engfracmech.2010.02.031>.
- [21] M. Achouri, G. Germain, P. Dal Santo, D. Saidane, Experimental characterization and numerical modeling of micromechanical damage under different stress states, *Materials and Design*. 50 (2013) 207–222. <https://doi.org/10.1016/j.matdes.2013.02.075>.
- [22] M. Achouri, G. Germain, P. Dal Santo, D. Saidane, Numerical integration of an advanced Gurson model for shear loading: Application to the blanking process, *Computational Materials Science*. 72 (2013) 62–67. <https://doi.org/10.1016/j.commatsci.2013.01.035>.
- [23] L. Malcher, F.M. Andrade Pires, J.M.A. César De Sá, An extended GTN model for ductile fracture under high and low stress triaxiality, *International Journal of Plasticity*. 54 (2014) 193–228. <https://doi.org/10.1016/j.ijplas.2013.08.015>.
- [24] F. Fritzen, S. Forest, T. Böhlke, D. Kondo, T. Kanit, Computational homogenization of elasto-plastic porous metals, *International Journal of Plasticity*. 29 (2012) 102–119. <https://doi.org/10.1016/j.ijplas.2011.08.005>.
- [25] H. Xin, J.A.F.O. Correia, M. Veljkovic, F. Berto, Fracture parameters calibration and validation for the high strength steel based on the mesoscale failure index, *Theoretical and Applied Fracture Mechanics*. 112 (2021). <https://doi.org/10.1016/j.tafmec.2021.102929>.
- [26] H. Xin, M. Veljkovic, J.A.F.O. Correia, F. Berto, Ductile fracture locus

- identification using mesoscale critical equivalent plastic strain, *Fatigue & Fracture of Engineering Materials & Structures*. 44 (2021) 1292–1304. <https://doi.org/https://doi.org/10.1111/ffe.13429>.
- [27] M. Pavlović, P. Manoleas, M. Veljkovic, E. Koltsakis, Calibration of the Ductile Damage Material Model Parameters for a High Strength Steel, *Nordic Steel Construction Conference*: 23/09/2015 - 25/09/2015. (2015) 231–232. <http://urn.kb.se/resolve?urn=urn:nbn:se:ltu:diva-37833>.
- [28] M. Feldmann, N. Schillo, S. Schaffrath, K. Viridi, T. Björk, N. Tuominen, M. Veljkovic, M. Pavlovic, P. Manoleas, M. Heinisuo, K. Mela, Rules on high strength steel, 2016. <https://op.europa.eu/en/publication-detail/-/publication/515285b0-c820-11e6-a6db-01aa75ed71a1/language-en/format-PDF/source-194823584>.
- [29] R. Yan, H. Xin, M. Veljkovic, Identification of GTN Damage Parameters as a Surrogate Model for S355, (2020) 582–589. https://doi.org/10.3850/978-981-11-0745-0_066-cd.
- [30] J. Fish, *Practical multiscaling*, (2013).
- [31] E. Voce, The relationship between stress and strain for homogeneous deformation, *Journal of the Institute of Metals*. 74 (1948) 537–562.
- [32] H.W. Swift, Plastic instability under plane stress, *Journal of the Mechanics and Physics of Solids*. 1 (1952) 1–18. [https://doi.org/10.1016/0022-5096\(52\)90002-1](https://doi.org/10.1016/0022-5096(52)90002-1).
- [33] ABAQUS, *ABAQUS Analysis User's Manual*, 2021 Version, 2021.
- [34] R. Yan, H. Xin, M. Veljkovic, Ductile fracture simulation of cold-formed high strength steel using GTN damage model, *Journal of Constructional Steel Research*. 184 (2021) 106832. <https://doi.org/https://doi.org/10.1016/j.jcsr.2021.106832>.
- [35] P. Turán, L. Horváth, Experimental behaviour of tension plates with centre hole made from high strength steel, in: *Nordic Steel Construction Conference 2015 Tampere, Finland*, 2015.
- [36] Y.B. Wang, Y.F. Lyu, Y.Z. Wang, G.Q. Li, J.Y. Richard Liew, A reexamination of high strength steel yield criterion, *Construction and Building Materials*. 230 (2020) 116945. <https://doi.org/10.1016/j.conbuildmat.2019.116945>.
- [37] Y.Z. Wang, G.Q. Li, Y.B. Wang, Y.F. Lyu, H. Li, Ductile fracture of high strength steel under multi-axial loading, *Engineering Structures*. 210 (2020) 110401. <https://doi.org/10.1016/j.engstruct.2020.110401>.
- [38] Y. Huang, B. Young, The art of coupon tests, *Journal of Constructional Steel Research*. 96 (2014) 159–175. <https://doi.org/10.1016/j.jcsr.2014.01.010>.

Appendix

Appendix 5.A ABAQUS user subroutine

```

subroutine vusdfld(
c Read only -
* nblock, nstatev, nfieldv, nprops, ndir, nshr,
* jElem, kIntPt, kLayer, kSecPt,
* stepTime, totalTime, dt, cmname,
* coordMp, direct, T, charLength, props,
* stateOld,
c Write only -
* stateNew, field )
c
include 'vaba_param.inc'
c
dimension jElem(nblock), coordMp(nblock,*),
* direct(nblock,3,3), T(nblock,3,3),
* charLength(nblock), props(nprops),
* stateOld(nblock,nstatev),
* stateNew(nblock,nstatev),
* field(nblock,nfieldv)
character*80 cmname
c
parameter(nrData=6,RPI=3.141592653D0)
character*3 cData(maxblk*nrData), jData(maxblk*nrData)
dimension rStrainData(maxblk*nrData)
dimension strain(nblock,nrData)
C Parameters used in the simulation
C #####
RVVFINITIAL = 0.001          ! Initial void volume fraction
RVVFINITIALC = 0.008        ! fc
RVVFFINALC = 0.055          ! ff
RA = 1.144                  ! Paramters to calculate Q1
RB = -0.263                 ! Parameters to calculate Q1
RQ2 = 0.668                 ! Parameter Q2
C #####
c
jStatus = 1
call vgetvrm( 'PE', rStrainData, jData, cData, jStatus )
strain = reshape(rStrainData,(/ nblock,nrData/))
c
if( jStatus .ne. 0 ) then
field(k,1) = RVVFINITIAL
call xplb_abqerr(-2,'Utility routine VGETVRM '//

```

```

*   'failed to get variable.',0,zero,')
    call xplb_exit
end if
do k = 1, nblock
PE11_OLD = stateOld(k,1)
PE22_OLD = stateOld(k,2)
PE33_OLD = stateOld(k,3)
stateNew(k,1) = strain(k,1)
stateNew(k,2) = strain(k,2)
stateNew(k,3) = strain(k,3)
PE11INC = strain(k,1) - PE11_OLD
PE22INC = strain(k,2) - PE22_OLD
PE33INC = strain(k,3) - PE33_OLD

IF(stateOld(k,4) .GT. 0.0) THEN
stateNew(k,4) = stateOld(k,4) + (1 - stateOld(k,4))*(PE11INC +
1      PE22INC + PE33INC)
ELSE
stateNew(k,4) = RVVFINITIAL
ENDIF

RQ1 = RA*(field(k,1))**RB
RQ3 = RQ1**2.0
RVOIDFAILURE = (RQ1 + SQRT(RQ1**2.0-RQ3))/RQ3

IF (field(k,1) .GT. RVOIDFAILURE) THEN
stateNew(k,5) = 0.0
ELSE
stateNew(k,5) = 1.0
C DEFINE THE VOLUME FRACTION
IF(stateNew(k,4) .LT. RVVFINALC) THEN
field(k,1) = stateNew(k,4)
ELSE IF (stateNew(k,4) .GT. RVVFINALC) THEN
field(k,1) = RVOIDFAILURE
ELSE
field(k,1) = RVVFINALC + (RVOIDFAILURE - RVVFINALC) / (
1 RVVFINALC-RVVFINALC)*(stateNew(k,4)-RVVFINALC)
ENDIF
ENDIF
end do
return
end

```

6.

Experimental investigation on the tensile behaviour of welded rectangular hollow section X-joints

The newest version of prEN 1993-1-8 (2022) prescribes a material factor (C_f) to reduce the design resistance of welded joints made of high strength steel (HSS) mostly due to the lack of available experiments, given the less ductility of HSS compared to mild steel. Additionally, it is stated that the material design yield strength should not exceed 0.8 times the ultimate strength (f_u) for the chord punching shear failure and the tensile brace failure. The mechanical background behind C_f and the $0.8f_u$ restriction for different types of joints and loading conditions is vague.

In this paper, the validity of C_f and the $0.8f_u$ restriction is investigated experimentally by considering 18 welded rectangular hollow section X-joints tested in tension. A bi-linear model, which is suitable for an elasto-plastic global analysis considering the post-yielding stiffness, is proposed to characterize the nonlinear behaviour of the joint. The predicted resistance and failure mode, with and without considering the C_f and/or the $0.8f_u$ restriction, are compared to the experimental results. In addition, the predicted resistance corresponding to the experimental failure mode is investigated. It is concluded, based on the tested joints in this paper and literature, that C_f and the $0.8f_u$ restriction are not necessary for the design according to prEN1993-1-8. However, the predicted brace failure resistance is unconservative for tested joints that failed by brace failure if C_f for S700 or the $0.8f_u$ restriction for all steel grades is not considered.

Parts of this chapter appear in the journal article: ‘Rui Yan et al., Experimental investigation on the tensile behaviour of welded RHS high strength steel X-joints, Engineering Structures, 2022’. Minor modifications have been made to suit the thesis. Credit is also given to the master thesis: ‘Hagar El Bamby, Experimental and numerical investigations on the structural performance of mild and high strength welded X-joints’.

6.1. Introduction

Welded joints between tubular members are often used in trusses and building frames, bridges, and off-shore structures. In Europe, welded tubular joints are designed according to the approved standard EN 1993-1-8 (2005) [1], which presents a series of design rules that take into account the configuration of the joint, and the various failure modes that have been identified in research. These rules have been developed based on extensive experimental and numerical investigations on joints made of mild steel (S235 and S355) before 2005. To allow using steel grades higher than S355, a material factor ($C_f = 0.9$) for reducing the design resistance has been stipulated for joints using materials higher than S355 and up to S460 [1].

Due to advanced material manufacturing techniques, such as Thermo-mechanical control process (TMCP) and Quenching & Tempering (QT), high strength steel (HSS) hollow sections ($460 \text{ MPa} < f_y \leq 700 \text{ MPa}$) have become more readily available in recent years. HSS has higher strength, but lower ductility compared to mild steel. The size of structural members can be effectively reduced using HSS, resulting in a lower self-weight, less welding because of thinner profiles, and consequently, substantial economic and environmental benefits. A very good practical example of considerable cost saving was accomplished in the Friends Arena in Stockholm [2], where HSS (S460, S690, and S900) hollow sections and other profiles were used for the roof of the stadium. The financial cost and greenhouse gas emissions were reduced by 14.5% and 17.0%, respectively, compared to the mild steel design.

Regarding the design of HSS welded tubular joints, EN 1993-1-12 [3] provides supplementary rules for EN 1993-1-8 [1], extending the range of steel grades up to S700. The general approach of EN 1993-1-12 [3] is that HSS welded tubular joints are designed by the same expressions as joints of mild steels, and the material factor ($C_f = 0.8$ for $460 \text{ MPa} < f_y \leq 700 \text{ MPa}$ steels) is applied to the obtained resistance. In the latest version of the updated revision, prEN1993-1-8 [4], C_f was increased from 0.8 to 0.86 for $460 \text{ MPa} < f_y \leq 550 \text{ MPa}$ materials. In addition, a material ductility restriction on the yield strength (f_y) was imposed for punching shear failure (PSF) and tension brace failure (BF), stating that in design, the value of the yield strength should be limited to 0.8 times the ultimate strength (f_u). However, applying C_f and the $0.8f_u$ restriction partially eliminates the benefits of using HSS, limiting its competitiveness.

Justifications of C_f were based on experimental and numerical studies on gap K-joints [5–8]. However, the mechanical background behind C_f for different types of joints and loading conditions is vague. For PSF and BF in HSS joints, the fracture occurs in the heat-affected zone (HAZ), whose mechanical properties are heavily influenced by the parameters of the welding process, such as the heat input, the cooling time, the welding technique [9,10], and mechanical properties of hollow section (the base) material. In general, the higher the steel grade is followed by the more severe the HAZ strength reduction [10,11]. Javidan et al. [12] found an approximate 30% strength reduction in S960 HAZ compared to the base material. A 15% ultimate strength reduction in S700

HAZ was observed in this study, while a limited strength reduction was observed in S700 HAZ using the laser welding technique [10]. Although BF and PSF are closely related to the HAZ strength, the HAZ material softening, especially for HSS, has not been explicitly considered in prEN1993-1-8 [4]. In the latest discussion regarding prEN1993-1-12 [13], the HAZ strength deterioration in ultra-high strength steel (UHSS) with steel grade above S700 is recognized as one of the important research questions.

In the last decade, many investigations have been carried out on different types of HSS joints. Björk and Saastamoinen [14] conducted 20 tensile tests on welded X-joints made of double grades S420MH/S355J2H RHS at a low ambient temperature (-40 °C). No adequate reason was found to use C_f (0.9) for S420 joints, which was confirmed in [15–17] at normal ambient temperature. Although the validity of the $0.8f_u$ restriction was not discussed in the original paper, the presented data proves that the restriction is not necessary. Besides, for tested joints with β (the brace-to-chord width ratio) ≥ 0.8 [14], the enhancement of the resistance and the deformation capacity was negligible by increasing the weld throat thickness from 1.11 to 1.48 times the brace thickness (t_1). The $1.11t_1$ weld might be sufficient for BF and PSF. For $\beta < 0.8$ joints where the chord face failure (CFF) dominated, the weld thickness is crucial for the resistance since the ultimate resistance was reduced by 22% due to a 15% weld thickness reduction (from $0.98t_1$ to $0.83t_1$) in specimens with $\beta = 0.53$ (XA4 and XA5).

Feldmann et al. [16] found that no reduction was needed for S500 joints, but a 0.9 and 0.8 reduction factor was necessary for S700 and S960 joints, respectively. This conclusion was drawn based on 106 RHS X- and K-joints tension and compression tests. The original report did not distinguish C_f for the different types of joints and loading conditions. The 16 tensile tests on X-joints, with a nominal 6.5 mm fillet weld (larger than $1.1t_1$, three welding passes), demonstrate that design rules could safely predict the resistance without considering C_f and the $0.8f_u$ restriction, except for two S960 joints with $\beta \geq 0.93$. Besides, a group of tensile tests on X-joints with a single welding pass (nominal thickness varying from 3 mm to 5 mm) was conducted to investigate the influence of a small weld on the joint resistance. The test results indicate that C_f and the $0.8f_u$ restriction are unnecessary for S500 and S700 joints (23 joints) even with a small weld (generally smaller than $1.1t_1$), while the prediction without considering C_f and the $0.8f_u$ restriction is unsafe for 5 out of 17 S960 joints. The experiments also show that by changing the fillet weld (nominal $0.79t_1$) to the butt weld ($\beta = 0.8$, S960), the failure mode transfers from BF to PSF, accompanying an up to 20% resistance reduction, indicating the weld type has a significant effect on the joint behaviour.

Tuominen and Björk [17] tested 20 X- (18 in tension and 2 in compression) and 10 K-joints made of cold-formed and hot-finished RHS. The material steel grades were S420 and S460. The joints were made with $1.0t_1$ single bevel weld and $1.1t_1$ fillet weld, which were relatively smaller than the stipulation in EN1993-1-8 [1]. It was found that the material factor was not necessary for S420 and S460 in validating all experiments. Based on the presented data in [17], it can also be concluded that the $0.8f_u$ restriction is not necessary. An attempt of the finite element analysis was made to demonstrate the influence of the weld thickness on the joint capacity. For a joint with $\beta = 0.67$ and $t_1 = 6$

mm, the resistance increased by 14% by changing the weld thickness from $0.88t_1$ to $1.18t_1$. Hence, the weld thickness is crucial for joints with a small β , as proved in [14]. Besides, it was found that the $-40\text{ }^\circ\text{C}$ temperature did not influence the joint resistance and the deformation capacity, indicating that the data in [14] should be included in the database of tensile X-joint regardless of the testing temperature.

Becque and Wilkinson [18] carried out tension and compression tests on 4 T- and 11 X-joints made of C450 RHS. It was concluded that C_f (0.9) was not necessary for ductile failure modes, CFF and the side wall buckling, provided the geometric constraints imposed on the CIDECT provisions [19] were satisfied. But C_f was required for PSF and BF. The conclusions were drawn considering a safety factor, $\gamma = 1.25$ for brittle failure modes and $\gamma = 1$ for ductile failure modes. Such distinction is not included in EN1993-1-8 [1]. However, based on the presented data, it is found that the predicted resistance without considering C_f and the $0.8f_u$ restriction is lower than the experiments.

In recent years, extensive experimental and numerical investigations on HSS and UHSS tubular X- and T-joints in compression were carried out [20–26]. Pandey and Young [20] investigated the compression capacity of welded cold-formed UHSS (S900 and S960) T-joints. 15 RHS-RHS and 7 CHS-RHS T-joints were tested with the chord fully supported. It was concluded that the design rules overestimated the resistance of joints with small β . However, the equal-width ($\beta = 1$) joint resistance was significantly underestimated, which was also reported by Kim et al. [21]. Hence, the material factor was required for joints with small β but not equal-width joints. Similar conclusions were drawn for welded cold-formed UHSS X-joints in compression based on 24 RHS-RHS and 10 CHS-RHS tests [22]. Lan et al. [23] investigated the axial compression behaviour of welded built-up RHS X-joints based on 8 UHSS X-joint experiments and intensive numerical studies. It was found that HSS and UHSS joints had sufficient deformation capacity, at least two times $3\%b_0$ deformation. The CIDECT strength prediction [19] was increasingly unconservative with increasing steel grade, increasing 2γ ratio, and decreasing β ratio for CFF. Similar conclusions were drawn in [24] based on 7 built-up UHSS RHS T-joint compression tests. Kim et al. [21] tested RHS X-joint made of mild steel and HSS. The tubes were fabricated by two 15 mm cold-formed channels. It was found that the experimental compressive resistance was higher than the EN1993-1-8 [1] prediction without using C_f . Lee et al. [25,26] investigated the compressive behaviour of cold-formed mild steel and HSS CHS X-joints based on 9 tests. The strength and ductility of HSS joints were comparable with that of mild steel joints. C_f for CFF was too conservative, and the joint strength equations were less conservative for joints with small β , aligning with conclusions for RHS joints [20–24].

Havula et al. [27] tested 20 RHS HSS T-joints to study the in-plane bending behaviour. The joints were fabricated using three types of welds, namely butt weld, 6 mm fillet weld, and 10 mm fillet weld. It was found that the thickness of the fillet weld significantly influenced the joint resistance and stiffness. Without considering the effect of weld thickness, the material factor was necessary for all butt-welded joints and S700 joints with small fillet welds. The material factor was re-evaluated for the chord side wall failure (CSWF) and BF by Wardenier et al. [28]. An equation was proposed to correlate

the steel grade and the material factor, which is more appropriate than prEN1993-1-8 [4], where the same factor is used for a range of steel grades.

All the above-mentioned literature is summarized in Table 6.1. Note that the information in the “Conclusions” and “Comments” columns are from the original paper and a re-evaluation of this study, respectively, based on the presented experimental data. It can be seen that the available tensile tests on cold-formed RHS X-joints with material above S460 are still quite limited. Therefore, in this study, the results of 18 tensile tests on welded RHS X-joints made of mild steel and HSS are reported and analysed. The aim of the research is to examine the validity of C_f and the $0.8f_u$ restriction. The predicted failure modes are compared to the experimental failure modes. Additionally, a bi-linear model, suitable for an elasto-plastic global analysis considering the post-yielding stiffness, is proposed to characterize the nonlinear behaviour of the joint. It is concluded that C_f and the $0.8f_u$ restriction are not necessary for the resistance prediction of tested joints in this paper and literature, using prEN1993-1-8 [4]. However, the predicted BF resistance is too optimistic for tested joints that failed in the brace if C_f for S700 or the $0.8f_u$ restriction for all steel grades is not considered.

Table 6.1 Summary of the literature review.

References	Joints	Shape	Steel grade	Load	Note	Conclusions	Comments
Björk and Saastamoinen, 2012 [14]	20 X-joints	RHS	S420MH (S355J2H)	Tension	-40 °C, cold-formed tubes, 1.03~1.62 t_1 fillet weld	C_f is not necessary.	Both C_f and $0.8f_u$ are not necessary.
Feldmann et al., 2016 [16]	68 X- and 38 K-joints	RHS	S500, S700, S960	Tension and compression	Cold-formed and hot-finished tubes, 0.69~1.57 t_1 fillet weld	C_f is necessary for S700 and S960 but not S500 joints.	Both C_f and $0.8f_u$ are not necessary for S500 and S700 X-joints in tension.
Tuominen and Björk, 2017 [17]	20 X- and 10 K-joint	RHS	S420, S460	Tension and compression	Cold-formed and hot-finished tubes, 1.0 t_1 single bevel butt weld and 1.04~1.45 t_1 fillet weld	C_f is not necessary.	Both C_f and $0.8f_u$ are not necessary for X-joints in tension.
Becque and Wilkinson, 2017 [18]	4 T- and 11 X-joints	RHS	C450 ($f_{yn} = 450$ MPa)	Tension and compression	Cold-formed tubes, single bevel butt weld + 0.5 t_1 fillet weld, $\gamma = 1.25$ for PSF and BF considered	C_f is necessary for PSF and BF but not CFF and the side wall buckling.	Both C_f and $0.8f_u$ are not necessary for X-joints in tension.
Lee et al., 2017 [25], 2018 [26]	9 X-joints	CHS	SM490 ($f_{yn} = 325$ MPa), SM570 ($f_{yn} = 420$ MPa), HSA800 ($f_{yn} = 650$ MPa)	Compression	Cold-formed tubes, single bevel butt weld + fillet weld	C_f (0.8) is too conservative.	
Kim et al., 2019 [21]	6 X-joints	RHS	SM490 ($f_{yn} = 325$ MPa), HSA800 ($f_{yn} = 650$ MPa)	Compression	Cold-formed channel tubes, single bevel butt weld	C_f is not necessary.	
Pandey and Young, 2019 [20], 2020 [22]	22 T- and 34 X-joints	CHS & RHS	S900, S960	Compression	Cold-formed tubes, 0.97~1.81 t_1 fillet weld	C_f is necessary for all joints but not the equal-width ($\beta = 1$) joint	
Lan et al., 2019 [23], 2021 [24]	8 X- and 7 T-joints	CHS & RHS	Q890 ($f_{yn} = 890$ MPa)	Compression	Built-up tubes, 0.77~1.0 t_1 fillet weld	New C_f was proposed. Conservative prediction for large β .	
Havula et al., 2018 [27]	20 T-joints	RHS	S420, S500, S700	Bending	Cold-formed tubes, single bevel butt weld, 0.75 t_1 fillet weld, 1.25 t_1 fillet weld	C_f is necessary for all butt weld joints and S700 joints with 0.75 t_1 fillet weld.	

6.2. Experiments

6.2.1. X-joint tensile tests

Consider a welded hollow section X-joint consisting of two braces and a chord, as shown in Fig. 6.1. The braces are welded to the opposite surfaces of the chord such that the joint is symmetric. A tensile load is applied to the braces.

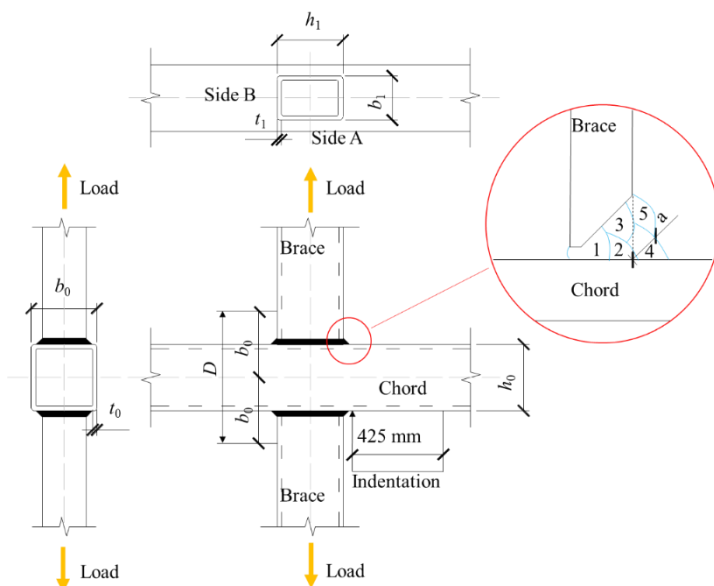


Fig. 6.1 Schematic of an X-joint.

The tested X-joints were made of three steel grades, namely S355, S500, and S700. S355 represents a reference case to which the HSS grades are compared. Specimens for each steel grade included three configurations with various brace width to chord width ratios (β). The main purpose for selecting three β values is to test joints with different deformation capacities and failure modes, as β governs the failure mode according to prEN 1993-1-8 [4]. Given the welding quality of different companies, two Dutch fabricator (A and B), experienced in welding HSS, were employed to fabricate 9 joints each, resulting in 18 joints in total. The nominal and measured dimensions of each joint are presented in Appendix 6.A and Table 6.2, respectively. The symbols “A” and “B” represent the specimens fabricated by the fabricator A and B, respectively. The nominal RHS dimensions for each joint were identical between Company A and B, except for the chord of XS500A/B1, XS700A/B2, and XS700A/B3. The length of the chord and the brace was 1.5 m and 0.4 m, respectively. The outer radius for nominal 4 mm, 5 mm, 6 mm, 8 mm, and 10 mm tubes were 8.5 mm, 9 mm, 13 mm, 20 mm, and 25 mm, respectively. Note the chord of XS500B1 and the brace of XS700A/B1 had the h_0/b_0 ratio of 0.45 and 3, respectively, which were beyond the stipulated limit (0.5 to 2).

Additionally, $\beta = 0.25$ for XS355A/B1 is below the required minimum value $0.1+0.01b_0/t_0 = 0.35$, according to the range of validity for welded joints [4].

Table 6.2 Measured geometric property of X-joints. (See Fig. 6.1 for the definition of dimensions.)

Specimen	Steel grade	b_0 [mm]	h_0 [mm]	t_0 [mm]	b_1 [mm]	h_1 [mm]	t_1 [mm]	β	a_{sideA} [mm]	a_{sideB} [mm]
XS355A1		199.0	100.4	7.9	50.2	100.3	5.0	0.25	5.1	5.3
XS355A2	S355	159.6	160.5	10.0	140.1	139.6	8.3	0.88	-	6.2
XS355A3		150.5	149.9	6.1	149.9	150.4	6.0	1	-	5.4
XS500A1		200.0	101.1	7.9	90.5	159.9	7.9	0.45	6.6	6.6
XS500A2	S500	160.9	160.8	9.8	140.4	140.4	7.9	0.87	-	8.6
XS500A3		150.7	150.2	6.0	150.5	150.3	6.0	1	-	5.1
XS700A1		120.4	120.3	7.9	51.0	153.2	6.0	0.42	6.3	6.2
XS700A2	S700	161.5	160.5	9.9	80.5	100.7	4.1	0.5	5.5	5.6
XS700A3		139.9	140.4	5.9	120.6	80.4	6.0	0.86	-	5.4
XS355B1		199.9	101.0	8.1	50.5	100.0	5.1	0.25	5.9	5.1
XS355B2	S355	160.5	160.5	10.0	140.1	140.1	8.1	0.87	-	7.5
XS355B3		150.5	151.0	6.2	150.8	150.8	6.2	1	-	7.7
XS500B1		180.5	80.7	8.0	90.7	160.0	8.1	0.5	8.5	9
XS500B2	S500	160.2	160.1	9.9	140.3	140.3	8.0	0.88	-	8.5
XS500B3		151.5	150.5	5.9	151.0	151.0	6.2	1	-	7.9
XS700B1		120.6	120.5	8.1	51.0	153.8	6.1	0.42	6.1	6.5
XS700B2	S700	151.9	200.0	9.8	80.9	100.7	4.2	0.53	5.8	6
XS700B3		141.8	181.0	5.3	120.3	80.8	6.1	0.85	-	6.8

The brace was welded to the chord with a full-penetration butt weld. A single-bevel groove was produced in the brace before welding. A butt weld typically consists of three types of welding pass: the root (pass 1), the fill (passes 2 and 3), and the cap (passes 4 and 5), as shown in Fig. 6.1. The cap pass results in an extra fillet weld, making the whole weld thicker than the parent plate. Therefore, the throat thickness (a) of the fillet weld was measured. Note that the throat thickness is not applicable on Side A (see Fig. 6.1) of the joint with a large β value. The average throat thickness is presented in Table 6.2. It is worth mentioning that the investigated joints are fabricated with one type of welding detail. As HSS is sensitive to the welding parameters, the welded connections must be properly and professionally executed. A comprehensive discussion regarding the execution rules can be found in [29,30].

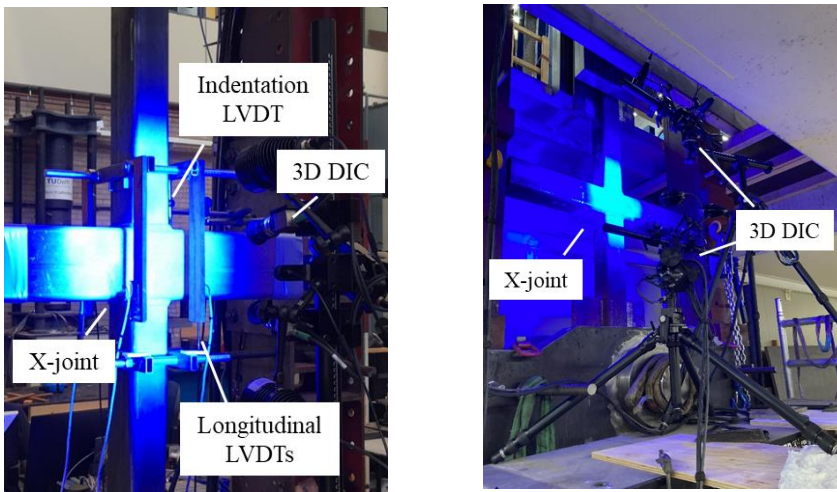
The fabricator A used the filler metal Carbofil 1 to weld S355 tubes, while the filler metal Union NiMoCr welded S500 and S700 tubes. The fabricator B used the filler metal MEGAFIL 710M for S355 and S500 joints and MEGAFIL 742M for S700 joints. Both companies used the metal active gas (MAG) welding process. The minimum preheated temperature, the maximum interpass temperature, the heat input, and the mechanical property of filler metal for each steel grade are presented in Table 6.3. The main reason for employing two welding companies instead of carrying out the welding in laboratory conditions was to get test specimens welded with current industry practices and quality control. The welding companies provided some data from their Welding Procedure Specification (WPS) as presented in Table 6.3. However, more detailed data of the welding process was not obtained for this study.

Table 6.3 Welding details.

Welding company	Steel grade	Filler metal	f_y [MPa]	f_u [MPa]	A [%]	Min preheat [°C]	Max interpass [°C]	Heat input [kJ/mm]
Company A	S355	Carbofil 1	502	574	28	20	200	1-1.4
	S500	Union NiMoCr	720	780	17	20	200	1-1.4
	S700	Union NiMoCr	720	780	17	20	200	1-1.4
Company B	S355	MEGAFIL 710 M	551	609	24	20	150	0.4-1.0
	S500	MEGAFIL 710 M	551	609	24	50	135	0.8-1.5
	S700	MEGAFIL 742 M	763	790	20	50	100	0.6-1.1

The X-joints were tested in a setup with 2 MN capacity (Fig. 6.2 a)), except for 8 X-joints X355A/B2, X355A/B3, X500A/B2, and X500A/B3, which were tested in a 10 MN setup (Fig. 6.2 b)). A constant loading rate of 0.01 mm/s was used during the whole testing process. For the joint XS355A/B1, the loading rate was changed to 0.1 mm/s at the plastic stage as a significant deformation appeared. All joints were tested until the final failure with an obvious fracture and a sudden load drop.

Four Linear Variable Differential Transformers (LVDTs) were used to measure the longitudinal deformation of the A-series joints based on a $2b_0$ initial gauge length. An indentation LVDT was positioned at the centre line of the chord top surface to measure the chord top surface indentation, as shown in Fig. 6.1 and Fig. 6.2 a). The measuring point was 30 mm from the out surface of the brace. The base for holding the LVDT was 425 mm from the measuring point. Besides, the 3D digital image correlation (DIC) was used to measure the deformation of the specimen. The calibrated measuring volume was $350\text{ mm}\times 280\text{ mm}\times 280\text{ mm}$ with a maximum 0.05 pixel deviation. It was found that the results from LVDT and DIC showed a good agreement. Therefore, the LVDTs were not used in the B-series testing.



a) Setup with 2 MN capacity.

b) Setup with 10 MN capacity.

Fig. 6.2 X-joint test setup.

6.2.2. Tensile coupon tests

Tensile coupon tests were conducted to obtain the mechanical property of RHS in X-joints. Coupon specimens were taken from the wall opposite the longitudinal weld of RHS, as shown in Fig. 6.3. Two specimens were symmetrically positioned around the symmetric axis of the tube with a distance (d), as summarised in Appendix 6.A. In Chapter 2, it is found that the testing results of two symmetrically positioned specimens do not show any significant scattering. Hence, only two specimens were designed for each profile. According to ISO 6892-1 [31], a 5.65 proportional coefficient was used, resulting in a 50 mm initial gauge length and an 80 mm^2 cross-sectional area. The basic dimensions of the coupon specimen are presented in Fig. 6.4.

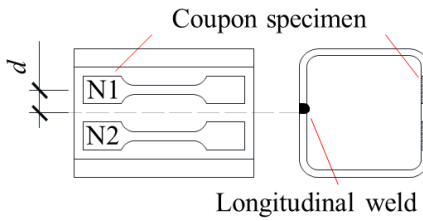


Fig. 6.3 Specimen cutting scheme.

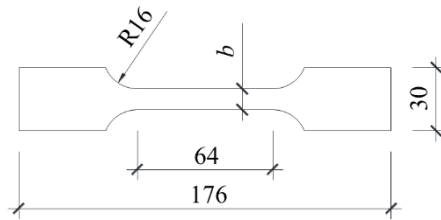


Fig. 6.4 Basic dimensions of coupon specimen [mm].

The measured thickness (t) and the width (b) are summarized in Appendix 6.B. Note that the cross-sectional area of minor specimens was not 80 mm^2 but 50 mm^2 initial gauge length was used for all coupons. The coupon specimen was only fabricated from the chords for the A-series joints. Since specimens XS355A3 and XS500A3 used the same profile for the chord and brace, the dimensions of the brace coupon specimen were the same as the chord. For other braces in A-series, the material property referred to other profiles with the same thickness as the brace and delivered as the same batch material. Besides, only one specimen was tested for the brace of XS355B3.

The tensile coupon test was carried out in an Instron testing machine with a 200 kN capacity. The loading controlled by the displacement was 0.01 mm/s , satisfying the loading rate requirement in [31]. The deformation was measured by two 3D DICs positioned perpendicular, as shown in Fig. 6.5. One DIC faced the side surface of the coupon specimen, while another DIC measured the convex surface of the specimen. The elongation of the specimen was extracted from DIC facing the side surface. Three virtual extensometers were created at three positions close to the concave side, close to the convex side, and at the centre, as shown in Fig. 6.6. Since an initial bow existed in the coupon specimen, the measured three deformations were averaged to obtain the elongation of the specimen. The measuring volume of two 3D DIC devices was $85 \text{ mm} \times 60 \text{ mm} \times 40 \text{ mm}$.

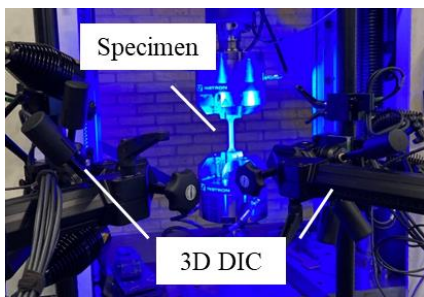


Fig. 6.5 Coupon test setup.

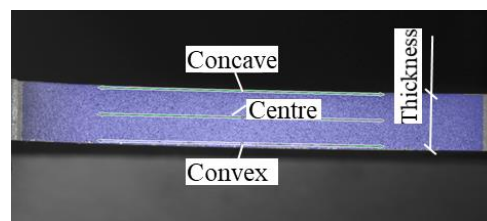


Fig. 6.6 Three virtual extensometers in DIC.

6.3. Results and discussions

6.3.1. Coupon test results

According to [32], the yield strength f_y (0.2% proof stress), the ultimate strength f_u , the ultimate strain ε_u , and the elongation at failure ε_f are determined for each specimen and summarised in Appendix 6.C. The stress-strain relationships are presented in Appendix 6.D. Note that ‘C’ and ‘B’ in the name of the specimen represent ‘chord’ and ‘brace’, respectively.

6.3.2. X-joint test results

All X-joints were broken at HAZ, either BF or PSF, except for XS355A3 with CSWF (for this joint, $\beta = 1$). The total deformation (D) of the joint was measured between two cross-sections with a $2b_0$ distance, see Fig. 6.1 and Fig. 6.2 a). The indentation of the chord surface was converted to a deformation ratio (D^*) by dividing the indentation by b_0 to trace the $3\%b_0$ deformation limit. If the $3\%b_0$ deformation limit was reached before the ultimate resistance (R_u), the joint failure was characterized as a combined failure mode of CFF and the failure mode corresponding to the final fracture, and the ultimate resistance was modified to the load at $3\%b_0$ deformation ($R_{u\&3\%}$). If the $3\%b_0$ deformation limit was not reached, $R_{u\&3\%}$ equals R_u .

The deformation measured by LVDTs and DIC was used for the A- and B-series specimens, respectively. Besides, the descending part corresponding to the final failure was missing for some of the load-deformation relationships presented in this section since 3D DIC could not recognize the speckle pattern on the specimen after the final failure. Therefore, the last point in the curve is the moment just before the final failure.

6.3.2.1. S355 X-joints

Fig. 6.7 presents the failure mode of S355 joints. Due to the small β value, a profound chord face plastification appeared in XS355A/B1, which eventually failed in the chord. From Fig. 6.8 b), it can be seen that the $3\%b_0$ deformation limit, highlighted in yellow, was reached at an early stage. Hence, the failure mode of XS355A/B1 was a combination of CFF and PSF. The load-displacement relationships of each configuration show good agreements. R_u , $R_{u\&3\%}$, and the failure mode are summarized in Table 6.4.

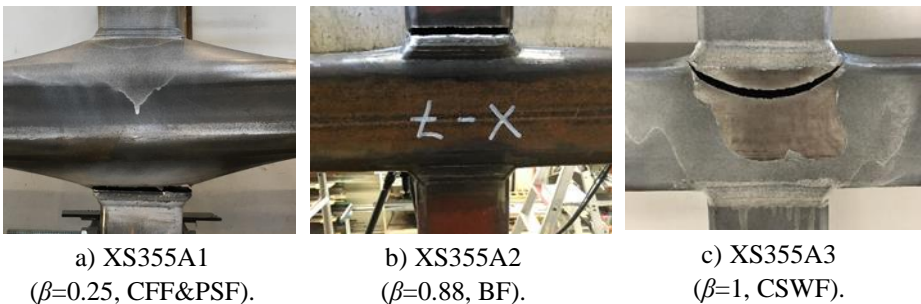




Fig. 6.7 Failure modes of S355 X-joints.

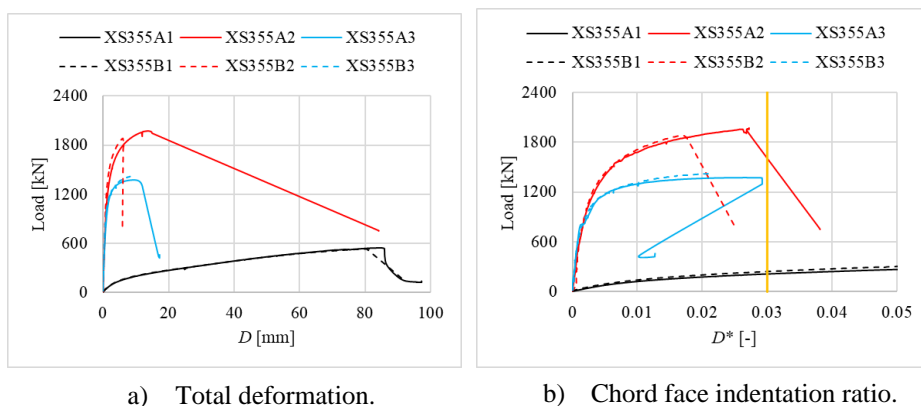


Fig. 6.8 Load-displacement relationship of S355 X-joints.

Table 6.4 X-joint test results.

Specimen	β	R_u [kN]	$R_{u\&3\%}$ [kN]	Failure mode	Specimen	β	R_u [kN]	$R_{u\&3\%}$ [kN]	Failure mode
XS355A1	0.25	546	215	CFF&PSF	XS355B1	0.25	532	240	CFF&PSF
XS355A2	0.88	1972	1972	BF	XS355B2	0.87	1883	1883	BF
XS355A3	1	1374	1374	CSWF	XS355B3	1	1424	1424	PSF
XS500A1	0.45	897	428	CFF&PSF	XS500B1	0.5	887	589	CFF&PSF
XS500A2	0.87	2213	2213	BF	XS500B2	0.88	1981	1981	PSF
XS500A3	1	1713	1713	BF	XS500B3	1	1557	1557	BF&PSF
XS700A1	0.42	890	852	CFF&PSF	XS700B1	0.42	1030	863	CFF&PSF
XS700A2	0.5	784	784	BF	XS700B2	0.53	788	788	BF
XS700A3	0.86	962	962	PSF	XS700B3	0.85	716	716	BF

The 3% b_0 deformation limit was not reached by specimens XS355A/B2 and XS355A/B3, although XS355A2 and XS355A3 were very close (see Fig. 6.8 b)). Hence, CFF did not appear in these four specimens. Both specimens with a moderate β (0.87 and 0.88) failed in the brace, while the specimens with $\beta = 1$ had different failure modes: CSWF and PSF for A-series and B-series, respectively. The ultimate resistance between the two series agreed well, with less than 5% variation.

6.3.2.2. S500X-joints

The chord width (b_0) used in XS500A1 was larger than that of XS500B1, while the dimension of the brace was kept the same. Consequently, the load at 3% b_0 deformation for XS500B1 (589 kN) was higher than XS500A1 (428 kN), as shown in Fig. 6.10 b). Note that the LVDT measuring the chord face indentation of XS500A1 reached the maximum range at approximately 500 kN. Hence, the curve went straight up after 500 kN. Both specimens had a PSF, where a thorough fracture around the brace appeared in the chord of XS500A1 (Fig. 6.9 a)), and only one side of XS500B1 (Fig. 6.9 d)) failed. The ultimate loads of XS500A1 and XS500B1 were 897 kN and 887 kN, respectively. Besides, the stiffness at the plastic stage increased as the load was above 700 kN, indicating that the dominant mechanism changes from the chord face in bending to the chord face in tension which is so called the membrane effect.

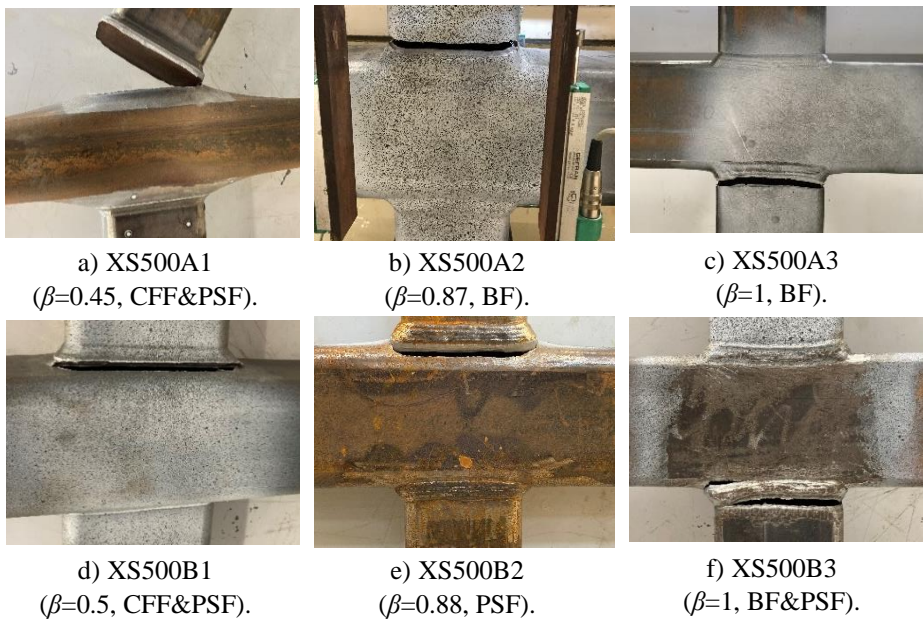


Fig. 6.9 Failure modes of S500 X-joints.

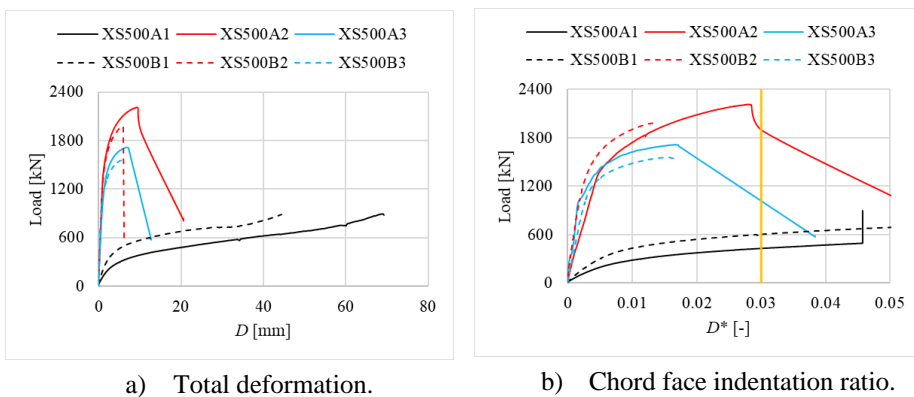


Fig. 6.10 Load-displacement relationship of S500 X-joints.

Different failure modes, BF and PSF, were obtained from XS500A2 and XS500B2 (Fig. 6.9 b) and e)), respectively, although the dimensions of the members were the same. The ultimate loads of XS500A2 and XS500B2 were 2213 kN and 1976 kN, respectively. Fig. 6.10 a) shows that the ultimate resistance and the deformation capacity of XS500B2 were smaller than XS500A2. The same trend was observed in the specimens XS500A/B3. A possible reason for this difference is that the filler metal used in S500 B-series was much weaker than A-series, resulting in a softer HAZ in B-series, and consequently lower deformation and resistance.

Both specimens with $\beta = 1$ failed in the brace, as shown in Fig. 6.9 c) and f). In addition, a short fracture occurred at the corner of the chord in XS500B3, indicating that the resistance of BF and PSF was very close. The ultimate resistance of XS500A3 and XS500B3 was 1713 kN and 1557 kN, respectively. The $3\%b_0$ deformation limit was not reached.

6.3.2.3. S700X-joints

The same failure mode PSF was obtained from the specimens XS700A/B1, as shown in Fig. 6.11 a) and d). Fig. 6.12 demonstrates a good match between XS700A1 and XS700B1 before the $3\%b_0$ deformation limit. Fig. 6.11 b) and e) present the failure mode (BF) of XS700A/B2. A thorough fracture involving the whole brace cross-section suddenly appeared at the end of testing. Neither specimen reached the deformation limit, as shown in Fig. 6.12 b). R_u , $R_{u\&3\%}$, and the failure mode are shown in Table 6.4.

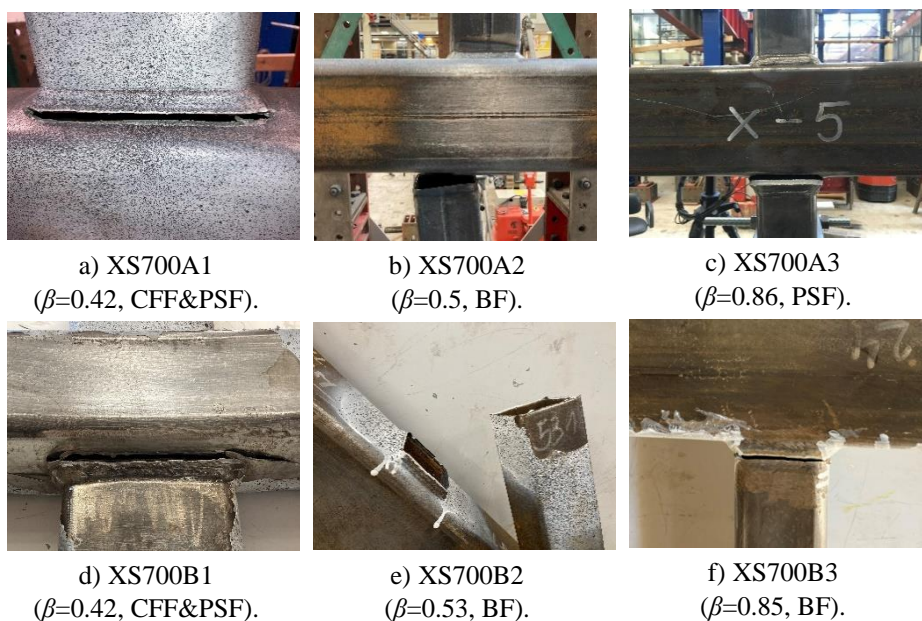


Fig. 6.11 Failure modes of S700 X-joints.

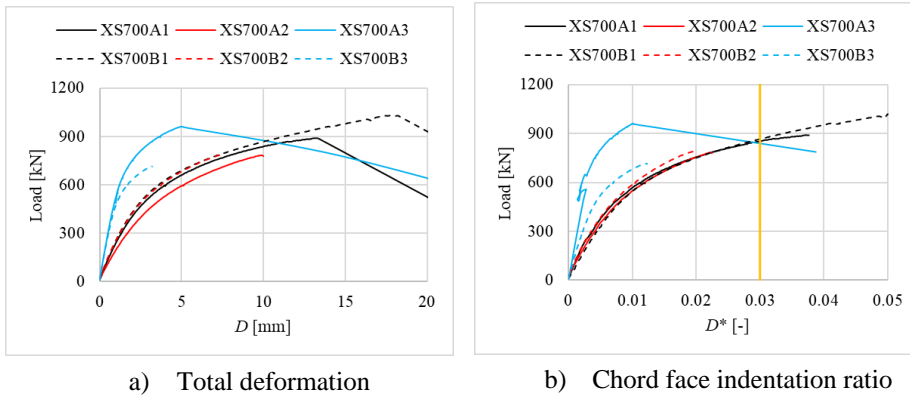


Fig. 6.12 Load-displacement relationship of S700 X-joints.

Fig. 6.12 b) demonstrates that XS700A/B3 did not reach the $3\%b_0$ deformation limit. Although the chord of XS700B3 was thinner than XS700A3, the failure mode transformed from PSF in XS700A3 to BF in XS700B3, as shown in Fig. 6.11 c) and f). And the resistance of XS700B3 (716 kN) was much lower than XS700A3 (962 kN). It indicates that the welding process, consequently the HAZ material property, has a crucial influence on the joint behaviour.

6.3.2.4. X-joints with different steel grades

As most of the specimens' dimensions among different steel grades are not identical, only two sets of specimens could be used to reveal the effect of the steel grade on the joint behaviour. The specimens XS355A/B2, XS500A/B2, and XS700A/B3 have a similar β value (around 0.87). The test results show that the ultimate deformation of S355 and S500 specimens is at least $0.014b_0$, while S700 specimens have a deformation of around $0.01b_0$. Similarly, with the same β value, XS700A2 has a significantly smaller ultimate deformation than XS500B1, indicating that the deformation capacity of the joint decreases with the increase of the steel grade. The explicit effect of the steel grade on the failure mode is not observed in the experiments. As the dimensions of the two sets of specimens vary, a direct comparison of the resistance is impossible.

6.3.3. Characterization of the joint yield resistance

According to the design guide [19], the joint resistance is defined by the lower of the ultimate resistance and the load corresponding to the $3\%b_0$ deformation limit (if reached). However, in an elasto-plastic global analysis, it is essential to describe the full-range behaviour of a joint using a simplified model, such as a bi-linear model in prEN 1993-1-8 [4].

Zanon and Zandonini [33] proposed a model for characterising the joint yield flexural resistance based on the initial and post-yielding stiffness, as shown in Fig. 6.13 a). It is straightforward to determine the initial stiffness using the linear part. However, the criterion for determining the post-yield stiffness is rather elusive. Different post-yielding part of the curve leads to different post-yielding stiffness, resulting in an arbitrary yield

resistance. Lee et al. [25] appraised the joint ductility based on the equal energy criterion, see Fig. 6.13 b). The initial tangential stiffness line is used as a reference. A horizontal line is adjusted such that the two hatched blue areas are equal. The ratio D_2/D_1 is used to identify joint ductility. The nonlinear load-deformation relationship is converted to an equivalent elasto-plastic bi-linear model. However, the post-peak part is involved in the energy equilibrium. The energy consumed at the hardening stage is overestimated, resulting in an unconservative equivalent elasto-plastic behaviour. Moreover, the joint hardening behaviour cannot be recognized by Model 2.

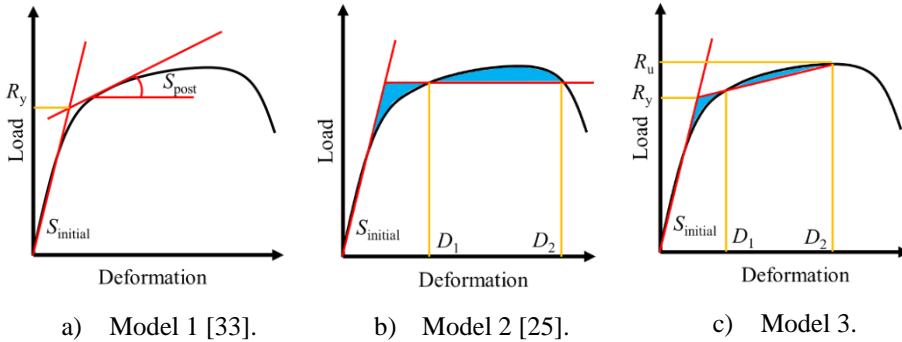


Fig. 6.13 Bi-linear models.

Based on the aforementioned two models, a modified bi-linear model is proposed in this paper, as shown in Fig. 6.13 c). The initial stiffness line is the same as in the other two models. The horizontal plastic line in Model 2 is modified to an inclined line that ends at the ultimate resistance point. Shifting the intersection point of elastic and plastic lines, the two hatched blue areas vary. The yield resistance (R_y) is characterised by making the two areas equal. The advantages of the proposed model are primarily on properly addressing the following three aspects. First, a yield resistance is determined uniquely without a potential variation due to the “arbitrary” determined post-yielding stiffness. Second, a higher yield ratio (R_y/R_u) is rather correctly influenced by better ductility, e.g. higher D_2/D_1 ratio of a joint, as discussed in the next section. Third, the bi-linear model properly considers the post-yielding behaviour, which enables an adequate elasto-plastic global analysis.

6.3.4. Comparison of experimental and semi-analytical results

The yield and ultimate strength of each profile, shown in Appendix 6.C, are averaged to calculate the joint resistance. C_f is derived for each yield strength according to Table 6.5 [4]. Table 6.6 presents the average yield strength of the chord (f_{y0}) and the brace (f_{y1}), the ultimate strength of the chord (f_{u0}) and the brace (f_{u1}), the modified yield strength of the chord ($f_{y0,M}$) and the brace ($f_{y1,M}$) according to the $0.8f_u$ restriction, and the corresponding C_f .

Table 6.5 Material factor C_f [4].

Yield strength range	Material factor C_f
$f_y \leq 355$ MPa	1.00
$355 \text{ MPa} < f_y \leq 460$ MPa	0.90
$460 \text{ MPa} < f_y \leq 550$ MPa	0.86
$550 \text{ MPa} < f_y \leq 700$ MPa	0.80

Table 6.6 Average material strength and corresponding material factor.

Specimen	Chord					Brace			
	f_{y0} [MPa]	C_{f0}	f_{u0} [MPa]	$f_{y0,M}$ [MPa]	$C_{f0,M}$	f_{y1} [MPa]	f_{u1} [MPa]	$f_{y1,M}$ [MPa]	$C_{f1,M}$
XS355A1	522	0.86	553	442	0.90	505	543	434	0.90
XS355A2	486	0.86	516	412	0.90	506	532	425	0.90
XS355A3	452	0.90	510	408	0.90	452	510	408	0.90
XS500A1	558	0.80	597	477	0.86	580	612	489	0.86
XS500A2	589	0.80	624	499	0.86	580	612	489	0.86
XS500A3	609	0.80	670	536	0.86	609	670	536	0.86
XS700A1	751	0.80	846	677	0.80	780	861	689	0.80
XS700A2	726	0.80	831	665	0.80	741	848	678	0.80
XS700A3	780	0.80	861	689	0.80	780	861	689	0.80
XS355B1	519	0.86	549	439	0.90	546	590	472	0.86
XS355B2	499	0.86	532	425	0.90	530	547	438	0.90
XS355B3	484	0.86	523	419	0.90	484	523	419	0.90
XS500B1	598	0.80	634	507	0.86	550	584	467	0.86
XS500B2	573	0.80	617	493	0.86	617	648	518	0.86
XS500B3	596	0.80	646	516	0.86	596	646	516	0.86
XS700B1	783	0.80	861	689	0.80	792	867	693	0.80
XS700B2	743	0.80	808	647	0.80	741	848	678	0.80
XS700B3	722	0.80	825	660	0.80	784	864	691	0.80

6.3.4.1. General comparison

The results of the bi-linear model and the prEN 1993-1-8 [4] are presented in Table 6.7. The equations for predicting the X-joint tensile resistance are presented in Appendix 6.E. R_y is the character yield resistance of the proposed bi-linear model (Model 3) in Section 6.3.3. Three design resistances are calculated, which consider a) C_f and the $0.8f_u$ restriction (R_{EC3}), b) the $0.8f_u$ restriction ($R_{EC3,non-Cf}$), and c) no restriction ($R_{EC3,non}$). Note that $R_{EC3,non-Cf}$ and $R_{EC3,non}$ are the same for the CFF and CSWF since the $0.8f_u$ restriction is not required for these two failure modes. The corresponding failure mode is also shown in the table. Since a linear interpolation is applied between the governing resistances at $\beta = 0.85$ and $\beta = 1$, a combined failure mode is presented for some joints.

Table 6.7 Results of the bi-linear model and prEN 1993-1-8 [4].

Specimen	Bi-linear model			prEN1993-1-8					
	R_y [kN]	$\frac{R_y}{R_u}$	$\frac{D_2}{D_1}$	R_{EC3} [kN]	Failure mode	$R_{EC3,non-cf}$ [kN]	Failure mode	$R_{EC3,non}$ [kN]	Failure mode
XS355A1	165	0.47	3.16	168	CFF	195	CFF	195	CFF
XS355A2	1563	0.79	3.41	1039	CFF&BF	1193	CFF&BF	1223	CFF&CSWF
XS355A3	1203	0.88	3.57	877	BF	974	BF	988	CSWF
XS500A1	357	0.52	3.75	233	CFF	291	CFF	291	CFF
XS500A2	1790	0.81	2.79	1090	CFF&BF	1343	CFF&BF	1379	CFF&CSWF
XS500A3	1388	0.81	2.91	1097	BF	1275	BF	1322	CSWF
XS700A1	605	0.68	2.49	357	CFF	446	CFF	446	CFF
XS700A2	501	0.64	2.14	467	CFF	583	CFF	583	CFF
XS700A3	707	0.74	2.37	421	CFF&BF	523	CFF&CSWF	523	CFF&CSWF
XS355B1	174	0.49	3.25	172	CFF	200	CFF	200	CFF
XS355B2	1448	0.77	2.88	1014	CFF&BF	1169	CFF&BF	1191	CFF&CSWF
XS355B3	1171	0.82	3.92	933	BF	1037	BF	1082	CSWF
XS500B1	540	0.74	2.77	283	CFF	354	CFF	354	CFF
XS500B2	1553	0.78	2.78	1140	CFF&BF	1395	CFF&BF	1428	CFF&CSWF
XS500B3	1235	0.79	2.86	1056	BF	1236	BF	1249	CSWF
XS700B1	662	0.64	2.90	391	CFF	489	CFF	489	CFF
XS700B2	508	0.64	2.20	495	CFF	619	CFF	619	CFF
XS700B3	525	0.73	2.21	286	CFF	357	CFF	357	CFF

Fig. 6.14 presents the varying range of $R_{EC3}/R_{u\&3\%}$ and $R_{EC3,non}/R_{u\&3\%}$ regarding the average yield strength for each steel grade. The average yield strength of S355, S500, and S700 are 498 MPa, 587 MPa, and 760 MPa, respectively. Since the β value of XS355A/B1 (0.25) is out of the valid geometry range in prEN 1993-1-8 [4] ($0.1+0.01b_0/t_0 = 0.35$), the resistance ratio is shown by the black point. Comparing R_{EC3} to $R_{u\&3\%}$, $R_{EC3}/R_{u\&3\%}$ of S355 and S500 joints varies in a similar range, as shown in Fig. 6.14 a). $R_{EC3}/R_{u\&3\%}$ of S700 joints is slightly lower than S355 and S500 joints. Note that the lower $R_{EC3}/R_{u\&3\%}$ of S700 joints does not mean the design rule for S700 joints is more conservative than S500 and S355 joints because the β value of tested specimens varies in different steel grades. Comparing Fig. 6.14 b) to a), the resistance ratio difference between S700 and S355/S500 slightly decreases without considering C_f and the $0.8f_u$ restriction. The maximum, average, and minimum resistance ratios are summarised in Table 6.8. The ratio excluding XS355A/B1 is presented in parentheses. Hence, a conclusion can be drawn that the design rule without using C_f and the $0.8f_u$ yield strength restriction predicts a conservative resistance. Note that this conclusion holds for all experimental studies of X-joints in tension presented in Table 6.1.

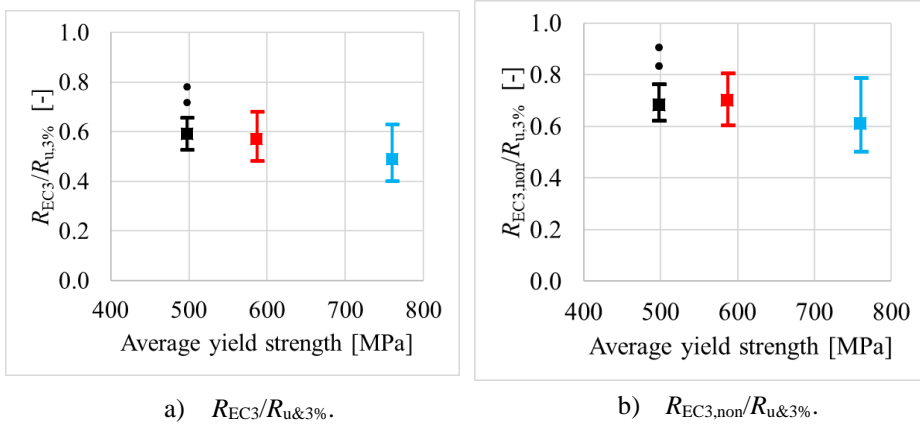


Fig. 6.14 Varying range of the resistance ratio.

Table 6.8 Range of resistance ratios.

Steel grade	Average f_y [MPa]	Type	$\frac{R_{EC3}}{R_{u,3\%}}$	$\frac{R_{EC3,non}}{R_{u,3\%}}$	$\frac{R_y}{R_u}$
S355	498	maximum	0.78 (0.66)	0.91 (0.76)	0.88
		average	0.64 (0.59)	0.75 (0.68)	0.70
		minimum	0.53	0.62	0.47
S500	587	maximum	0.68	0.80	0.81
		average	0.57	0.70	0.74
		minimum	0.48	0.60	0.52
S700	760	maximum	0.63	0.79	0.74
		average	0.49	0.61	0.68
		minimum	0.40	0.50	0.64

In addition, the joint nonlinear behaviour is characterised by the proposed bi-linear model. Note that the point where the post-yielding stiffness starts increasing is considered the ultimate resistance point of XS355A/B1 and XS500A/B1 since the membrane effect appeared. The yield ratio R_y/R_u varies between 0.47 and 0.88. For S355/S500 joints with $\beta < 0.5$, the ratio is around 0.5. For S355/S500 joints with $\beta \geq 0.5$ and S700 joints, the ratio is close to 0.7-0.8.

An example is presented in Fig. 6.15 a) to reveal the relationship between the joint ductility D_2/D_1 and the yield ratio R_y/R_u . The bi-linear model is characterised for two specimens with different ductility. Since the nominal dimensions of the two specimens are identical, the initial stiffness is the same. XS355A3 displays more ductile behaviour than XS500A3. $D_2/D_1 = 3.57$ and $R_y/R_u = 0.88$ for XS355A3 whereas $D_2/D_1 = 2.91$ and $R_y/R_u = 0.81$ for XS500A3. R_y/R_u is plotted against D_2/D_1 in Fig. 6.15 b), including all tested joints. In general, the better the joint ductility is, the higher the yield ratio is. Besides, D_2/D_1 and R_y/R_u decrease with the increase of the steel grade. Consequently, a

larger safety margin ($1-R_y/R_u$) is obtained for joints made of HSS than for mild steel. Three joints (XS355A/B1 and XS500A1 with low β) show good ductility (above 3) but a rather conservative yield ratio (below 0.6) because the joints yielded at a very early stage and the deformation at the ultimate stage was substantially larger than other joints (see Fig. 6.8 and Fig. 6.10). Regardless of the low R_y/R_u , the three joints also demonstrate the same trend between D_2/D_1 and R_y/R_u as other joints.

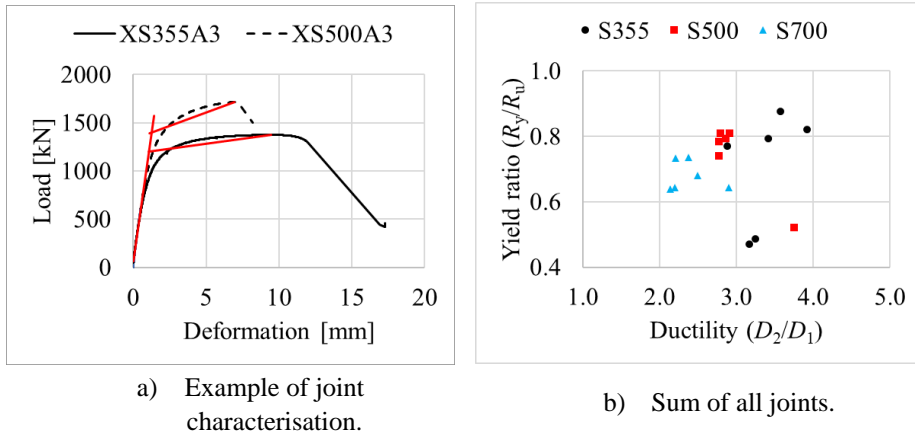


Fig. 6.15 Relationship of the yield ratio and the ductility.

6.3.5. Comparison of specific failure modes

Comparing Table 6.4 to Table 6.7, it can be seen that the failure mode of HSS joints is often mispredicted, which was also reported in the RUOSTE project [16]. Therefore, the resistance corresponding to the experimental failure mode is discussed in this section.

CFF is a dominant failure mode for tested joints with $\beta \leq 0.85$, as shown in Table 6.7. However, CFF was not observed in the experiments for XS700A2 ($\beta = 0.5$), XS700B2 ($\beta = 0.53$), and XS700B3 ($\beta = 0.85$), even though prEN 1993-1-8 predicts CFF to be the governing failure mode. The same phenomenon is observed in the RUOSTE project [16]. Two configurations of X-joints, namely TTX8 and TTX8W with $\beta = 0.67$, were made of S500, S700, and S960. CFF was predicted for all six joints, while BF was observed from two S960 and one S700 specimens. Besides these six joints, most of the joints had BF or PSF, while CFF was predicted. This discrepancy in the predicted and observed failure modes indicates that the design rule of prEN 1993-1-8 for X-joints in tension may need to be revised. One option might be the reduce the upper bound of β (0.85) for CFF as a function of steel grade. For joints with β between 0.85 and 1, the CFF resistance is used to determine the joint resistance by linear interpolation. Since CFF was not observed in the joints with $\beta > 0.85$, it might be reasonable to exclude CFF from the resistance determination. Besides, PSF appeared in joints with $\beta = 1$, which was also reported in [14,17,18], indicating that the upper bound of β which is $1-2t_0/b_0$ for PSF may need to be revised.

The resistances of the joints according to prEN 1993-1-8 corresponding to the experimental failure modes are summarised in Table 6.9. $R_{EC3,i}$, $R_{EC3,i,non-C_f}$, and $R_{EC3,i,non}$ are the predicted resistance considering a) C_f and the $0.8f_u$ restriction, b) the $0.8f_u$ restriction, and c) no restriction, respectively. The PSF resistance of XS500B3 is presented in parentheses.

Table 6.9 Comparison of the resistance for the experimental failure mode.

Specimen	β	Experimental Failure mode	$R_{u\&3\%}$ [kN]	$R_{EC3,i}$ [kN]	$R_{EC3,i,non-C_f}$ [kN]	$R_{EC3,i,non}$ [kN]
XS355A1	0.25	CFF	215	168	195	195
XS355A2	0.88	BF	1972	1429	1588	1882
XS355A3	1	CSWF	1374	988	988	988
XS500A1	0.45	CFF	428	233	291	291
XS500A2	0.87	BF	2213	1556	1810	2137
XS500A3	1	BF	1713	1097	1275	1449
XS700A1	0.42	CFF	852	357	446	446
XS700A2	0.5	BF	784	766	958	1045
XS700A3	0.86	PSF	962	493	616	698
XS355B1	0.25	CFF	240	172	200	200
XS355B2	0.87	BF	1883	1449	1610	1920
XS355B3	1	PSF	1424	570	633	731
XS500B1	0.5	CFF	589	283	354	354
XS500B2	0.88	PSF	1981	1106	1286	1494
XS500B3	1	BF(PSF)	1557	1056(625)	1228(727)	1414(838)
XS700B1	0.42	CFF	863	391	489	489
XS700B2	0.53	BF	788	793	991	1082
XS700B3	0.85	BF	716	712	890	997

$R_{EC3,i}$ and $R_{EC3,i,non}$ are compared to $R_{u\&3\%}$ in Fig. 6.16 for all 6 CFF joints. The resistance ratio is the predicted resistance ($R_{EC3,i}$ or $R_{EC3,i,non}$) over the experimental resistance ($R_{u\&3\%}$). The names in the legend, for example, ‘S355’ and ‘S355,non’, denote the ratio with and without considering C_f and the $0.8f_u$ restriction, respectively. Fig. 6.16 shows that all resistance ratio is below 1, including the joints out of the valid geometry range. Comparing S700 joints to S500 joints, the average $R_{EC3,i,non}/R_{u\&3\%}$ ratio decreases from 0.53 to 0.44, although the average elongation at failure of S700 material is 41% lower than S500. The reduced material ductility has a limited influence on the conservative level of CFF prediction. In the literature, CFF of HSS X-joints in tension was only observed in the RUOSTE project [16], where the resistance ratio varies between 0.36 and 0.38 for joints up to S700 without using C_f and the $0.8f_u$ restriction. Hence, among the tested specimens in this study and literature, the material factor C_f is unnecessary among the tested specimens with CFF.

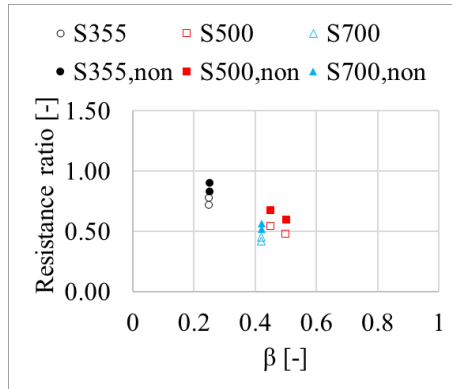


Fig. 6.16 Resistance ratio against β for CFF.

Besides, XS500A/B1 shows that the prediction is slightly more conservative with the increase of the β value, and XS700A/B1 shows that the prediction is less conservative with the rise of the material yield strength. These two observations align with the conclusion in [23,24]. With the increase of the steel grade, the elastic strain at yielding, f_y/E , increases. For example, the elastic strains at yielding of nominal S700 and S500 are 0.0035 and 0.0025, respectively, considering a 200GPa Young's Modulus. For a joint with a small β , the chord face bending dominates the deformation. Assuming the plane section remains plane at the plastic hinge, with the same 3% b_0 deformation, S700 and S500 plastic hinges are expected to have the same linear strain distribution through the thickness. Since S700 has a larger elastic strain at yielding, the material central layer remaining in the elastic stage is thicker, and the portion of the elastic strain over the total strain in the outer (yielding) layer is higher, compared to S500. Hence, the higher the steel grade is, the less the plastic deformation and the material strain hardening are. In addition, material strain hardening generally reduces with the rise of the steel grade. Therefore, with less material hardening at the same deformation, the resistance prediction is less conservation for joints made of HSS and UHSS than mild steel. It might seem strange that the resistance ratio of S700 is lower than for S500, which seems against the trend explained above. This is due to the stronger material hardening behaviour of S700 than S500, as the average strength ratio (f_u/f_y) of S500 and S700 is 1.07 and 1.12, respectively.

8 joints failed with BF. $R_{EC3,i}/R_{u\&3\%}$ of S355 and S500 joints vary in a small range (0.64–0.77), with 0.75 and 0.67 on average, respectively, as shown in Fig. 6.17. Without applying C_f , the varying range of the resistance ratio increases to 0.74–0.86 for S355 and S500 joints. And the range further increases to 0.85–1.02, if C_f and the $0.8f_u$ restriction are not applied. However, the $R_{EC3,i}/R_{u\&3\%}$ of S700 joints varies between 0.98 to 1.01. The average ratio is 1.37 if C_f and the $0.8f_u$ restriction are not applied. The reason for the prediction difference among different steel grades is that a more severe HAZ strength reduction was found in S700 material than in S500 and S355 material, as illustrated in Chapter 4. Hence, the HAZ strength has a significant influence on the BF resistance. As the weld type could influence the shape of HAZ, consequently the resistance of BF, only

the butt-welded X-joints in literature are included in this discussion. The resistance of four butt-welded X-joints made of C450 [18], S420 and S460 [17] with BF are safely predicted without using C_f . The resistance ratio varies between 0.73 and 0.88, which shows good agreement with the current experimental study. Therefore, among the tested specimens in this study and literature, C_f is not necessary for BF joints with steel grades up to S500, while the $0.8f_u$ restriction is needed for all steel grades.

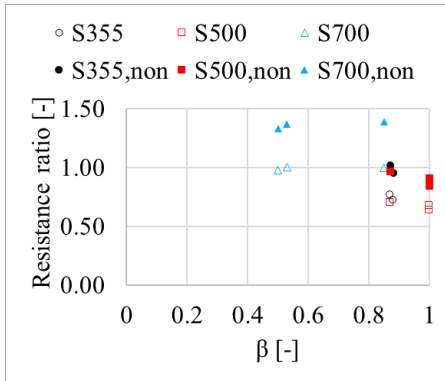


Fig. 6.17 Resistance ratio against β for BF.

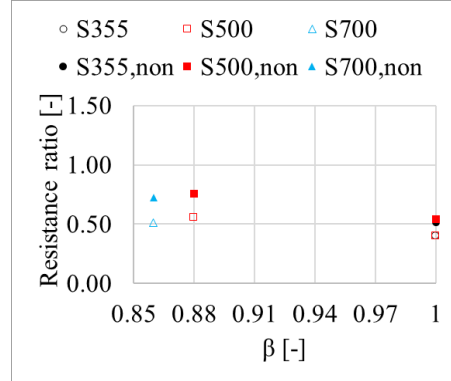


Fig. 6.18 Resistance ratio against β for PSF.

The PSF resistance is substantially underestimated, especially for joints with $\beta = 1$, by design rules considering C_f and the $0.8f_u$ restriction, as $R_{EC3,i}/R_{u\&3\%}$ is generally below 0.57 among all steel grades, see Fig. 6.18. Relaxing C_f and the $0.8f_u$ restriction, the maximum resistance ratio increases to 0.75, which is still relatively low. Only one butt-welded X-joint with PSF is found in the literature [18]. The X-joint is made of C450 and the resistance ratio is 0.87 (without considering C_f and the $0.8f_u$ restriction). Hence, among the tested specimens in this study and literature, C_f and the $0.8f_u$ restriction could be relaxed for PSF for steel grades up to S700.

XS355A3 is the only specimen with CSWF, which has a 0.72 $R_{EC3,i}/R_{u\&3\%}$. C_f and the $0.8f_u$ restriction are not relevant for this failure mode.

To conclude, among the tested specimens in this paper and in the literature, the material factor C_f is not necessary for X-joints with a butt weld except for BF with S700 material. The $0.8f_u$ strength restriction can be relaxed for PSF but not for BF for butt-welded X-joints with steel grades up to S700. Although the prediction on PSF and CFF is conservative in general, it has to be emphasized that the weld type (butt weld or fillet weld) and the weld thickness have a significant influence on the joint resistance and stiffness, as illustrated in [27]. The tested specimen presented in this paper has the extra fillet weld due to the cap pass which may increase the ultimate resistance and stiffness of the joint. Hence, a further study should be carried out to investigate the effect of the weld type and the cap pass on the joint behaviour. Besides, BF and PSF highly depend on the HAZ strength. Since the HAZ strength reduction depends on the base material type and the welding parameters, it is essential to consider the HAZ strength reduction in the BF and PSF design.

6.4. Conclusions

The 18 tests on RHS X-joints in tension presented in this study, and a review of published results within the same area, provide additional insight into the requirement for the material factor C_f and the $0.8f_u$ restriction. The experiments of this study cover the steel grades S355J2H, S500MH, and S700MLH. The most relevant geometric parameters, β (the width ratio) and the member thickness, were varied in a wide range of values. For example, the β ratio had values between (and including) 0.25 and 1.0 such that all relevant failure modes could be obtained. The nominal chord and brace wall thickness ranged between 4 mm and 10 mm, which covers many practical design situations. In all specimens, the braces were connected to the chord by butt welds. The potential of quantified improvements of the joint resistance using fillet welds, rather common in practice and in the most of literature, is left out of the scope. The role of welding specifications (heat input, cooling time, etc.) should be explored further, especially for newer sorts of S500 and S700. The following key observations are highlighted:

- 1) The latest version of prEN 1993-1-8 predicts a conservative tensile resistance ($R_{EC3,non}$), for steel grade up to S700, even without applying C_f and the $0.8f_u$ restriction. This conclusion also holds for the X-joints tested in tension found in the literature, regardless of the weld type (butt weld or fillet weld). Comparing $R_{EC3,non}$ to $R_{u\&3\%}$ (the lower of the ultimate resistance (R_u) and the load at 3% b_0 deformation), the maximum $R_{EC3,non}/R_{u\&3\%}$ is 0.8, excluding two S355 joints ($\beta = 0.25$, out of validated geometry range $0.1+0.01b_0/t_0 = 0.35$) which have a maximum of $0.91 R_{EC3,non}/R_{u\&3\%}$.
- 2) Except for joints with chord face failure (CFF), prEN 1993-1-8 (2022) does not in general accurately predict the governing failure mode of the specimens presented in this paper and in the literature. The scope of the resistance expressions for the various failure modes should be explored further. For example, prEN 1993-1-8 predicts CFF in cases where it was not observed in the tests, especially for S700.
- 3) A modified bi-linear model is proposed to characterise the joint nonlinear behaviour and the yield resistance (R_y). The yield ratio R_y/R_u varies between 0.47 and 0.88. For S355/S500 joints with $\beta < 0.5$, the ratio is around 0.5. For S355/S500 joints with $\beta \geq 0.5$ and S700 joints, the ratio is close to 0.7-0.8. The better the joint ductility is, the higher the yield ratio is.
- 4) Regarding the predicted resistance corresponding to the experimental failure mode, it is found that C_f factor is not necessary except for the brace failure (BF) with S700 material. The $0.8f_u$ restriction could be relaxed for PSF but not for BF concerning steel grades up to S700. This conclusion holds for X-joints with a butt weld in this study and in the literature.
- 5) The material elongation at failure ε_f has a limited influence on the CFF resistance, but the material hardening behaviour does influence the CFF resistance. The material strength reduction in the heat-affected zone significantly affects the BF resistance.

The above observations and the results of the experiments lead to the following recommendations for updating the design rules for welded X-joints under tension loading in the braces:

- 1) The experimental results imply that the upper bound of β for CFF decreases with increasing steel grade, and the upper bound of β for punching shear failure (PSF) might not be necessary, regardless of the weld type (butt weld or fillet weld).
- 2) C_f and the $0.8f_u$ restriction are not necessary based on the current design rules, regardless of the mispredicted failure modes and the weld type.
- 3) For X-joints with a butt weld, if the failure mode is well predicted, C_f can be set to 1.0 for all failure modes for steel grades up to S700, except for BF for S700.
- 4) For X-joints with a butt weld, if the failure mode is well predicted, the $0.8f_u$ restriction can be neglected for all steel grades up to S700, except for BF for all steel grades.
- 5) As the heat-affected zone (HAZ) governs BF, a strength reduction factor for HAZ, especially for HSS and ultra-HSS, should be included in the formula of BF. Then, neither C_f nor the $0.8f_u$ restriction may be necessary for BF, regardless of the steel grade.

These recommendations are based on two experimental campaigns (18 experiments) and all available data in literature, and certainly more evidence obtained on modern steel types and welding technologies is needed to improve the competitiveness of welded joints in design standards.

Reference

- [1] EN 1993-1-8:2005 - Design of steel structures - Part 1-8: Design of joints, (2005).
- [2] Molybdenum in Architecture, Building and Construction, Friends Arena, Stockholm, (2013).
imoa.info/download_files/sustainability/IMOA_FriendsArena_12.pdf.
- [3] EN 1993-1-12:2007 - design of steel structures - part 1–12: additional rules for the extension of EN 1993 up to steel grades S700, (2007).
- [4] prEN 1993-1-8:2021 - Design of steel structures - Part 1-8: Design of joints (draft of EN1993-1-8: 2021), (2022).
- [5] Y. Kurobane, New developments and practices in tubular joint design, in: IIW Doc. XV-488-81 and IIW Doc. XIII-1004-81, 1981.
- [6] D.K. Liu, J. Wardenier, Effect of the yield strength on the static strength of uniplanar K-joints in RHS (steel grades S460, S355 and S235), in: IIW Doc. XV-E-04-293, 2004.
- [7] F. Mang, Untersuchungen an Verbindungen von geschlossenen und offenen Profilen aus hochfesten Stählen, Abschlussbericht AIF. (1978).
- [8] C. Noordhoek, A. Verheul, R.J. Foeken, H.M. Bolt, P.J. Wicks, Static strength of high strength steel tubular joints, CIDECT Rep. 5BD-9/98. (1998).
- [9] R. Stroetmann, T. Kästner, A. Hälsig, P. Mayr, Influence of the cooling time on the mechanical properties of welded HSS-joints, Steel Construction. 11 (2018) 264–271. <https://doi.org/10.1002/stco.201800019>.
- [10] M. Amraei, A. Ahola, S. Afkhami, T. Björk, A. Heidarpour, X.L. Zhao, Effects of heat input on the mechanical properties of butt-welded high and ultra-high strength steels, Engineering Structures. 198 (2019). <https://doi.org/10.1016/j.engstruct.2019.109460>.
- [11] J. Wang, S. Afshan, N. Schillo, M. Theofanous, M. Feldmann, L. Gardner, Material properties and compressive local buckling response of high strength steel square and rectangular hollow sections, Engineering Structures. 130 (2017) 297–315. <https://doi.org/10.1016/j.engstruct.2016.10.023>.
- [12] F. Javidan, A. Heidarpour, X.L. Zhao, C.R. Hutchinson, J. Minkkinen, Effect of weld on the mechanical properties of high strength and ultra-high strength steel tubes in fabricated hybrid sections, Engineering Structures. 118 (2016) 16–27. <https://doi.org/10.1016/j.engstruct.2016.03.046>.
- [13] prEN 1993-1-12:2021 - Design of steel structures - Part 1-12: Additional rules for steel grades up to S960, (2021).
- [14] T. Björk, H. Saastamoinen, Capacity of CFRHS X-joints made of double-grade S420 steel, Tubular Structures XIV - Proceedings of the 14th International Symposium on Tubular Structures, ISTS 2012. (2012) 167–176. <https://doi.org/10.1201/b13139-26>.
- [15] T. Wilkinson, A. Syam, Connections in higher strength coldformed rectangular

- hollow sections, CIDECT Report 5BV-1/14, 2014.
- [16] M. Feldmann, N. Schillo, S. Schaffrath, K. Viridi, T. Björk, N. Tuominen, M. Veljkovic, M. Pavlovic, P. Manoleas, M. Heinisuo, K. Mela, Rules on high strength steel, 2016. <https://doi.org/https://op.europa.eu/en/publication-detail/-/publication/515285b0-c820-11e6-a6db-01aa75ed71a1/language-en/format-PDF/source-194823584>.
- [17] N. Tuominen, T. Björk, Capacity of RHS-joints made of high strength steels, CIDECT Report 5BZ, Final report, 2017.
- [18] J. Becque, T. Wilkinson, The capacity of grade C450 cold-formed rectangular hollow section T and X connections: An experimental investigation, *Journal of Constructional Steel Research*. 133 (2017) 345–359. <https://doi.org/10.1016/j.jcsr.2017.02.032>.
- [19] J. Packer, J. Wardenier, X. Zhao, G. Van der veget, Y. Kurobane, Design guide for rectangular hollow section (RHS) joints under predominantly static loading (2nd ed), 2009.
- [20] M. Pandey, B. Young, Compression capacities of cold-formed high strength steel tubular T-joints, *Journal of Constructional Steel Research*. 162 (2019) 105650. <https://doi.org/10.1016/j.jcsr.2019.05.040>.
- [21] J.-H. Kim, C.-H. Lee, S.-H. Kim, K.-H. Han, Experimental and Analytical Study of High-Strength Steel RHS X-Joints under Axial Compression, *Journal of Structural Engineering*. 145 (2019) 04019148. [https://doi.org/10.1061/\(asce\)st.1943-541x.0002435](https://doi.org/10.1061/(asce)st.1943-541x.0002435).
- [22] M. Pandey, B. Young, Structural performance of cold-formed high strength steel tubular X-Joints under brace axial compression, *Engineering Structures*. 208 (2020) 109768. <https://doi.org/10.1016/j.engstruct.2019.109768>.
- [23] X. Lan, T.M. Chan, B. Young, Structural behaviour and design of high strength steel RHS X-joints, *Engineering Structures*. 200 (2019) 109494. <https://doi.org/10.1016/j.engstruct.2019.109494>.
- [24] X. Lan, T.M. Chan, B. Young, Testing, finite element analysis and design of high strength steel RHS T-joints, *Engineering Structures*. 227 (2021) 111184. <https://doi.org/10.1016/j.engstruct.2020.111184>.
- [25] C.-H. Lee, S.-H. Kim, D.-H. Chung, D.-K. Kim, J.-W. Kim, Experimental and Numerical Study of Cold-Formed High-Strength Steel CHS X-Joints, *Journal of Structural Engineering*. 143 (2017) 04017077. [https://doi.org/10.1061/\(asce\)st.1943-541x.0001806](https://doi.org/10.1061/(asce)st.1943-541x.0001806).
- [26] C.-H. Lee, S.-H. Kim, Structural performance of CHS X-joints fabricated from high-strength steel, (2018). <https://doi.org/10.1002/stco.201800021>.
- [27] J. Havula, M. Garifullin, M. Heinisuo, K. Mela, S. Pajunen, Moment-rotation behavior of welded tubular high strength steel T joint, *Engineering Structures*. 172 (2018) 523–537. <https://doi.org/10.1016/j.engstruct.2018.06.029>.
- [28] J. Wardenier, X. Lan, J.A. Packer, Re-analysis of full-width RHS T- and X-joints under brace axial tension and brace in-plane bending, 2021.

-
- [29] R. Stroetmann, T. Kästner, B. Rust, J. Schmidt, Welded connections at high-strength steel hollow section joints, *Steel Construction*. 15 (2022) 10–21. <https://doi.org/10.1002/stco.202100036>.
- [30] R. Stroetmann, J. Hensel, U. Kuhlmann, T. Ummenhofer, I. Engelhardt, T. Kästner, B. Rust, M. Neumann, W. Knecht, A. Münch, J. Schmidt, A. Hälsig, P. Weidner, J. Weinert, V. Larasser, Ausführung und Fertigung von geschweißten, hochfesten Hohlprofilknoten, *Stahlbau*. 91 (2022) 647–659. <https://doi.org/10.1002/stab.202200053>.
- [31] Metallic materials - Tensile testing - Part 1: Method of test at room temperature (ISO 6892-1:2019), 1 (2019).
- [32] EN 1993-1-1:2005 - Design of steel structures - Part 1-1: General rules and rules for buildings, (2005).
- [33] P. Zanon, R. Zandonini, Experimental analysis of end plate connections, in: *Proceedings of the State of the Art Workshop on Connections and the Behaviour of Strength and Design of Steel Structures*, Cachan, 1988: pp. 41–51.

Appendix

Appendix 6.A Nominal dimension of X-joints and position of coupon specimens.

Specimen	Steel grade	b_0 [mm]	h_0 [mm]	t_0 [mm]	d_0 [mm]	b_1 [mm]	h_1 [mm]	t_1 [mm]	d_1 [mm]
XS355A1		200	100	8	20	50	100	5	20
XS355A2	S355	160	160	10	25	140	140	8	25
XS355A3		150	150	6	20	150	150	6	20
XS500A1		200	100	8	25	90	160	8	25
XS500A2	S500	160	160	10	25	140	140	8	25
XS500A3		150	150	6	20	150	150	6	20
XS700A1		120	120	8	20	51	152	6	25
XS700A2	S700	160	160	10	25	80	100	4	20
XS700A3		140	140	6	25	120	80	6	25
XS355B1		200	100	8	25	50	100	5	20
XS355B2	S355	160	160	10	25	140	140	8	25
XS355B3		150	150	6	25	150	150	6	25
XS500B1		180	80	8	25	90	160	8	25
XS500B2	S500	160	160	10	25	140	140	8	25
XS500B3		150	150	6	25	150	150	6	25
XS700B1		120	120	8	20	51	152	6	25
XS700B2	S700	150	200	10	25	80	100	4	20
XS700B3		140	180	5	25	120	80	6	25

Appendix 6.B Measured dimensions of coupon specimens.

Specimen	NO.	Chord [mm]		Brace [mm]		Specimen	NO.	Chord [mm]		Brace [mm]	
		t	b	t	b			t	b	t	b
XS355A1	N1	7.9	10.0	4.9	16.0	XS355B1	N1	7.9	10.2	5.1	16.2
	N2	7.8	10.0	4.9	16.0		N2	8.0	10.2	5.1	16.2
XS355A2	N1	9.8	7.8	8.1	10.0	XS355B2	N1	9.9	8.3	8.0	20.3
	N2	9.8	7.9	8.1	10.0		N2	9.9	8.1	8.1	20.2
XS355A3	N1	6.0	13.0	6.0	13.0	XS355B3	N1	5.9	20.3	6.0	20.2
	N2	5.9	12.9	5.9	12.9		N2	6.0	20.2	-	-
XS500A1	N1	7.9	10.2	7.9	10.1	XS500B1	N1	7.9	10.2	7.8	13.3
	N2	7.8	10.1	7.9	10.0		N2	7.8	10.1	7.9	13.2
XS500A2	N1	9.8	7.8	7.9	10.1	XS500B2	N1	9.8	8.3	7.9	20.3
	N2	9.7	7.9	7.9	10.0		N2	9.9	8.1	7.9	20.2
XS500A3	N1	5.9	13.0	5.9	13.0	XS500B3	N1	6.0	20.2	6.0	20.2

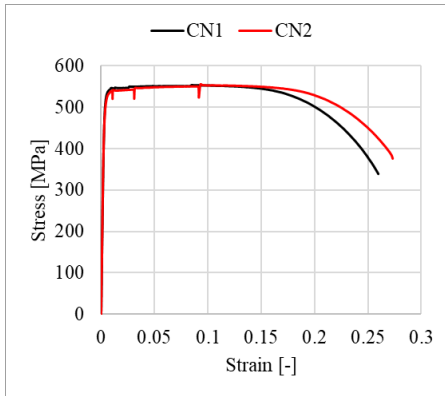
	N2	5.9	13.0	5.9	13.0		N2	6.0	20.3	5.9	12.6
XS700A1	N1	7.9	10.3	5.8	13.3	XS700B1	N1	7.9	10.2	6.3	10.2
	N2	7.8	10.1	5.8	13.3		N2	8.0	10.1	6.4	10.2
XS700A2	N1	9.9	10.4	4.0	20.3	XS700B2	N1	9.4	8.4	4.0	20.3
	N2	9.8	8.3	4.0	20.2		N2	9.4	8.2	4.0	20.2
XS700A3	N1	5.8	13.3	5.8	13.3	XS700B3	N1	5.2	15.9	6.0	13.2
	N2	5.8	13.3	5.8	13.3		N2	5.2	16.4	5.9	13.2

Appendix 6.C Coupon test results.

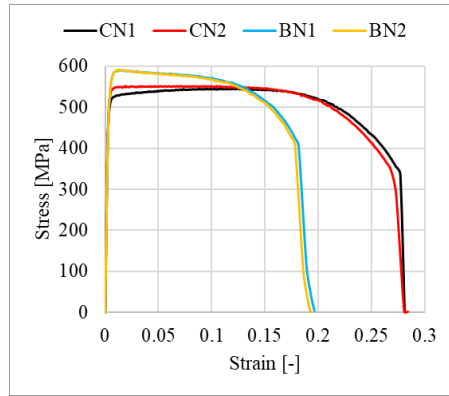
Specimen	NO.	Chord				Brace			
		f_y [MPa]	f_u [MPa]	ϵ_u [%]	ϵ_f [%]	f_y [MPa]	f_u [MPa]	ϵ_u [%]	ϵ_f [%]
XS355A1	N1	528	552	7.0	26.0	510	539	8.8	23.3
	N2	516	553	10.5	27.3	499	546	5.0	25.3
XS355A2	N1	477	515	9.5	27.2	504	535	8.1	26.9
	N2	495	516	10.3	30.6	508	528	8.1	26.6
XS355A3	N1	461	510	12.5	28.2	461	510	12.5	28.2
	N2	442	509	13.4	29.3	442	509	13.4	29.3
XS500A1	N1	571	603	1.6	22.3	575	609	5.2	24.8
	N2	544	590	5.2	24.6	585	614	1.9	24.9
XS500A2	N1	600	631	1.3	20.3	575	609	5.2	24.8
	N2	578	617	2.6	20.5	585	614	1.9	24.9
XS500A3	N1	612	671	6.9	22.9	612	671	6.9	22.9
	N2	605	668	8.4	24.1	605	668	8.4	24.1
XS700A1	N1	734	853	2.7	12.8	781	858	3.6	12.0
	N2	768	839	1.8	12.5	779	864	3.1	13.1
XS700A2	N1	710	836	2.9	17.3	740	850	3.5	10.1
	N2	742	826	1.9	12.5	741	846	3.3	10.4
XS700A3	N1	781	858	3.6	12.0	781	858	3.6	12.0
	N2	779	864	3.1	13.1	779	864	3.1	13.1
XS355B1	N1	506	545	11.9	27.7	551	590	1.5	18.2
	N2	532	552	10.5	26.8	541	590	1.3	17.8
XS355B2	N1	501	535	1.3	26.7	524	547	1.6	29.7
	N2	496	528	7.8	27.9	535	547	1.8	27.3
XS355B3	N1	471	520	13.6	29.3	487	524	11.3	29.2
	N2	493	526	12.2	29.0	-	-	-	-
XS500B1	N1	593	629	1.7	19.5	541	574	1.9	23.8
	N2	603	639	1.7	19.5	558	593	1.2	18.7

XS500B2	N1	574	610	1.7	19.7	609	648	1.4	19.8
	N2	572	623	1.3	19.8	624	648	1.2	18.7
XS500B3	N1	595	644	7.5	22.8	598	643	6.9	23.2
	N2	580	638	9.0	24.3	610	657	6.0	21.2
XS700B1	N1	773	855	2.4	14.4	791	864	2.9	12.5
	N2	792	867	2.0	13.5	792	869	2.7	12.7
XS700B2	N1	745	808	3.1	17.5	740	850	3.5	10.1
	N2	741	808	3.1	16.8	741	846	3.3	10.4
XS700B3	N1	720	823	4.9	13.5	777	860	2.2	12.1
	N2	724	827	4.7	15.6	791	867	2.2	12.7

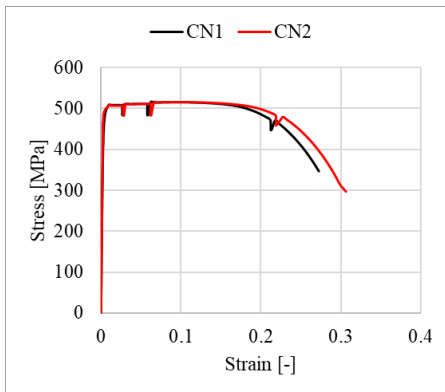
Appendix 6.D Stress-strain relationships of tested coupon specimens.



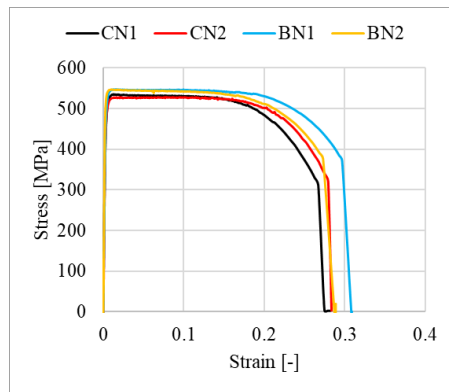
a) XS355A1.



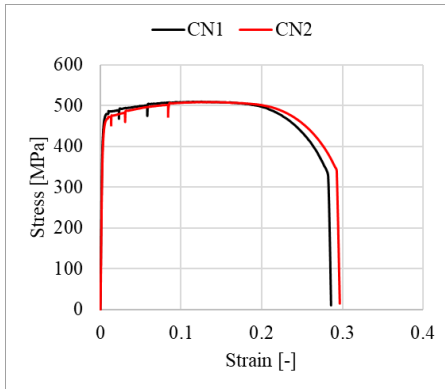
b) XS355B1.



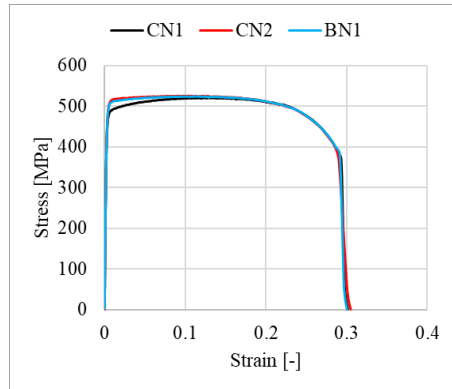
c) XS355A2.



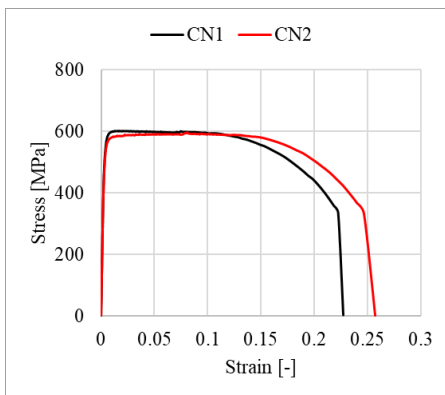
d) XS355B2.



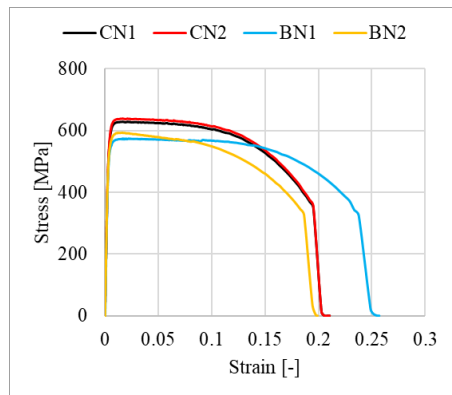
e) XS355A3.



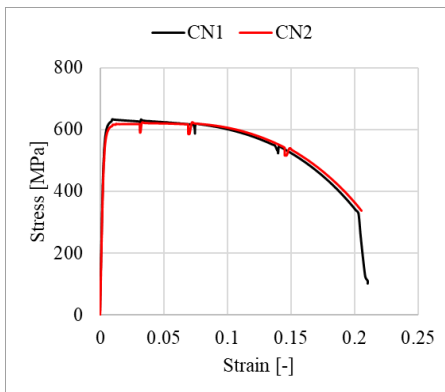
f) XS355B3.



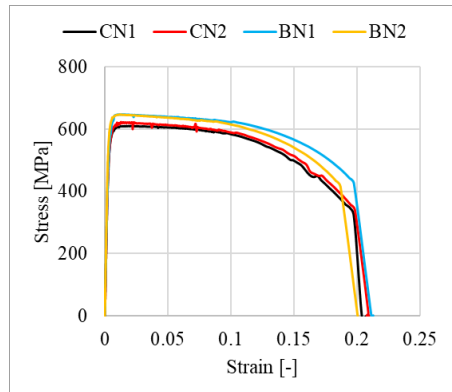
g) XS500A1.



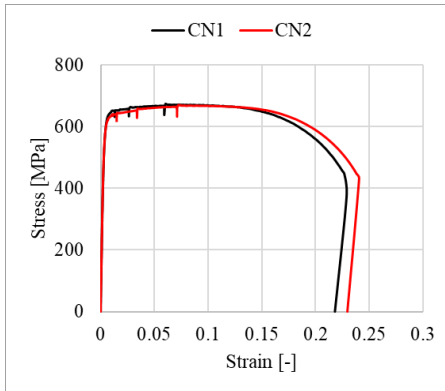
h) XS500B1.



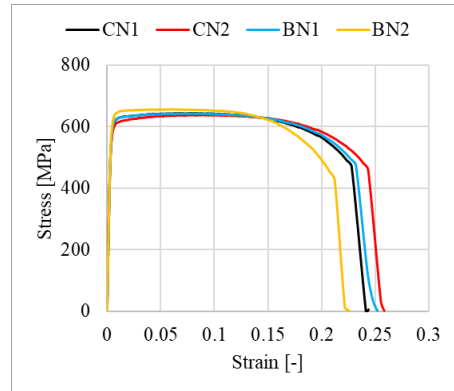
i) XS500A2.



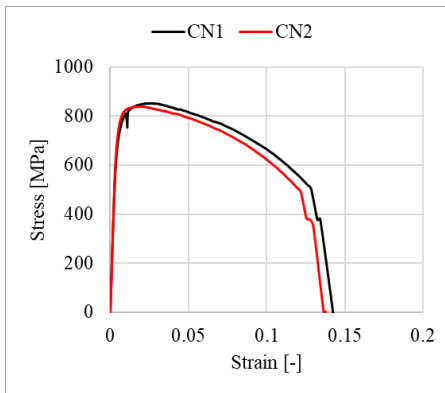
j) XS500B2.



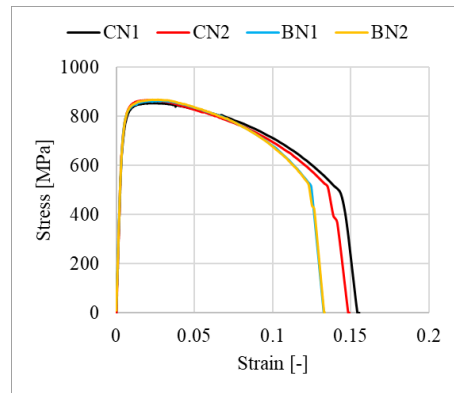
k) XS500A3.



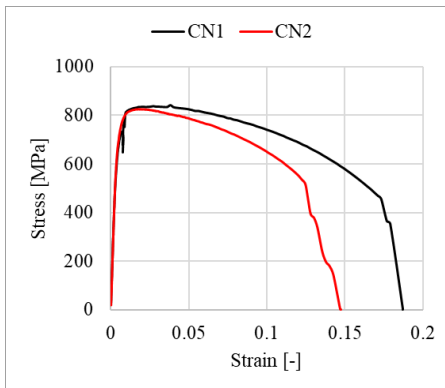
l) XS500B3.



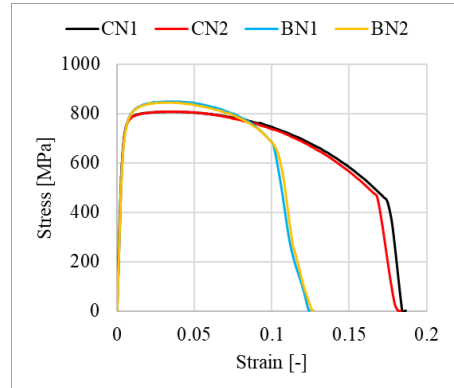
m) XS700A1.



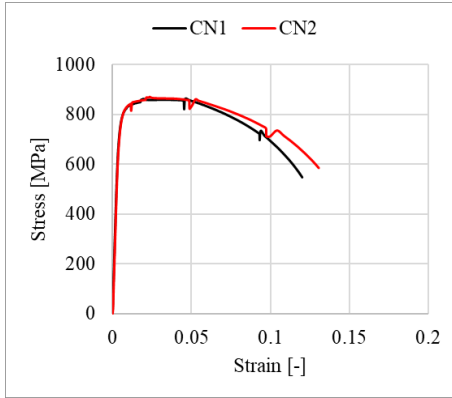
n) XS700B1.



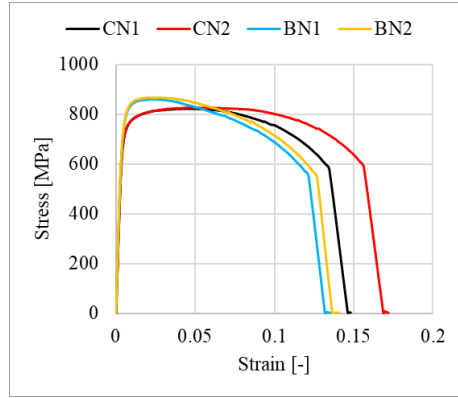
o) XS700A2.



p) XS700B2.



q) XS700A3.



r) XS700B3.

Appendix 6.E Design equations in prEN 1993-1-8 for X-joints in tension.

Failure mode	Equations
CFF $\beta \leq 0.85$	$N_{1,Rd} = C_f \frac{f_{y0} t_0^2}{\sin \theta_1} \left(\frac{2\eta}{(1-\beta) \sin \theta_1} + \frac{4}{\sqrt{1-\beta}} \right) \frac{Q_f}{\gamma_{M5}}$
CSWF $\beta = 1.0$	$N_{1,Rd} = \frac{f_b t_0}{\sin \theta_1} \left(\frac{2h_1}{\sin \theta_1} + 10t_0 \right) \frac{Q_f}{\gamma_{M5}}$
BF	$N_{1,Rd} = C_f f_{y1} t_1 (2h_1 - 4t_1 + 2b_{eff}) \frac{1}{\gamma_{M5}}$ $b_{eff} = \min \left(\frac{10t_0}{b_0} \frac{f_{y0} t_0}{f_{y1} t_1} b_1, b_1 \right)$
PSF $b_i \leq b_0 - 2t_0$	$N_{1,Rd} = C_f \frac{f_{y0} t_0}{\sqrt{3} \sin \theta_1} \left(\frac{2h_1}{\sin \theta_1} + 2b_{e,p} \right) \frac{1}{\gamma_{M5}}$ $b_{e,p} = \min \left(\frac{10t_0}{b_0} b_1, b_1 \right)$

where θ_1 is the angle between the brace and the chord ($\theta_1 = 90^\circ$ for the tested specimens), Q_f is the chord stress factor ($Q_f = 1$ for the tested specimens). For $0.85 < \beta < 1.0$ linear interpolation may be applied between the governing resistances as $\beta = 0.85$ (CFF, BF, and PSF) and $\beta = 1$ (CSWF and BF).

7.

Fracture simulation of welded rectangular hollow section X-joints using Gurson-Tvergaard-Needleman (GTN) damage model

A welded rectangular hollow section (RHS) X-joint exposed to tension loading has three typical fracture-related failure modes: Punching shear failure, Brace failure, and Chord side wall failure. Implementing an appropriate damage model accurately predicts the behaviour of the fracture zone and provides the necessary information to improve design rules for welded high-strength steel (HSS) rectangular hollow section (RHS) X-joints based on parametric studies using validated model.

In this chapter, the Gurson-Tvergaard-Needleman (GTN) damage models calibrated for the base material and the heat-affected zone of welded cold-formed RHS connections are used in the fracture simulation of nine welded cold-formed RHS X-joints in monotonic tension. The finite element model successfully predicts the experimental load-displacement relationships and fractured zones, indicating the calibrated GTN models could effectively be used in parametric study of welded cold-formed RHS X-joints. Then, the importance of including HAZ in the FE model is illustrated by conducting the FE analysis without using HAZ constitutive model. Finally, the semi-empirical HAZ constitutive model is extended to a semi-empirical material damage model, which is further used in the simulation of all 18 X-joints.

Parts of this chapter appear in the journal article: ‘Rui Yan et al., Fracture simulation of welded RHS X-joints using GTN damage model, *Advances in Structural Engineering*, 2022’. Minor modifications have been made to suit the thesis. Credit is also given to the master thesis: ‘Hagar El Bamby, Experimental and numerical investigations on the structural performance of mild and high strength welded X-joints’.

7.1. Introduction

Welded hollow section joints may fail with a fracture in the heat-affected zone (HAZ) or in the base material (BM). It is essential to conduct an advanced numerical study considering both the stress-strain relationship of HAZ and the material damage model. Such advanced numerical models enable a better understanding of the various failure mechanisms and provide confidence in numerically generated data to improve the design rules of welded hollow section joints.

Different damage models have been implemented in the fracture simulation of welded joints in recent years [1–5]. Ma et al. [1] extended a damage-mechanics-based model to predict PSF in hollow section joints, considering the effect of the stress triaxiality and the Lode angle. It was argued that the fracture strain at the fracture initiation point of the joint would be overestimated under a shear-dominated stress state if the effect of the Lode angle was not considered in the damage model. However, the paper did not present the global load-deformation relationship from the model without considering the Lode angle. The effect of the high fracture strain in a limited number of elements on the joint global behaviour is vague. Liu et al. [2] proposed a shear-modified Gurson-Tvergaard-Needleman (GTN) model [6] to simulate the fracture propagation of the X-joint PSF. The shear-modified GTN model was first calibrated against traditional tensile specimens, notched specimens, and shear specimens for the base material (BM) of the hollow sections and the weld metal (WM). The calibrated shear-modified GTN model was subsequently implemented in the X-joint fracture simulation. It was found that the original GTN model without considering the material shear damage could properly predict the crack initiation point (the ultimate resistance) but failed to predict the fracture propagation under a shear-dominated stress state. The shear-modified GTN model showed a better performance in predicting the fracture process after the peak load compared to the original GTN model. The accurate prediction of the ultimate state considering the Lode angle is necessary at a low triaxiality in the fracture zone, but the Lode angle has limited influence on the fracture plastic strain at a high stress triaxiality and can be neglected [1,7–9].

Although many numerical studies have been carried out on welded hollow section joints, the mechanical and geometric properties of the heat-affected zone (HAZ) are rarely considered in the FE analysis, which may lead to an unsafe prediction of the joint resistance, especially for HSS joints. Lan et al. [10] conducted experimental and numerical studies on the welded HSS RHS X-joints in compression. HAZ was modelled based on some simplified mechanical and geometric assumptions. It was concluded that the strength degradation of the HAZ significantly influenced the joint resistance.

The mechanical properties of HAZ have been reported by many researchers [11–16]. Chapter 4 shows a 13% yield and 4% ultimate strength degradation in HAZ compared to BM in S355 and S500 butt-welded cold-formed RHS connections, while a larger strength reduction, 24% and 19% for the yield strength and the ultimate strength, respectively, were observed in S700 connections. A constitutive model correlating to BM mechanical properties was proposed for HAZ, which was established based on experimental and

numerical studies on the tensile behaviour of milled welded coupon specimens with a butt weld in the middle. The HAZ strength degradation in butt-welded connections was also examined in [16] using the Vickers hardness test. The strength of HAZ was predicted according to the empirical relationship between hardness results and material strength. The HAZ strength degradation varies in a very similar range with less than a 5% difference compared to the results presented in Chapter 4 concerning the material strength ratio and the complete welded connection strength ratio. Moreover, Cai et al. [16] investigated the effect of the BM processing method (TMCP or QT) on the HAZ mechanical properties, which is not considered in the current design rules and might lead to an unsafe design for HSS or ultra HSS welded hollow section joints. It is worth mentioning that the HAZ strength degradation is closely related to the welding technique and parameters used. The HAZ strength could be comparable to the BM if appropriate welding technique and parameters are employed, as demonstrated in [11].

In this chapter, the fracture simulation of welded cold-formed RHS X-joints is conducted using the GTN damage model. First, the calibrated GTN damage model is implemented in the fracture simulation of the A-series X-joints. A good agreement is obtained between the experimental and FE results, indicating that the calibrated GTN model for HAZ and BM can effectively predict fracture failure in welded RHS X-joints. Then, the HAZ constitutive model is excluded from the X-joint FE model to demonstrate the importance of HAZ in the FE analysis. Finally, the semi-empirical constitutive model for HAZ, presented in Chapter 4, is extended to a semi-empirical material damage model, which is further used in the simulation of all 18 X-joints.

7.2. Finite element analysis

7.2.1. X-joint models

As the A-series X-joint and the butt-welded short tubes were fabricated by the same company using the same welding parameters, the calibrated GTN damage model for HAZ and BM, presented in Chapter 5, is employed to simulate the fracture failure of the tested A-series X-joints in Chapter 6. FE models are generated to verify the GTN damage model and the experiments. The models are built up with the measured geometric dimension, as shown in Fig. 7.1. Only a quarter of the joint is created to reduce the computational burden. Fig. 7.1 shows an example of the FE model for specimen XS500A2. Reference points (RP1 and RP2) are made at the centre of the entire RHS end surfaces (marked with yellow). Each reference point controls all translations and rotations of the corresponding end surface through the MPC beam constraint. The loading is applied as a positive displacement at RP1 in the Y direction. The remaining degrees of freedom at reference points are fixed. In addition, symmetry boundary conditions are applied on Surface 1 and Surface 2, see Fig. 7.1. The quasi-static analysis is conducted using the explicit solver with a 100 s period and a 0.0001 s target time increment.

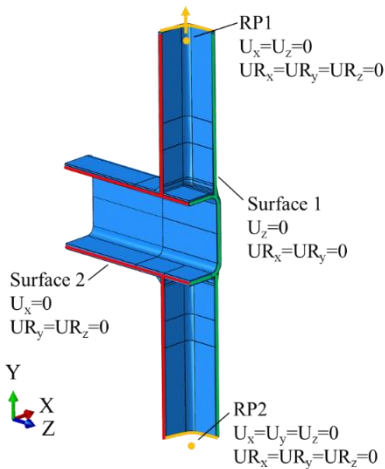


Fig. 7.1 Finite element model for X-joints.

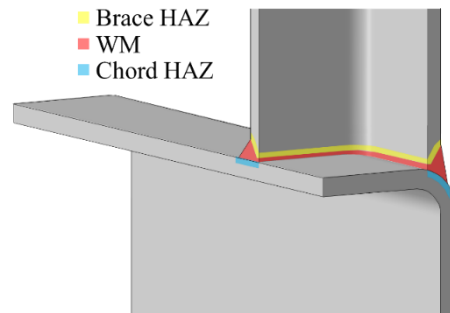


Fig. 7.2 HAZ and WM regions in a weld zone.

The weld zone consists of five material regions: Chord, Chord HAZ, WM, Brace, and Brace HAZ. Fig. 7.2 shows the HAZ and WM regions in the FE model. The HAZ width in the butt welded tubes, referring to Fig. 2.3, is measured based on the Vickers hardness tests. It was found that the majority (92%) of the HAZ width varies between 2 mm and 4 mm, with an average 3.2 mm width regardless of the steel grade and the thickness of the profile. Hence, a 3.2 mm HAZ width is used in all X-joint models. The HAZ region in the brace is oriented parallel to the bevelled surface, while the HAZ in the chord is oriented through the thickness of the cross-section.

The C3D8R element is used for modelling joints with $\beta < 0.8$, i.e. the joints XS355A1, XS500A1, XS700A1, and XS700A2 (see Table 6.2). A 0.5 mm mesh size is adopted for critical regions concerning HAZ, WM, and part of BM close to HAZ. The BM mesh size along the profile length direction gradually changes to 5 mm (100 mm far from the weld zone). Due to the complex geometry at the chord corner of joints with $\beta > 0.8$ (XS355A2, XS355A3, XS500A2, XS500A3, and XS700A3), it is not possible to mesh using the C3D8R element. The ten-node tetrahedral element C3D10 is employed. A universal 1 mm mesh size is used for HAZ, WM and part of BM close to HAZ. Note that the chord front face of XS355A3 also meshed with 1 mm elements as a chord side wall failure (CSWF) appeared in the experiment. Two examples of FE mesh using C3D8R and C3D10 elements are presented in Fig. 7.3 a) and b), respectively.

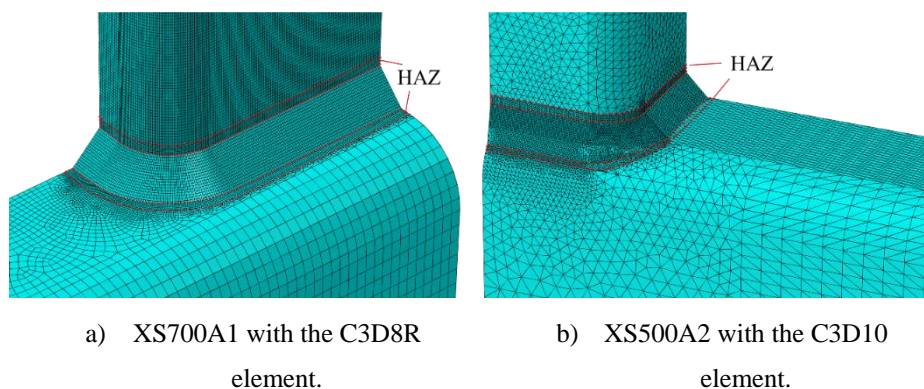


Fig. 7.3 Examples of mesh used in the FE models.

7.2.2. Calibrated material damage model

HAZ exists in both the brace and the chord of X-joints. The constitutive model of the HAZ that was developed for the butt-welded short tube is used for modelling the HAZ in the X-joint. The material model varies according to the thickness of the profile. The calibrated constitutive parameters for BM and HAZ are summarized in Table 5.7 and Table 5.8, respectively.

Table 7.1 Calibrated constitutive parameters for BM.

Material	W	k	n	ϵ_0	a	b	f_c	f_t	f_c^*	f_t^*
XS355A1B	0.9	836.2	0.1460	0.0095	598.2	549.9	0.0645	0.10	-	-
XS355A2B	0.9	772.7	0.1400	0.0068	563.3	511.8	0.0350	0.05	0.0350	0.05
XS355A3B	1.0	750.0	0.1400	0.0336	473.3	520.7	0.0350	0.05	0.0300	0.05
XS500A1B	0.8	738.1	0.0635	0.0150	508.1	595.8	0.1120	0.15	-	-
XS500A2B	0.6	696.0	0.0240	-0.0041	763.0	615.4	0.1290	0.15	0.0900	0.10
XS500A3B	0.7	851.4	0.0631	-0.0022	739.0	667.0	0.0760	0.10	0.0700	0.08
XS700A1B	0.1	942.9	0.0216	-0.0066	1237.4	834.6	0.0990	0.15	-	-
XS700A2B	0.1	919.0	0.0200	-0.0070	1293.2	816.7	0.0500	0.10	-	-
XS700A3B	0.1	997.2	0.0324	-0.0051	1052.0	853.4	0.0482	0.05	0.0706	0.08
S355t5B	0.8	801.5	0.1400	0.0151	557.4	539.4	0.0267	0.05	-	-
S355t8B	1.0	785.4	0.1400	0.0142	549.0	527.6	0.110	0.15	0.0600	0.08
S500t8B	0.9	757.1	0.0626	0.0196	493.2	616.6	0.123	0.15	0.0900	0.10

Table 7.2 Calibrated constitutive parameters for HAZ.

Material	k_0	Q	β_0	f_c	f_t	f_c^*	f_t^*
S355t5H	480.7	274.7	4.26	0.0116	0.05	-	-
S355t8H	481.0	285.1	4.03	0.0329	0.05	0.0186	0.05
S355t10H	459.5	191.6	13.89	0.0280	0.05	0.0550	0.10
S500t4H	552.0	191.6	8.33	0.0094	0.05	0.0250	0.05
S500t8H	363.3	336.7	17.25	0.0145	0.05	0.01447	0.05
S500t10H	578.6	207.2	8.68	0.0226	0.05	0.0150	0.05

S700t5H	627.7	355.7	5.28	0.0165	0.05	0.0470	0.05
S700t8H	598.6	205.0	10.47	0.0337	0.05	-	-
S700t10H	661.0	179.4	13.59	0.0177	0.05	-	-

The WM constitutive model is obtained from the milled welded coupon tests. The stress-strain relationship of WM extracted from DIC results is extrapolated using the Swift model. The same WM constitutive model is used for S500 and S700 joints, as the same electrode was used for welding. As coupon tests were not conducted for the brace, the material property of the brace refers to BM of the chord and the welded short tubes, according to the thickness. The employed materials for the X-joint simulation are summarized in Table 7.3, and the corresponding undamaged true stress-true plastic strain relationships are shown in Appendix 7.A. The 1 mm C3D10 element is used at the possible fracture regions (HAZ, WM, BM close to HAZ) for joints with $\beta > 0.85$. Since the fracture parameters are closely related to the element volume, the values of f_c and f_t are adjusted for coupon models with 1 mm C3D10 element following the calibration procedure presented in Section 5.4.2. The adjusted values are shown as f_c^* and f_t^* in Table 5.7 and Table 5.8.

Table 7.3 Employed material for A-series X-joint analysis.

X-joint	Chord		Brace		WM
	BM	HAZ	BM	HAZ	
XS355A1	XS355A1B	S355t8H	S355t5B	S355t5H	S355t8W
XS355A2	XS355A2B	S355t10H	S355t8B	S355t8H	S355t8W
XS355A3	XS355A3B	S355t8H	XS355A3B	S355t8H	S355t8W
XS500A1	XS500A1B	S500t8H	S500t8B	S500t8H	S700t8W
XS500A2	XS500A2B	S500t10H	S500t8B	S500t8H	S700t8W
XS500A3	XS500A3B	S500t4H	XS500A3	S500t4H	S700t8W
XS700A1	XS700A1B	S700t8H	XS700A3B	S700t5H	S700t8W
XS700A2	XS700A2B	S700t10H	XS700A3B	S700t5H	S700t8W
XS700A3	XS700A3B	S700t5H	XS700A3B	S700t5H	S700t8W

7.2.3. A semi-empirical material damage model

In Section 4.4, a semi-empirical material model for HAZ is proposed as a simplified approach for generating the HAZ stress-strain relationship (before necking), which is purely based on the mechanical property of BM. The generated stress-strain relationship is further used in the X-joint simulation and validated against all 18 X-joint tests. In order to extend the semi-empirical material model to a semi-empirical damage model, two issues related to the extrapolated stress-strain relationship after necking and the GTN parameters should be addressed.

It is found that the Voce model is suitable for generating the undamaged constitutive model for all HAZ, as demonstrated in Section 5.4.2. Hence, the generated semi-empirical model is extended, starting from the necking point, according to Eq. (5.15). Considering the continuity of the stress-strain relationship at the necking point, three conditions in Eq. (7.1) should be satisfied. The expressions for the Swift and Voce

models are presented in Eq. (4.4) and Eq. (5.15), respectively. Based on these three conditions, the three parameters in the Voce model can be determined for all HAZs, which are summarized in Table 7.4.

$$\begin{aligned} \sigma_{u,S} &= \sigma_{u,V} \\ \left. \frac{d\sigma_{t,S}}{d\varepsilon_{t,S}} \right|_{\varepsilon_{t,S}=\varepsilon_{t,u}} &= \left. \frac{d\sigma_{t,V}}{d\varepsilon_{t,V}} \right|_{\varepsilon_{t,S}=\varepsilon_{t,u}} \\ \left. \frac{d^2\sigma_{t,S}}{d\varepsilon_{t,S}^2} \right|_{\varepsilon_{t,S}=\varepsilon_{t,u}} &= \left. \frac{d^2\sigma_{t,V}}{d\varepsilon_{t,V}^2} \right|_{\varepsilon_{t,S}=\varepsilon_{t,u}} \end{aligned} \quad (7.1)$$

Table 7.4 Determined parameters for HAZ using the semi-empirical model.

BM	Element	Parameters for corresponding HAZ								
		f_y [MPa]	f_u [MPa]	ε_u [%]	k	n	ε_0	k_0	Q	β_0
XS355A1B	Chord	444	525	16.0	826	0.175	0.02700	486	271	4.08
XS355A2B	Chord	413	490	17.3	789	0.193	0.03332	452	282	3.56
XS355A3B	Chord	384	484	17.3	771	0.177	0.01761	439	262	4.24
XS500A1B	Chord	474	567	14.1	857	0.148	0.01604	525	245	5.21
XS500A2B	Chord	501	593	12.2	864	0.127	0.01125	553	218	6.33
XS500A3B	Chord	517	636	14.1	958	0.143	0.01101	585	271	5.57
XS700A1B	Chord	526	677	10.1	934	0.096	0.00003	629	196	9.37
XS700A2B	Chord	508	665	11.9	953	0.114	0.00161	611	230	7.65
XS700A3B	Chord	546	689	10.0	949	0.096	0.00057	641	198	9.34
S355t5B	-	429	515	14.6	787	0.153	0.01710	476	233	4.97
S355t8B	-	430	505	16.1	797	0.179	0.02997	468	265	3.93
S500t8B	-	493	581	14.9	897	0.161	0.02247	539	274	4.56
XS355B1B	Chord	441	521	16.4	826	0.181	0.02926	482	278	3.90
	Brace	464	561	10.8	789	0.108	0.00506	523	176	7.92
XS355B2B	Chord	424	505	16.4	799	0.179	0.02693	466	268	4.00
	Brace	450	520	17.1	840	0.201	0.04294	485	307	3.28
XS355B3B	Chord	410	497	17.5	799	0.188	0.02685	455	282	3.78
	Brace	414	498	17.5	802	0.191	0.02934	457	286	3.68
XS500B1B	Chord	508	602	11.7	868	0.120	0.00934	562	209	6.80
	Brace	467	554	12.8	817	0.133	0.01275	516	214	5.96
XS500B2B	Chord	487	586	11.9	845	0.120	0.00789	545	205	6.89
	Brace	524	616	11.6	885	0.119	0.01012	576	212	6.80
XS500B3B	Chord	499	609	14.1	919	0.145	0.01246	561	261	5.45
	Brace	513	618	13.3	919	0.137	0.01203	572	249	5.79

XS700B1B	Chord	548	689	11.2	974	0.108	0.00226	638	223	8.08
	Brace	554	693	10.1	957	0.097	0.00090	645	201	9.23
XS700B2B	Chord	520	646	13.7	965	0.137	0.00857	594	265	5.92
	Brace	518	678	8.2	894	0.077	0.00172	637	157	12.24
XS700B3B	Chord	505	660	11.6	941	0.111	0.00135	608	223	7.88
	Brace	549	691	9.9	950	0.095	0.00048	643	196	9.47

Regarding the GTN parameters, the calibrated yield surface parameters (A , B , q_2) for two HAZ materials are very close to each other, as shown in Table Table 5.6. Hence, the average values, 1.43, -0.0735, and 1.015, are used for A , B , and q_2 , respectively. Table 5.8 presents the calibrated values of the fracture-related parameters f_c and f_t for different types of elements. The majority of f_c is below 0.02 regardless of the element type, although two of them are close to 0.05. Therefore, as a conservative estimation of the parameters, 0.01 and 0.05 are adopted for f_c and f_t , respectively.

7.3. Results and discussions

7.3.1. Using the calibrated material model

The failure mode and the load-displacement relationship of X-joint FE models are compared to the experimental results in Fig. 7.4-Fig. 7.9. The predicted load-displacement relationships show a good agreement with the experimental results, although the resistance of FE results is slightly lower than the experiments at the plastic stage, which might be due to the pessimistic assumption of the constitutive model of the corner region in the cold-formed RHS. The material in the corner region has higher strength but lower ductility than the material in the flat region [17,18]. The absence of the corner material model may also result in a more significant deformation at the ultimate load since the stress concentration is relaxed at the corner region, where the low ductility may lead to a premature fracture. For a joint with a small β , the deformation is mainly due to the deflection of the chord surface, and the role of the corner in the overall behaviour of the joint is less pronounced. For a joint with a large β , the corner region acts more strongly in the load transfer, and the material at the corner undergoes more severe yielding that may lead to failure. Consequently, omitting the work-hardening of the corner region in the material model may have a stronger influence on the FE results for joints with larger β values. In addition, the FE model is only one-quarter of the specimen, and symmetric boundary conditions are applied. The deformation obtained from the FE model may be larger than the experiments, as the fracture appears only on the weaker side of most joints.

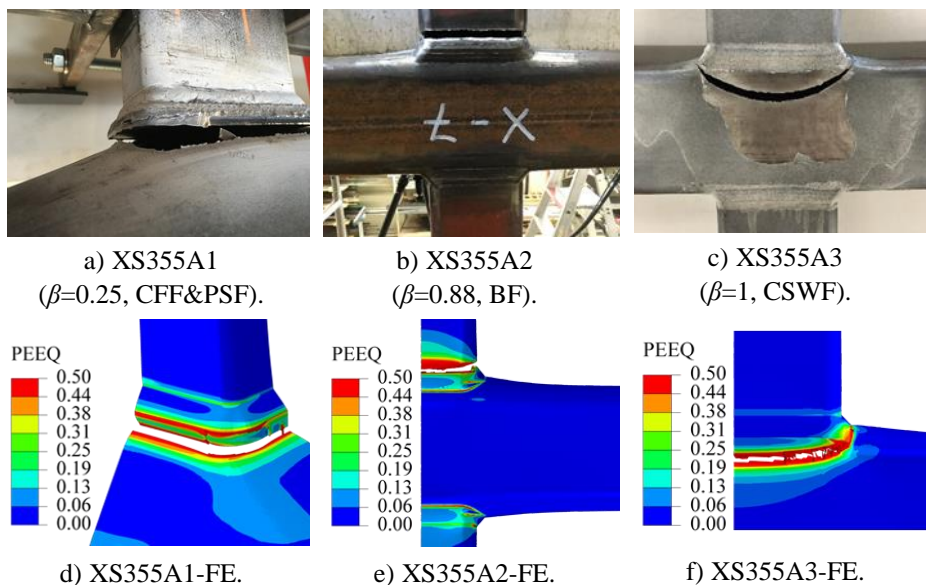


Fig. 7.4 Failure modes of S355 X-joints.

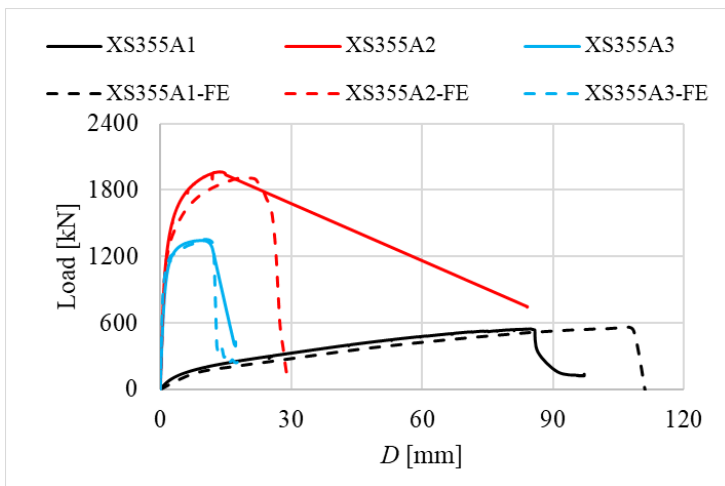
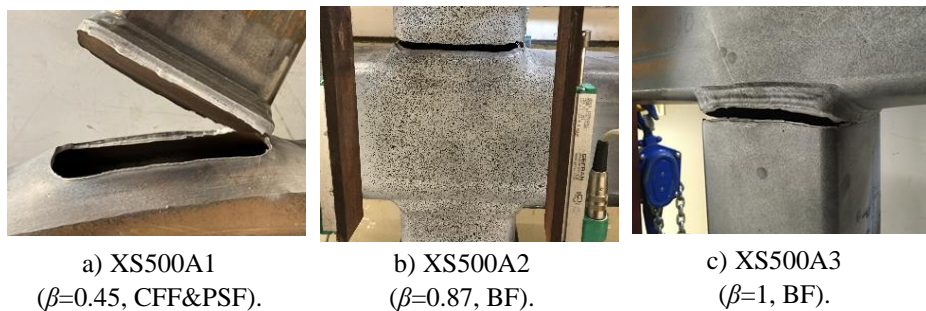


Fig. 7.5 Load-displacement relationship of S355 X-joints.



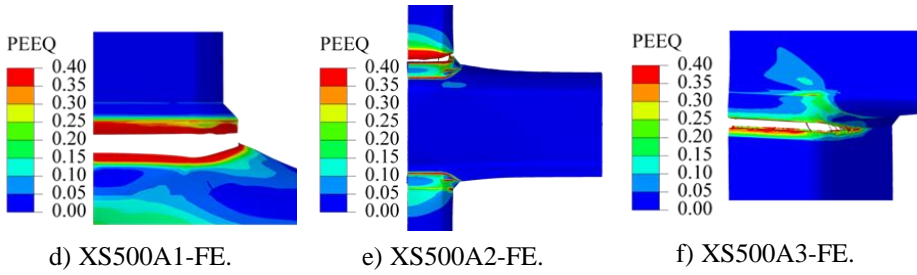


Fig. 7.6 Failure modes of S500 X-joints.

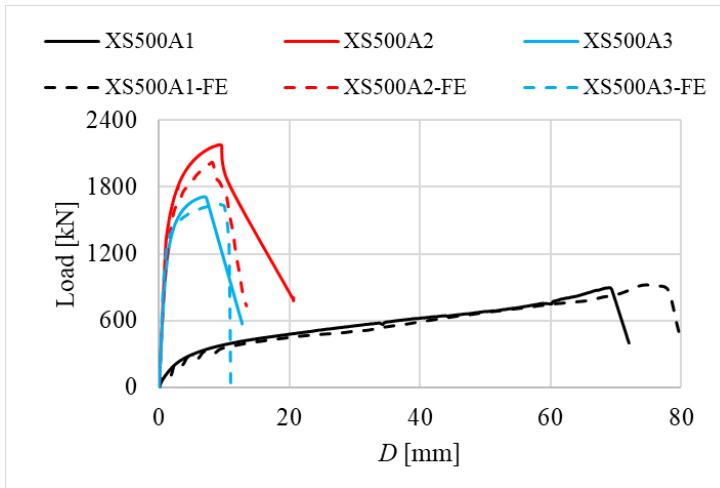


Fig. 7.7 Load-displacement relationship of S500 X-joints.

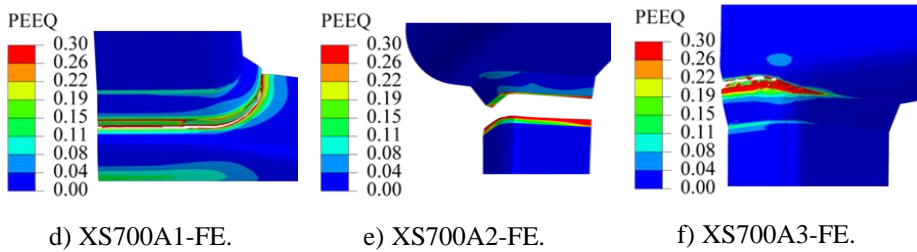
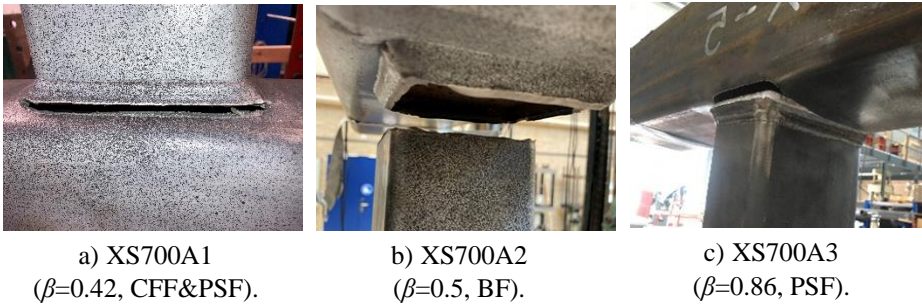


Fig. 7.8 Failure modes of S700 X-joints.

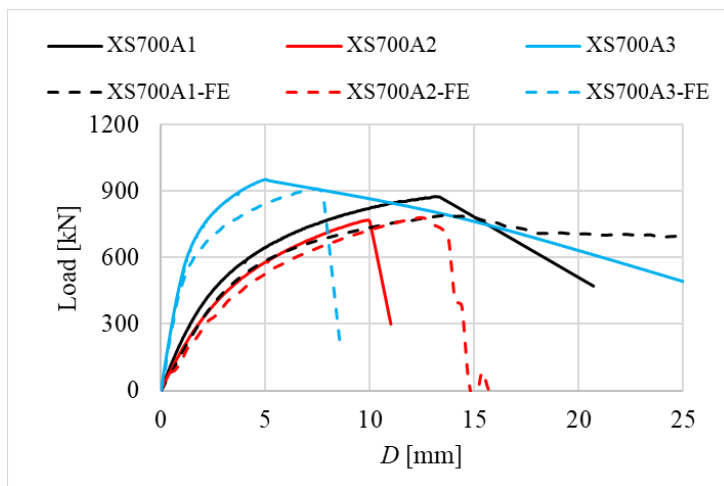


Fig. 7.9 Load-displacement relationship of S700 X-joints.

The ultimate resistances obtained from FE models are compared to the experiments in Table 7.5. The FE/EXP resistance ratio varies from 0.91 to 1.02, with an average value of 0.98. It is worth mentioning that the resistance of PSF is well predicted even though the shear damage model is not considered in the employed GTN model. The same finding was reported by Liu et al. [2], where the proposed shear-modified GTN model can improve the results of the fracture propagation but not the ultimate resistance and the corresponding deformation. The reason for the accurate prediction of the ultimate resistance is that the Lode angle has limited influence on the fracture plastic strain under a high stress triaxiality [1,7–9]. The stress triaxiality in the elements involved in fracture of four PSF models varies between 0.6 and 1.5. In addition, the number of elements in the FE model exposed to a shear stress state is very limited, which has a minor influence from a joint global behaviour perspective.

Table 7.5 Comparison of FE and experimental ultimate resistances.

	A1			A2			A3		
	EXP [kN]	FE [kN]	FE/EXP [-]	EXP [kN]	FE [kN]	FE/EXP [-]	EXP [kN]	FE [kN]	FE/EXP [-]
XS355	546	555	1.02	1964	1911	0.97	1344	1355	1.01
XS500	897	919	1.02	2181	2020	0.93	1713	1647	0.96
XS700	875	793	0.91	769	780	1.01	952	910	0.96

The fracture surface of all joints, except for XS700A1, is well predicted using the calibrated GTN damage model. Only XS355A3 had CSWF with an arc-shaped fracture. The FE predicted fracture has a similar shape but is slightly closer to the corner of the chord, which might be due to the absence of the constitutive model of the corner region.

Two orientations of the fracture surface for PSF were observed in the experiments. The fracture of XS355A1, XS500A1, and XS700A3 initiated at the weld toe and cut through the thickness of the tube (see Fig. 7.4, Fig. 7.6, and Fig. 7.8), which is successfully

predicted by the FE model. The fracture surface of XS700A1 propagated below the weld, as shown in Fig. 7.10 (solid red line for the experiment and red dash line for the FE model), which fails to predict.

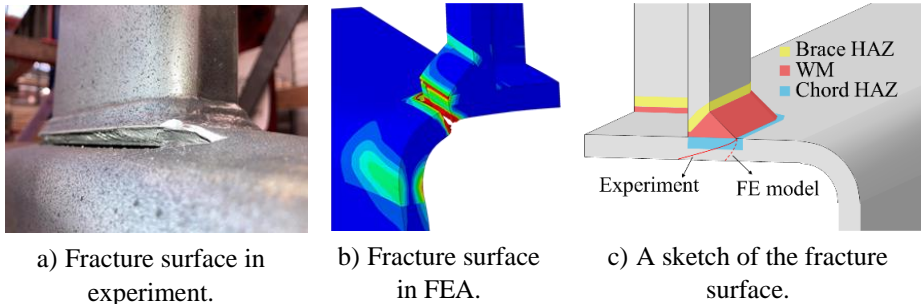


Fig. 7.10 Fracture surface in the experiment and FEA of XS700A1.

The fractures of all BF have the same orientation, as shown in Fig. 7.4, Fig. 7.6, and Fig. 7.8. A detailed shape of the fracture surface is shown in Fig. 7.11 a). The normal direction of the fracture surface points out of the X-joint. As the fracture starts from the toe of the weld, the fracture involves HAZ and BM. The FE model successfully predicts the failure mode.

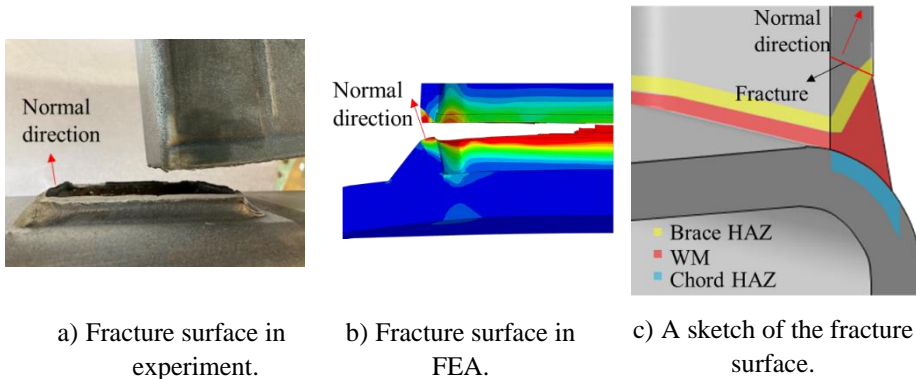


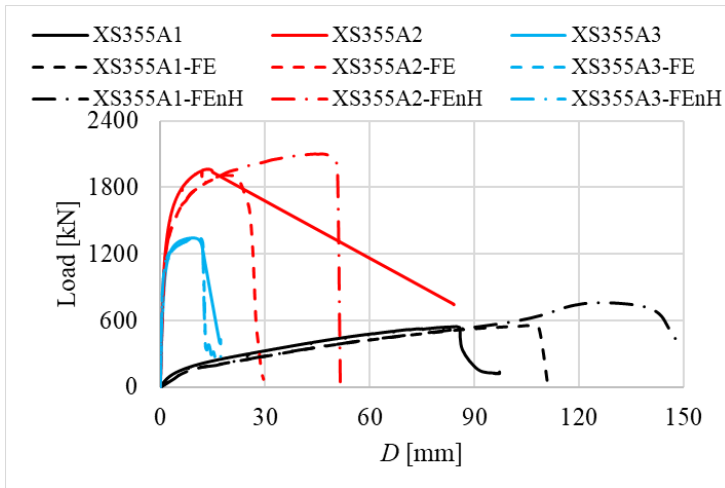
Fig. 7.11 Fracture surface in experiments and FEA of XS700A2.

7.3.2. Without considering HAZ

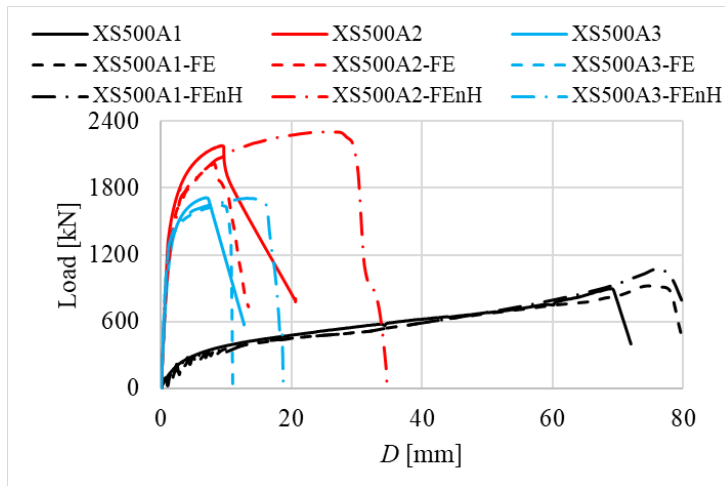
The GTN damage models calibrated for BM and HAZ are used in the X-joint fracture simulation in Section 7.3.1. The FE model without considering HAZ (denoted as FEnH), where the calibrated BM constitutive model is used in the HAZ region, is employed to reveal the importance of HAZ in the simulation of X-joint.

The load-deformation relationships predicted by the model without considering HAZ are compared to the experimental results in Fig. 7.12. In addition, the FE results discussed in Section 7.3.1 are also presented for comparison. It is rational that FEnH predicts a larger ultimate resistance and deformation than the model considering HAZ, as the constitutive model of HAZ is weaker than BM. The resistance predicted by FEnH is

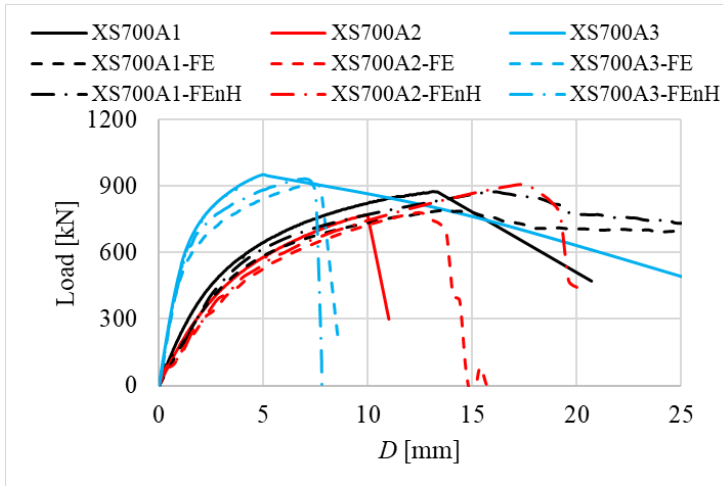
compared to the experimental results in Table 7.6. The prediction of only one joint is on the safe side, although the effect of the corner material in cold-formed profiles is not taken into consideration. The resistance ratio varies between 0.98 and 1.39. The ultimate deformation is generally overestimated, especially for joints with BF where the deformation is overestimated up to 3.31 times (XS355A2). The reason is that the higher resistance results in a higher strain in the brace and the chord, consequently a larger ultimate deformation. Depending on the material hardening level in the brace and the chord, the level of the deformation overestimates varies, as the strain increment is larger at a higher material hardening level given the same stress increment. For example, the joint with BF normally has a higher strain level in the brace. A limited increase in resistance results in a significant increase in deformation.



a) S355 X-joints.



b) S500 X-joints.



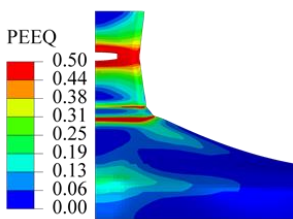
c) S700 X-joints.

Fig. 7.12 Load-deformation relationships.

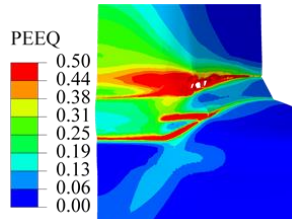
Table 7.6 Comparison of FEnH and experimental ultimate resistances.

	A1			A2			A3		
	EXP [kN]	FEnH [kN]	FE/EXP [-]	EXP [kN]	FEnH [kN]	FE/EXP [-]	EXP [kN]	FEnH [kN]	FE/EXP [-]
XS355	546	762	1.39	1964	2100	1.07	1344	1353	1.01
XS500	897	1074	1.20	2181	2305	1.06	1713	1709	1.00
XS700	875	874	1.00	769	907	1.18	952	932	0.98

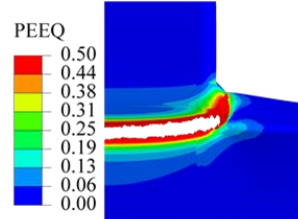
The failure modes of the FE models without considering HAZ are presented in Fig. 7.13. The FE models successfully predict the experimental failure modes except for two joints, XS355A1 and XS500A3, where a fracture in the brace and CSWF are observed, respectively. Although BF is predicted in XS355A2-FEnH, the fracture initiates at the corner of the brace and propagates to Side B (referring to Fig. 6.1), while the fracture is on Side A in the experiment.



a) XS355A1-FEnH.



b) XS355A2-FEnH.



c) XS355A3-FEnH.

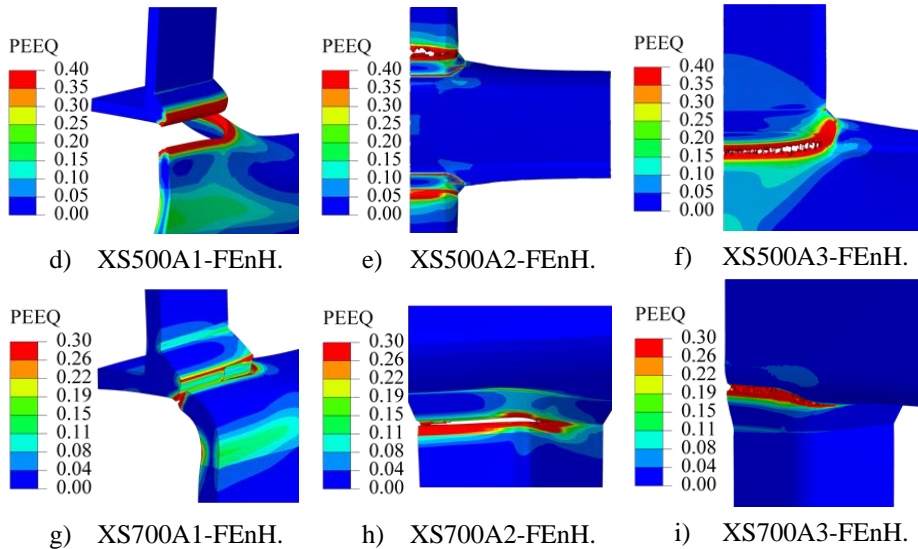


Fig. 7.13 Failure modes of FE models without considering HAZ.

7.3.3. Using the semi-empirical material model

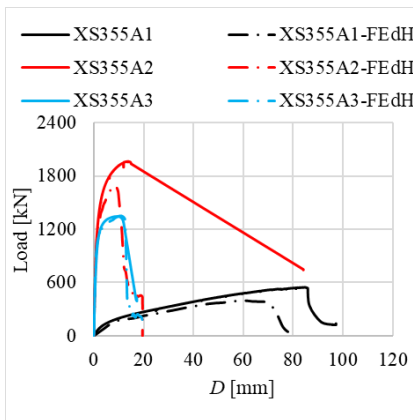
The FE models are created for the second batch of X-joint (B-series) using the same parameter settings illustrated in Section 7.2.1. As the engineering stress-strain relationship of BM in the B-series X-joint is very close to at least one material model in the A-series, the calibrated GTN model for BM of the A-series is employed in the B-series simulation. The employed materials are shown in Table 7.7.

Table 7.7 Employed material for B-series X-joint analysis.

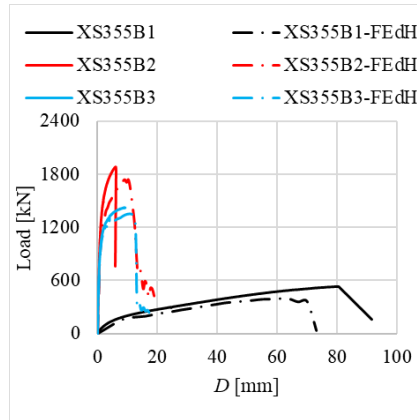
X-joint	Chord BM	Brace BM	WM
XS355B1	XS355A1B	S355t5B	S355t8W
XS355B2	XS355A2B	S355t8B	S355t8W
XS355B3	XS355A3B	XS355A3B	S355t8W
XS500B1	XS500A2B	XS500A1B	S700t8W
XS500B2	XS500A2B	XS500A2B	S700t8W
XS500B3	XS500A3B	XS500A3B	S700t8W
XS700B1	XS700A1B	XS700A1B	S700t8W
XS700B2	XS700A2B	XS700A3B	S700t8W
XS700B3	XS700A2B	XS700A3B	S700t8W

For A-series, the name of the employed constitutive model for BM is shown in Table 7.3. And the HAZ semi-empirical model corresponding to the employed BM is used in the FE analysis. For B-series, the GTN damage model for BM refers to BM of the A-series and welded RHS profiles, as illustrated in Table 7.7. The HAZ semi-empirical model is derived based on tested results of the chord and the brace in the B-series X-joint. The semi-empirical material models of HAZ for all BMs are presented in Table 7.4.

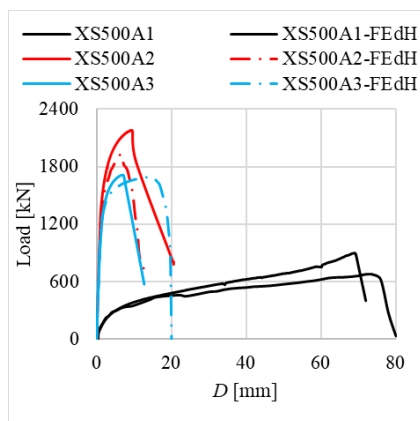
The load-deformation relationships of FE models using the derived HAZ (dH) constitutive property are compared to experiments in Fig. 7.14. Generally, the load-deformation relationship of the FE model shows a good agreement with the experimental result. Table 7.8 compares the ultimate resistance of the FE model and the experiment. The resistance ratio (EF/EXP) of the A-series varies between 0.73 and 1.01. For the B-series, the resistance of most joints, 7 out of 9, can be well predicted with a resistance ratio ranging between 0.74 and 1.02, while the predictions of two joints, XS500B3 and XS700B3, are rather unconservative with a 1.07 and 1.19 resistance ratio, respectively. Section 6.3.2.3 presents that the failure mode transformed from PSF in XS700A3 to BF in XS700B3, although the chord of XS700B3 was thinner than XS700A3. It was argued that the welding process has a crucial influence on the joint behaviour. As the semi-empirical material model is established based on the welded connections fabricated by welding Company A (producer of A-series X-joints), the parameters in the semi-empirical material model might not be very suitable for joints manufactured by welding Company B. Additionally, in the B-series, the resistance ratio increases with the steel grade, indicating that the semi-empirical material model tends to be unconservative with an ascending steel grade. A more significant scattering concerning the HAZ strength degradation is expected for HSS than the mild steel. Hence, further studies are required to calibrate the semi-empirical material model for different welding processes and parameters, especially for HSS.



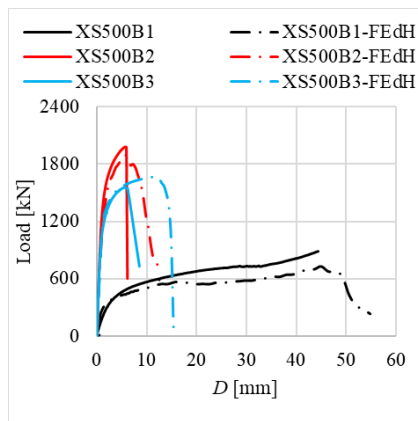
a) S355 X-joints A-series.



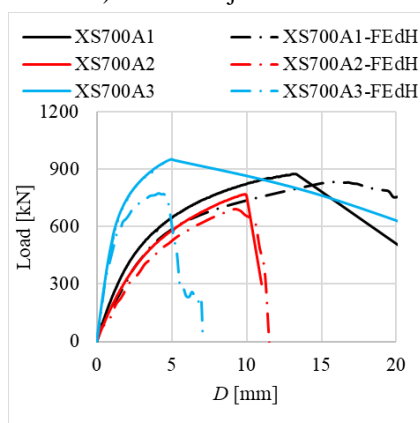
b) S355 X-joints B-series.



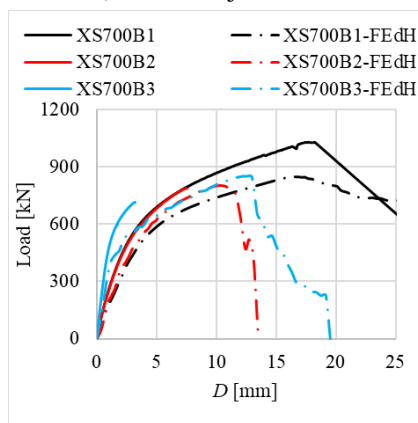
c) S500 X-joints A-series.



d) S500 X-joints B-series.



e) S700 X-joints A-series.



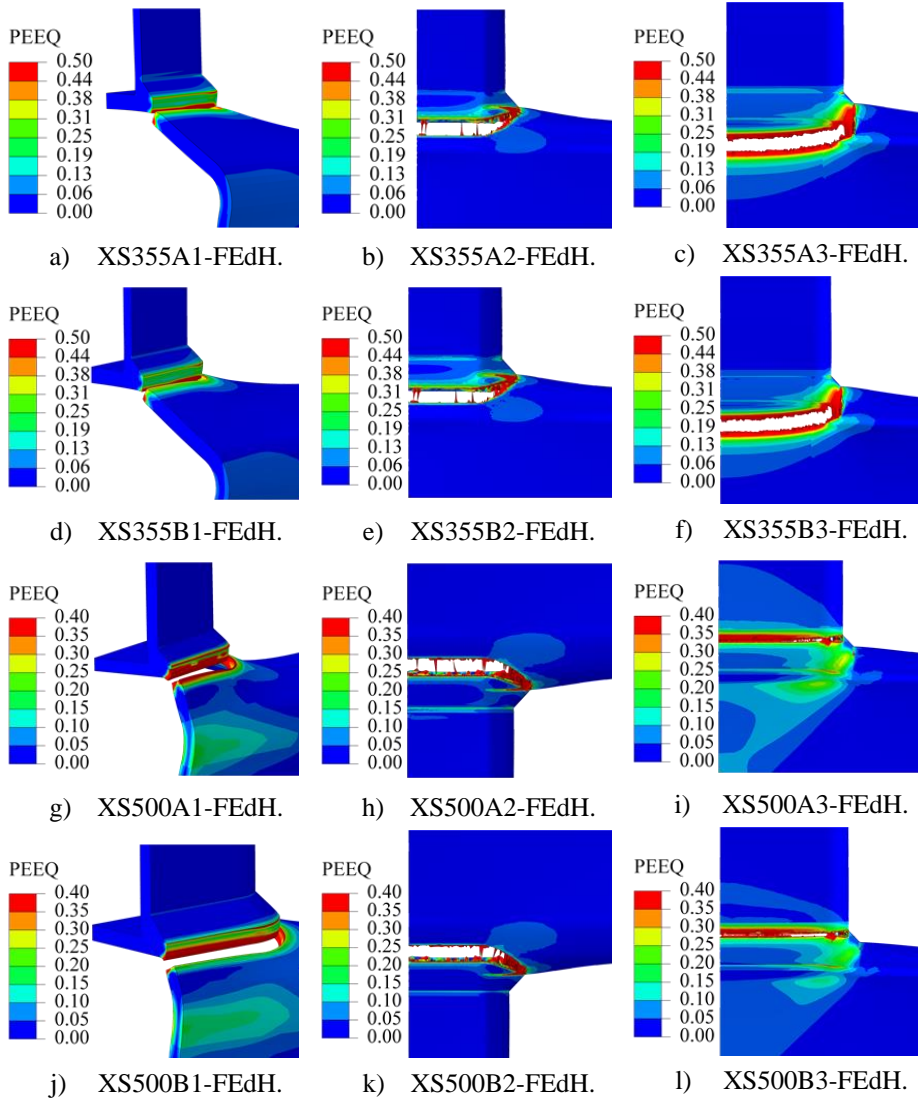
f) S700 X-joints B-series.

Fig. 7.14 Load-deformation relationships.

Table 7.8 Comparison of FEdH and experimental ultimate resistances.

Specimen	EXP [kN]	FEdH [kN]	FEdH/EXP [-]	Specimen	EXP [kN]	FEdH [kN]	FEdH/EXP [-]
XS355A1	546	397	0.73	XS355B1	532	396	0.74
XS355A2	1964	1695	0.86	XS355B2	1883	1740	0.92
XS355A3	1344	1352	1.01	XS355B3	1424	1353	0.95
XS500A1	897	676	0.75	XS500B1	887	730	0.82
XS500A2	2181	1926	0.88	XS500B2	1981	1898	0.96
XS500A3	1713	1693	0.99	XS500B3	1557	1668	1.07
XS700A1	875	834	0.95	XS700B1	1030	848	0.82
XS700A2	769	692	0.90	XS700B2	788	803	1.02
XS700A3	952	774	0.81	XS700B3	716	851	1.19

The failure modes of the FE models using the derived HAZ constitutive model are presented in Fig. 7.15. The FE models well predict the experimental failure modes of 13 joints. The mispredicted failure modes involve three S355, one S500, and one S700 X-joints. BF in XS355A2, XS355B2, XS500A2, and XS700B3 are predicted as PSF. A possible reason for this is that the material property of the chord corner is not considered in the FE model, resulting in a weak corner in the chord. In addition, CSWF is predicted for XS355B3, while a PSF appeared in the experiment.



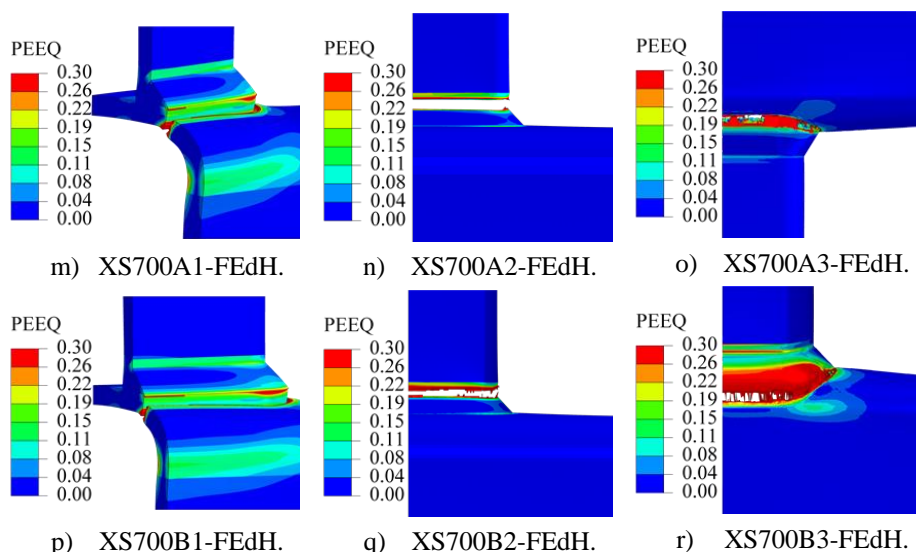


Fig. 7.15 Failure modes of FE models using derived HAZ constitutive model.

7.4. Conclusions

The GTN damage model is implemented into the fracture simulation of welded cold-formed rectangular hollow section (RHS) X-joints. Based on the presented results, the following conclusions are drawn:

- 1) The calibrated GTN damage model for BM and HAZ could effectively predict the fracture-related failure modes: Punching shear failure (PSF), Brace failure (BF), and Chord side wall failure (CSWF) of welded RHS X-joints in tension, although the material shear failure mechanism is not considered. Comparing the ultimate resistance of the finite element (FE) models and the experiments (EXP), the FE/EXP ultimate resistance ratio varies from 0.91 to 1.02, with an average 0.98 ratio.
- 2) Two orientations of the PSF fracture surface are observed in experiments. The FE model successfully predicts the fracture cutting through the profile thickness of the chord, while the fracture propagated below the weld was not accurately predicted. The fractures of BF and CSWF are well predicted. Both BM and HAZ contributed to the fracture of BF. The predicted fracture shape of CSWF may be improved by considering the constitutive model of the corner material in cold-formed RHS tubes.
- 3) Based on the calibrated X-joint FE model, an attempt is made to investigate the tensile behaviour of X-joint without considering the heat-affected zone (HAZ) constitutive model. Compared to the experimental results, the predicted resistance of only one joint is on the safe side, although the effect of the corner material in cold-formed profiles is not considered. The resistance ratio (FE/EXP) varies between 1.00 and 1.39 except for one joint with 0.98 ratio.

- 4) A semi-empirical material damage model is proposed for HAZ based on the calibrated parameters for all HAZs. The load-deformation relationship of the FE model shows good agreement with the experimental result. Generally, the failure mode is well predicted. The mispredicted failure mode could be improved by considering the constitutive model of the chord corner. The resistance ratio (FE/EXP) varies between 0.73 and 1.01 for the A-series X-joint. The ratio varies between 0.74 and 1.02 for B-series except for two joints with a 1.07 and 1.19 resistance ratio. Further studies are required to calibrate the semi-empirical material model for different welding processes and welding parameters, especially for HSS.

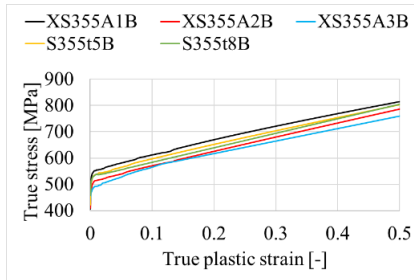
Reference

- [1] X. Ma, W. Wang, Y. Chen, X. Qian, Simulation of ductile fracture in welded tubular connections using a simplified damage plasticity model considering the effect of stress triaxiality and Lode angle, *Journal of Constructional Steel Research*. 114 (2015) 217–236. <https://doi.org/10.1016/j.jcsr.2015.07.023>.
- [2] J. Liu, S. Yan, X. Zhao, Simulation of fracture of a tubular X-joint using a shear-modified Gurson–Tvergaard–Needleman model, *Thin-Walled Structures*. 132 (2018) 120–135. <https://doi.org/10.1016/j.tws.2018.07.054>.
- [3] X. Huang, C. Wei, J. Zhao, W. Zhao, J. Ge, Fracture prediction of circular steel tubular X-joints using a Lode parameter enhanced cyclic void growth model, *Engineering Structures*. 245 (2021) 112869. <https://doi.org/10.1016/j.engstruct.2021.112869>.
- [4] M. Mohan, T. Wilkinson, Damage criterion approach to high-strength steel RHS truss joints, *Steel Construction*. (2022). <https://doi.org/https://doi.org/10.1002/stco.202100027>.
- [5] H. Xin, M. Veljkovic, Evaluation of high strength steels fracture based on uniaxial stress-strain curves, *Engineering Failure Analysis*. 120 (2021) 105025. <https://doi.org/10.1016/j.engfailanal.2020.105025>.
- [6] V. Tvergaard, A. Needleman, Analysis of the cup-cone fracture in a round tensile bar, *Acta Metallurgica*. 32 (1984) 157–169. [https://doi.org/10.1016/0001-6160\(84\)90213-X](https://doi.org/10.1016/0001-6160(84)90213-X).
- [7] Y. Bai, T. Wierzbicki, A new model of metal plasticity and fracture with pressure and Lode dependence, *International Journal of Plasticity*. 24 (2008) 1071–1096. <https://doi.org/10.1016/j.ijplas.2007.09.004>.
- [8] X. Huang, J. Ge, J. Zhao, W. Zhao, A continuous damage model of Q690D steel considering the influence of Lode parameter and its application, *Construction and Building Materials*. 262 (2020) 120067. <https://doi.org/10.1016/j.conbuildmat.2020.120067>.
- [9] T. Cao, J. Gachet, P. Montmitonnet, P. Bouchard, A Lode-dependent enhanced Lemaitre model for ductile fracture prediction at low stress triaxiality, *Engineering Fracture Mechanics*. 124–125 (2014) 80–96. <https://doi.org/10.1016/j.engfracmech.2014.03.021>.
- [10] X. Lan, T.M. Chan, B. Young, Structural behaviour and design of high strength steel RHS X-joints, *Engineering Structures*. 200 (2019) 109494. <https://doi.org/10.1016/j.engstruct.2019.109494>.
- [11] M. Amraei, A. Ahola, S. Afkhami, T. Björk, A. Heidarpour, X.L. Zhao, Effects of heat input on the mechanical properties of butt-welded high and ultra-high strength steels, *Engineering Structures*. 198 (2019). <https://doi.org/10.1016/j.engstruct.2019.109460>.
- [12] M. Amraei, S. Afkhami, V. Javaheri, J. Larkiola, T. Skriko, T. Björk, X.L. Zhao, Mechanical properties and microstructural evaluation of the heat-affected zone in ultra-high strength steels, *Thin-Walled Structures*. 157 (2020).

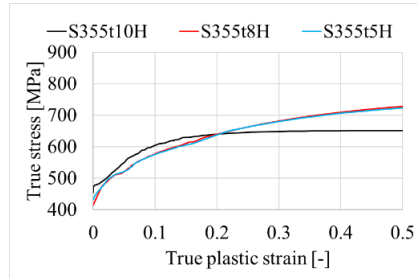
- <https://doi.org/10.1016/j.tws.2020.107072>.
- [13] Y. Peng, C. Wu, J. Gan, J. Dong, Characterization of heterogeneous constitutive relationship of the welded joint based on the stress-hardness relationship using micro-hardness tests, *Construction and Building Materials*. 202 (2019) 37–45. <https://doi.org/10.1016/j.conbuildmat.2018.12.218>.
- [14] C. Chen, S.P. Chiew, M.S. Zhao, C.K. Lee, T.C. Fung, Welding effect on tensile strength of grade S690Q steel butt joint, *Journal of Constructional Steel Research*. 153 (2019) 153–168. <https://doi.org/10.1016/j.jcsr.2018.10.009>.
- [15] Y. Peng, C. Wu, J. Gan, J. Dong, Determination of the local constitutive properties of the welded steel joints using digital image correlation method, *Construction and Building Materials*. 171 (2018) 485–492. <https://doi.org/10.1016/j.conbuildmat.2018.03.182>.
- [16] W. Cai, Y. Wang, G. Li, R. Stroetmann, Comparative study on strength of TMCP and QT high-strength steel butt-welded joints, *Journal of Constructional Steel Research*. 197 (2022) 107447. <https://doi.org/10.1016/j.jcsr.2022.107447>.
- [17] T. Wilkinson, *The plastic behaviour of cold-formed rectangular hollow sections*, 1999.
- [18] J. Wang, S. Afshan, N. Schillo, M. Theofanous, M. Feldmann, L. Gardner, Material properties and compressive local buckling response of high strength steel square and rectangular hollow sections, *Engineering Structures*. 130 (2017) 297–315. <https://doi.org/10.1016/j.engstruct.2016.10.023>.

Appendix

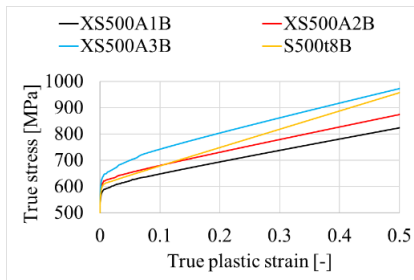
Appendix 7.A Undamaged true stress-true plastic strain relationships for X-joint simulations.



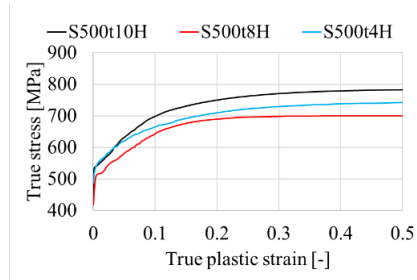
a) Base material of S355.



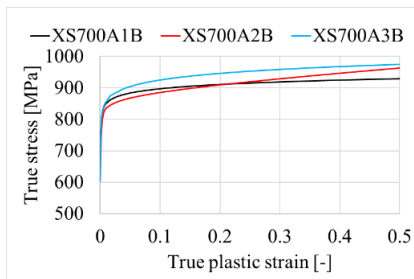
b) Heat-affected zone of S355.



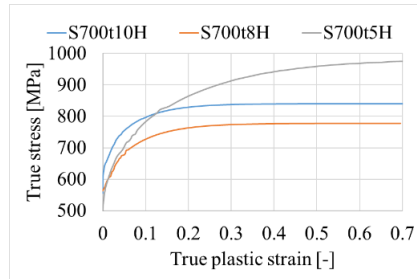
c) Base material of S500.



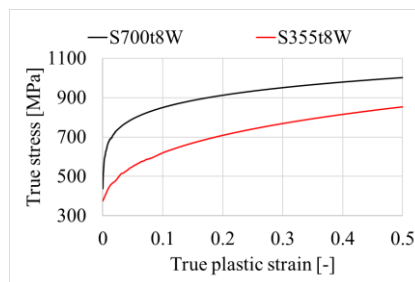
d) Heat-affected zone of S500.



e) Base material of S700.



f) Heat-affected zone of S700.



g) Weld metal.

8.

Conclusions and future work

8.1. Conclusions

This dissertation presents a systematic approach toward the heat-affected zone (HAZ) in welded connections from the material level to the structural joint level concerning S355, S500, and S700 materials. The final goal of this research is to promote the application of high-strength steel (HSS) on welded hollow section joints. A weld region consists of three material zones: HAZ, the base material (BM), and the weld metal (WM). Under certain conditions, HAZ has the lowest strength among the three material zones, which may govern the failure. The strength degradation in HAZ is more significant for HSS than mild steel. Therefore, it is essential to evaluate the HSS joint behaviour considering the HAZ constitutive model.

On the material level, this research provides new knowledge on obtaining the uniaxial stress-strain relationship of HAZ considering ductile failure mode (under the monotonic loading) using the digital image correlation (DIC) technique and the finite element (FE) analysis. The obtained HAZ constitutive model provides necessary information for the FE analysis of welded connections. The Gurson-Tvergaard-Needleman (GTN) damage model is calibrated for BM and HAZ of the welded connection. On the joint level, the tensile behaviour of welded cold-formed rectangular hollow section (RHS) X-joints is investigated experimentally. The necessity of the material factor C_f and the design yield strength restriction ($f_y \leq 0.8f_u$) for HSS is evaluated. Finally, the calibrated GTN model was successfully implemented in the fracture simulation of welded RHS X-joints. Based on the presented study, the following conclusions are drawn.

1. A method is proposed to identify the HAZ boundaries of the milled welded coupon specimen in DIC results. The boundary is identified by comparing the slope of the minor true strain-major true strain relationship (also called the strain ratio for simplicity) in the stage beyond yielding, as the transverse constraint at the boundary of two material zones may result in different stress states, consequently, a varying strain ratio. The strain ratio in HAZ is close to a "V" shape or "Monotonic" shape distribution, which is successfully validated against the hardness result. The identified boundary reveals the width of HAZ and WM, which provides geometry information for determining the gauge length of virtual extensometers in DIC and for creating FE models to validate the HAZ stress-strain relationship.
2. A method is proposed to correct the measured stress-strain relationship of HAZ, as the measured HAZ stress is overestimated during the plastic deformation due to the transverse constraint imposed by BM and WM. A linear modification factor (MF_1 and MF_2), as a function of the true strain, is used to modify the measured HAZ stress. The modified stress-strain relationship is successfully validated against the coupon test based on the load-deformation relationship and the strain distribution on the specimen surface. In an example of S700 welded connections, the ultimate strength of HAZ in the unmilled welded coupon specimen is 17% higher than the modified ultimate strength of HAZ.

The difference is increased to 29% if the complete butt-welded SHS is considered.

3. The mechanical properties of HAZ are correlated to BM using three reduction factors (RFs), which is an alternative simplified approach to obtaining the HAZ constitutive model. The proposed RFs for the yield strength, the ultimate strength, and the ultimate strain of HAZ are 0.85, 0.95, 0.6 for S355 and S500, and 0.7, 0.8, 0.8 for S700, respectively. Note that the ultimate strain of HAZ is correlated to the elongation at fracture of BM. The derived HAZ mechanical properties are used to generate a semi-empirical constitutive model before necking based on the Swift model. The derived HAZ constitutive model for each steel grade is successfully validated against the experiments.
4. A metallurgical investigation is carried out based on the low-force Vickers hardness test and the microstructure observation. It is found that the majority (92%) of HAZ width varies between 2 mm and 4 mm. The HAZ width does not show any correlation to the steel grade and plate thickness. The average HAZ width is 3.2 mm.
5. The GTN damage model is calibrated for HAZ and BM of the butt-welded cold-formed RHS. The computational homogenization analysis is conducted to evaluate the effect of hydrostatic pressure on the yield strength, considering the relationship between the material accumulated initial hardening strain and the void volume fraction f . An equation is proposed to correlate the parameters q_1 and f with a constant q_2 . All values of q_2 for different materials are close to 1. Parameter q_1 gradually decreases from 3 to 1.5 with an increasing f . The undamaged true stress-true strain relationship of BM is generated using a weighting factor (W) based on the Swift model and the linear model. The weighting factor decreases with the increase of the steel grade, which is around 0.9, 0.7, and 0.1 for S355, S500, and S700 materials, respectively. The Voce model is suitable for generating the post-necking undamaged constitutive model for all HAZ materials. The fracture parameters f_c and f_t in the GTN model are calibrated based on the tensile coupon tests. The damage of the element is sensitive to the value of f_c . f_t has a minor influence on the failure process. The value of f_t , up to 5% larger than f_c , is validated in this study.
6. The tensile behaviour of welded cold-formed RHS X-joint is investigated experimentally based on 18 joint tests. The profiles are mild and high-strength steel, including S355, S500, and S700. It is found that prEN 1993-1-8 predicts a conservative tensile resistance for steel grade up to S700, even without applying the material factor C_f and the $0.8f_u$ yield strength restriction. In addition, a bi-linear model is proposed to characterise the joint nonlinear behaviour and the yield resistance. The better the joint ductility is, the higher the yield ratio (yield resistance over ultimate resistance) is.
7. The calibrated GTN damage model for BM and HAZ could effectively predict the fracture-related failure modes: Punching shear failure (PSF), Brace failure (BF), and Chord side wall failure (CSWF) of welded RHS X-joints in tension, although the material shear failure mechanism is not considered. Comparing the

ultimate resistance of the finite element (FE) models and the experiments (EXP), the FE/EXP ultimate resistance ratio varies from 0.91 to 1.02. The FE model overestimates the ultimate resistance of most joints (17 out of 18) without considering the HAZ constitutive model. The resistance ratio (FE/EXP) varies between 1.00 and 1.39 except for one joint with 0.98 ratio.

8. The semi-empirical constitutive model for HAZ is extended to a semi-empirical material damage model based on the GTN model. Generally, using the semi-empirical material damage model, the FE model predicts the experimental load-deformation relationship and the failure mode well. The resistance ratio (FE/EXP) varies between 0.73 and 1.01 for the A-series X-joint. The ratio varies between 0.74 and 1.02 for B-series except for two joints with a 1.07 and 1.19 resistance ratio. The reason for the overestimated resistance of the B-series is that the reduction factors for generating the semi-empirical constitutive model of HAZ are determined based on A-series welding procedures and parameters. Further studies are required to calibrate the semi-empirical material model for different welding processes and parameters.

8.2.Future work

1. The mechanical property of HAZ is sensitive to the welding processes and parameters, such as the cooling time $t_{8/5}$ (from 800°C to 500°C), the heat input, and the weld matching type. Although the proposed constitutive model for HAZ can be adopted in the FE analysis of welded connections using the same BM and the welding parameters as in the experiments, more experiments with different BM and welding parameters are required to expand the valid range of the reduction factors which correlates the mechanical properties of HAZ and BM. This work is more necessary for HSS and ultra-HSS than mild steel, as the strength degradation in HAZ generally increases with an ascending steel grade, indicating a more critical HAZ in HSS and ultra-HSS welded connection. In addition, the effect of strain ageing is not considered in the presented work. Given the plastic deformation during the cold-forming process and the high temperature introduced by welding, strain ageing may influence the mechanical property of HAZ in welded cold-formed hollow section joints and should be further studied.
2. For some X-joints with a large brace-to-chord width ratio (β), the fracture appears in HAZ at the corner region of the chord. The presented research does not consider the constitutive model of BM and HAZ at the corner region, which should be considered in future studies. Using the validated corner material model, the FE model will be completed to evaluate the effect of the high strength and low ductility of corner material on the joint mechanical behaviour.
3. The main limitation of the employed GTN damage model is that the effect of the Lode angle on the material yield and failure criterion is not considered, although the predicted ultimate resistance fits the experiments well. It should be considered in future work, and a generic FE model should be validated at

various stress states. Moreover, the calibrated GTN damage model is valid for monotonic loading. The fatigue behaviour is not considered in this study.

4. The current design rule for welded connections does not consider the HAZ strength degradation and the HAZ strength enhancement due to the transverse constraint. The numerical example of the welded SHS connection shows that the HAZ strength degradation could be compensated by the transverse constraint, which may increase the HAZ ultimate strength by 29%. Hence, the combined effect of strength degradation and enhancement in HAZ on the behaviour of the welded connection should be systematically evaluated to develop a safe and economical design approach.

Acknowledgement

While writing the acknowledgement, I have been in the Netherlands, also doing my PhD, for almost five years. It has been a challenging and unbelievable journey. Many unique and beautiful memories keep popping up in my mind. I truly enjoyed the whole process, whether it brought me happiness or sadness. But still, I have to say, it was tougher than I expected, especially in the mid of my fourth year when I had no published journal paper, suspended the majority of experiments, and accidentally Covid-19 infection with a nine-day fever in a row. Fortunately, I survived, and research results were gradually published. Looking back to the past years, I was very lucky never to have depression or other mental issues, thanks to the support from colleagues, friends, and family.

First of all, I would like to express my most sincere appreciation to my promotor and supervisor, professor Milan Veljkovic. Thank you for giving me the chance to work with you. I still remember the day when you offered me the PhD position. It meant a lot to me, who was trying to catch up after wasting a good study opportunity at Tongji University. Your question, "do you learn something from it?" motivated me every day to gain new knowledge. You helped me develop a scientific perspective and critical thinking from the countless meetings and conversations. I appreciate the freedom and trust you gave me to explore new research opportunities. Your passion and attitude toward research did and will always inspire me. Moreover, thank you for your immense patience and careful guidance on other research-related activities, such as giving lectures, supervising master students, and presenting in project meetings. I will benefit from these experiences for my entire career.

Then, I would like to thank my promotor, professor Max A.N. Hendriks. Thank you for your constructive suggestions, critical feedback, and swift response to my research and presentations. I really appreciate your time and help. Professor Haohui Xin, thanks for your guidance in my research. You showed me what an outstanding young scholar is. I learned a lot from your rigorous attitude and profound comments. Special thanks to Assistant professor Kristo Mela for providing me with the research project. I sincerely appreciate your efforts for the critical comments, language polishing, project coordination, and advice for the career/life choice. Thank SSAB for funding this research. I would also like to thank my bachelor's and master's supervisors professor Yongfeng Luo, professor Hua Yang, and professor Yuyin Wang for your help, encouragement, and advice on my career development. Your attitude and passion for research always inspire me.

Thank you, Peter de Vries. You played a vital role in my experimental study. I can't imagine how it would be without your help, especially when I struggled with the steel-cutting company. Besides, you set a perfect example for me to be a cool guy with a good work-and-life balance and a great passion for sports. Assistant professor Marko Pavlovic,

thanks for sharing with me advanced measuring devices, which provide fundamental data for this dissertation. Fei Yang, I truly appreciate your encouragement and patience. Whenever I doubted my research, you always provided me with essential feedback. I would not submit my paper to a good journal without your support. Giorgos Stamoulis and Louis den Breejen, thank you very much for helping me with the experiments. The valuable information on the experiments and life is truly appreciated. Besides, after your five-year lecture on Dutch, I can use "Hop hop opschieten" properly now. I would like to thank John Hermsen, Fred Schilperoort, Kevin Mouthaan, and Kees van Beek for your tremendous contribution to the experiments. Your help and suggestions are truly appreciated. Sander Van Asperen, it was not easy for me to conduct those metallurgical investigations considering my knowledge background. Thank you very much for your instruction and coordination.

I would like to thank my (ex)colleagues, Abhijith Kamath, Haohui Xin, Weijian Wu, and Martin Paul Nijgh, for the wonderful time we shared and for the help you offered. Those beers, hotpots, gym training, BIOCEO summer school, the first Christmas day in Amsterdam, and the table tennis tournament from UBASE will undoubtedly be good memories in my life. And calling Diergaarde Blijdorp to find Mr Lion was a classic one. Many thanks to Xiuli Wang, Lu Cheng, Pei He, Weikang Feng, Linda Bucking, Jincheng Yang, Mathieu Koetsier, Tao Yang, Florentia Kavoura, Trayana Tankova, Angeliki Christoforidou, Michele Mirra, Giorgio Pagella, Rong Liu, Shuang Qiu, Xiaoling Liu, Zhanchong Shi, Da Xiang, Ding Liao, Geert Ravenshorst, and David Malschaert. I really enjoyed those jokes, coffee breaks, parties, and board games. I appreciate your help and suggestions on research and daily life. Wolfgang Gard, thank you for your kindness and help. Conversations with you were always full of information and pleasure. Your experience at my age encouraged me to do research bravely and peacefully.

I would also like to thank all the master students that I have supervised. Special thanks to Hagar El Bamby and Bart Adegeest. Thank you for your support and hard work. I learned a lot while we were exploring new knowledge. It was not easy to conduct the experiments at the beginning of the pandemic. I'm glad that we overcame those difficulties and achieved our goals.

There were a lot of great moments with friends. I cherish the time spent with my Call of Duty & Alcohol gang. Hongpeng Zhou, Jun Xu, Yusheng Yang, and Yuxuan Feng, thank you for your accompany. It was an exceptional time. We went through it with support from each other. All the happiness, tears, and surprises will certainly be a colourful page in my life. By the way, I have to say, I am the best sniper. Huan Wang, Langzi Chang, and Yuxuan Feng, you made the last year of my PhD extraordinary. You helped me to know myself after every interesting debate and "yangshier". I would also like to thank Xiangcou Zheng, Qin Qin, Ze Chang, Zhaoying Ding, Ren'an Gong, Biyue Wang, Xiujie Shan, Tao Hou, Tianyun Yuan, Wenting Ma, Yi Xia, Mengmeng Gao, Fengqiao Zhang, FanXiang Xu, Min Zhang, Dengxiao Lang, Qingpeng Li, Maolong Lv, Xuehui Zhang. We shared some great times. I truly enjoyed those beers and parties. I appreciate your kindness and help. My gratitude goes to my basketball gang, Mingyan Fu, Chao Ma, Jian Zhang, Hanqing Liu, Xiaocong Lv, Liqi Cao, Yi Luo, Zhiqiang Peng, Mutu Ha, Baozhou

Zhu, Jianing Zhu, Runsheng Zhou, Ding Luo, Zhen Cui, Junhai Cao, Dawei Fu, Qianyi Chen, and Ke Zhang. There are still some friends who often met on the court but without knowing their full names. I sincerely appreciate the intense competitions, which undoubtedly saved me from the heavy research work for a while and refreshed me. I hope to see you again on the basketball court and wish all injuries be away from you.

Marco van Arragon and Xiao Yu, thanks for helping my wife and me in daily life. We had a lot of fun on your farm, at your home, and without forgetting the Christmas dinner at your parent's home. Every conversation with you made me feel peaceful. You can always provide me with another perspective to review my plan. Special thanks to Zhang Ting's family. Thank you for your help and the delicious hometown food, which were very important to me living in a foreign land. Viswajeeth Kushwala, it is unbelievable that we often talked about the truth of life and happiness, given my limited vocabulary. But fortunately, we understood each other well and had quite some interesting consensus.

Finally, I would like to send my sincerest thank to my family for their unconditional support and endless love during the last thirty years. I have received so much from you but could not repay. I have been waiting for this moment for years, and finally, I'm here. It has been more than three years since the last time I went home due to the pandemic. It was agonizing that I couldn't go back when my paternal grandmother passed away. I have no idea how many times I browsed old photos on my cell phone and how many times I went home in my dream but woke up with disappointment. A fun fact is that I always woke up before eating delicious hometown food, even though sometimes I knew it was a dream and wanted to get the food as soon as possible. The regular video call with my parents, Junqiang Yan and Ouxia Yin, is my spiritual pillar. Sometimes, I could talk to my grandparents and relatives when there was a family gathering. How I wish I could be there! Those video calls brought me a lot of strength to face any challenges. I still remember the day when I said goodbye to my parents in front of Tongji University. That was the beginning of my life being far away from you. Now, I see the light at the end of the tunnel. I will be back to your daily life soon. Last but not least, I would like to thank my wife, Yuxuan Feng. Although I have thanked you several times, I still want to give my gratitude again. Thank you for accompanying me during the past eight years. I spent a lot of time on my research in libraries and offices. You are the only one who accompanied me in libraries in different cities. I appreciate your understanding that I didn't have time to hang out with you often. We maintained our long-distance relationship for five years until we married in 2019. Thank you for sacrificing your work and life in Hong Kong and moving to The Netherlands in September 2019. It was not easy at first, as you were almost isolated from all social activities due to the pandemic. We both know how difficult it was. Fortunately, we overcame all difficulties, from which we learned and grew together. I am so happy to see that you gradually find where your passion is. Thanks for all the unique experiences you brought me, happiness or sadness, laughs or tears. The days with you are colourful and real.

Curriculum vitae

YAN Rui 延睿

21-03-1992 Born in Xianyang, China.

Education

2010-2014 Bachelor of Engineering in Civil Engineering
Tongji University, China

2015-2017 Master of Engineering in Architectural and Civil Engineering
Harbin Institute of Technology, China

2017-2022 PhD. in Steel & Composite Structures
Delft University of Technology, The Netherlands

Research projects

2020.2-2022.9 Tensile behaviour of welded X-joints made of rectangular hollow sections, funded by SSAB Europe.

2017.11-2020.12 INNOvative 3D JOINTS (INNO3DJOINT) for robust and economic hybrid tubular construction, funded by the Research Fund for Coal and Steel (RFCS).

2016.3-2017.7 Post-fire behaviours of reinforced concrete stub columns confined by steel tubes, funded by the National Natural Science Foundation of China.

Other academic activities

2018-2021 Supervise master students (as daily supervisor):

- Ajay Katta, Non-symmetrical column splice, 2019
- Milco Hahury, Component characterisation of T-plug bending around weak axis, experiment design and numerical study of a new type plug-and-play joint, 2020
- Bart Adegeest, Material factors for high strength rectangular hollow section X joints, 2020

- Hagar El Bamby, Experimental and numerical investigations on the structural performance of mild and high strength welded X-joints, 2021

2018.9-2022.2 Teaching assistance on master student course – CIE4115 Steel Structures 2:

- Independently prepare and give three lectures (two lectures in 2018) every year on the topic component method, which is one-third of the course major topics.
- Design and grade exams relating to the component method.
- Lectures were given on campus in 2018 and 2019. Then it was switched to online lectures since 2020 due to the pandemic.

2021.2 – 2021.9 Committee member of BEST Connections Tree Competition:

- Prepare the design task for the competition
- Review submitted works

List of publications

Journal papers

- **Rui Yan***, Hagar El Bamby, Milan Veljkovic, Kristo Mela. Experimental investigation on the tensile behaviour of welded RHS high strength steel X-joints, *Engineering Structures*, 2022.
- **Rui Yan***, Milan Veljkovic, Kristo Mela. Material properties of the heat-affected zone in welded cold-formed rectangular hollow section connections, *Thin-walled structures*, 2022.
- **Rui Yan***, Hagar El Bamby, Milan Veljkovic, Kristo Mela. Fracture simulation of welded RHS X-joints using GTN damage model, *Advances in Structural Engineering*, 2022.
- **Rui Yan***, Haohui Xin, Fei Yang, Hagar El Bamby, Milan Veljkovic, Kristo Mela. A method for determining the constitutive model of the heat-affected zone using digital image correlation. *Construction and Building Materials*, 2022.
- **Rui Yan***, Hagar El Bamby, Milan Veljkovic, Haohui Xin, Fei Yang. A method for identifying the boundary of regions in welded coupon specimens using digital image correlation. *Materials & Design*, 2021.
- **Rui Yan**, Haohui Xin*, Milan Veljkovic. Ductile fracture simulation of cold-formed high strength steel using GTN damage model. *Journal of Constructional Steel Research*, 2021.
- Lijun Li, Rui Wang, Hui Zhao*, Haoran Zhang, **Rui Yan**. Combined effects of elevated temperatures and high strain rates on compressive performance of S30408 austenitic stainless steel. *Structures*, 2021.
- Faqi Liu, Hua Yang*, **Rui Yan**, Wei Wang. Experimental and numerical study on behaviour of square steel tube confined reinforced concrete stub columns after fire exposure. *Thin-Walled Structures*, 2019.

Conference papers

- **Rui Yan***, Hagar El Bamby, Milan Veljkovic. Experimental and numerical study of butt welded joints made of high strength steel, *The 8th International Conference on Structural Engineering, Mechanics and Computation*, Cape Town, 2022.
- **Rui Yan**, Haohui Xin*, Milan Veljkovic. Identification of GTN damage parameters as a surrogate model for S355, *The 17th International Symposium on Tubular Structures*, Singapore, 2019.

- **Rui Yan***, Haohui Xin, Milan Veljkovic. Finite element pre-study of a beam-column bolted connection with an inclined endplate, International Conference on Engineering Research and Practice for Steel Construction, Hong Kong, 2018.

Contributions to EU-project INNO3DJOINT deliverables

- INNO3DJOINT Deliverable D2.1: Section 3 (Tensile tests of column splices) and Section 4 (bending tests of column splices), 2020.
- INNO3DJOINT Deliverable D2.2: Section 3 (Finite element analysis and parametric study of column splices in tension), Section 4 (Finite element analysis and parametric study of column splices in bending), and Section 5 (Characterization of components and validation of component method), 2020.
- INNO3DJOINT Deliverable D3.1: Section 3.3 and Section 6 (Finite element analysis of T-plug bending around weak axis), 2020.
- INNO3DJOINT Deliverable D3.2: Section 2.4, Section 3.3, and Section 6 (Experimental tests on T-plug bending around weak axis), 2020.
- INNO3DJOINT Deliverable D3.3: Section 2.3, Section 3.4, and Section 4.3 (Characterization of components), 2020.
- INNO3DJOINT Deliverable D7.1: Annex A.33 (Basic component – T-plug in minor axis bending), Annex A.36 (Basic component – corner and edge plate in bending), and Annex G (Design recommendations for moment-resisting bolted tubular splices), 2020.
- INNOvative 3D JOINTS for robust and economic hybrid tubular construction – final report, Section 7.2.2 (Column splices in tension), Section 7.2.3 (Column splices in bending), Section 7.2.3 and Section 8.2.3.2 (T-plug under transverse bending), 2020.

The project deliverables are part of the research project “INNOvative 3D JOINTS for robust and economic hybrid tubular construction” INNO3DJOINT supported by the European Commission through the Research Fund for Coal and Steel.